



Trinity College Dublin

Coláiste na Tríonóide, Baile Átha Cliath

The University of Dublin

PLATE-TYPE ACOUSTIC VALVE RESONATOR FOR, LOW-FREQUENCY SOUND ABSORPTION

MD ROBIUL HOSSAIN

SUPERVISOR: PROF. GARETH J. BENNETT

Department of Mechanical, Manufacturing & Biomedical Engineering

School of Engineering

Trinity College Dublin, *the University of Dublin*

D02 PN40, Ireland

May 10, 2024

A dissertation submitted in partial fulfillment of the requirements for the
degree of Doctor of Philosophy (PhD) in Mechanical & Manufacturing
Engineering

Declaration

I, declare that this report has not been submitted as an exercise for a degree at this or any other university and it is entirely my own work.

I agree to deposit this dissertation in the University's open access institutional repository or allow the library to do so on my behalf, subject to Irish Copyright Legislation and Trinity College Library conditions of use and acknowledgement.

I consent to the examiner retaining a copy of the thesis beyond the examining period, should they so wish (EU GDPR May 2018).

Md Robiul Hossain, May 10, 2024

Abstract

Plate-type acoustic metamaterials with deep-subwavelength thickness have generated considerable enthusiasm for addressing low-frequency noise. These metamaterials can be tailored to obtain high absorption efficiency by manipulating the vibro-acoustics behavior of the flexible structures.

A plate-type acoustic valve resonator is developed and optimised to maximise absorption by enhancing the Helmholtz resonance with coincident structural vibrations of the plate-type acoustic valve. The current research initially examines the concept experimentally with a 3D printed valve, then with the use of analytical and numerical modelling, a structural analysis is performed which allows the eigenmodes and eigenfrequencies of the plate to be determined. When the resonator properties are modified, either by changing the depth of the backing cavity, or the thickness of the plate, for example, the system can be designed such that the Helmholtz resonance can be coincident with a particular eigenfrequency leading to higher absorption than can be achieved in the absence of such a flexible plate. In addition, absorption also occurs at frequencies other than the Helmholtz frequency due to the vibration of the plate at additional eigenfrequencies. Both of these aspects of the technology advance the state-of-the-art in Helmholtz resonator design. A good agreement has been found between the modelling and experimental results. Near-perfect absorption was achieved experimentally, e.g. up to $\alpha = 0.995$ below 1 kHz, and given that the thickness of the technology can be a very small percentage of the acoustic wavelength that it is absorbing, deep sub-wavelength ratio absorbers can be designed, e.g. a ratio of up to 58 was achieved in this study with a 5 mm deep technology at 1.18 kHz.

The plate-type acoustic valve resonator was further characterized using thin plate theory and 2D-3D numerical simulation. Experimental modal analysis was performed to support the theoretical approximation, using the laser Doppler vibrometry (LDV) method. The theoretical results showed good agreement with the experimental measurements, validating the accurate identification of the structural resonance modes. It was also demonstrated that the structural resonance of the thin plate can be tailored to achieve high amplitude and broadband sound absorption at low frequencies by incorporating the Helmholtz resonance.

To my parents– Nur & Jebal

*In loving memory of my father!
Abbu, I miss you!*

Acknowledgements

Everyone says doing a PhD is a lonely journey. I am grateful that I've met so many nice and talented people on the way.

I would like to thank my supervisor Gareth J. Bennett for his support, enthusiasm, and guidance over the last four years. I am indebted to Henry Rice and John Kennedy for their valuable advice and suggestions. A massive thanks to them.

This research work was supported by Provost's PhD Project award from Trinity College Dublin. I gratefully acknowledge the financial support.

I would like to thank Andrew and Raphael for their time and advice. Thanks to Mick and Alex for their assistance with the office work and lab facilities. Thanks to Mads and Kiril for their generous support in setting up the FEM numerical model of the acoustic metamaterial.

Thanks to Wahid *bhai* and Mamun *bhai* for their guidance and valuable suggestions.

I am truly grateful to Eoghan for being there for me always. I couldn't ask for a better teammate than him. Thanks to Lara, Parth, Karina, Morgane, Muhammad, Kelvin, Jiayu, Seyi, Agnieszka for making our office cheerful.

Thanks to all of my friends who supported me always. Heartfelt thanks to a special one for understanding me and making me smile during difficult times.

Finally to my family, thanks to my parents Nur and Jebal for their unconditional love and support. I would like to thank my elder brother Zakir, for his tremendous support throughout my life. His generosity and kindness always inspire me. Thanks to my younger sister Moni, younger brother Shaon, and lovely nephews Amayr and Aadil.

I would like to remember my niece Maisha, my *Nanu* and my *Babu*. Although I lost you, you will always be with me.

Thanks to all of you, who made this possible.

Contents

Declaration	i
Acknowledgements	v
List of Figures	xvii
List of Tables	xx
Nomenclature	xxiii
1 Introduction	1
1.1 Context and Research Motivation	2
1.2 Objectives of the Research	4
1.3 Organization of the Thesis	5
2 Flexible Acoustic Metamaterial: A Review	7
2.1 Acoustic Metamaterials (AMM's)	8
2.2 Acoustic Metamaterial with Flexible Parts	10
2.2.1 Flexible Microperforated Plate	12
2.2.2 Membrane-type AMM	15
2.2.3 Beam-type AMM	17
2.2.4 Plate-type AMM	19
2.2.5 Cavity Based AMM's	21
2.2.6 Helmholtz Resonator With a Flexible Plate	23
2.3 Miscellaneous Flexible Structures	25
2.4 Conclusions	26
2.5 Contribution of the Thesis	26
3 Mathematical Modelling of Acoustics and Structural Vibrations	29
3.1 Numerical Modelling of Acoustics	30
3.1.1 Acoustic Wave Equation	30

3.1.2	Finite Element Method	31
3.2	Numerical Modelling of Structural Mechanics	33
3.3	Analytical Modelling of the Vibration of a Circular Plate	34
3.3.1	Vibration of Plate-type Acoustic Valve	35
3.3.2	Calculation of λ_{10} and f_{10}	39
3.3.3	Effect of Fluid-structure Interaction	40
3.4	Numerical Modelling of Thermo-viscous Acoustics	41
3.4.1	Boundary Layers	42
3.5	Numerical Modelling of Fluid-Structure Interactions	44
3.6	Summary	45
4	Development of Novel Plate-type Acoustic Valve Resonator	47
4.1	Plate-type Acoustic Valve Resonator	48
4.1.1	Prototypes Design	49
4.1.2	Additive Manufacturing Process	50
4.1.2.1	Additive Manufacturing	50
4.1.2.2	Manufacturing the Sample	52
4.2	Summary	54
5	Experimental Rig and Measurements Techniques	55
5.1	Experimental Setup	56
5.2	Measurements Techniques	58
5.2.1	Transfer Function Method	58
5.2.2	Laser Doppler Vibrometry (LDV) Method	59
5.3	Summary	62
6	Numerical Prediction of Plate-type Acoustic Valve Resonator	63
6.1	2D FEM Model: Modeling with Thermo-viscous Acoustics	64
6.1.1	Boundary Conditions	65
6.1.2	Meshing	67
6.1.3	Calculation of the Absorption Coefficient	69
6.2	Mesh Convergence	69
6.3	Parametric Analysis of Plate-type Acoustic Valve Resonator	71
6.3.1	Influence of the Material Properties	71
6.3.1.1	Young's Modulus (E_m) and structural loss factor η_m	72

6.3.1.2	Density (ρ_m) and Poisson's ratio ν_m	73
6.3.1.3	The ratio of Young's modulus and density ($\frac{E_m}{\rho_m}$)	74
6.3.2	Thickness of the plate-type acoustic valve (t_{APV})	75
6.3.3	Air-gap between Mounting plate and plate-type acoustic valve (h_d)	76
6.3.4	Cavity Depth (l_{cav})	77
6.4	Alternative Modelling Techniques in COMSOL	79
6.4.1	Modelling with Narrow-region Acoustics Interface	79
6.4.2	Modelling with Thermoviscous Boundary Layer Impedance	80
6.5	Summary	82
7	Characterisation of the Sub-wavelength Plate-type Acoustic Valve Resonator	83
7.1	Helmholtz Resonance of the Plate-type Acoustic Valve Resonator	85
7.2	Vibrational Analysis of the Plate-type Acoustic Valve	89
7.2.1	Analytical and Numerical Eigenfrequency Analysis	91
7.3	Particle Velocity in Plate-type Acoustic Valve Neck/Gap	95
7.4	Structural-Helmholtz Resonance Coincidence.	99
7.5	Effect of Thickness	100
7.6	Summary	101
8	Vibration Analysis of Plate-type Acoustic Valve Resonator	103
8.1	Three-dimensional FEM Model	104
8.2	Results & Discussions	105
8.3	Experimental Structural Resonance Modes	111
8.3.1	Identifying the radial modes ($0, n$)	123
8.3.2	Identifying the azimuthal modes (m, n) and $m \neq 0$	124
8.4	Measured Structural Loss Factor	127
8.5	Summary	127
9	Conclusions and Future Recommendations	129
	Bibliography	132
A		149
A.1	Paper	150
A.2	Numerical Prediction of Plate-type Acoustic Valve Resonator using Time Domain Analysis	165

A.2.1	Initial Strategies for Numerical Modeling	165
A.2.2	2D FEM Model: Time Domain	166
A.2.2.1	FEM Geometric Model	166
A.2.2.2	Boundary Conditions	167
A.2.2.3	Meshing	170
A.2.2.4	Estimation of the Reflection and Absorption Coefficient	171
A.2.2.5	Model including Structural Damping	172
A.2.3	Results	174
A.2.4	Conclusions	176
A.3	FEM Modeling of Microperforated plate	178
A.3.1	Frequency Domain Analysis	178
A.3.2	Time Domain Analysis	180
B		185
B.1	Eigenfrequency Analysis	186
B.2	Experimental Modal Analysis	187
C		189
C.1	Cambered Design of Plate-type acoustic valve resonator	190

List of Figures

2.1	Examples of the acoustic metamaterial with different values of the mass density and bulk modulus. (a) Ordinary materials with positive values for the mass density and bulk modulus.(b) A single-negative acoustic metamaterial, exhibiting a negative effective mass density [30]. (c) Acoustic metamaterial exhibiting negative bulk modulus [31]. (d) Double negative AMM's with negative effective mass density and negative bulk modulus [32]. (e) Density near zero AMM's [34]. (f) bulk modulus near zero AMM's [35]. (g) A fabricated double zero AMM's [36] taken from [37].	10
2.2	Traditional microperforated plate with circular perforation. (a) The schematic diagram for a numerical model with plane wave excitation [45], (b) fabricated sample [46] and (c) A flexible MPP backed by air cavity Temiz et al. [11].	13
2.3	Membrane type acoustic metamaterial. a) Transmission amplitude of the sample obtained by experimental measurements (solid red curve) and phase (dotted green curve) where the blue dashed line represents the transmission amplitude predicted by the mass density law (b) Transmission amplitude of the sample obtained by numerical simulation (solid red curve) and phase (dotted green curve) c) The normal velocity field distribution predicted by the numerical simulation at the vicinity to the membrane corresponding dip frequency of 272 Hz [33].	16
2.4	A beam in-parallel acoustic metamaterial. a) Measured the absorption coefficient of the resonator (magenta symbols). The blue and red lines are the absorption coefficients of the in-parallel resonators (IPR) and in-series resonator (ISR) models respectively. The dotted cyan line represents the absorption coefficient calculated by the lumped element model and the black circles correspond to the absorption coefficient obtained from numerical simulation. b) Some of the fundamental mode shapes of the thin titanium beam obtained from the numerical simulation[19].	20

2.5	Beam type acoustic metamaterial. a) A mono-articulated beam with a micro-slit loaded by a cavity b) First ($f=709$ Hz) and second ($f=4412$ Hz) structural resonance mode of the cantilevered beam and c) Absorption coefficient of the bi-articulated plate: Experimental measurements (blue curves) and analytical results (red curves) [18].	21
2.6	A schematic of the basic Helmholtz resonator and the spring-mass analogy of the Helmholtz resonator (Reproduced from [83]).	22
2.7	a) Schematic of the circular Helmholtz resonator with a flexible plate inside a plate holder and a second cavity b) The scattering coefficients of the Helmholtz resonator with a second cavity and a flexible plate [92].	25
3.1	Centrally fixed free edge thin circular plate of outer radius a , inner radius b and thickness t_{AD}	35
3.2	Displacement w of the circular plate as a function of r . The first five symmetric mode shapes for the centrally fixed circular plate with a free edge.	38
3.3	At standard conditions (1-atmosphere pressure and 20° C), the viscous and thermal boundary layers in air demonstrate distinctive thicknesses.	43
4.1	Elastomeric Valves tested. Umbrella Valves: UM 145, UM 180, CR 150, DU 120 . . .	48
4.2	(a) Cross-slit valves installed in mounting plate. (b) Test configuration with solid backing plate creating a cavity depth behind the sample [125].	48
4.3	Experimental absorption coefficient measured for off-the-shelf elastomeric valves with hardwall backing 43 mm from mounting plate [125].	49
4.4	Nominal geometric parameters of the plate-type acoustic valve.	50
4.5	Axisymmetric schematic of plate-type acoustic valve and cavity.	51
4.6	A pie chart showing the use of additive manufacturing technologies in acoustic research [126]	52
4.7	3D printed plate-type acoustic valve sample.	53
4.8	Mounting plate for plate-type acoustic valve.	53
4.9	Mounted 3D printed plate-type acoustic valve sample (Bottom View).	53
4.10	Mounted 3D printed plate-type acoustic valve sample (Top View).	54
5.1	Impedance tube schematic	57
5.2	Photograph of the experimental test section with impedance tube.	57

5.3	Impedance tube configuration for vibrational analysis.	60
5.4	Photograph of the experimental test section with PDV-100.	61
6.1	Simplified 2D axisymmetric geometric model for numerical simulation.	68
6.2	Simplified 2D axisymmetric geometric model for numerical simulation (meshed). . .	69
6.3	Absorption coefficient for different no. of DOFs in the 2D FEM numerical simulation.	70
6.4	Relative percentage of error in the absorption coefficient using different mesh. The maximum relative error is less than 1%.	70
6.5	Mesh element quality for different quality measures obtained from mesh statistics of COMSOL.	71
6.6	Absorption coefficient with different Young's modulus (E_m) of the material in the 2D numerical model.	72
6.7	Absorption coefficient with different structural damping of the material in the 2D numerical model.	73
6.8	Absorption coefficient with different density (ρ_m) of the material in the 2D numerical model.	74
6.9	Absorption coefficient with different Poisson's ratio (ν_m) of the material in the 2D numerical model.	74
6.10	Absorption coefficient with different specific modulus ($\frac{E_m}{\rho_m}$) of the material in the 2D numerical model.	75
6.11	Absorption coefficient with different thickness (t_{APV}) of the plate-type acoustic valve in the 2D numerical model.	76
6.12	Schematic of pumping effect where \mathbf{u}_{air} is the motion of the air and \mathbf{u}_{plate} is the motion of the flexible plate [121].	76
6.13	Absorption coefficient with different air-gap in the 2D model.	77
6.14	Absorption coefficient with different cavity depth in the 2D model.	78
6.15	Comparison between simulated absorption coefficients using thermo-viscous acous- tics, narrow region acoustics, and boundary layer impedance interfaces in 2D numer- ical modelling.	81
7.1	Absorption coefficient for mounting plate only with no plate-type acoustic valve. 40 mm cavity depth.	84
7.2	Absorption coefficient for 5 mm cavity depth.	85

7.3	Absorption coefficient for 10 mm, 20 mm, 30 mm and 40 mm cavity depths. Solid line: Experimental. Dotted line: Numerical.	86
7.4	Axisymmetric schematic of the plate-type acoustic valve and cavity (restated from Chapter 4, highlighting its importance in comprehending the absorption mechanism of Helmholtz resonance within the acoustic plate-valve configuration).	87
7.5	Absorption coefficient for 10 mm, 20 mm, 30 mm and 40 mm cavity depths. Numerical solution for a rigid plate which does not vibrate ($h_d = 1.3mm$).	88
7.6	Particle velocity in the vicinity of the air gap from a 2D axisymmetric FEM simulation. Numerical solution for rigid plate which does not vibrate ($l_{cav} = 40mm, h_d = 1.3mm$).	89
7.7	Plate-type acoustic valve absorption results as a function of cavity depth.	90
7.8	Comparison of absorption response when the material properties in the numerical model are altered (40 mm cavity depth).	91
7.9	The distribution of the particle velocity from the 2D axisymmetric FEM simulation. Viscous boundary layer formation can be seen inside the airgap between the mounting plate and plate-type acoustic valve (Excitation level = 94 dB).	97
7.10	Displacement amplitude at the edge point of plate-type acoustic valve concerning the Absorption coefficient in the 2D numerical model.	98
7.11	Velocity Magnitude at the edge point of plate-type acoustic valve concerning the Absorption coefficient in the 2D numerical model.	98
7.12	Structural-Helmholtz resonance coincidence through varying the cavity depth.	100
7.13	Structural-Helmholtz resonance coincidence through varying the plate thickness.	101
8.1	Conversion steps from 2D to 3D numerical model (vibroacoustic simulation) for plate-type acoustic valve resonator using frequency domain analysis.	105
8.2	3D FEM model of plate-type acoustic valve for eigenfrequency analysis. The small central circular portion is clamped with fixed constraints.	105
8.3	Absorption coefficient for $l_{cav} = 40$ mm cavity depth from experiment, 2D and 3D numerical simulation (without damping).	106
8.4	Experimental absorption coefficient and velocity profile from acoustic measurements and laser Doppler vibrometer measurements, respectively.	107
8.5	Absorption coefficient for $l_{cav} = 40$ mm cavity depth from experiment, 2D and 3D numerical simulation (with damping factor $\eta=0.03$).	108

8.6	Comparison between experimental and 2d-3D numerical velocity profile.	108
8.7	3D Numerical simulation using parametric analysis varying Young's modulus (E_m) of the material.	109
8.8	3D Numerical simulation using parametric analysis varying structural loss factor (η_m) of the material.	109
8.9	3D Numerical vibrational modes for plate-type acoustic valve in presence of acoustic cavity with structural damping (loss factor $\eta_m=0.005$). Also, coupled mode can be seen at 280 Hz and 1598 Hz.	110
8.10	The experimental frequency response function (FRF) in different points (19–24) along the nodal diameter of the thin circular plate.	112
8.11	The imaginary part of the experimental frequency response function (FRF) in different points (19–24) along the nodal diameter of the thin circular plate.	113
8.12	The experimental coherence function in different points (19–24) along the nodal diameter of the thin circular plate.	114
8.13	The experimental frequency response function (FRF) in different points (43–48) along the nodal diameter of the thin circular plate.	115
8.14	The imaginary part of the experimental frequency response function (FRF) in different points (43–48) along the nodal diameter of the thin circular plate.	116
8.15	The experimental coherence function in different points (43–48) along the nodal diameter of the thin circular plate.	117
8.16	The experimental FRF magnitude diagram in different points (19–24) along the nodal diameter of the thin circular plate.	118
8.17	The experimental FRF phase diagram in different points (19–24) along the nodal diameter of the thin circular plate.	119
8.18	The experimental FRF magnitude diagram in different points (43–48) along the nodal diameter of the thin circular plate.	120
8.19	The experimental FRF phase diagram in different points (43–48) along the nodal diameter of the thin circular plate.	121
8.20	Section view of experimental measurements with LDV(Considering the scanning points 19–24) (left) and numerical (right) mode shapes for the plate-type acoustic valve in the presence of an acoustic cavity.	123

8.21	Experimental azimuthal mode shapes for (1, 1) and (2, 1) vibrational modes. Corresponding resonance frequencies are $f_{11}= 280$ Hz and $f_{21}= 385$ Hz. a) Vibrational mode shape for resonance frequency $f_{11}= 280$ Hz a1) Mode shape along the points 43-48 and 19-24 a2) Mode shape along the points 7-12 and 31-36. b) Vibrational mode shape for resonance frequency $f_{21}= 385$ Hz b1) Mode shape along the points 43-48 and 19-24 b2) Mode shape along the points 7-12 and 31-36.	125
A.1	Simplified 2D axisymmetric geometric model for numerical simulation.	167
A.2	Close up of the deforming domain in the open area between plate-type acoustic valve and mounting plate. In the inset we can see the deformation from the equilibrium position with movement of the mesh.	170
A.3	Comparison between absorption coefficients as a function of frequency from numerical results with moving mesh and experimental results.	175
A.4	Comparison of absorption coefficients as a function of frequency from numerical results with two different airgap $h_d = 0.1$ mm and 0.4 mm.	176
A.5	Comparison of absorption coefficients as a function of frequency from numerical results with two different incident pressure $p_{inc} = 20$ Pa and 1 Pa.	176
A.6	Simplified 2D axisymmetric geometric model of the numerical simulation for time domain analysis (top), overview of the mesh for the setup (bottom) and the mesh shown in the vicinity of the hole with boundary layer (inset).	179
A.7	Comparison of absorption coefficients in frequency domain and time domain model as a function of frequency.	181
A.8	Comparison of the velocity field vicinity to the perforations with user defined mesh in (a) time domain and (b) frequency model.	182
A.9	Comparison of absorption coefficients as a function of frequency from analytical, numerical (time domain) and experimental results.	183
B.1	Linear elastic material model for eigenfrequency analysis.	186
B.2	Flow chart for the experimental modal analysis.	188
C.1	3D printed cambered plate-type acoustic valve sample.	190
C.2	Mounted 3D printed cambered plate-type acoustic valve sample.	191
C.3	Mounted 3D printed cambered plate-type acoustic valve sample(Top View).	191
C.4	Mounted 3D printed cambered plate-type acoustic valve sample (Bottom View).	191

C.5	Experimental absorption coefficients as a function of frequency for different cavity depths with $SPL=94$ dB.	192
C.6	2D axisymmetric numerical model of the cambered plate-type acoustic valve for eigenfrequency analysis.	193
C.7	Structural eigenfrequencies in the experimental absorption coefficients as a function of frequency for different cavity depths with $SPL=94$ dB.	193

List of Tables

3.1	Modelling parameter for plate-type acoustic valve	35
3.2	Modal parameters for uniform thickness centrally fixed free edge thin circular plate Leissa [93].	39
3.3	Analytical eigenvalues[93] and eigenfrequencies of the centrally fixed free edge cir- cular plate.	39
4.1	Off-the-shelf elastomeric valves by Minivalve [124]	49
6.1	Properties of air	68
7.1	Parameters and values of the terms in Fig. 7.4.	88
7.2	Helmholtz frequencies as a function of backing cavity depths.	88
7.3	Eigenfrequencies of a completely free thin circular plate in a vacuum.	92
7.4	Modal frequency comparison.	93
7.5	Eigenfrequencies and corresponding mode shape from 2D axis-symmetric numerical model for the centrally fixed free edge circular plate: Eigenfrequency Analysis. . . .	95
8.1	Eigenfrequencies and corresponding mode shape from 3D numerical model: Eigen- frequency Analysis.	122
8.2	Experimental radial modes and corresponding resonance frequencies using different scanning points.	124
8.3	Comparison between experimental and numerical azimuthal modes.	125
8.4	Comparison of experimental modal frequencies to those obtained using an analytical model and numerical model.	126
A.1	Parameters for linear elastic material model	169
A.2	Geometrical parameters of the microperforated plates	178

C.1	Some of the eigenfrequencies and corresponding mode shape from 2D numerical model: Eigenfrequency Analysis.	194
C.2	Comparison between experimental and numerical structural resonance frequencies. .	195

Nomenclature

Acronyms

<i>AFC</i>	Active Force Control
<i>AMM</i>	Acoustic Metamaterial
<i>BC</i>	Boundary Conditions
<i>BEM</i>	Boundary Element Method
<i>CFD</i>	Computational Fluid Dynamics
<i>DMR</i>	Decorated Membrane Resonator
<i>DNS</i>	Direct Numerical Simulation
<i>DOF</i>	Degrees-of-Freedom
<i>EM</i>	Electro-magnetic
<i>f – MPP</i>	Flexible Microperforated Plate
<i>FDTD</i>	Finite Difference Time Domain
<i>FEM</i>	Finite Element Method
<i>FRF</i>	Frequency Response Function
<i>LDV</i>	Laser Doppler Vibrometry
<i>MAMM</i>	Membrane-type Acoustic Metamaterial
<i>MPP</i>	Microperforated Plate
<i>MPPA</i>	Microperforated Plate Absorber

<i>PDE</i>	Partial Differential Equation	
<i>PWE</i>	Plane Wave Expansion	
<i>SPL</i>	Sound Pressure Level	dB
<i>STL</i>	Sound Transmission Loss	dB

Greek Symbols

α	Absorption Coefficient	
β_{mn}	Added virtual mass incremental (AVMI) factor	
δ	Loss Tangent	
η	Loss Factor	
γ_p	Non-dimensional Mass	
λ	Wavelength	m
λ_{mn}	Eigenvalue	
ν	Poisson's Ratio	
ω	Angular frequency	rad/s
ϕ	Porosity	
ρ	Density	kg/m ³
ε	Total strain tensor	
ξ	Dissipation Factor	

Roman Letters

<i>A</i>	Area	m ²
<i>B</i>	Bulk modulus	Pa
<i>c</i>	Speed of Sound	m/s
<i>D</i>	Bending Stiffness	Pa · m ³

E	Young's Modulus	Pa
f	Frequency	Hz
f_{HR}	Helmholtz Resonance Frequency	Hz
f_{mn}	Eigenfrequency	Hz
f_r	Resonance Frequency	Hz
H_{12}	Transfer function between microphones 1 and 2	
h_d	Air-gap height	m
J	Moment of Inertia	$\text{kg} \cdot \text{m}^2$
k_f	Accession coefficient	
k_p	Mass coefficient	
l_{cav}	Cavity Depth	m
p	Total sound pressure	Pa
p_b	Background pressure	Pa
p_{inc}	Incident pressure	Pa
p_r	Reflected pressure	Pa
p_t	Total acoustic pressure	Pa
r	Reflection Coefficient	
r, z	2D axis-symmetric coordinates	m
t_{AD}	Thickness of the valve	m
v	Wave Velocity	m/s
Z	Acoustic Impedance	$\text{Pa} \cdot \text{s}/\text{m}^3$

List of Publications & Presentations

- Hossain, M. R., & Bennett, G. J. (2023). Vibration Analysis and Numerical Modeling of Plate-type Acoustic Valve Resonator, *In draft*.
- Hossain, M. R., Ross, E. P., & Bennett, G. J. (2023). Acoustic Plate-Valve Resonator for Low-Frequency Sound Absorption. *AIP Advances* 13, 065210 (2023). <https://doi.org/10.1063/5.0142908>.
- Hossain, M. R., Ross, E. P., and Bennett, G. J. Acoustic diode metamaterial for broadband low frequency sound absorption varying cavity depths. In 28th AIAA/CEAS Aeroacoustics Conference, Southampton, UK, 2022.
- Bennett, Gareth J., Robiul Hossain, Andrew McKay, and Eoghan P. Ross. Acoustic Diode Metamaterial for Sound Absorption. In 25th AIAA/CEAS Aeroacoustics Conference, Delft, the Netherlands, p. 2422. 2019.
- Bennett, Gareth J., Eoghan P. Ross, and Robiul Hossain. "Membrane Metamaterials For Use In Broadband Noise Attenuation." 25th AIAA/CEAS Aeroacoustics Conference, Delft, the Netherlands, 2019.
- Md Robiul Hossain, Andrew McKay, Eoghan P. Ross and Gareth J. Bennett. Time Domain Prediction of a Microperforated Plate Absorber Using the Finite Element Based Numerical Model. In COMSOL Conference, Cambridge, UK. 2019.
- "Acoustic Valve for Broadband Low-frequency Sound Absorption."- presented for the selection of Sir Bernard Crossland Symposium at TCD Parsons Building. Feb 2020.
- "Quiet, Hybrid and Long Endurance UAV"- Ana V., Ferdinand G., Robiul H., Wensheng Z., Hongzhuo L., and Nana C. -awarded presentation in International Graduate Summer School in Aeronautics and Astronautics 2019 (IGSS), Beihang University, Beijing, P.R. China.

Chapter 1

Introduction

1.1 Context and Research Motivation

Noise is an alarming concern due to its harmful effects on the environment, health, and the quality of human life. Growing urban populations lead to growth in the construction of buildings and private or public transportation systems. The aviation industry has also seen dramatic growth over 20 years with passenger numbers rising from 1.5 billion in 1998 to 4 billion in 2017. People who live in the vicinity of major airports experience considerable amounts of sound pollution. Exposure to loud noise increases the risk of developing several adverse health conditions such as high blood pressure, hypertension, fatigue, stress, coronary heart diseases, etc. [1] Sleep disturbance due to noise pollution also leads to reduced work and school performance hence making it vital to eliminate this undesired noise.

Traditional natural porous materials such as wool and cotton as well as synthetic glass fiber and melamine foams etc. have been used for noise reduction for many years. However, these materials are effective only at reducing high-frequency noise at reasonable thicknesses. According to the mass density law, thicker porous material is required to attenuate low-frequency noise. Adding mass and increasing thicknesses (which can equate to reducing useful space) is to be avoided in the construction of buildings and factories where people can be exposed to noise. With regards to transportation noise, both weight and space are critical parameters that need to be minimized in order to reduce fuel consumption and the associated environmental cost [2, 3]. Although composite structures such as perforated absorbers, acoustic mufflers, double walls with cladding, etc. have been used in rooms, auditoriums, offices, aircraft fuselages, cars, trains, etc. to attenuate low-frequency noise, the attenuation of low-frequency noise in a thin form factor still remains an intractable challenge.

Since the early 2000s, research in the field of acoustic metamaterials (AMM's) has expanded considerably in the application of low-frequency noise reduction. Originating in the fields of electromagnetics and optics, the extension to acoustic metamaterials has led to this nascent research activity in acoustics which has tremendous potential for the development of fundamental science and for revolutionary technological breakthroughs. Acoustic metamaterials are artificial structures that are periodic in nature and which often involve local resonators designed to resonate at specific frequencies, rendering them, therefore, often tonal or highly narrow bands in nature. The early acoustic metamaterials primarily consisted of periodic microstructures characterized by specific resonance properties, and these microstructures were embedded within a matrix material. Later, due to advancements in research, the notion of acoustic metamaterials has broadened and evolved. Torrent and Sánchez-Dehesa [4] proposed that any artificial acoustic structure, whether it employs a periodic or random structural

unit, with the capacity to notably change the material's equivalent acoustic properties, can be categorized as an "acoustic metamaterial." While resonators are a common mechanism in AMM's, there are other mechanisms and structures that can be employed to achieve unique and desirable properties. These mechanisms include: scattering elements, phase discontinuities, local resonances, mass inclusions etc.

Traditionally, micro-perforated panel absorbers (MPPA) have been used for broadband sound absorption, but typically these only work in mid to high-frequency ranges. Some AMMs research has been reported for low-frequency sound absorption. Mei et al. [5] demonstrated an elastic membrane decorated with asymmetric rigid iron platelets, known as a decorated membrane, for low-frequency absorption as low as 164 Hz. The dimensions of this system are 159 mm x 15 mm x 0.2 mm. Subsequently, Li and Assouar [6] proposed a metasurface-based structure that can absorb incident acoustic energy at a low frequency of approximately 125 Hz, with the total thickness of the system being 12.2 mm. Their structures are composed of a perforated plate and a labyrinthine structure. They also presented extremely low-frequency absorption (around 50 Hz with the total thickness of the system being 13 mm) with multi-coiled metasurface [7] and broadband sound absorption in the frequency ranges of 460 Hz–972 Hz and 232 Hz–494 Hz from the two individual supercell-based acoustic metasurface coiled absorbers and having thickness of 4.5 cm and 9 cm respectively[8]. Lee et al. [9], Wang et al. [10], Temiz et al. [11], Martincic et al. [12] etc. all studied the MPP-based low-frequency absorber including the vibroacoustic and panel vibration effect of the structure. McKay et al. [13] very successfully developed a novel low-frequency broadband sound absorber called a SeMSA. It is achieved by combining decorated membranes and micro-perforated plates. This absorber consists of 15 mm deep cells with a plate thickness of 0.15 mm and 25 mm deep cells with a plate thickness of 0.1 mm. Following that, Davis et al. [14] used graph theory based on a two-point impedance method to optimize a multi-chamber SeMSAs which resulted in a very broadband low-frequency absorption response or even an absorption response tailored for fan noise. Killeen, Jack et al. [15] applied the SeMSA to reduce the fan noise of data-center telecommunications server racks which is particularly challenging as it is a grazing acoustic and grazing flow boundary condition. Wang and Bennett [16] applied the two-point impedance method to optimize a multi-chamber MPPA which has resulted in a very broadband low-frequency absorber.

In the literature, it's evident that all AMM's with a low thickness to wavelength ratio depend on acoustic resonances. Research has demonstrated that in the case of a Single Degree Of Freedom (SDOF) resonator, the operating frequency band becomes narrower as the wavelength becomes longer

in relation to the size of the absorber. Some exceptions to this are cited here where the motion of a cantilever beam absorbs sound through resultant micro-slits. Farooqui and Aurégan [17], Delia et al. [18] proposed a numerical and analytical model for a structure composed of a flexible cantilever beam producing acoustic micro-slit with a compact cavity and demonstrating attenuation around 500 Hz with a 3 cm cavity depth. Aurégan and Farooqui [19] developed a sub-wavelength acoustic absorber using an MPP-based thin flexible beam with micro-slits for perfect sound absorption in the mid-frequency range.

In the current work, the concept of a plate-type acoustic valve design has been developed based on the promising preliminary investigations of off-the-shelf elastomeric valves [20] which are used as one-way valves in fluidic-control. As is well understood, the standard Helmholtz resonator consists of a rigid volume with an orifice that is stationary. In this work, a Helmholtz resonator has been developed which has an unusual plate valve located at the opening. The plate valve is flexible with the capacity to vibrate at its natural frequencies. When the resonator properties are modified, either by changing the depth of the backing cavity, or the thickness of the plate-valve, for example, the system can be designed such that the Helmholtz resonance can be coincident with a particular eigenfrequency leading to higher absorption than can be achieved in the absence of such a flexible plate-valve.

1.2 Objectives of the Research

The primary aim of the current research is to develop a novel acoustic metamaterial capable of mitigating low-frequency noise. The developmental process encompasses designing a 3D-printable plate-type acoustic valve and determining the plate-valve characteristics that influence their acoustic performance. Additionally, the research involves experimental testing of the plate valve's acoustic performance.

Analytical, experimental, and numerical studies constitute the core methodologies employed to achieve this objective. The analytical approximations are based on thin plate theory. Experiments are conducted within an impedance tube setup, utilizing two microphone methods and laser Doppler vibrometry (LDV). For numerical modeling, the finite-element method (FEM) is employed through the commercial FEM software COMSOL Multiphysics v. 6.0 [21]. This involves utilizing built-in modules such as pressure acoustics, thermoviscous acoustics, structural mechanics, and multi-physics coupling to implement a comprehensive numerical model. The acoustic performance of the numerical model is predicted using eigenfrequency and frequency domain analyses. Validation of simulation results against theory and measurements precedes the formulation of conclusions.

1.3 Organization of the Thesis

The thesis is organized as follows:

Chapter 2 is a detailed review of the flexible acoustic metamaterials. The plate-type, membrane-type, beam-type, and cavity-based acoustic metamaterial are presented in this chapter.

Chapter 3 delves into the mathematical principles governing acoustics, viscothermal effects, and structural vibrations.

Chapter 4 provides the design and 3D printing of novel acoustic metamaterial (termed as “plate-type acoustic valve resonator”) and shows total sample design and fabrication procedure with relevant sketches, design samples, and photographs of fabricated samples.

Chapter 5 includes the documentation of experimental setup and measurement techniques with brief discussions.

Chapter 6 presents the finite element modeling techniques with COMSOL Multiphysics and modeling validation with comparison study between several models.

Chapter 7 contains an investigation of the absorption mechanism of the plate-type acoustic valve resonator.

Chapter 8 provides the vibration analysis of plate-type acoustic valve resonators including the structural resonance using experimental measurements with a laser Doppler vibrometer.

Chapter 9 concludes the thesis by summarizing research work, perspective future works, and recommendations.

Chapter 2

Flexible Acoustic Metamaterial: A Review

2.1 Acoustic Metamaterials (AMM's)

Acoustic Metamaterials (AMMs) represent an emerging technology aimed at mitigating the challenge of attenuating low-frequency noise in thin form factors.

The concept of metamaterials was initially proposed by Veselago in the late 1960s for electromagnetic waves [22]. Initially, metamaterials were conceived around the idea of achieving simultaneously negative dielectric constants and magnetic permeability, ultimately resulting in a negative refractive index for electromagnetic (EM) waves. However, it wasn't until almost three decades later that Pendry et al. [23, 24] physically realized this concept. Their research introduced designs for artificially structured materials demonstrating effectively negative permeability and permittivity, showcasing that a negative refractive index could be achieved through periodic structures.

These seminal papers established a new field in EM metamaterials, sparking subsequent intense research activity that led to breakthroughs such as overcoming the diffraction limitation for imaging [23], cloaking EM waves [25], and achieving ultra-broadband light absorption [26].

The development of metamaterials for acoustic wave applications traces back to the initial concept of a phononic crystal proposed by Kushwaha et al. in 1993 [27]. Phononic crystals are artificially structured materials with a regular arrangement of individual components, acting as acoustic scatterers within a matrix. These components possess significant differences in mass densities and/or elastic moduli, giving rise to distinct acoustic dispersions and band structures. This is achieved through periodic Bragg scattering and localized Mie scatterings from these individual elements.

Phononic crystals find utility in creating band gaps in the sound wave spectrum, where certain frequencies of sound cannot propagate through the material, finding applications in sound insulation, waveguides, and the control of acoustic energy flow. The formation of acoustic band gaps in a phononic crystal heavily relies on the impedance contrast between the periodic elements constructing the crystal and the surrounding medium.

Similar to the phononic crystal, the initial experimental demonstration of sound attenuation using a sonic crystal was documented by Martinez and Sanchez-Prez in 1995 [28]. An example of a sonic crystal, an artistic creation by Eusebio Sempere in Madrid, comprised a periodic arrangement of steel cylinders in air. Sonic crystals, composed of regularly arranged sound scatterers, obstruct sound propagation within specific frequency ranges, termed bandgaps. These gaps form due to the physical mechanism of destructive interference between waves reflected by successive planes of sound scatterers, akin to photonic crystals designed for controlling electromagnetic wave propagation.

The foundational research area of AMMs, drawing analogies to Maxwell's equations by equating permeability and permittivity to effective density and effective bulk modulus, only began to emerge in the early '90s.

Acoustic Metamaterials refer to structures involving local resonators typically resonating in lower frequencies and are characterized by two relevant material properties: effective mass density and effective bulk modulus. The equation governing scalar pressure wave propagation within a homogenous linear fluid, without any excitation sources, is represented as:

$$\nabla^2 p - \frac{\rho}{B} \frac{\partial^2 p}{\partial t^2} = 0 \quad (2.1)$$

where, p is the acoustic pressure while ρ and B represent the mass density and bulk modulus respectively within the natural media. These values are taken as positive in traditional scenarios, where the wave velocity (v) is given by $v = \sqrt{\frac{B}{\rho}}$. However, in the case of Acoustic Metamaterials (AMMs), these properties not only can exhibit positive values (such as very large or very small), but also negative values, and even zero. This characteristic leads to distinctive physical phenomena that can be harnessed to manipulate acoustic wave propagation. These phenomena are defined by Newton's law of motion, the continuity equation of fluid, and the adiabatic process of the thermodynamic equation of state [29].

Figure (2.1) illustrates examples of AMMs compared to extreme consecutive parameters. The first localized resonant structure with negative mass density was demonstrated by Liu et al. [30], utilizing a cubic unit cell of a lead sphere coated with a thin uniform layer of silicone rubber. AMMs exhibiting negative bulk modulus due to the frequency dispersion of local resonances were presented by Fang et al. [31], employing a series of Helmholtz resonators connected to one side of a channel.

Furthermore, AMMs showcasing double negativity, involving negative mass density and negative bulk modulus, were experimentally demonstrated by Lee et al. [32]. They used a composite structure consisting of a periodic array of thin membranes and side holes. In this structure, the array of thin membranes represents the negative density component, while the combination of side holes and the tube section volume forms an array of Helmholtz resonators representing the negative bulk modulus component.

Additionally, Yang et al. [33] and Mei et al. [5] presented membrane-type metamaterials with a negative effective mass density, offering nearly perfect low-frequency sound absorption with a deep sub-wavelength ratio. These research endeavors paved the way for developing acoustic absorbers

using flexible structures, enabling the tailoring of resonance frequency(-ies) to achieve low-frequency absorption.

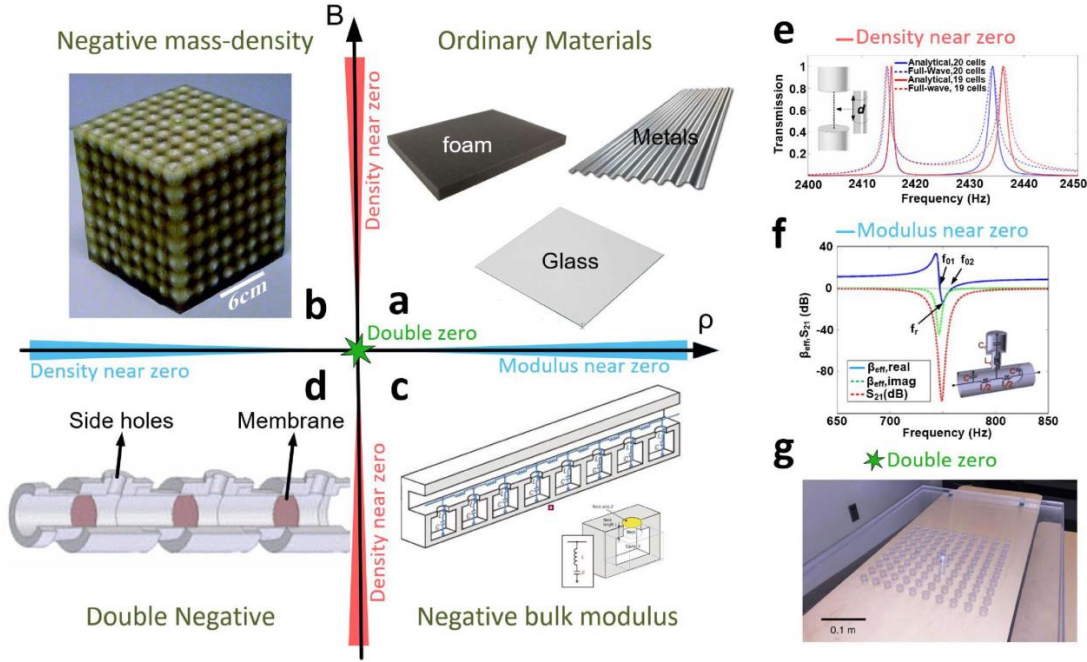


Figure 2.1: Examples of the acoustic metamaterial with different values of the mass density and bulk modulus. (a) Ordinary materials with positive values for the mass density and bulk modulus. (b) A single-negative acoustic metamaterial, exhibiting a negative effective mass density [30]. (c) Acoustic metamaterial exhibiting negative bulk modulus [31]. (d) Double negative AMM's with negative effective mass density and negative bulk modulus [32]. (e) Density near zero AMM's [34]. (f) bulk modulus near zero AMM's [35]. (g) A fabricated double zero AMM's [36] taken from [37].

2.2 Acoustic Metamaterial with Flexible Parts

In recent years, the development of acoustic metamaterial with flexible parts (i.e. plate, membrane, beam, etc.) for low-frequency noise reduction has drawn tremendous enthusiasm. Plate-type and membrane-type structures such as Micro-perforated plate (MPP) [38] [39], conventional elastic membranes, and decorated membrane resonators (DMR's) [33] [5] has been proposed as an acoustic absorber over the years. Generally, traditional sound absorbers, such as foam or porous materials, adhere to the mass density law, requiring structures to be sufficiently thick for effective use in low-frequency applications. Microperforated plates with an acoustic cavity became a popular choice of sound absorbers due to their high absorption and wide-band performance in low-frequency ranges. Combining MPP with different resonator structures or slow sound structures has been proposed to obtain very

low-frequency absorption or multiple absorption peaks. The phenomenon known as 'slow sound,' is related to the manipulation of acoustic waves in a system by exploiting strong dispersion around resonances. This unique phenomenon provides the capability to easily modify the speed of sound and reduce inherent losses by making alterations to the geometry and properties of the resonators within the system. For example, an acoustic metasurface-based perfect absorber has been developed by Li et al. [40] combining labyrinthine structures and MPP, which provides unity absorption at 125.8 Hz with total thickness of the system being 12.2 mm. Also, Gai et al. [41] has investigated the acoustic properties of the acoustic absorber, named MPP mounted with Helmholtz resonators (MPPHR) which provides two peak frequencies and one anti-resonant frequency. However, most of the absorbers are designed with a rigid structure, and the vibration of the structure is often neglected for simplicity or considered as negligible. As a vibrating structure, several resonance modes can be present. For a flexible structure, it is possible to take advantage of their resonance modes that appear in low frequencies to obtain multiple absorption peaks. The first flexible panel as a sound absorber has been introduced by Ford and McCormick [42] in 1969. They developed a theoretical model including the mass, stiffness, and internal damping of the panel and successfully validated the model using experimental investigation. This research demonstrated that the resonant frequencies of the flexible panel can be manipulated to obtain sound absorption performance. While the amplitude of the first absorption peak at the initial resonant frequency is quite low, the second absorption peak is comparatively higher but exhibits a narrower bandwidth. This paves the way to investigate the resonance modes of the structure to obtain higher and multiple absorption peaks in further research. Lee and Swenson [43] has developed a compact sound absorber with a perforated panel backed by a cavity. In the experimental results, they reported some "unexpected" resonance peaks and concluded those as the effect of the vibration of the panel. Frommhold et al. [44] has proposed an analytical model of a flexible perforated membrane absorber considering the effect of panel vibration. The membrane is considered a thin plate with clamped edge and the model included the material properties of the plate as well as the lowest symmetrical resonance modes of the plate. After that, several research has been reported including the effect of sound-induced vibration in acoustic absorbers.

The benefits of using the flexible panel as an acoustic absorber can be summarized in several points.

- Flexible structures provide the flexibility and deformability which is necessary in many applications.

- As a resonant structure, several structural resonances can appear and can provide multiple acoustic absorption peaks.
- Considering the flexural rigidity of the structure, the natural frequencies are proportional to the thickness of the structure particularly for beam, plate, or membrane-type structures. So, the thin flexible structure can be used for low-frequency applications.
- Other resonant structures (i.e. Helmholtz resonator, MPP, labyrinthine structure) can be combined with flexible structures to improve the absorption amplitude and bandwidth.
- The natural frequencies of the vibro-acoustic/elastic material can be modified using different materials. Several selections of materials are available for additive manufacturing (i.e. PLA, ABS, Nylon). The convenience of additive manufacturing (popularly known as 3D printing) technology also helps to rapid prototyping acoustic metamaterial at a very low cost and in a less time-consuming process.

In the next section, a detailed review of flexible acoustic metamaterial has been presented starting with the flexible microperforated plate.

2.2.1 Flexible Microperforated Plate

Micro-and perforated plate as an absorber has been studied extensively after the classical Maa model presented in 1975 [38]. This analytical model was further extended with approximate formulae, quantitative analyses, and straightforward design procedures in 1987 and parametric analyses in 1998 [39] by Maa himself. Figure (2.2) illustrates a traditional and flexible microperforated plate with circular perforations. Based on the solution by Crandall [47] the specific acoustic impedance of the short tube is

$$Z_{ST} = i\omega\rho_0 l_t \left[1 - \frac{2}{\sigma\sqrt{-i}} \frac{J_1(\sigma\sqrt{-i})}{J_0(\sigma\sqrt{-i})} \right]^{-1} \quad (2.2)$$

where

$$\sigma = d\sqrt{\frac{\omega\rho_0}{4\mu}} \quad (2.3)$$

and J_0 and J_1 are the Bessel functions of zeroth order and first order respectively, μ is the dynamic viscosity, l_t the tube length, and d the diameter of the tube, ρ_0 is the air density and ω is the angular frequency. Using the end correction, for microperforated plate, Eq. (2.2) can be simplified as [48]

$$Z_{MPP} = \frac{Z_{ST}}{\phi} + \frac{\sqrt{2\omega\rho_0\mu}}{2\phi} + \frac{i1.7\omega\rho_0 d}{\phi} \quad (2.4)$$

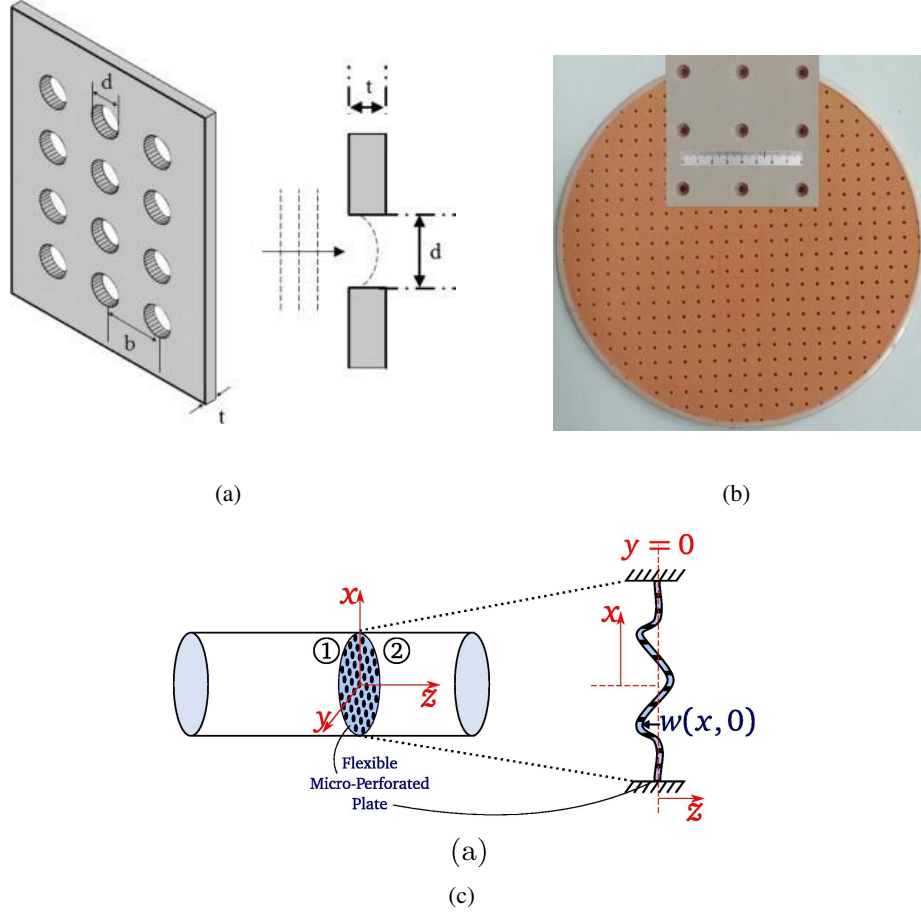


Figure 2.2: Traditional microperforated plate with circular perforation. (a) The schematic diagram for a numerical model with plane wave excitation [45], (b) fabricated sample [46] and (c) A flexible MPP backed by air cavity Temiz et al. [11].

where ϕ is the porosity which can be defined as the ratio of the overall area of circular holes and the total area of the plate. If the MPP is placed in front of the air-filled cavity of depth l_{cav} followed by a hard wall, the impedance of the acoustic cavity can be written as:

$$Z_{cav} = -i\rho_0 c_0 \cot(k_0 l_{cav}) \quad (2.5)$$

where k_0 is the wave number and c_0 is the speed of sound. Though the Maa model works reasonably well, it assumes the panel to be rigid and does not account for panel vibration. Especially for very thin plates, significant differences exist between experimental results and predictions from analytical models. While Ford and McCormick [42] and Frommhold et al. [44] have provided experimental and theoretical investigations of acoustic panel absorbers without considering the effect of perforations, Sakagami et al. [49] and Kang and Fuchs [50] developed theoretical models for micro-perforated

membrane absorbers. These models include the specific acoustic resistance and reactance of the membrane but do not incorporate the flexural rigidity or bending stiffness of the panel. Notably, only Frommhold et al. [44] included the bending stiffness of the panel in their analytical model. Since the MPP with an acoustic cavity system can be represented by the analogy to an electrical circuit and the normalized acoustic impedance of the total system, Z_t can be rewritten as

$$Z_t = \frac{Z_{MPP}Z_{Vib}}{Z_{MPP} + Z_{Vib}} + Z_{cav} \quad (2.6)$$

$$Z_{Vib} = \frac{D_p B_{mn} \xi}{\omega t_p^4} + \frac{1}{j\omega} \left(\frac{D_p B_{mn}}{t_p^4} + \frac{\rho_0 c_0^2}{l_{cav}} \right) + j\omega M_p A_{mn} \quad (2.7)$$

where, A_{mn} and B_{mn} are the modal constants that depend on the boundary conditions of the plate, ξ is the dissipation factor of the plate material, M_p is the mass per unit area of the panel, t_p is the thickness of the panel, l_{cav} is the air cavity depth, and D_p is the flexural rigidity of the panel and can be written as

$$D_p = \frac{E_p t_p^3}{12(1 - \nu_p^2)} \quad (2.8)$$

where, E_p is the Young modulus and ν_p is the Poisson's ratio of the plate material. Sakagami et al. [51] developed an analytical model of a micro-perforated panel (MPP) that incorporates the effect of sound-induced vibration as a mass parameter. This simplified approach is based on an electro-acoustical equivalent circuit model, which is valid under simplified conditions. For instance, it works well when the mass per unit area does not exceed 2 kg/m^2 . Beyond this threshold, the difference in absorption peaks becomes relatively small, and the absorption performance of the vibrating MPP panel becomes similar to that of a rigid MPP panel.

Lee et al. [9] developed an analytical model combining the effects of the micro-perforated panel and panel absorbers, including acoustical-structure interactions, and proved experimental validation of the model. In their model, the wave equation considered only the first acoustic mode and the first and second structural resonant frequencies. This research concludes that if the structural resonant frequency is higher than the Helmholtz resonant frequency, the absorption bandwidth can be widened by selecting the proper value of panel thickness, perforation diameter, etc. The effect of backing cavity depth and structural damping effect has also been discussed.

Yoo [52] developed the Maa-Flex model based on the flexural movement of the panel. Li et al. [40] developed an analytical model for finite-sized circular micro-perforated membranes, predicting overall impedance by combining the acoustic impedance for perforation and vibration using an electric-acoustic analogy. Temiz et al. [11] presented an efficient numerical model for a flexible

micro-perforated plate (*f*-MPP's) by coupling linear acoustics with classical shell plate theory. The model included the effect of plate vibration using Kirchhoff's thin plate equation coupled with the Helmholtz equation for micro-perforations.

Recently, Zhao et al. [53] proposed a local resonator-based flexible rectangular micro-perforated panel with simply supported and clamped boundary conditions, demonstrating the acoustic absorption of the flexible acoustic metamaterial under different boundary conditions using modal displacement patterns and acoustic impedance. Liu et al. [54] developed a hybrid structure consisting of a flexible plate and an MPP, adopting the active force control (AFC) technique for low-frequency (100–500 Hz) broadband quasi-perfect absorption. Their theoretical models included the higher modes of AFC plate vibration but were limited to the odd-odd combination of the structural modes.

2.2.2 Membrane-type AMM

The concept of Membrane-type Metamaterial (MAMM), introduced by Yang et al. [33], incorporates negative dynamic mass characteristics, enabling sound attenuation within the 100–1000 Hz frequency range. The basic unit of MAMM consists of a circular thin elastic membrane (20 mm in diameter and 0.28 mm thick) with a fixed boundary and a small mass (50–300 mg) attached to the center of the membrane. The fundamental principle underlying this research is the added mass effect. The resonance frequency (f_r) of a mass-spring system is defined by the equation:

$$f_r = \frac{1}{2\pi} \sqrt{\frac{k}{m}} \quad (2.9)$$

where, k is the spring constant and m is the mass. According to Eq. (2.9), increasing the added mass of the system can reduce the resonance frequency.

It has been demonstrated that the vibrational eigenfrequencies of the membrane can be tuned by placing a small mass at the centre of the elastic membrane. Two transmission peaks have been observed: the first one is due to the eigenmode of the combined vibration of the membrane and the central weight at low frequencies, while the second transmission peak is due to the eigenmode of the membrane vibration only at high frequencies (where the central weight remains almost in rigid body mode). A transmission dip between these two eigenmodes has been reported. The vibration amplitude at the dip frequency can be explained as the combination of the amplitudes for the two eigenmodes, which are out-of-phase. This membrane-type metamaterial demonstrates near-total reflection of acoustic waves in very low frequencies, as low as 200–300 Hz, due to an increase in the central mass.

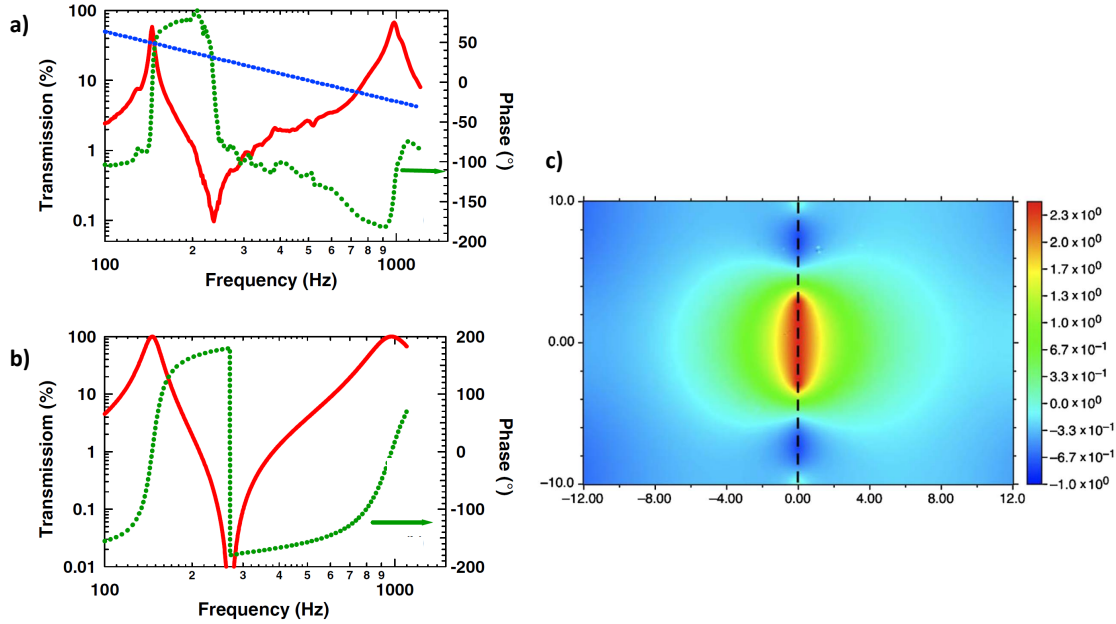


Figure 2.3: Membrane type acoustic metamaterial. a) Transmission amplitude of the sample obtained by experimental measurements (solid red curve) and phase (dotted green curve) where the blue dashed line represents the transmission amplitude predicted by the mass density law (b) Transmission amplitude of the sample obtained by numerical simulation (solid red curve) and phase (dotted green curve) c) The normal velocity field distribution predicted by the numerical simulation at the vicinity to the membrane corresponding dip frequency of 272 Hz [33].

Baz [55] has presented one-dimensional active acoustic metamaterials (AAMM's) with programmable effective densities using an array of fluid cavities separated by piezoelectric diaphragms. Bongard et al. [56] has implemented the composite right/left-handed transmission line (CRLH TL) metamaterial combining circular membranes clamped to an acoustic wave guide and radial open channels. This structure exhibits negative refractive index properties which are independent of resonance phenomena. Naify et al. [57] has demonstrated membrane-type metamaterials with multi-celled arrays that provide TL at low frequencies (50–1000 Hz) using different membrane materials such as polyetherimide (PEI) and silicone rubber with thickness of 0.076 mm and 0.176 mm respectively. Ma et al. [58] has presented a purely flexible lightweight membrane-type acoustic metamaterial for low-frequency vibration reduction and sound insulation. An acoustic metamaterial with elastic membrane-coated perforated plates is demonstrated in Fan et al. [59] which produces a sound reduction of 30–70 dB below 500 Hz with membrane thickness as thin as 20 μm . Wang et al. [60] has presented a constrained membrane-type acoustic metamaterial (CMAM) that successfully obtained desirable operating frequencies with STL peaks at 100 Hz and 200 Hz altering the constraint area with a membrane thickness of 0.05 mm. Ang et al. [61] has proposed a large-scale membrane-type acoustic metama-

terial ($800 \times 800 \text{ mm}^2$) for low-frequency noise control with sandwich-type designs. Aurégan [62] has demonstrated an ultra-thin low-frequency perfect sound absorber combining three elements: a mass supported by a slightly tensioned latex membrane with a thickness of $20 \mu\text{m}$, a cavity, and a resistive layer. Mei et al. [5] has presented a thin-film acoustic metamaterial, that consists of an elastic membrane decorated with asymmetric rigid platelets (consists of a rectangular elastic membrane that is 31 mm by 15 mm and 0.2 mm thick) which is particularly effective for sub-wavelength low-frequency acoustic absorption. Zhang et al. [63] has proposed membrane-type smart metamaterials based on a multi-modal resonance effect which can be used for sound insulation by simply tuning the external circuits rather than optimizing the structure itself. The proposed smart metamaterial with a rectangular membrane thickness of 0.17 mm, exhibits average STL of 22 dB in the frequency ranges 160-200 Hz and 26 dB in the frequency ranges 1300-1500 Hz. Liu et al. [64] has presented membrane-type metamaterials membrane with a width of 21 mm, a length of 36 mm, and a thickness of 0.2 mm for low-frequency (in the range of 400–650 Hz) broadband absorption using the acoustical siphon effect. McKay et al. [13] has proposed a super absorber termed a Segmented Membrane Sound Absorber (SeMSA) combining MPP and DMR made from a sheet of latex rubber with a thickness of 0.18 mm which works in either the frequency ranges of 20–1000 Hz or 20–1200 Hz for depths of up to 120 mm. Also, Davis et al. [14] used graph theory based on a Two-point Impedance Method to optimise multi-chamber microperforated panel absorbers for the same research. Sampaio et al. [65] has demonstrated a smart rectangular membrane-type metamaterial with a membrane thickness of 0.043 mm that consists of an arrangement of shunted piezoelectric elements which is capable of providing a broadband STL performance. Li et al. [66] has demonstrated membrane-type acoustic metamaterials loaded with arbitrarily shaped mass blocks of variable surface density using a semi-analytical model and finite element simulation results. The membrane is made of polyether amide (20 mm \times 20 mm) with a thickness of $25 \mu\text{m}$. An attenuation bandgap of 175.5 Hz width was created when shunting, demonstrating peak performance using multiple cells.

2.2.3 Beam-type AMM

Beam type AMM has been designed as the locally resonant engineering structures predominantly for the vibration control suppressing the elastic wave propagation [67][68][69]. Pai et al. [70] have introduced an acoustic metamaterial based on a beam with a length of 100 cm, width of 5 mm, and thickness of 3 mm, incorporating a uniform isotropic beam along with smaller two-mass spring-mass-damper subsystems. This design aims to achieve broadband, multi-frequency vibration absorption. Mi and Yu [71] has demonstrated an acoustic beam metamaterial attaching periodic inertial ampli-

fication (IA) mechanisms to a host beam. The finite length of the designed beam consists of 10 unit-cells with thickness of 0.005 m which has a total length of 1 m. The development of beam-type structures for sound absorption and transmission is a comparatively new idea for controlling acoustic wave propagation. In general, very little research work has been reported in this particular research area. Using the classical theory of structural dynamics the natural frequencies of a cantilevered beam can be written as

$$f_{1...3} = \frac{\lambda_{1...3}^2}{2\pi} \sqrt{\frac{E_b J_b}{\rho_b A_b}}$$

$$f_e = \frac{\lambda_e^2}{2\pi} \sqrt{\frac{E_b J_b}{\rho_b A_b}} \quad (2.10)$$

where, E_b is Young's modulus and ρ_b is the density of beam material, J_b is the moment of area, l_b is the length of the beam, A_b is the area of the beam and λ is the frequency parameter or eigenvalue term and given as $\lambda_{1,2,3} l_b = 1.875, 4.694, 7.855$ and $\lambda_e l_b = [(e - 0.5)\pi]^2$ where $e = 4 \dots n$. It can be seen from the Eq. (2.10), the natural frequencies of the cantilevered beam can be modified by changing the material properties (e.g. E_b, ρ_b) or design parameters (e.g. l_b, A_b) and can be used to obtain particular resonance frequency.

Chen et al. [72] has presented a beam-type metamaterial consisting of sandwich beams (consists of face sheets and foam core of thickness of 7.62×10^{-4} m and 3.02×10^{-2} m respectively with beam length of 0.019 m) containing interior dissipative multi-resonators which provide a broadband wave transmission dip from approximately 40–350 Hz. A compact liner based on a cantilever beam with the thickness of 0.1 mm for a single beam and 0.1 mm and 0.15 mm for a double beam in a duct for low-frequency application has been demonstrated by Farooqui and Aurégan [17] with the finite difference-based multi-modal method and numerical simulation. The main objective of this research was to make use of a cantilevered beam with a micro-slit that produces a leakage from the cavity. As a result compressibility effect can be reduced in a small-sized cavity. This technology offers better attenuation in the frequency range of 500–600 Hz with a thickness of around 1/6 th of acoustic wavelength. Aurégan and Farooqui [19] has presented a thin flexible beam of 30 mm thickness and surface area of 20×20 mm², made of titanium with a micro-slit as a beam in-parallel absorber which works in the mid-frequency range. Absorption peaks due to the resonance of the beam can be seen in the presented results. Both symmetric and torsional modes of the micro-slit resonator have been obtained using numerical simulation. But only symmetric modes (modes 1, 3, 7, ...) seem to influence the performance of the micro-slit resonator. So, it can be concluded that torsional modes do not affect the acoustic behavior of the resonator. Similar to the work in Farooqui and Aurégan [17],

an acoustic absorber based on a cantilevered beam with micro-slits to tackle low-frequency noise has been presented by Delia et al. [18]. However, experimental validation of the theoretical model is not presented by Farooqui and Aurégan [17]. So, Delia et al. [18] included theoretical models with experimental measurements of both acoustic and laser vibrometers using a 0.5 mm thick composite beam made with a carbon fibre/epoxy material (M21E/IMA). Interestingly, in this research, the sole purpose was to make use of beam resonances that appear at the low frequency, and the beam in the inertial regime was not considered in the model. Two beam resonance modes are included in the model. When only the first resonance mode is present the beam is termed as a mono-articulated beam and while the first two modes are present the beam is termed as a bi-articulated beam. The influence of several modes of j -th order can be written in terms of the impedance as

$$Z_{bj} = jk_{bj}t_{b,eq} \frac{\omega}{\omega_b} \left(1 - \frac{\omega_{bj}^2}{\omega^2} \right) + \delta_j \quad (2.11)$$

where, $k_b = \omega_b/c_0$, ω_b is the resonance (angular) frequency of the beam, $t_{b,eq}$ is the equivalent thickness of the beam, δ is the dimensionless structural damping factor. For this particular case, the first resonance frequency of the beam[18] calculated as

$$\omega_1^2 = 0.5 \frac{E_b}{\rho_b} b_b t_b^2 / (B_c a_b l_b^3) \quad (2.12)$$

where, t_b is the thickness of the beam, b_b is the width and a_b is the length at the base and B_c is the thickness of the cavity. This technology provides perfect absorption in 735 Hz (which corresponds to the first beam resonance) with liner thickness around 1/16 th of acoustic wavelength.

2.2.4 Plate-type AMM

Although membrane-type metamaterials work well for low-frequency sound absorption, the pretension of the membrane introduces considerable complexity in determining the vibroacoustic properties of the metamaterial. Additionally, controlling the pretension can be challenging due to thermal variation and relaxation effects in the membrane material. To overcome these limitations, a plate-type metamaterial with multiple sub-wavelength arrays of spring-mass resonators was introduced by Xiao et al. [73] using plane wave expansion (PWE) formulations and an effective medium method.

Considering a thin plate (i.e., 0.004 m) with a single array of resonators, the resonance frequency (f_r) of the resonators has been tuned to both the mass-law region and the coincidence region. Numerical demonstrations show that, with the same surface mass density, a metamaterial-based plate can provide significantly higher Sound Transmission Loss (STL) than a bare plate within the frequency

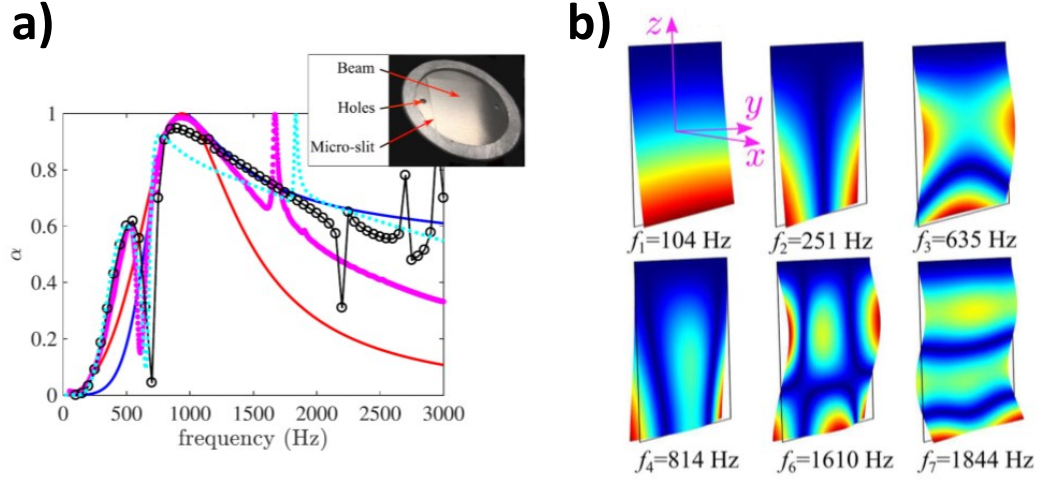


Figure 2.4: A beam in-parallel acoustic metamaterial. a) Measured the absorption coefficient of the resonator (magenta symbols). The blue and red lines are the absorption coefficients of the in-parallel resonators (IPR) and in-series resonator (ISR) models respectively. The dotted cyan line represents the absorption coefficient calculated by the lumped element model and the black circles correspond to the absorption coefficient obtained from numerical simulation. b) Some of the fundamental mode shapes of the thin titanium beam obtained from the numerical simulation[19].

range of the mass-law region and the coincidence region. The formation of a bandgap can be observed in the metamaterial-based plate, where the lower edge frequency can be expressed as $f_L = f_r$ and the upper edge frequency is $f_U = f_r \sqrt{1 + \gamma_p}$ for the corresponding band gap, with γ_p being the non-dimensional mass (the ratio of the oscillator mass to the mass of the string). Furthermore, using an extremely thin plate (i.e., 0.2 mm) has resulted in higher and broadband STL at the resonance frequencies.

Badreddine Assouar et al. [74] experimentally demonstrated plate-type acoustic metamaterials designed for low-frequency sound attenuation, showcasing selective resonance frequencies ranging from 650 to 3500 Hz. They utilized composite stubs (tungsten/silicone rubber) deposited on a thin aluminum plate with a thickness of 0.5 mm. In a different approach, Li et al. [75] proposed an acoustic metamaterial device comprising a multilayered flexible thin plate made of epoxy material with a thickness of 0.4 mm, designed specifically for underwater sonar detection. For a unique solution, Wang et al. [76] introduced an acoustic metamaterial featuring a plate with a thickness of 0.005 m. This metamaterial incorporates a lateral local resonance (LLR) substructure, consisting of a four-link mechanism, two lateral resonators, and a vertical spring.

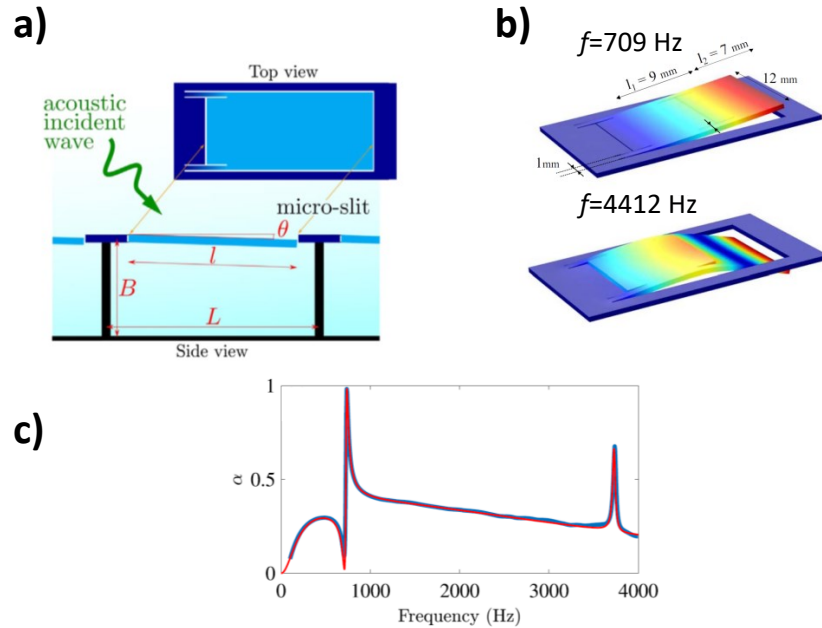


Figure 2.5: Beam type acoustic metamaterial. a) A mono-articulated beam with a micro-slit loaded by a cavity b) First ($f=709$ Hz) and second ($f=4412$ Hz) structural resonance mode of the cantilevered beam and c) Absorption coefficient of the bi-articulated plate: Experimental measurements (blue curves) and analytical results (red curves) [18].

Shifting away from membrane-type metamaterials, Ang et al. [77] and Ang et al. [78] expanded their work on plate-type acoustic metamaterials, introducing both designs without and with an internal Tonraum resonator. These innovations provide customizable acoustical performance, demonstrating scalability and modularity using Mylar films ($127 \mu\text{m}$ thick). In a different approach to addressing low-frequency noise, Delia et al. [18] presented an acoustic absorber based on articulated plates with micro-slits. Despite these significant advances, reducing low-frequency noise with a thin structure remains a formidable challenge.

2.2.5 Cavity Based AMM's

The idea of Cavity-based AMM's originated from the classical Helmholtz resonator. Coiled-up-space structures, perforations over a honeycomb core, perforated and micro-perforated plates with cavities behind them, etc. also can be represented by the Helmholtz resonator. Based on the principle of local resonance of the Helmholtz resonator, there are several studies have been presented for the application of sound absorption [79–82]. The Helmholtz resonator can simply be represented by the 1-D mass-spring system. Using the equivalent spring-mass system, the applied force, F_h can be written as

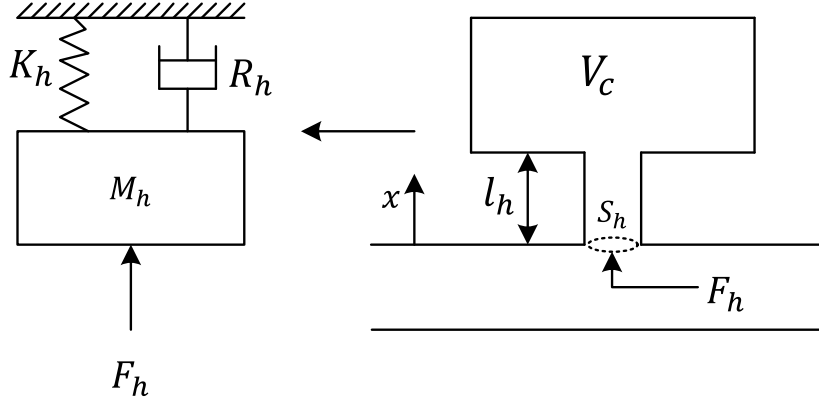


Figure 2.6: A schematic of the basic Helmholtz resonator and the spring-mass analogy of the Helmholtz resonator (Reproduced from [83]).

$$F_h = p_h S_h \quad (2.13)$$

where p_h is the amplitude of the sound pressure and S_h is the cross-sectional area of the neck of the Helmholtz resonator cavity. The equivalent mass M_h is

$$M_h = \rho_0 (l_h + \Delta l_h) S_h \quad (2.14)$$

And, the equivalent stiffness K_h is

$$K_h = \frac{dp_0 S_h}{-x} = -S_h \frac{dp_0}{\frac{dV_c}{S_h}} = -S_h^2 \frac{dp_0}{dV_c} \quad (2.15)$$

where, ρ_0 is the air density, l_h is the neck length, Δl_h is the length correction term and V_c is the volume of the Helmholtz cavity. For a more precise calculation of the Helmholtz resonance frequency, accounting for an end correction becomes essential. The effective mass of air involved in the movement within and around the neck is slightly greater than the neck's geometric dimensions. This adjustment accommodates the kinetic energy present in the airflow near the neck ends, commonly addressed by adding a slight extra length (length correction term) to the actual measured length. As an adiabatic process, change in pressure and volume involves a constant γ ($= 1.4$ for air) and the resulting equation can be written as

$$p_0 \cdot V_c^\gamma = (p_0 + dp_0) \cdot (V_c - dV_c)^\gamma \quad (2.16)$$

where γ is the specific heat capacity ratio. Eq. (2.16) can be further simplified as

$$\frac{p_0 + dp_0}{p_0} = \left(\frac{V_c - dV_c}{V_c} \right)^{-\gamma} \approx 1 - \gamma \frac{dV_c}{V_c} \quad (2.17)$$

After rearranging we get,

$$\frac{dp_0}{dV_c} = -\frac{\gamma \cdot p_0}{V_c} = -\frac{\rho_0 c_0^2}{V_c} \quad (2.18)$$

where, c_0 is the speed of sound in air. As a final form, the equivalent stiffness is

$$K_h = S_h^2 \frac{\rho_0 c_0^2}{V_c} \quad (2.19)$$

The Helmholtz resonance frequency (f_{HR}) can be written as

$$f_{HR} = \frac{c_0}{2\pi} \sqrt{\frac{S_h}{V_c(l_h + \Delta l_h)}} \quad (2.20)$$

From the mechanical analogy of the Helmholtz resonator, the impedance can be written as:

$$Z_h = R_a + i \left(\omega M_a - \frac{1}{\omega C_a} \right) \quad (2.21)$$

where, $M_a = M_h/S_h^2$, $R_a = R_h/S_h^2$ and $C_a = S_h^2/K_h$ are considered as the sound mass, sound resistance and sound capacitance respectively.

2.2.6 Helmholtz Resonator With a Flexible Plate

In general, Helmholtz resonators are very effective in providing high absorption peaks at resonance frequency with very narrow frequency bandwidth. Several techniques i.e. adding porous material [48] [84], a parallel coupling of Helmholtz resonator [85], combining multiple resonant frequencies [86], Helmholtz resonator loaded with a wire mesh [87], have been adapted to obtain the broad bandwidth with Helmholtz resonator. Sanada and Tanaka [88] has proposed a sound absorber using two-degrees-of-freedom Helmholtz-based resonators with a flexible panel of 2 mm thickness. Nudehi et al. [89] and Kurdi et al. [90] have demonstrated a Helmholtz resonator with a flexible end plate (thickness of 0.25 mm) employing a receptance coupling approach. A novel liner concept (FlexiS) has been demonstrated by Knobloch et al. [91] with the combination of flexible walls and conventional liner cavity structure. The materials considered in this research are Thermoplastic-polyurethan (TPU) sheets of type 1195A in thicknesses 0.1 mm and 0.5 mm and type 1170A in thickness 0.3 mm. The mathematical modeling of Helmholtz resonators coupled with a second cavity by flexible walls has been presented by Kohlenberg et al. [92]. The flexible circular plate that has been used in this research is usually clamped at the edge. The combined effect of Helmholtz resonance and plate resonance has

been demonstrated. The velocity of the circular plate, $\hat{v}_p(r)$ can be defined by the combination of an infinite number of eigenmodes (ψ_{mn}) as

$$\hat{v}_p(r) = \sum_{n=0}^{\infty} \hat{v}_{p,n}(r) \psi_{mn} \quad (2.22)$$

The eigenmodes of a circular plate with a clamped edge can be written as[92]

$$\psi_{ccp}(r, \theta, m, n) = \left[J_m \left(\frac{\lambda_{mn}}{a} r \right) - \frac{J_m(\lambda_{mn})}{I_m(\lambda_{mn})} I_m \left(\frac{\lambda_{mn}}{a} r \right) \right] \cos(m\theta) \quad (2.23)$$

The λ_{mn} can be obtained using the transcendental equation[93]

$$\frac{J_m(\lambda)}{J_{m+1}(\lambda)} + \frac{I_m(\lambda)}{I_{m+1}(\lambda)} = 0 \quad (2.24)$$

Because the plates motion is dominated by the fundamental eigenmode, the first mode shape function ($m = 0, n = 0$) can be expressed as

$$\psi_{00}(r) = J_0 \left(\frac{\lambda_{00}}{a} r \right) - \frac{J_0(\lambda_{00})}{I_0(\lambda_{00})} I_0 \left(\frac{\lambda_{00}}{a} r \right) \quad (2.25)$$

where $\lambda_{00} \approx 3.196$. Considering only the fundamental mode, the resonance frequency of the clamped circular plate is expressed as

$$\omega_{00,p} = \sqrt{\frac{K_0}{M_0}} = \left(\frac{\lambda_{00}}{a} \right)^2 \sqrt{\frac{D_p}{\rho_p t_p}} \quad (2.26)$$

where, M_0 is a modal mass and K_0 is a modal stiffness of the flexible plate with respect to the fundamental mode. The resonance frequency of the clamped circular plate is 380 Hz which corresponds to the first resonance peak in Fig. (2.7) providing additional attenuation due to plate resonance in the form of material damping below the Helmholtz resonance. Langfeldt et al. [94] has presented an acoustic metamaterial with flexible plate-integrated Helmholtz resonators with 0.55 mm thick polycarbonate (PC) plate as a new technique for increasing the bandwidth of AMM anti-resonances. It has been demonstrated numerically that, if the Helmholtz resonance frequency and the anti-resonance frequency of the AMM are placed reasonably far from each other, the separate STL peaks can be identified from the curves which can be useful for multi-tonal sound sources. But, if the Helmholtz resonance frequency and the anti-resonance frequency of the AMM are placed reasonably very close to each other, the combined effect provides a single STL peak with wide bandwidth. Recently, Neubauer et al. [95] Neubauer et al. [96] has presented novel acoustic liners with Helmholtz resonator with flexible walls and the plate resonator (PR) concept and their optimized design for aero-engine ap-

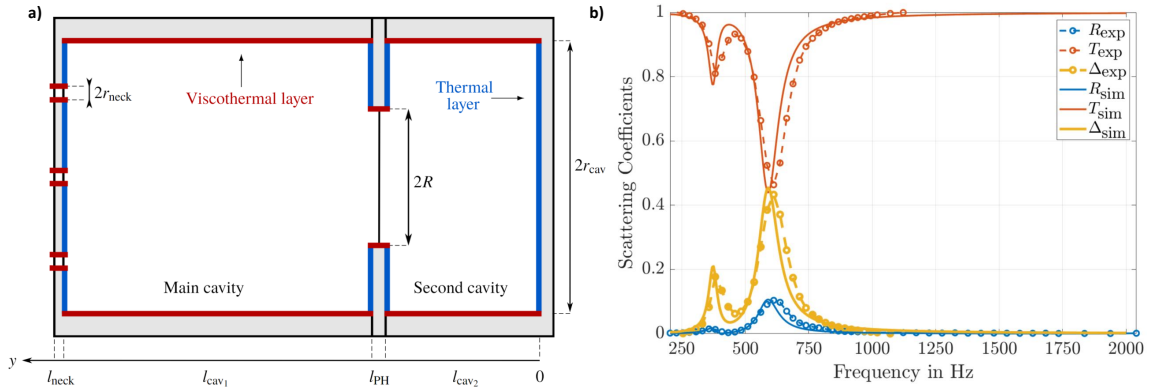


Figure 2.7: a) Schematic of the circular Helmholtz resonator with a flexible plate inside a plate holder and a second cavity b) The scattering coefficients of the Helmholtz resonator with a second cavity and a flexible plate [92].

plications. The concept of PR utilizes a plate resonator silencer comprising an expansion chamber entirely enveloped by a plate. Apart from effectively dampening low-frequency noise with shallow cavities, plate silencers offer an advantage over porous absorbers or Helmholtz resonator structures with perforated surfaces. This advantage lies in their ability to be exposed to contaminated air without experiencing the issue of contaminants aggregating within the cavity. The proposed structure includes a plate thickness of 0.3 mm and a cavity depth of 65 mm. These dimensions contribute to the lower frequency peak, starting from around 550 Hz, attributed to the plate resonance. Additionally, the second resonance frequency, beginning around 900 Hz, is due to the Helmholtz resonance. A new approach of model-based material selection for the PR concept has been demonstrated using the parametric analysis of Young's modulus and loss factor of the plate material.

2.3 Miscellaneous Flexible Structures

Several other flexible structures with unusual shapes and designs as acoustic metamaterials have been reported. Miller et al. [97] has presented a flexible acoustic metamaterial with metalorganic framework materials for low-frequency (100–1250 Hz) sound attenuation and contrast agent applications. Three variations of flexible MIL-53(Al) (Basolite A100) have been demonstrated. The original MIL-53(Al) resonates within the 160-315 Hz range. Modifications were made by introducing glutaric acid

(MIL-53(Al)-GA) and adipic acid (MIL-53(Al)-AA) to enhance the framework's flexibility. Greater and tunable transmission loss for both MIL-53(Al)-GA and MIL-53(Al)-AA has been obtained due to the inclusion of enhanced flexibility in the frameworks. Zhang and Cheng [98] has proposed a novel meta-absorber for broadband low-frequency underwater sound absorption below 2 kHz. The unit cell of this structure consists of multiple thickness-graded circular-elastic-plate scatterers (CPS's) placed in a manner to form an elastomer matrix which is backed by a metallic backing plate. The proposed design demonstrates the formation of coupled resonance modes inside the complete structure. The experimental results demonstrate high broadband absorption (greater than 0.82 on average) from 800 Hz to 6000 Hz. This was achieved using a backing plate with a thickness of 9.1 mm. A flexible meta-curtain has been proposed by Cui et al. [99] that provides simultaneous soundproofing and ventilation using two parallel thin and soft perforated polyvinyl chloride (PVC) films. The designed meta-curtain has a total thickness of 1.16 cm and weighs 0.72 kg. The flat meta-curtain typically exhibits greater STL values compared to the contrast sample (meta-unit without acoustic cavity inside) between 1300 Hz and 1700 Hz, reaching a prominent 45 dB peak specifically at 1520 Hz. Tsuruta et al. [100] has presented two reconfigurable metamaterial absorbers consisting of flexible tube resonators. The presence of hybrid resonances by the interaction between acoustic and structural modes has been demonstrated using the Rabi splitting and Fano resonance.

2.4 Conclusions

Several flexible acoustic metamaterials have been reviewed in the previous section. The potential use of circular plates integrating with Helmholtz resonators to obtain hybrid resonances has been demonstrated in recent times. However, most of the prior related research works are based on tailoring the fundamental structural resonance mode (only one radial mode) to obtain mid to low-frequency sound absorption. The effects of higher-order structural resonance modes (both radial and azimuthal modes) on acoustic absorption remain substantially underinvestigated. Although acoustic absorber with flexible structures for tonal noise reduction has been proposed, low-frequency noise reduction with thin structures remains a challenging task.

2.5 Contribution of the Thesis

The current research is aimed at designing a novel acoustic metamaterial based on a one-way acoustic valve termed a "plate-type acoustic valve" for sound absorption in the low-frequency range (< 1500

Hz) with a very thin structure. The primary aim of this research endeavor has been fulfilled through the subsequent contributions:

- Introduction of a centrally fixed free edge thin circular plate as a unique design for low-frequency sound absorber.
- Design of a novel acoustic one-way valve as a unique acoustic metamaterial for low-frequency sound absorption. Near perfect absorption was achieved experimentally, e.g. up to $\alpha = 0.995$ below 1 kHz, and given that the thickness of the technology can be a very small percentage of the acoustic wavelength that it is absorbing deep sub-wavelength ratio absorbers can be designed, e.g. a ratio of up to 58 was achieved in this study with a 5 mm deep technology at 1.18 kHz.
- Proposal of efficient 2D FEM numerical model for plate-type acoustic valve resonator including the structural resonance (radial vibrational modes) and the Helmholtz resonance. A 3D FEM numerical model replicating a complete plate-type acoustic valve resonator system including the radial and azimuthal modes of vibrations.
- Experimental validation of the analytical and FEM numerical model using acoustic measurements in a normal incidence impedance tube and vibrational modal analysis using single point laser Doppler vibrometer.
- Successful identification of structural resonance modes from the laser Doppler vibrometry (LDV) measurements.

Chapter 3

Mathematical Modelling of Acoustics and Structural Vibrations

3.1 Numerical Modelling of Acoustics

3.1.1 Acoustic Wave Equation

In general, the constitutive equation for sound wave propagation through an elastic medium can be derived from the elementary equations of fluid dynamics (i.e., the conservation of mass, conservation of momentum, polytropic process). The so-called *acoustic wave equation* is the governing equation of acoustics, representing the motion of a fluid, including non-linearities, viscosity, and thermal conduction. The derivation of the acoustic wave equation in a direct way from the elementary equations is not viable due to the complex nature of those equations. Using relevant assumptions close to real-world conditions, the acoustic wave equation can be deduced to create a simplified mathematical model that reasonably accurately replicates reality [101].

In the study of the propagation of sound, if the fluid acts as an ideal gas and the acoustic field is assumed to be a continuum, the perturbation process around the equilibrium should be relatively small and can be considered linear. Apart from the linearity, changes in pressure are considered adiabatic. This implies that there are no heat transfer or thermal effects present in the system; it represents an isentropic process with no loss or gain of acoustic energy. The geometry of the space through which sound propagates can affect wave behaviour. In certain cases, like open spaces or uniform mediums, sound may exhibit behaviour more closely resembling an idealized isentropic process with minimal losses. However, in more complex geometries, reflections, diffraction, and interactions with boundaries or obstacles can cause changes in sound energy, leading to losses or gains. The constitutive equation of the acoustic wave equation can be written under all these assumptions, as shown by Kinsler et al.[102]:

$$\nabla^2 p(\mathbf{x}, t) - \frac{1}{c^2} \frac{\partial^2 p(\mathbf{x}, t)}{\partial t^2} = 0 \quad (3.1)$$

where $p(x, t)$ is a pressure fluctuation of the static pressure at the location x at time t and c is the speed of sound, which can be defined as:

$$c = \sqrt{\frac{\gamma p_0}{\rho_0}} \quad (3.2)$$

where, p_0 is the absolute pressure of the gas, and ρ_0 is the density of the gas and γ is defined as:

$$\gamma = \frac{C_p}{C_v} \quad (3.3)$$

where, C_p the specific heat capacity for constant pressure and C_v the specific heat capacity for constant volume and for air γ calculated as 1.4.

The acoustic wave equation can be solved conveniently using the frequency domain representation of the Eq. (3.1) considering a time-harmonic formulation (or using the Fourier transformation):

$$p(\mathbf{x}, t) = \Re\{p(\mathbf{x})e^{i\omega t}\} \quad (3.4)$$

where $p(\mathbf{x})$ is the complex pressure amplitude, i is the imaginary unit, and ω is the angular velocity. Eliminating the time-dependency of the Eq. (3.1) we get

$$\nabla^2 p(\mathbf{x}) + k^2 p(\mathbf{x}) = 0 \quad (3.5)$$

which is popularly known as the Helmholtz equation where $k = \omega/c = 2\pi/\lambda$ is the wavenumber. The acoustic wavelength ($\lambda = c/f$) is a crucial quantity defined by the ratio of the speed of sound to the frequency (f). In order to build a mathematical model for a particular system, one must also include the boundary conditions (BC) (i.e., Dirichlet BC, Neumann BC) or impedance in the Helmholtz equation. Theoretical investigations of wave propagation often encounter various computational problems, including complex geometry, band structures, leaky cavities, and waveguides [103], as well as multi-physics coupling.

Several analytical and numerical techniques, namely Plane Wave Expansion (PWE), Boundary Element Method (BEM), Computational Fluid Dynamics (CFD), Finite Difference Time Domain (FDTD), Finite Element Method (FEM), and Layer Multiple Scattering Theory (LMST), have been adopted to solve computational problems of acoustic wave propagation, especially in acoustic meta-materials [103].

Combining all the mentioned steps, the mathematical modelling of acoustic wave propagation can be achieved not only through analytical calculations but also using numerical methods. This thesis presents both analytical and numerical methods, specifically focusing on the Finite Element Method (FEM), for the mathematical modeling of acoustic wave propagation.

3.1.2 Finite Element Method

Originally developed for structural stiffness and deflection analysis, the finite element method (FEM) can also be applied to represent various physical phenomena. Currently, FEM is the most widely used numerical technique to accurately model a wide range of physical phenomena and efficiently solve partial differential equations (PDEs). It considers various boundary conditions and multiple physics interactions, working efficiently in both the time and frequency domains. Complex geometries with

unstructured mesh can be discretized by the finite element method, making it a versatile tool for a wide range of applications.

FEM can be applied to the Helmholtz equation in two steps, which is essentially the process of obtaining a weak form from the PDE. First, the Helmholtz equation is multiplied by a test (weighing) function (ϕ_f) and integrated over the domain (Ω) [104]:

$$\int_{\Omega} \phi_f [\Delta p + k^2 p] d\Omega = 0 \quad (3.6)$$

The next step is to apply Greens theorem (also called Greens first identity), to reduce the highest order of the derivatives. The Laplace operator in the Greens theorem can be transformed into a domain (Ω) and a boundary domain (Γ) integral and the weak form reads:

$$-\int_{\Omega} \nabla \phi_f \cdot \nabla p d\Omega + \int_{\Gamma} \phi_f (\nabla p \cdot \mathbf{n}) d\Gamma + \int_{\Omega} k^2 \phi_f p d\Omega = 0 \quad (3.7)$$

To get the matrix equation from the discrete weak form we need to consider a shape function (\mathbf{N}_s) and following to the Galerkin approach, the test function is assumed to be the same as the shape functions. The pressure can be approximated as:

$$p \approx \mathbf{N}_s \mathbf{p} \quad (3.8)$$

The FEM representation of the isentropic acoustic wave propagation can be written as the following expression:

$$-\int_{\Omega} \nabla \mathbf{N}_s^T \cdot \nabla \mathbf{N}_s d\Omega \mathbf{p} + \int_{\Gamma} \mathbf{N}_s^T (\nabla \mathbf{N}_s \cdot \mathbf{n}) d\Gamma + \int_{\Omega} k^2 \mathbf{N}_s^T \mathbf{N}_s d\Omega \mathbf{p} = 0 \quad (3.9)$$

which can be represented as real, sparse and symmetric matrices form not considering the damping where the first term from left to right is known as stiffness matrix, the second term is natural boundary condition matrix and the third term is a mass matrix. This can be written in the form of the global system matrices with an additional damping term and the global system of equations become:

$$(\mathbf{K} + i\omega\mathbf{D} - \omega^2\mathbf{M})\mathbf{p} = 0 \quad (3.10)$$

where \mathbf{K} , \mathbf{M} and \mathbf{D} are the element stiffness, mass and damping (i.e. Rayleigh damping, viscous damping) matrices respectively. The modelling techniques of different damping using FEM can be found in the Appendix A.2.2.5. This system consists of n number of unknowns and n is the total number of degrees of freedom (DOFs). For acoustics applications, there is one DOF per node which is essentially the number of nodes for the system.

3.2 Numerical Modelling of Structural Mechanics

In order to investigate the solid structure in the plate-type acoustic valve resonator through numerical simulation, the structural mechanics need to be studied using the main constitutive equations. The governing equation, which is essentially the basis for the derivation of these constitutive equations, is Hooke's law of elasticity and provides the linear relationship between stress and strain of isotropic elastic materials. Applying this law to an infinitesimal solid control volume, the elastic wave equation can be written as, under the assumption of infinitesimal strain and a homogeneous, isotropic medium:

$$\rho \frac{\partial^2 \mathbf{u}}{\partial t^2} = (\lambda_L + 2\mu_L) \nabla(\nabla \cdot \mathbf{u}) - \mu_L \nabla \times \nabla \times \mathbf{u} + \mathbf{F}_S \quad (3.11)$$

where, \mathbf{u} represents the solid displacement in the three spatial dimensions (x, y, z) , \mathbf{F}_S is the body force per unit volume applied to the solid, and λ_L and μ_L are the Lamé coefficients of the solid material. For engineering applications, the elastic wave equation can be simplified using specific assumptions, such as those applied to the Euler-Bernoulli beam, and particular boundary conditions. For example, in the case of the Euler-Bernoulli beam, the basic assumption is straight cross-sections of the beam stay straight even under deformation, and transverse loads cause the bending for the beams and very small deformations [105]. The transverse displacement in these beams can be expressed using the simplified elastic wave equation:

$$E_m J_b \frac{\partial^4 u}{\partial x^4} = -\rho \frac{\partial^2 u}{\partial t^2} + F_t \quad (3.12)$$

where, u is the transverse displacement of the beam, x is the location along the length of the beam, E_m is the Young's modulus of the material, J_b is the cross-sectional moment of inertia of the beam, ρ_m is the density of the material and F_t is the acting transverse load. For two-dimensional structures (i.e. thin plates), this general formulation can be modified to analyze the vibration of the plates including the bending effect. The modified elastic wave equation defined by the Kirchhoff-Love plate theory as:

$$D_p \left(\frac{\partial^4 u}{\partial x^4} + 2 \frac{\partial^4 u}{\partial x^2 \partial y^2} + \frac{\partial^4 u}{\partial y^4} \right) = -\rho \frac{\partial^2 u}{\partial t^2} + F_t \quad (3.13)$$

where, x and y represents the in-plane location and D_p is the plate bending stiffness or flexural rigidity, which is defined as:

$$D_p = \frac{E_m t_p^3}{12(1 - \nu_m^2)} \quad (3.14)$$

where, t_p is the plate thickness, E_m is the Young modulus and ν_m is the Poisson's ratio of the plate material. To apply FEM in structural mechanics, a similar approach can apply as in Section (3.1.1). The wave equation should be modified with displacement fields which are the main field variables

for structural mechanics replacing sound pressure. The dynamic equation with 3-DOF per geometric node becomes:

$$(\mathbf{K} + i\omega\mathbf{D} - \omega^2\mathbf{M})\mathbf{u} = \mathbf{F}_s \quad (3.15)$$

where, \mathbf{u} is the nodal displacements and \mathbf{F}_s is the excitation or forcing vector. For a 1-DOF mass-spring-damper system, the equation of motion can be expressed as:

$$(k + i\omega c - \omega^2 m)u = F_s \quad (3.16)$$

where u is the displacement of the mass, F_s is the applied load, k is the stiffness of the spring, c the damping factor and m is the mass. Mechanical damping encompasses a variety of mechanisms, among them being viscous damping, frictional damping, and structural damping etc.

3.3 Analytical Modelling of the Vibration of a Circular Plate

The vibration of a free-edge circular plate was first systematically studied by Ernst Florens Friedrich Chladni in *Entdeckungen über die Theorie des Klanges*, published in 1787. In this book, he included seventy-five drawings of modal shapes of a circular copper plate, popularly known as 'Chladni figures' or 'Chladni patterns.' The experimental method is based on sand sprinkled on a plate, and the plate is excited by a violin bow to show the nodal lines. He expanded on this work in his publication *Die Akustik* (1802, second edition 1830), establishing a relationship between frequency (f), the number of nodal diameters (m), and the number of nodal circles (n). Lord Rayleigh [106] termed that relationship as the 'Chladni law.' According to Chladni's equation

$$f = C(m + bn)^p \quad (3.17)$$

where, C , b , and p are coefficients that can be obtained from the properties of the plate. For a flat circular plate ($b = 2, p = 2$), Chladni's law states that f is proportional to $(m + 2n)^2$ in the case of large f . Later, in 1850 G. R. Kirchhoff published two papers on the vibration of plates considering the boundary conditions more accurately. After that, several scientists such as Savart, Strelke, Faraday, Koenig, Debye, Young, Wood, Mary D. Waller, etc. [107] have employed Chladni's patterns for studying plate vibrations. The solution for the vibration of the circular plate obtained by Kirchhoff is presented as follows. The differential equation for the vibration of a circular plate is

$$\nabla^4 w = k^4 w \quad (3.18)$$

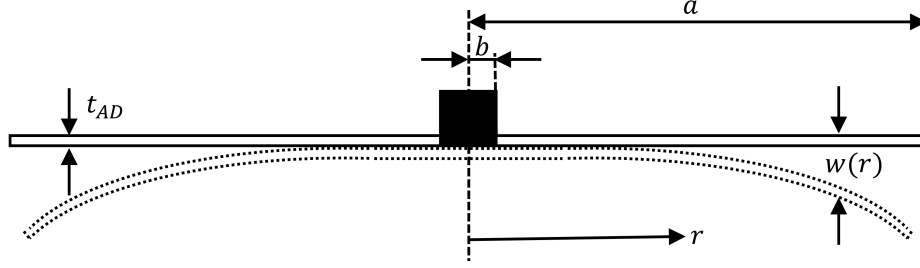


Figure 3.1: Centrally fixed free edge thin circular plate of outer radius a , inner radius b and thickness t_{AD} .

Parameter	Value	Unit
t_{AD}	0.52	[mm]
b	5	[mm]
a	62	[mm]
ρ_m	1240	[kg · m ⁻³]
E_m	3.8	[GPa]
ν_m	0.33	[-]
η_m	0.03	[-]

Table 3.1: Modelling parameter for plate-type acoustic valve

where, $k = \sqrt{\omega}/c$ and $c^4 = Et^2/12\rho(1 - \nu^2)$ and w is the displacement from the normal position of the plate, ω is the angular frequency, E is the Young's modulus, t the thickness of the plate, ρ the density, and ν Poisson's ratio. Each normal modes with nodal diameters can be obtained by $\cos(m\theta - \alpha) = 0$ and for n concentric circle the solution for the Eq.(3.18) can be written as

$$J_m(kr) + \lambda J_m(ikr) = 0 \quad (3.19)$$

where, $J_m(kr)$ and $J_m(ikr)$ are Bessel functions, and α and λ are arbitrary constants that can be calculated using boundary conditions. Kirchhoff's method was only able to compute the simplest modes of vibrations. To compute all modes of vibrations it is required to solve the Bessel functions which are complicated. Lord Rayleigh and Ritz also proposed different methods to avoid the calculation of Bessel functions. Further analysis of plate vibrations using the Bessel functions for different boundary conditions are provided by Timoshenko et al. [108], Southwell [109] Colwell and Hardy [110] and well documented by Leissa [93].

3.3.1 Vibration of Plate-type Acoustic Valve

For analytical modelling of the plate-type acoustic valve, the valve has been considered as a centrally fixed thin circular plate (i.e. $t_{APV} \ll a$) as shown in Fig. (3.1). The modelling parameters are presented in Table 3.1.

For free vibration, the wave equation for a thin circular plate with uniform thickness can be depicted using classical thin plate theory

$$D\nabla^4 w + \rho_m t_{AD} \frac{\partial^2 w}{dt^2} = 0 \quad (3.20)$$

where, $\nabla^4 w = \nabla^2(\nabla^2 w)$ and

$$\nabla^2 = \nabla \cdot \nabla = \frac{\partial^2}{\partial r^2} + \frac{1}{r} \frac{\partial}{\partial r} + \frac{1}{r^2} \frac{\partial^2}{\partial \theta^2}$$

using Laplace's equation in cylindrical coordinates. Considering the displacement amplitude (w) with a separable solution

$$w(r, \theta, t) = \mathbf{W} e^{j\omega t} \quad (3.21)$$

where, $\mathbf{W} = \mathbf{W}_r(r)\mathbf{W}_\theta(\theta)$ is the function of the position. Substituting this into Eq. (3.20) we get

$$\nabla^4 \mathbf{W} - k_p^4 \mathbf{W} = 0 \quad (3.22)$$

where, $k_p^4 = \omega^2 \rho_m t_{APV} / D$ and D is the flexural rigidity and defined as

$$D = \frac{E_m t_{APV}^3}{12(1 - \nu_m^2)}$$

The solution of the Eq. (3.22) can be written as Leissa [93]

$$\mathbf{W}_m(r, \theta) = \left[B_m J_m(k_p r) + C_m I_m(k_p r) \right] \cos(m\theta) \quad (3.23)$$

where, J_m is the Bessel's function of first kind of the m -th order, I_m is the modified Bessel's function of the first kind of the m -th order, and B_m, C_m are the constants which can be obtained using the relevant boundary conditions.

At the fixed center $r = b$ we have the boundary conditions

$$\mathbf{W}_m(r, \theta) \Big|_{r=b} = 0, \quad \frac{d\mathbf{W}_m(r, \theta)}{dr} \Big|_{r=b} = 0 \quad (3.24)$$

and at the free edge $r = a$ the bending moment, $M_r(r, \theta)$ as well as the effective transverse shear force, $V_r(r, \theta)$ both are zero

$$M_r(r, \theta) \Big|_{r=a} = -D \left[\frac{\partial^2 w}{\partial r^2} + \nu_m \left(\frac{1}{r} \frac{\partial w}{\partial r} + \frac{1}{r^2} \frac{\partial^2 w}{\partial \theta^2} \right) \right] \Big|_{r=a} = 0, \quad (3.25)$$

and

$$V_r(r, \theta) \Big|_{r=a} = -D \left[\frac{\partial}{\partial r} (\nabla^2 w) \right]$$

$$+ \frac{1 - \nu_m}{r} \frac{\partial}{\partial \theta} \left(\frac{1}{r} \frac{\partial^2 w}{\partial r \partial \theta} - \frac{1}{r^2} \frac{\partial w}{\partial \theta} \right) \Big|_{r=a} = 0 \quad (3.26)$$

Substituting Eq. (3.23) in the first part of the Eq. (3.24) we can write

$$B_m J_m(k_p b) + C_m I_m(k_p b) = 0$$

$$\frac{C_m}{B_m} = - \frac{J_m(k_p b)}{I_m(k_p b)} \quad (3.27)$$

And substituting Eq. (3.23) into eq. (3.25) yields (since $D \neq 0$)

$$B_m \left[J_m''(\lambda) + \frac{\nu_m}{\lambda} J_m'(\lambda) \right] + C_m \left[I_m''(\lambda) + \frac{\nu_m}{\lambda} I_m'(\lambda) \right] = 0$$

$$\frac{C_m}{B_m} = - \frac{J_m''(\lambda) + \frac{\nu_m}{\lambda} J_m'(\lambda)}{I_m''(\lambda) + \frac{\nu_m}{\lambda} I_m'(\lambda)} \quad (3.28)$$

where, $J_m'(\lambda) = dJ_m(\lambda)/d\lambda$. Substituting $\lambda = k_p a$ in the Eq. (3.28), we introduce the eigenvalue parameter λ . Combining the Eq. (3.27) and Eq. (3.28) the final form can be written as

$$\frac{C_m}{B_m} = - \frac{J_m''(\lambda) + \frac{\nu_m}{\lambda} J_m'(\lambda)}{I_m''(\lambda) + \frac{\nu_m}{\lambda} I_m'(\lambda)} = - \frac{J_m(\lambda b/a)}{I_m(\lambda b/a)} \quad (3.29)$$

where,

$$J_m'(\lambda) = \frac{m}{\lambda} J_m(\lambda) - J_{m+1}(\lambda)$$

$$I_m'(\lambda) = \frac{m}{\lambda} I_m(\lambda) + I_{m+1}(\lambda)$$

$$J_m''(\lambda) = \left(\frac{m^2}{\lambda^2} - 1 \right) J_m(\lambda) - \frac{1}{\lambda} J_m'(\lambda)$$

$$I_m''(\lambda) = \left(\frac{m^2}{\lambda^2} + 1 \right) I_m(\lambda) - \frac{1}{\lambda} I_m'(\lambda)$$

As a deformable system, a plate-type acoustic valve provides several vibrational modes. For several eigenfrequencies and modes, the λ can be written as λ_{mn} and can be calculated using Eq. (3.29) where m represents the number of nodal diameters and n stands for the number of nodal circles. Figure (3.2) plots the calculated mode shapes for a centrally fixed circular plate with a free edge.

The natural frequencies (f_{mn}) of the plate-type acoustic valve can be represented as Chiang and Huang [111]

$$f_{mn} = \frac{\lambda_{mn}^2}{2\pi a^2} \sqrt{\frac{D}{\rho_m t_{APV}}} \quad (3.30)$$

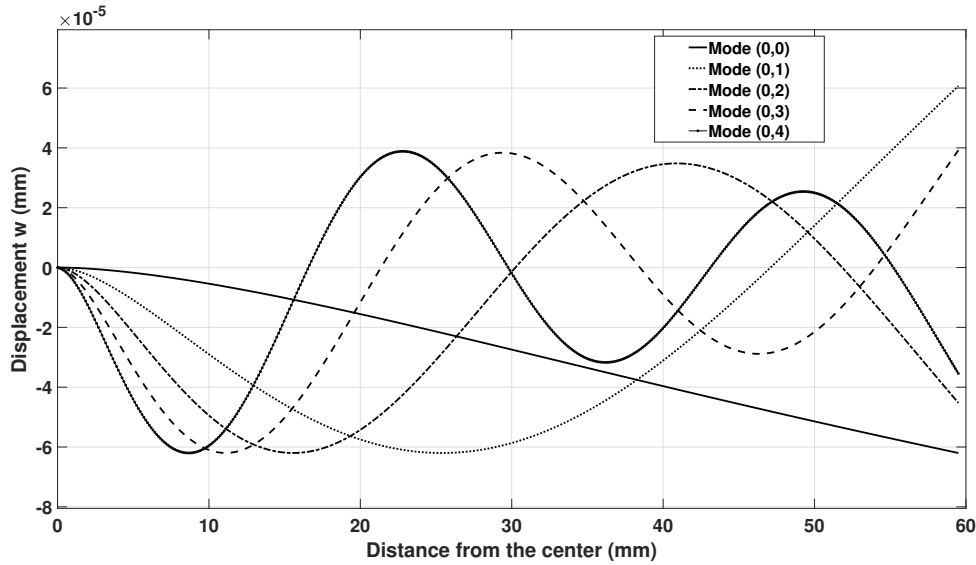


Figure 3.2: Displacement w of the circular plate as a function of r . The first five symmetric mode shapes for the centrally fixed circular plate with a free edge.

where, for symmetric (or radial) modes $m = 0$, $n = 0,1,2,3\dots$ and for azimuthal modes $m > 0$, $n = 0,1,2,3\dots$. When $\nu_m = 0.3$, for completely free plate λ_{00} is the rigid mode so, $n = 1,2,3,4,\dots$ and $\lambda_{0n} = 300052, 620025, 936751, 1252271\dots$ Amabili et al. [112]

According to Southwell [109], Timoshenko [113] and Leissa [93], when $m > 0$ the eigenvalues of the centrally fixed free edge thin circular plate are the same as for a completely free thin circular plate. Only for the symmetric mode ($m = 0$) the eigenvalues of the centrally fixed free edge plate are different from those of the completely free plate.

The effect of the clamped portion in the analytical model is considered as negligible using the b/a ratio approximation by Southwell [109]. Vogel and Skinner [114] later theoretically and experimentally demonstrated that, when $b/a \leq 0.2$ (for the current case it's 0.08), the change in natural frequencies is relatively small. The squared eigenvalues of the plate-type acoustic valve are tabulated in Table 3.2 for $\nu_m = 0.33$. Substituting D into the Eq. (3.30), it can be seen that the relationship between the ν_m and λ_{mn} is inversely proportional. The calculated eigenvalues are tabulated for $\nu_m = 0.33$. It should be noted that the correct value of the eigenvalues depends on the actual value of the Poisson's ratio of the 3D printed material. Table 3.2 and 3.3 shows the eigenvalues[93] and eigenfrequencies for the analytical model of the plate-type acoustic valve (modelled as a centrally fixed free edge thin plate), respectively.

λ_{mn}^2 for $\nu_m = 0.33$					
m \ n	0	1	2	3	4
0	3.752	20.91	61.2	120.6	199.9
1	–	20.52	59.86	119.0	198.2
2	5.253	35.25	83.9	154.0	242.7
3	12.23	52.91	111.3	192.1	290.7
4	21.6	73.1	142.8	232.3	340.4
5	33.1	95.8	175.0	274.6	392.4

Table 3.2: Modal parameters for uniform thickness centrally fixed free edge thin circular plate Leissa [93].

Natural Frequencies of plate-type acoustic valve (f_{mn})					
m \ n	0	1	2	3	4
0	43.0711	240.036	702.5455	1384.4	2294.8
1	–	235.559	687.1630	1366.1	2275.2
2	60.3018	404.652	963.1302	1767.8	2786.1
3	140.3943	607.38	1277.7	2205.2	3353.2
4	247.9572	839.152	1639.3	2666.7	3907.6
5	379.9715	1099.7	2008.9	3152.3	4504.6

Table 3.3: Analytical eigenvalues[93] and eigenfrequencies of the centrally fixed free edge circular plate.

3.3.2 Calculation of λ_{10} and f_{10}

In this particular case of the eigenmode with one nodal diameter ($m=1$) and without having any nodal circles ($n=0$), which attributes the smooth transition from the rigid body to rocking about the diameter [115]. When $\nu_m=0.33$, λ_{10} can be calculated according to Aireys solution [116],

$$\lambda_{mn} = \beta - \frac{3m\lambda + 13}{3(8\beta)} + \frac{40(3m\lambda + 5)}{9(8\beta)^2} \dots \quad (3.31)$$

where, $\beta = \frac{\pi}{2}(m + 2n)$ and $m\lambda = 4m^2$. So, $\lambda_{10} \approx 1.386$ and $f_{10} \approx 22.144$ Hz . The “trial and error” method or interpolation from the tables of Bessel functions has been used to find the approximate solutions. Colwell and Hardy [110] has demonstrated a series that converges rapidly and provides more accurate approximations.

$$\lambda_{mn} = \beta - \frac{m\lambda + 1}{8\beta} - \frac{4[7m\lambda^2 + 22m\lambda + 11]}{3[8\beta]^3} \quad (3.32)$$

So, $\lambda_{10} \approx 1.0311366$ and $f_{10} \approx 12.25$ Hz.

3.3.3 Effect of Fluid-structure Interaction

McLachlan [117], Kwak and Kim [118], Amabili et al. [112] and Amabili et al. [119] have extensively studied the effect of free vibration of the thin circular plate in contact with fluids (e.g. air, water) and concluded that in contact with air, the difference in resonance frequency is almost negligible or in some cases same as *in vacuo*. McLachlan [117] has demonstrated that for a free edge circular plate with the stationary centre, in contact with air provides only 5.3 % reduction in frequency compared to *in vacuo* case. The relationship between the resonance frequency *in vacuo* (f_v) and in contact with the fluid (f_f) can be expressed according to Amabili et al. [119]. Thus,

$$f_f = f_v \sqrt{\frac{1}{1 + \beta_{mn}}} \quad (3.33)$$

where, $\beta_{mn} = M_f/M_p$ is the added virtual mass incremental (AVMI) factor, M_p is the equivalent mass of the plate during vibration *in vacuo* and M_f is the accession to inertia due to the fluid on both sides of the plate. The β_{mn} can be also represented in terms of the reference kinetic energy of the plate (T_p^*) and the reference kinetic energy of the fluid due to the vibration of the plate (T_f^*).

$$\beta_{mn} = \frac{T_f^*}{T_p^*} = \frac{1}{\pi} \frac{k_f \rho_f a}{k_p \rho_m t_{APV}} \quad (3.34)$$

where, k_f is the accession coefficient and k_p is the mass coefficient McLachlan [117]. presence of air introduces added mass, added stiffness, and damping effects in the system. In a closed cavity, the added mass is the inertial effect due to air pumping, resulting in a reduction of the eigenfrequencies of the plate compared to a vacuum. As the air-gap height decreases, the pumping effect increases significantly, leading to an increase in added mass and a consequent decrease in eigenfrequencies.

Conversely, the added stiffness effect can lead to an increase in frequency for some modes. In certain modes, plate vibration causes a significant change in cavity volume in a closed system, resulting in a pressure disturbance. This pressure disturbance, acting in phase with the plate's motion, induces an added stiffness effect. In such cases, the frequency increases as the pressure disturbance intensifies with decreasing air-gap height, affecting the mode shape of the plate [120] [121].

Energy dissipation mainly occurs in the air gap due to viscous and thermal effects. Damping is explained by viscous shear and thermal conduction, processes that remove energy from the plate during vibration. Air pumping is associated with viscous shear, while air compression represents the thermal component of damping. According to Fox and Whitton [122], a high level of damping is primarily introduced by the viscosity of the air.

3.4 Numerical Modelling of Thermo-viscous Acoustics

Thermo-viscous acoustics represents the sound wave propagation in small geometries and structures consisting of small dimensions, which results in sound waves becoming attenuated due to the thermal and viscous losses in the boundary layers near the walls of the system. The governing equation of thermo-viscous acoustics is expressed by a set of linearized Navier-Stokes equations. The governing equations for thermo-viscous acoustics in the frequency domain can be derived under the assumption of small harmonic oscillations, and the dependent variables, such as pressure and velocity, can be written in the form:

$$p = p_0 + p' e^{i\omega t}, \quad \mathbf{v} = \mathbf{v}_0 + \mathbf{v}' e^{i\omega t}, \quad T = T_0 + T' e^{i\omega t} \quad (3.35)$$

where \mathbf{v} , p , and T denote the velocity vector, pressure, and temperature respectively, and components of the degrees of freedom (DOFs). \mathbf{v}' , p' , and T' are the acoustic variables and \mathbf{v}_0 , p_0 , and T_0 are the relevant background quantities. If the background fluid is quiescent so $\mathbf{v}_0 = 0$ and removing primes ($'$) from all the acoustic variables, under the assumption of small perturbations, the governing equations for the thermo-viscous acoustics, in the frequency domain can be expressed as [101]:

$$i\omega\rho_0\mathbf{v} - \nabla \cdot \boldsymbol{\tau}_t + \nabla p = 0 \quad (\text{Momentum equation}) \quad (3.36a)$$

$$i\omega C_p T - k_T \nabla T - i\omega p = 0 \quad (\text{Energy or enthalpy equation}) \quad (3.36b)$$

$$\nabla \cdot \mathbf{v} - i\omega \frac{T}{T_0} + i\omega \frac{p}{p_0} = 0 \quad (\text{Continuity equation}) \quad (3.36c)$$

Viscous and thermal losses are included with the terms which represent the viscous stress tensor ($\boldsymbol{\tau}_t$) and the heat conduction coefficient (k_T) and without them, the governing equations can be written as Helmholtz equation. The viscous tensor can be expressed with dynamic viscosity μ and a second viscosity term (λ_t):

$$\boldsymbol{\tau}_t = \lambda_t (\nabla \cdot \mathbf{v}) \mathbf{I} + \mu \left(\nabla \mathbf{v} + (\nabla \mathbf{v})^T \right) \quad (3.37)$$

The weak formulation has been created using a similar procedure in Section (3.1.2) from the set of Navier Stokes equations with test functions of \mathbf{v}_f , T_f and p_f respectively. The weak forms can be

written as:

$$\int_{\Omega} \left(\boldsymbol{\tau}_t : (\nabla \mathbf{v}_f) + i\omega \rho_0 \mathbf{v} \cdot \mathbf{v}_f + p(\nabla \cdot \mathbf{v}_f) \right) d\Omega - \int_{\Gamma} (p + \boldsymbol{\tau}_t \cdot \mathbf{n}) \cdot \mathbf{v}_f d\Gamma = 0 \quad (3.38a)$$

$$\int_{\Omega} \left((k_T \nabla T) \cdot (\nabla T_f) + i\omega \rho_0 C_p T T_f - i\omega p T_f \right) d\Omega - \int_{\Gamma} (k_T \nabla T) \cdot \mathbf{n} T_f d\Gamma = 0 \quad (3.38b)$$

$$\int_{\Omega} \left(\nabla \cdot \mathbf{v} - i\omega \frac{T}{T_0} + i\omega \frac{p}{p_0} p_f \right) d\Omega = 0 \quad (3.38c)$$

The thermo-viscous finite element model is obtained by discretizing this set of weak equations using standard FEM shape functions. It is advisable to use a lower order shape function for the pressure-dependent variable [101]. Applying the natural boundary conditions, the complete system matrix can be identified as symmetric or asymmetric, with important implications for the computational solution.

3.4.1 Boundary Layers

When acoustic waves propagate in a fluid bounded by solid walls, such as narrow slits, tubes, or holes, the no-slip boundary condition applies. This condition dictates that the fluid velocity at the solid boundary is zero ($\mathbf{v} = 0$), significantly influencing fluid flow behaviour near these boundaries. Temperature boundary conditions may vary based on the situation, assuming either an isothermal condition where the temperature at the wall remains constant or an adiabatic condition where there is no heat transfer between the fluid and the solid wall. Viscous boundary layers arise due to shear stresses between the fluid and the solid boundary, while thermal boundary layers emerge due to temperature gradients near the wall. The main factors contributing to sound energy dissipation are viscous forces and thermal conduction, primarily occurring in the viscous and thermal boundary layers.

It is crucial to include boundary layer effects in thermo-viscous acoustics. Figure (3.3) displays the thicknesses of viscous and thermal boundary layers in the air within the audible frequency range at $T = 20^\circ \text{C}$. For air, these boundary layer thicknesses are much smaller than the acoustic wavelength. In air at normal conditions, the thickness of the boundary layer can range from micrometres (for low-speed flows) to a few millimetres (for higher-speed flows). In comparison, the wavelengths of audible acoustic waves in air range from centimetres to meters. In this frequency range, the boundary layer thickness is several orders of magnitude smaller than the acoustic wavelengths, requiring a large number of elements in the boundary layers. The viscous boundary layer (δ_v) is a function of fluid viscosity (μ), and the thermal boundary layer is defined by the fluid thermal conductivity (k_T). The thickness of the thermal boundary layer (δ_t) is defined as

$$\delta_t = \sqrt{k_T / \pi f \rho_0 C_p} \quad (3.39)$$

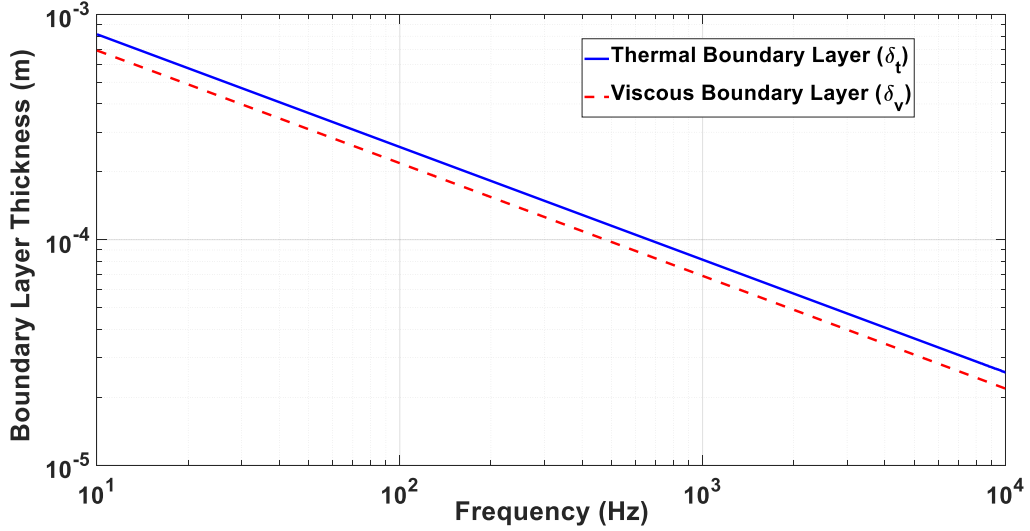


Figure 3.3: At standard conditions (1-atmosphere pressure and 20° C), the viscous and thermal boundary layers in air demonstrate distinctive thicknesses.

where C_p is the fluid heat capacity at constant temperature and the thickness of the viscous boundary layer is defined as

$$\delta_v = \sqrt{\mu / \pi f \rho_0} \quad (3.40)$$

The thicknesses of the viscous and thermal boundary layers can be represented by the Prandtl number which is the ratio of these lengths and represented as:

$$\text{Pr} = \left(\frac{\delta_v}{\delta_k} \right)^2 \quad (3.41)$$

For air in the audible frequency range and at $T = 20^\circ \text{C}$, the $\text{Pr} \approx 0.7$. The boundary layer thicknesses are crucial for accurately modelling the total energy dissipation in the system. The meshed domain can be created and controlled by parameters defining boundary layer thicknesses. Precise and careful meshing is crucial when incorporating visco-thermal effects into the complete model.

In this thesis, visco-thermal effects are incorporated into the complete model by utilizing the thermo-viscous acoustics interface available in the acoustics module of COMSOL. Several techniques and alternative approaches can be employed to model acoustic phenomena near solid boundaries without resorting to full thermo-viscous modelling with a fine boundary layer mesh in COMSOL. These include narrow region acoustics, thermoviscous boundary layer impedance, etc. In COMSOL's

FEM implementation, boundary layers have been included in the meshing process by adjusting the control parameters provided by COMSOL to achieve an accurate representation of the visco-thermal effects.

3.5 Numerical Modelling of Fluid-Structure Interactions

The combined effect of structural mechanics and fluid dynamics is often represented using the coupling mechanism of vibro-acoustics. Given the widespread use of the Finite Element Method (FEM) for modelling both acoustics and structural dynamics, it is convenient for addressing this multi-physics phenomenon. Considering structural dynamics, we can introduce a coupling matrix \mathbf{K}_c , and the complete equation describing coupled structural vibrations is as follows:

$$(\mathbf{K}_s + i\omega\mathbf{D}_s - \omega^2\mathbf{M}_s)\mathbf{u} + \mathbf{K}_c\mathbf{p} = \mathbf{F}_s \quad (3.42)$$

where the subscript s stands for the structural system matrices. Since the structural vibrations affect the acoustic domain in a common region the complete equation describing the coupled acoustics can be written as

$$(\mathbf{K}_a + i\omega\mathbf{D}_a - \omega^2\mathbf{M}_a)\mathbf{p} + \omega^2\rho_0\mathbf{K}_c^T\mathbf{u} = \mathbf{F}_a \quad (3.43)$$

where, the subscript a stands for the structural system matrices. After combining the Eq. (3.42) and Eq. (3.43) we get the coupled equation of fluid-structure interaction in FEM as:

$$\left(\begin{bmatrix} \mathbf{K}_s & \mathbf{K}_c \\ 0 & \mathbf{K}_a \end{bmatrix} + i\omega \begin{bmatrix} \mathbf{C}_s & 0 \\ 0 & \mathbf{C}_a \end{bmatrix} - \omega^2 \begin{bmatrix} \mathbf{M}_s & 0 \\ -\rho_0\mathbf{K}_c^T & \mathbf{M}_a \end{bmatrix} \right) \begin{bmatrix} \mathbf{u} \\ \mathbf{p} \end{bmatrix} = \begin{bmatrix} \mathbf{F}_s \\ \mathbf{F}_a \end{bmatrix} \quad (3.44)$$

which can be written in a simplified form as:

$$(\mathbf{K}_{f_{si}} + i\omega\mathbf{D}_{f_{si}} - \omega^2\mathbf{M}_{f_{si}})\mathbf{x} = \mathbf{F}_{f_{si}} \quad (3.45)$$

This system equation has the same shape as in the FEM model of structural dynamics and the acoustics where $\mathbf{K}_{f_{si}}$, $\mathbf{M}_{f_{si}}$ and $\mathbf{D}_{f_{si}}$ are the coupled element stiffness, mass and damping matrices respectively which are no longer symmetric due to the presence of coupling matrix \mathbf{K}_c . The Eq. (3.45) considers vibro-acoustics effects as a strong coupling effect (e.g. structural interaction with heavy fluids, using high sound pressure levels). In the case of weak coupling, the coupled acoustic structural interactions consider the term $\mathbf{K}_c\mathbf{p}$ as negligible which is basically the system of the equation of the structural vibrations.

Thermo-viscous acoustics can be coupled to the structure, using three velocity components (in 3-D) and the temperature. The structural vibration may be described with displacement \mathbf{u} or velocity $\dot{\mathbf{u}}$ degrees of freedom. The essential fluid boundary conditions at fluid-structure interface ($d\Gamma_{fsi}$) can be expressed as:

$$\begin{aligned}\mathbf{v} &= i\omega\mathbf{u} \\ \mathbf{v} &= \dot{\mathbf{u}}\end{aligned}\tag{3.46}$$

The load of the fluid on the structure can be written as:

$$F_s = -\boldsymbol{\sigma} \cdot \mathbf{n}\tag{3.47}$$

where, \mathbf{n} is the unit vector normal to the boundary, $\boldsymbol{\sigma}$ the stress tensor phasor and F_s the load on the structure at $d\Gamma_{fsi}$. Since air can barely heat the structure in most cases, a coupled formulation for heat conduction in the structure is usually avoided. Instead, the isothermal boundary condition is widely used in thermoviscous acoustics which is an accurate approximation as validated by Bruneau et al. [123].

3.6 Summary

In this chapter, the physical theories of acoustics, thermo-viscous acoustics, and structural mechanics (specifically, the vibration of plates) have been presented. The multi-physics coupling of relevant interfaces has been described following the Finite Element Method (FEM) formulation, which is essential for accurately replicating the system. Finally, the application of the FEM to different physics interfaces has been discussed.

Chapter 4

Development of Novel Plate-type Acoustic Valve Resonator

4.1 Plate-type Acoustic Valve Resonator

A range of off-the-shelf elastomeric valves were initially tested. These valves were sourced from the company minivalve [124] and are typically used in fluidic control. Figure (4.1) shows the full range of four elastomeric valves which were tested. Two umbrella valves of different diameters as well as one duckbill valve and a cross-slit valve. Basically, these valves allow flow to pass in only one direction. Figure (4.2) shows how the valve is fixed to a thin plate via a small mounting hole in the centre, with six additional holes required in the plate to allow for fluid flow. Also, Fig. (4.2) shows the plate with the 16 cross-slit valves installed for testing in the impedance tube. It can be seen how the impedance tube is adapted to allow for circular samples. The test configuration is shown in Fig. (4.2(b)) where a solid end cap is mounted creating a cavity behind the metasurface plate. Table 4.1 shows the properties of the valves, the number of valves used in each plate as well as the open area in the plate through which flow may pass once the valve is open.

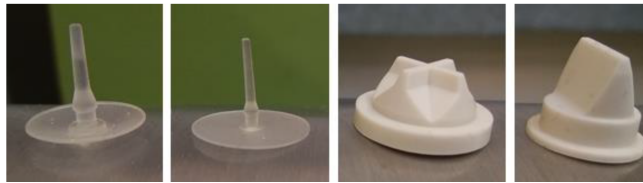


Figure 4.1: Elastomeric Valves tested. Umbrella Valves: UM 145, UM 180, CR 150, DU 120

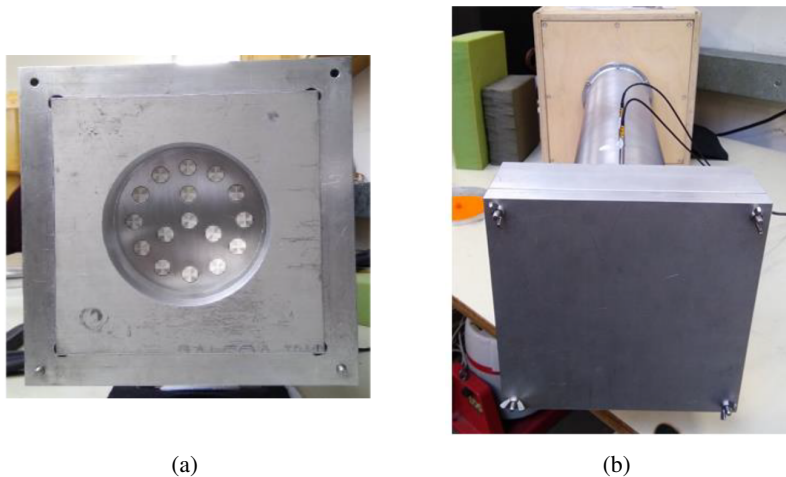


Figure 4.2: (a) Cross-slit valves installed in mounting plate. (b) Test configuration with solid backing plate creating a cavity depth behind the sample [125].

Table 4.1: Off-the-shelf elastomeric valves by Minivalve [124]

Valve Code	Valve Type	Diameter [mm]	No. of valves used	Open area [m^2]
UM145	Umbrella valve	14.5	9	0.5×10^{-3}
UM180	Umbrella valve	18	12	0.9×10^{-3}
CR150	Cross-Slit Valve	15	16	2.8×10^{-3}
DU120	Duck-Bill valve	12	16	1.8×10^{-3}

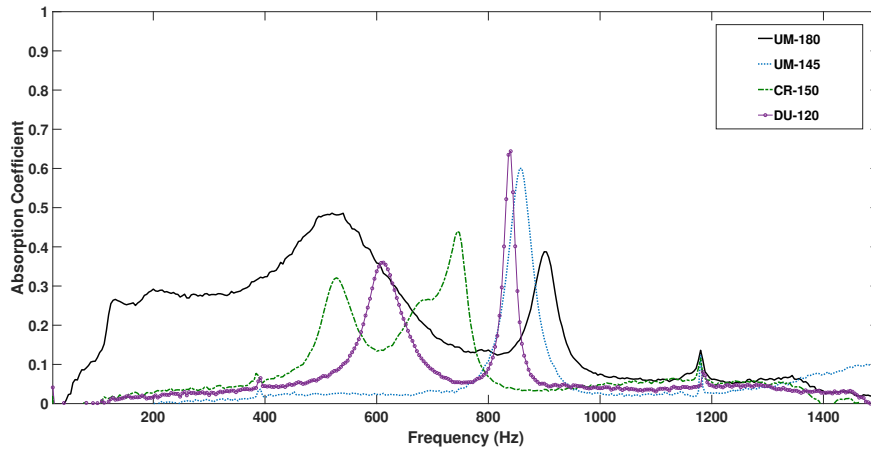


Figure 4.3: Experimental absorption coefficient measured for off-the-shelf elastomeric valves with hardwall backing 43 mm from mounting plate [125].

Figure (4.3) shows the experimental results of the absorption coefficient for the elastomeric valves tested for the situation where the meta-surface would be installed on the inside surface of a solid wall such as within a cavity. The performance of the valves is extremely promising with absorption coefficients of up to 0.7 at maximum and with some valves absorbing noise over a broad range of frequencies. Valves perform well for frequencies below 1000 Hz which was the objective of the test. It is difficult to compare one valve with another as the physics of their mechanisms are quite different, and both the number of valves and open area in the plate change from one test to another. However, it seems that the 18 mm diameter umbrella valve seems to perform best overall, with absorption coefficients up to 0.5 maximum and over 0.3 over a broad range of frequencies.

4.1.1 Prototypes Design

As discussed in the introduction, further to the work of Bennett et al. [20], testing was performed with 3D printed valves similar to one of the original elastomeric umbrella valves but of much larger diameter, $\phi_{AD} = 124$ mm, with a thickness of $t_{AD} = 0.5$ mm as shown in Fig. (4.4). Fig. (4.5) shows the simplified axisymmetric representation of plate-type acoustic valve and cavity. In the schematic,

mounting plate hole radius denoted as r_p , plate-type acoustic valve radius as r_{APV} , impedance tube inner radius as r_{tube} , nominal neck length as l_n , neck area as S_n , mounting plate thickness as t_{MP} , nominal air-gap as h_d , plate thickness as t_{APV} , and cavity depth as l_{cav} . The diameter of 124 mm was chosen to maximise the size of the plate-type acoustic valve in the duct of 127 mm diameter, but, by allowing for a gap of 1.5 mm between the outer diameter of the plate-type acoustic valve and the inner diameter of the tube, local edge viscous losses are minimised focusing the attention of the study on the interaction between the plate-type acoustic valve and the mounting plate.

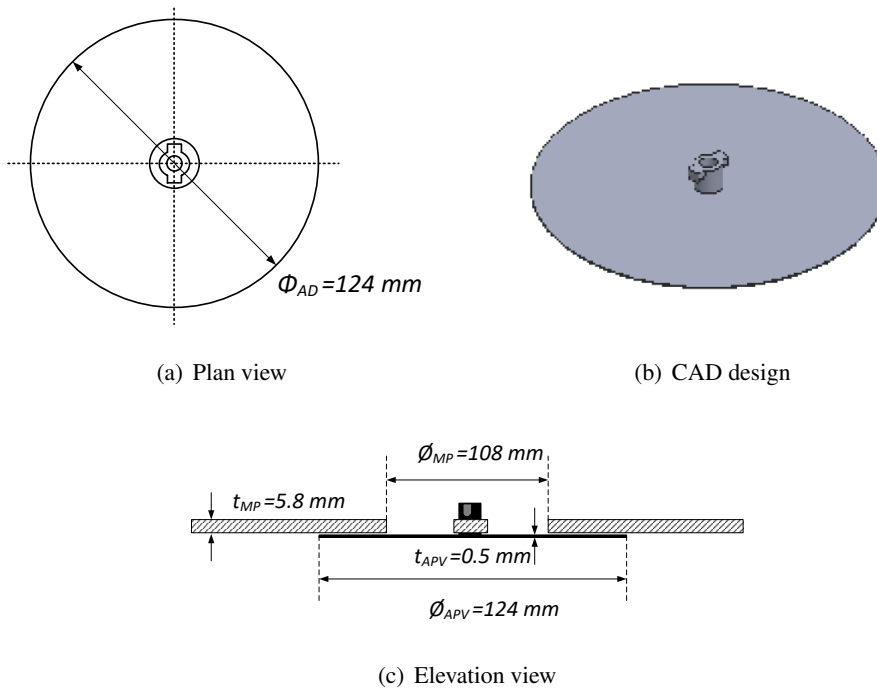


Figure 4.4: Nominal geometric parameters of the plate-type acoustic valve.

4.1.2 Additive Manufacturing Process

4.1.2.1 Additive Manufacturing

Additive Manufacturing is a layer-by-layer construction of a three-dimensional structure using liquid, solid or powdered materials. The use of additive manufacturing technologies has shown great potential in acoustic metamaterial research for rapid prototyping of the structure. This technology helps to intelligently design to develop the novel acoustic metamaterial overcoming the difficulties associated with using the traditional materials and manufacturing techniques. A wide range of acoustic devices can be designed and developed with meticulous details using additive manufacturing. Also, growing development in additive manufacturing provides a reliable way for rapid prototyping of structures

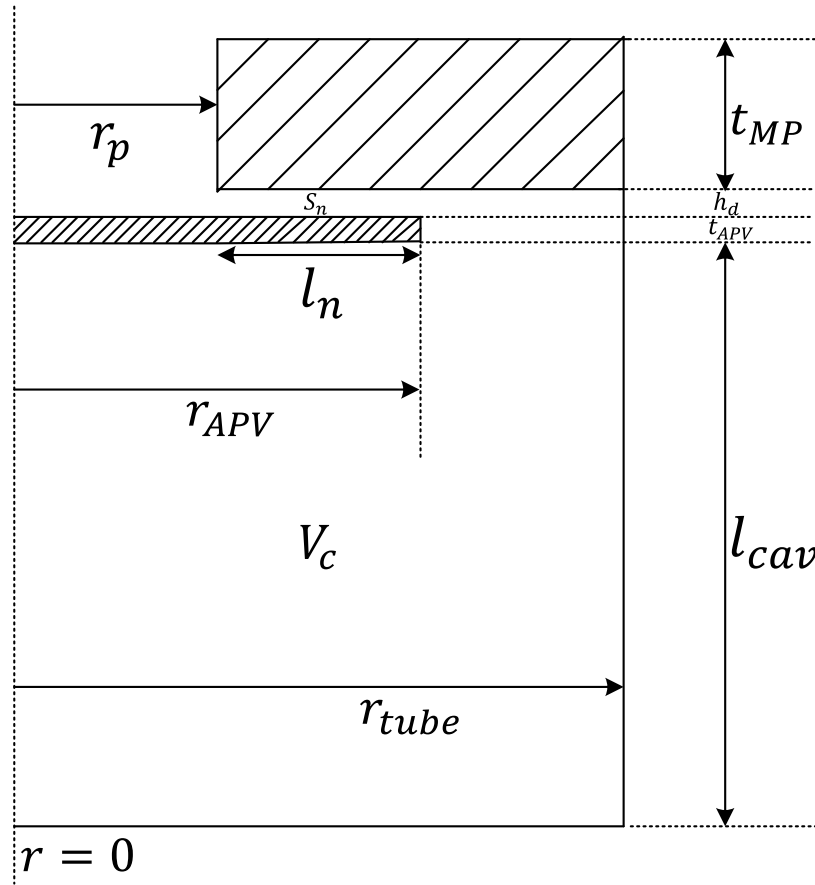


Figure 4.5: Axisymmetric schematic of plate-type acoustic valve and cavity.

with complex geometries. There are several additive manufacturing technologies available such as stereolithography (SL), fused deposition modelling (FDM), selective laser sintering (SLS), multi-jet modelling (MJM) or digital light processing (DLP). Among them, FDM and SL are the widely used technologies based on the references analysed by Suárez and del Mar Espinosa [126] and shown in Fig. (4.6). The acoustic metamaterial research has been dominated by the use of polymeric materials: thermoplastics (ABS, PLA, Nylon, TPU ...) and photo-curable resins. In this work, FDM has been extensively used for the 3D printing of the samples. In FDM, the process of manufacturing the metamaterial samples starts with designing a model in computer-aided design (CAD) software and then it is converted to a .STL file where the CAD design is approximated by triangles. In the process, the CAD model further translated into a .GCODE file that is usable by the 3D printer using a slicer software. The .GCODE file contains the information for each sliced layer that is going to be printed individually and the instructions for the printing machine to move in certain coordinates.

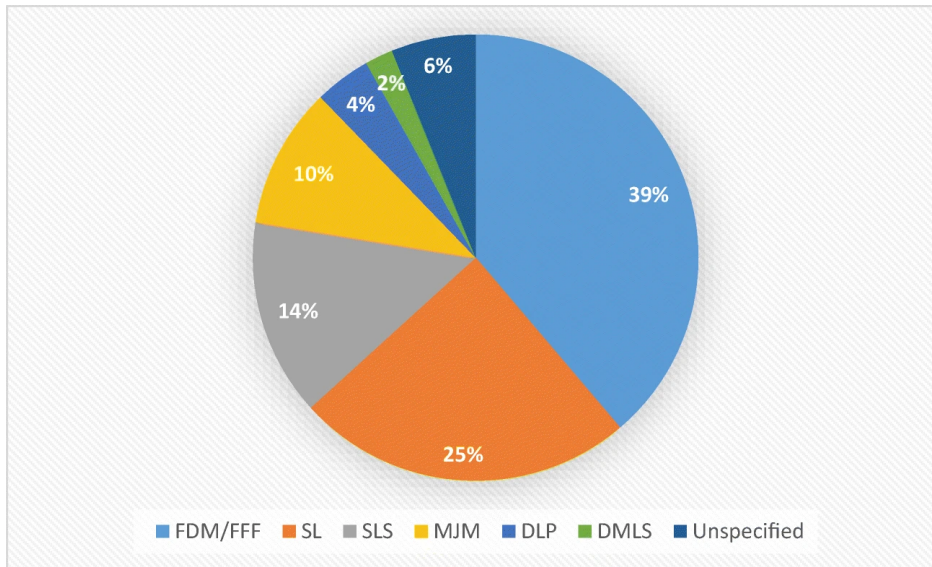


Figure 4.6: A pie chart showing the use of additive manufacturing technologies in acoustic research [126]

4.1.2.2 Manufacturing the Sample

This one-way valve was manufactured with an Ultimaker-3 FDM 3D printer using a print layer resolution of 0.15 mm. The Ultimaker-3 was chosen as it has two printer heads which enables printing with two different materials at the same time. In this case, PLA was chosen as the main material of the plate-type acoustic valve while water-soluble PVA was used as the support scaffolding. By using water-soluble PVA, the scaffolding is more easily and completely removed resulting in a more accurate shape and a better surface finish.

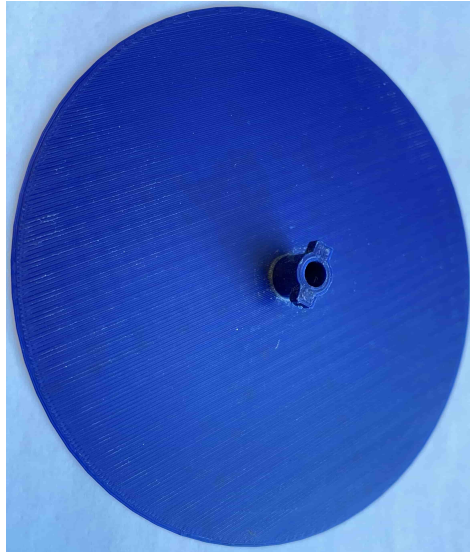


Figure 4.7: 3D printed plate-type acoustic valve sample.

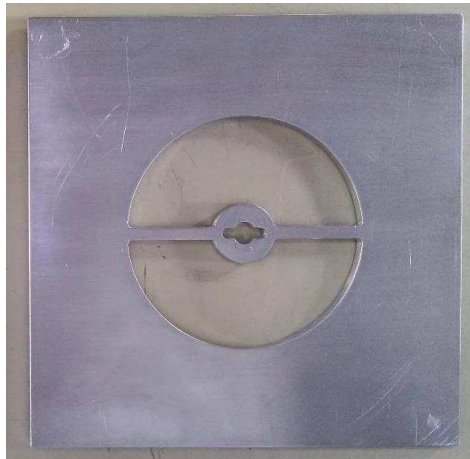


Figure 4.8: Mounting plate for plate-type acoustic valve.



Figure 4.9: Mounted 3D printed plate-type acoustic valve sample (Bottom View).

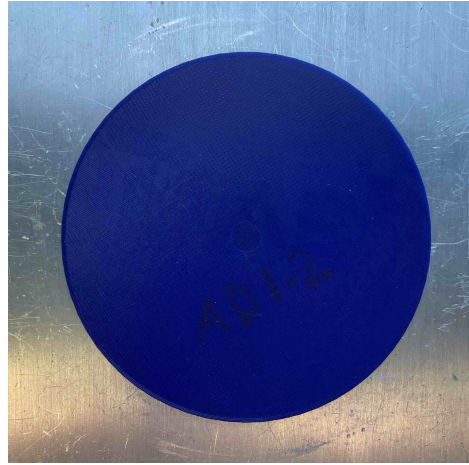


Figure 4.10: Mounted 3D printed plate-type acoustic valve sample (Top View).

Figure (4.7)-(4.10) shows the one-way valve examined in this current research along with its mounting plate. The mounting plate was also manufactured from aluminium and is 5.8 mm thick. Like the spacer plates, it is square, 200 mm X 200 mm, and designed to have a sliding fit inside the square test section. Its hole is designed to provide maximum open area while allowing an overlap of 8 mm with the plate-type acoustic valve, see Fig (4.4(c)). Due to the need to mount the plate-type acoustic valve to the plate, two narrow ribs are required so the opening is not complete, see Fig. (4.9). The plate-type acoustic valve was designed with a central strut which allows for a simple push-and-twist installation process into the mounting plate. The length of the strut was designed so that the plate-type acoustic valve is in contact with the mounting plate around its perimeter once installed.

Although the designed thickness of the valve was 0.5 mm, the printed sample had a slightly non-uniform thickness over the surface area. The average thickness was measured to be 0.52 mm using a micrometer calipers. The value of 0.52 mm was subsequently used for the numerical and analytical analysis.

4.2 Summary

In this chapter, a new acoustic meta-material termed the “plate-type acoustic valve resonator” has been introduced. The plate-type acoustic valve is essentially a thin circular plate free at the edge and clamped at the centre, mounted on a rigid plate with maximum porosity. The development process of the 3D-printable one-way valves has been described using relevant sketches. Additionally, the design inspiration and manufacturing process have been discussed.

Chapter 5

Experimental Rig and Measurements Techniques

The absorption coefficients for acoustic materials under random and normal incidences can be measured using two methods: either within a reverberation chamber or through an impedance tube (Kundt's tube) under normal incidence conditions. The reverberation time method mainly simulates the conditions experienced in buildings (reverberation chamber with a volume of 200 m³). But for layers of textiles with a small diameter (usually less than 10 cm) impedance tube measurement has been widely used to obtain the normal incidence absorption coefficient. In 1977, Seybert and Ross [127] proposed the two-microphone random-excitation technique for the determination of normal acoustic properties. Measurement of absorption coefficient conducted by Chung and Blaser [128] in 1980 based on the transfer function method using impedance tube with two microphones. Several modifications and different techniques have been reported after that. The techniques reported are the four-microphone method using an anechoic chamber at the end for transmission loss measurement [129], [48], the two-microphone dual cavity-backed method [130], a modified variant of the Iwase method [131], multiple microphone method [132], [133] and simplified three-microphone acoustic test method [134].

5.1 Experimental Setup

Experimental measurement of the absorption coefficient was performed using the two-microphone impedance tube method. The tube was designed under the ISO standard 10534-2:2001 [135] for impedance, reflection and absorption measurements. A schematic of the experimental setup is shown in Fig. 5.1. The impedance tube, designed for high amplitude testing, is made of aluminium of 12.7 mm wall thickness minimizing leakage and external noise ingress interfering with the data acquisition process. The tube has a circular cross-section with an internal diameter of $\phi_{tube}=0.127$ m and therefore has a plane wave cut-off frequency of approximately 1.5kHz. The tube has a length $L=0.78$ m with the capacity to attach a second length of tube for sound transmission loss measurements under the ASTM standard E2611 [136] although this is not investigated in this work. A high-amplitude loudspeaker is attached to the tube at one end. The loudspeaker used in this rig is a JBL 2206H/J 12 subwoofer. The subwoofer's frequency response ranges from 45 Hz to 3.5 kHz, allowing for testing at low frequencies often not reproducible by smaller speakers and impedance tube rigs. The speaker is contained in a custom-built 18 mm thick plywood unit with a flange opening allowing it to be mounted to the tube.

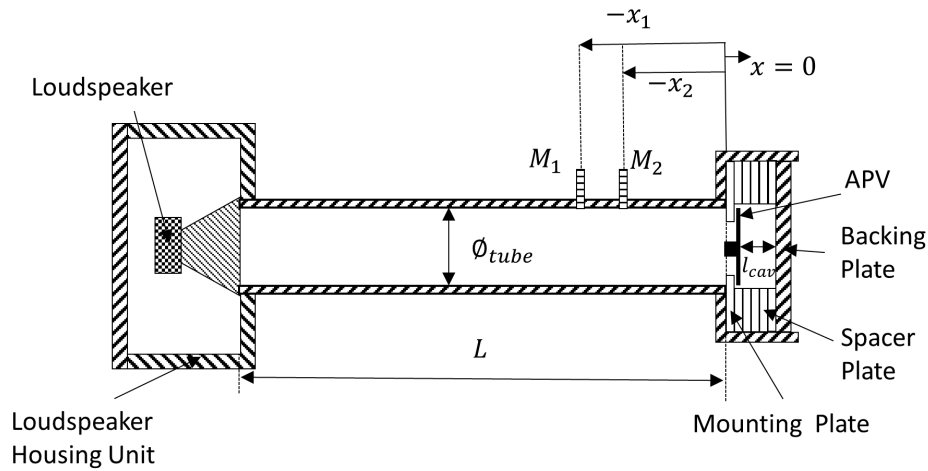


Figure 5.1: Impedance tube schematic

A termination/test section to the tube was designed to allow for adjustable back-cavity depths. The termination is an aluminium, square section housing with a 24.75 mm wall thickness which allows square spacer plates with circular holes of the same diameter as the internal diameter of the tube to be inserted behind the mounting plate creating a back cavity. Spacer plates of different thicknesses can be combined to create a variety of back-cavity depths. A thick, 20 mm, solid aluminium backing plate with no hole was inserted downstream of the spacer plates to form the hard wall termination. Figure 5.2 shows a photo of the test set-up with an additional solid hard wall backing bolted to the rear of the square test section.

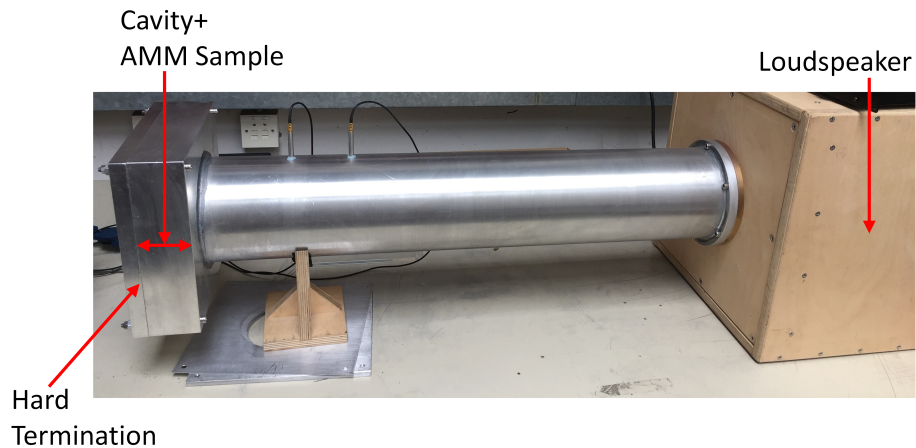


Figure 5.2: Photograph of the experimental test section with impedance tube.

Two G.R.A.S. 40PH microphones, (M_1 and M_2), with a frequency range of 20 Hz - 20 kHz were used in the rig and calibrated under the ISO 10534-2:2001 standard. The microphones were recessed into the wall of the impedance tube and were separated from the internal pressure field of the tube by a 2 mm diameter hole of 1 mm in length. The microphones were located $x_1 = 0.212$ m and $x_2 = 0.127$ m from the face of the plate-type acoustic valve mounting plate. The sample was tested using white noise with a sound pressure level (SPL) of 94 dB for 120 seconds. Other SPLs ranging from 100 dB to 120 dB were tested but no significant non-linear effects were observed.

5.2 Measurements Techniques

5.2.1 Transfer Function Method

The experiments were conducted in the impedance tube with a two-microphone measurement principle based on the transfer function method. The cavity configuration after the sample and hard termination at the end of the tube were considered for the experiments.

During experiments, white noise is generated through the speaker and the sound pressures from microphones 1 and 2 are measured as p_1 and p_2 . The complex sound pressures at the two microphones are given by the sum of the forward and backward travelling waves in the tube [137]:

$$p_1 = Ae^{jkx_1} + Be^{-jkx_1} \quad (5.1)$$

$$p_2 = Ae^{jkx_2} + Be^{-jkx_2} \quad (5.2)$$

where x_1 and x_2 are distances of the microphones 1 and 2 respectively from the face of the sample. These two complex pressures can then be used to find the transfer function H_{12} , which can be defined as:

$$H_{12} = \frac{p_2}{p_1} = \frac{Ae^{jkx_2} + Be^{-jkx_2}}{Ae^{jkx_1} + Be^{-jkx_1}} \quad (5.3)$$

The reflection coefficient (r) is defined as the ratio of the reflected wave amplitude (B) to the incident wave amplitude (A):

$$r = \frac{B}{A} \quad (5.4)$$

Eq. (5.3) can be written as:

$$H_{12} = \frac{Ae^{jkx_2} + rAe^{-jkx_2}}{Ae^{jkx_1} + rAe^{-jkx_1}} \quad (5.5)$$

After rearranging, the reflection coefficient (r) and absorption coefficient (α) calculated as:

$$r = \frac{H_{12}e^{jkx_1} - e^{jkx_2}}{e^{-jkx_2} - H_{12}e^{-jkx_1}} \quad (5.6)$$

$$\alpha = 1 - |r|^2 \quad (5.7)$$

5.2.2 Laser Doppler Vibrometry (LDV) Method

The experimental modal analysis of the plate-type acoustic valve was performed using a single-point vibrometer (PDV-100, Polytec GmbH) based on a Laser Doppler Vibrometry (LDV) methodology. The working principle of the LDV is related to a laser beam focused on the vibrating structure so that the relative movement between the laser and the structure causes the presence of the Doppler effect (or Doppler shift) i.e. the apparent difference caused by relative motion in wavelength and frequency of a wave when the observer and the source are moving. The modal analysis has been used to identify the resonant frequencies and mode shapes of the plate-type acoustic valve using a frequency-based measurement function known as the frequency response function (FRF). FRF is defined as the ratio of output signal to input signal and can be written in the following form:

$$H(\omega) = \frac{\text{movement}}{\text{excitation force}} \quad (5.8)$$

Considering the hysteretic model with N set of complex eigenvalues λ_r^2 and corresponding eigenvectors $\{\Psi_r\}$, the system of equations for the multiple degrees of freedom system has the form of homogeneous equation as:

$$\left[[K] + i[D] - \lambda_r^2[M] \right] \{\Psi_r\} = \{0\} \quad (5.9)$$

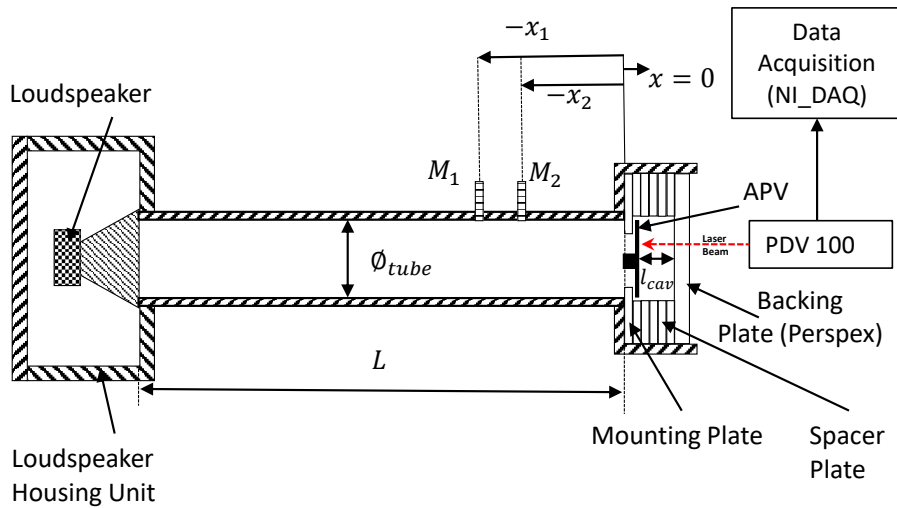
where, $[M]$, $[D]$ and $[K]$ are $N \times N$ mass, hysteretic damping and stiffness matrices, respectively. At a frequency ω , when a thin plate is excited at a point p by an excitation function $f_p(\omega)$, a response spectrum $v_q(\omega)$ can be obtained at a point q . The Eq. (5.8) can be re-written as:

$$H(\omega) = \frac{v_q(\omega)}{f_p(\omega)} = \sum_{r=1}^N \frac{r\bar{A}_{pq}}{\omega_r^2 - \omega^2 + i\eta_r\omega_r^2} \quad (5.10)$$

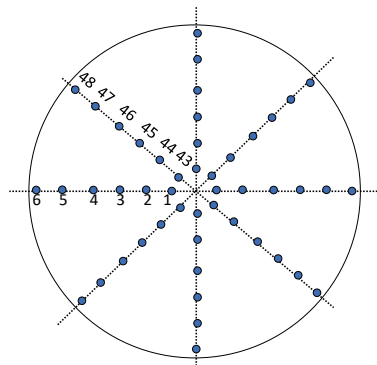
where, ω_r and η_r are the angular natural frequency of the vibration and damping loss factor for the mode order of r respectively and $rA_{pq} = |\Omega_{pr}\Omega_{qr}| = |\Psi_{pr}\Psi_{qr}/m_r|$ is a modal constant and Ψ_{pr} and Ψ_{qr} are the elements p and q , respectively, of the mode shape vector of $\{\Psi_r\}$ and m_r is the generalised modal mass [138] [139].

Experimentally, movement can be obtained in the form of displacement or velocity or acceleration and excitation force can be provided from the impact hammer or electrodynamic shakers. Since the plate-type acoustic valve is very thin, the impact hammer was not effective in providing accurate measurements. Hence, acoustic excitation has been provided by generating a noise signal with the loudspeaker. Considering the thinness of the plate-type acoustic valve, using accelerometers as a

response measurement device has been avoided to prevent modification of its mass. In the presence of acoustic excitation, the velocity of the plate-type acoustic valve was measured using the laser vibrometer and the FRF of the system was obtained. The hard solid wall at the end of the cavity was replaced by a perspex plate with the same thickness as the solid hard wall. Figure (5.3) shows the



(a) Schematic diagram of the setup for impedance tube experiments using a Laser Doppler vibrometer to evaluate vibrational measurements.



48
Measurement
Points

(b) Measurements scanning points

Figure 5.3: Impedance tube configuration for vibrational analysis.

complete configurations of the impedance tube setup for modal analysis of the plate-type acoustic valve. Figure (5.3(a)) shows the schematic diagram of the setup for impedance tube experiments with laser vibrometer and the distribution of the 48 measurements points on the plate-type acoustic valve

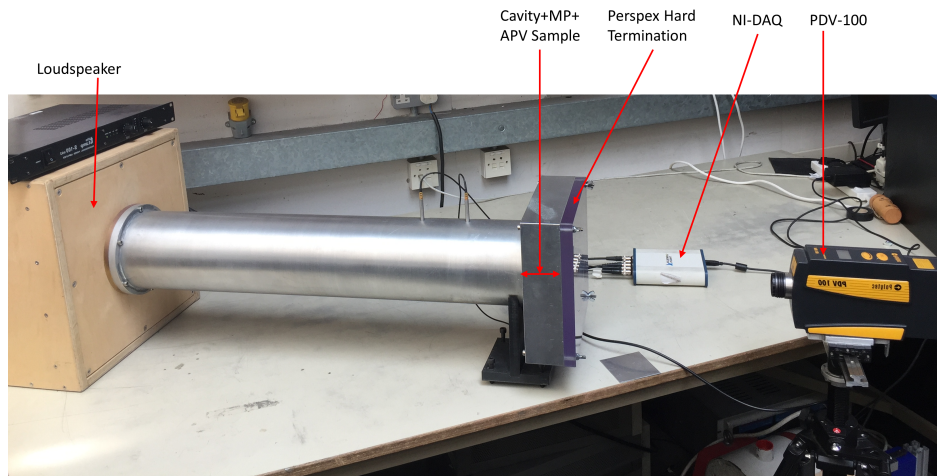


Figure 5.4: Photograph of the experimental test section with PDV-100.

with angel steps $\theta_s = 45^\circ$ and the radius steps $\Delta_r = 10$ mm are shown in the Fig. (5.3(b)). Figure (5.4) shows the photograph of the experimental setup during the modal analysis.

5.3 Summary

In this chapter, the ensemble of the experimental test rig and the measurement techniques have been presented. In the acoustic measurements, the main focus was on obtaining the reflection and absorption coefficients, while laser Doppler measurements were performed to capture the vibrational modes and corresponding modal shapes. The cavity end section was constructed with a solid wall and a transparent wall of the same thickness to maintain consistent boundary conditions for both Laser Doppler Velocimetry (LDV) and acoustic measurements. These measurements were repeated multiple times to ensure the repeatability of the experimental results.

Chapter 6

Numerical Prediction of Plate-type Acoustic Valve Resonator

In this chapter, numerical techniques of the FEM model have been provided for the complete plate-type acoustic valve resonator system. Modelling techniques in the frequency domain are described in detail. The numerical model provides an understanding of the acoustic absorption mechanism, vibration analysis of the plate-type acoustic valve, and the multi-physics coupling of the acoustic, thermoviscous, and structural domains.

6.1 2D FEM Model: Modeling with Thermo-viscous Acoustics

FEM simulations were performed using the commercial software COMSOL Multiphysics version 6.0 with preset pressure acoustics, thermoviscous acoustic and solid mechanics interfaces. The Acoustics module is well suited for all frequency-domain simulations with harmonic variations of the pressure field. A frequency domain analysis of the plane wave propagation has been performed where the plate-type acoustic valve was modelled as a linear elastic material using the solid mechanics interface and the interior of the impedance tube was modelled as air with the pressure and thermoviscous acoustics interfaces. Coupling between thermoviscous acoustic and pressure acoustics is achieved with an acoustic-thermoviscous acoustic boundary while coupling between solid mechanics and thermoviscous acoustics is done with a thermoviscous acoustic-structure boundary. The geometric parameters used in the simulation are chosen from the experimental setup described in Section 5.1 with a variable cavity length (l_{cav}). The geometric model for the FEM simulation, as shown in Fig. (6.1), is a simplified 2D axisymmetric model to reduce computational costs and time with little compromise of the fundamental characteristics. The model represents the cylindrical impedance tube set-up with the plate-type acoustic valve, mounting plate, and back cavity. The geometric coordinates for the plane in the 2D axisymmetric implementation are (r, z) and the angle φ is not defined since it is not part of the computational domain implemented in the simplified model. The material properties of PLA were taken from the literature [140]: mass density $\rho = 1270 \text{ kgm}^{-3}$, Youngs modulus $E = 3.5 \times 10^9 \text{ Pa}$, Poissons ratio $\nu = 0.3$ [141] and damping factor $\eta = 0.025$ [142], with typical values taken for air: mass density $\rho_0 = 1.23 \text{ kgm}^{-3}$ and the speed of sound in air being $c_0 = 343 \text{ ms}^{-1}$. To avoid domain overlapping in the FEM modelling, a very small gap was introduced between the mounting plate and the plate-type acoustic valve. Due to the meshing requirements, it is not possible to model the setup without the gap. The value for the air gap ($h_d = 0.4 \text{ mm}$) was chosen iteratively to match the experimental results.

Additionally, an eigenfrequency analysis was also performed using only the solid mechanics part of the model for the plate-type acoustic valve to obtain its structural resonance modes. The free

vibration of the plate-type acoustic valve (considered as a centrally fixed thin circular plate) *in vacuo* was investigated using this eigenfrequency analysis (for further details, see Appendix B.1). The boundary conditions, meshing and the calculations of the reflection and absorption coefficient are demonstrated in the following sections.

6.1.1 Boundary Conditions

The vibroacoustic behaviour of plate-type acoustic valve resonators under normal incidence is investigated using an acoustics module and structural mechanics module in the frequency domain. The following boundary conditions were used in the numerical simulations. A plane incident wave, p_{inc} , is applied from the upstream end of the impedance tube with unit amplitude. Some part of the acoustic energy is reflected from the downstream end and the rest is absorbed by the plate-type acoustic valve and the cavity. Sound-hard boundary walls and symmetry conditions are also applied to the model as shown in Fig. (6.1). Pressure acoustics is defined by the Helmholtz equations, visco-thermal acoustics is defined by linearized Navier Stokes equations and structural mechanics is defined as a linear elastic material. To model a plate-type acoustic valve as a linear elastic material we need three equations: an equilibrium balance, a constitutive expression defining the relationship between stress and strain, and a kinematic equation connecting displacement to strain. The equilibrium equation can be represented by Newtons second law and can be demonstrated in the tensor form as:

$$\nabla \cdot \boldsymbol{\sigma} + F_v = \rho \frac{\partial^2 \mathbf{u}}{\partial t^2} \quad (6.1)$$

where, $\boldsymbol{\sigma}$ is stress, F_v is body force per volume, ρ is density, and \mathbf{u} is displacement vector. The constitutive equation can be defined by the generalized Hookes law:

$$\boldsymbol{\sigma} = \mathbf{C} : \boldsymbol{\varepsilon} \quad (6.2)$$

where, $\boldsymbol{\varepsilon}$ is the strain and \mathbf{C} is the fourth-order elasticity tensor. For COMSOL applications, the expression expanded to

$$\boldsymbol{\sigma} - \boldsymbol{\sigma}_0 = \mathbf{C} : (\boldsymbol{\varepsilon} - \boldsymbol{\varepsilon}_0 - \boldsymbol{\varepsilon}_{inel}) \quad (6.3)$$

where, $\boldsymbol{\sigma}_0$ is the initial stress, $\boldsymbol{\varepsilon}_0$ is the initial strain, and $\boldsymbol{\varepsilon}_{inel}$ is the inelastic strain and are all zero. The elasticity tensor matrix (D_ε) can be reduced to 6×6 matrix considering linear elastic material as isotropic material.

$$\begin{pmatrix} 2\mu_L + \lambda_L & \lambda_L & \lambda_L & 0 & 0 & 0 \\ \lambda_L & 2\mu_L + \lambda_L & \lambda_L & 0 & 0 & 0 \\ \lambda_L & \lambda_L & 2\mu_L + \lambda_L & 0 & 0 & 0 \\ 0 & 0 & 0 & \mu_L & 0 & 0 \\ 0 & 0 & 0 & 0 & \mu_L & 0 \\ 0 & 0 & 0 & 0 & 0 & \mu_L \end{pmatrix}$$

where, λ_L and μ_L are the Lamé constants and expressed by the Young's modulus (E_m) and Poisson's ratio (ν_m) of the material as:

$$\lambda_L = \frac{E_m \nu_m}{(1 + \nu_m)(1 - 2\nu_m)}, \quad \mu_L = \frac{E_m}{2(1 + \nu_m)} \quad (6.4)$$

The kinematic equation provide the relation between displacements u and strains ε in tensor form as:

$$\varepsilon = \frac{1}{2}[\nabla \mathbf{u} + (\nabla \mathbf{u})^T] \quad (6.5)$$

where T denotes the transpose of the tensor. Considering the small displacements, the normal strain components and the shear strain components can be represented by the deformation components u , v and w in 3D.

$$\varepsilon_x = \frac{\partial u}{\partial x} \quad \varepsilon_{xy} = \frac{1}{2}\gamma_{xy} = \frac{1}{2}\left(\frac{\partial u}{\partial y} + \frac{\partial v}{\partial x}\right) \quad (6.6)$$

$$\varepsilon_y = \frac{\partial v}{\partial y} \quad \varepsilon_{yz} = \frac{1}{2}\gamma_{yz} = \frac{1}{2}\left(\frac{\partial v}{\partial z} + \frac{\partial w}{\partial y}\right) \quad (6.7)$$

$$\varepsilon_z = \frac{\partial w}{\partial z} \quad \varepsilon_{zx} = \frac{1}{2}\gamma_{zx} = \frac{1}{2}\left(\frac{\partial w}{\partial x} + \frac{\partial u}{\partial z}\right) \quad (6.8)$$

The symmetric strain tensor can be expressed as:

$$\varepsilon = \begin{pmatrix} \varepsilon_x & \varepsilon_{xy} & \varepsilon_{xz} \\ \varepsilon_{xy} & \varepsilon_y & \varepsilon_{yz} \\ \varepsilon_{xz} & \varepsilon_{yz} & \varepsilon_z \end{pmatrix} \quad (6.9)$$

Since the thin circular plate is fixed at the centre with the clamping portion, a fixed constraint boundary condition has been applied to replicate the problem which is ideally an annular plate fixed at the inner ring boundary. The material damping can be included in the linear elastic material using different damping types (e.g. isotropic loss factor, an-isotropic loss factor, viscous damping, etc.).

The impedance tube and backing cavity have been modelled using the Pressure Acoustics, Frequency Domain interface and defined by the homogeneous Helmholtz equation:

$$\nabla \left(-\frac{1}{\rho_0} \nabla p \right) - \frac{\omega_0^2 p}{\rho_0 c_0^2} = 0 \quad (6.10)$$

where, ω_0 is the angular frequency, p is the total acoustic pressure, p_b is the the background pressure, ρ_0 is the density of the air and c_0 is the speed of sound in air. A plane wave radiation boundary condition with incident pressure field has been applied to the inlet of the impedance tube and end of the backing cavity considered as a solid hard boundary wall.

Because acoustic waves travel through narrow areas i.e. air-gap between plate-type acoustic valve and mounting plate, the thermal and viscous boundary layers in the vicinity of the walls will generate thermal and viscous loss effects. To include the thermo-viscous effect in the model, the Thermo-viscous Acoustics, Frequency Domain interface has been used which is defined by the linearized Navier Stokes equations with scattered field formulation (the field solved for the acoustic pressure p , the particle velocity \mathbf{v} , and the acoustic temperature T). The governing equations are the set of equations of conservation of momentum, conservation of energy, and conservation of mass with the constitutive equations of state in the case of an ideal gas in linearized form.

$$\begin{aligned} i\omega\rho &= -\rho_0(\nabla \cdot \mathbf{v}) \\ i\omega\rho\mathbf{v} &= \nabla \cdot \left\{ -p\mathbf{I} + \mu(\nabla\mathbf{v} + (\nabla\mathbf{v})^T) + \left(\mu_B - \frac{2}{3}\mu\right)(\nabla \cdot \mathbf{v})\mathbf{I} \right\} \\ i\omega(\rho_0 C_p T - T_0 \alpha_0 p) &= -\nabla \cdot (-k_T \nabla T) \\ \rho &= \rho_0(\beta_T p - \alpha_0 T) \end{aligned} \quad (6.11)$$

where, $\alpha_0 = -\left(\frac{1}{\rho_0}\right)\left[\frac{\partial\rho_0}{\partial T_0}\right]_{p_0}$ is the coefficient of thermal expansion (isobaric) and $\beta_T = \left(\frac{1}{\rho_0}\right)\left[\frac{\partial\rho_0}{\partial p}\right]_{T_0}$ is the isothermal compressibility.

The coupling between pressure acoustics and thermo-viscous acoustics has been performed using the Acoustic-Thermoviscous Acoustic Boundary interface while the coupling between solid mechanics and thermo-viscous acoustics has been performed with the Thermoviscous Acoustic-Solid Interaction interface.

6.1.2 Meshing

A user-controlled mesh with free triangular elements was used to create the mesh. The acoustic mesh element size criterion depends on the smallest acoustic wavelength (λ_0) of interest. The largest elements, situated at the impedance tube and within the cavity, were 0.02 meters in length. The

Symbol	Value	Unit
Equilibrium temperature (T_0)	293.15	K
Equilibrium pressure (p_0)	101325	Pa
Density (ρ_0)	1.2043	kg/m ³
Dynamic viscosity (μ)	$1.8140e^{-3}$	Pa · s
Bulk viscosity (μ_B)	0	Pa · s
Heat capacity at constant pressure (C_p)	1005.4	J/(kg · K)
Thermal conductivity (k_T)	0.0258	W/(m · K)

Table 6.1: Properties of air

wavelength of the highest computed frequency ($f_{max} = 1500$ Hz) is 0.23 m, resulting in an element per wavelength ratio of $\frac{0.23}{0.02} = 11.5$. Considering that the largest acoustic mesh element should never be larger than $\frac{1}{12}$ of the wavelength λ_0 , the maximum and minimum element sizes are defined as: $\frac{c_0}{12f_0}$ and $d_v/4 = \frac{1}{3} \sqrt{\left(\frac{2\mu}{\omega\rho_0}\right)} = 220\mu m \cdot \frac{1}{3} \cdot \sqrt{\left(\frac{100Hz}{f_0}\right)}$ respectively. Figure 6.2 shows a portion of the mesh plot and highlights some of the mesh features in the vicinity of the plate-type acoustic valve. To

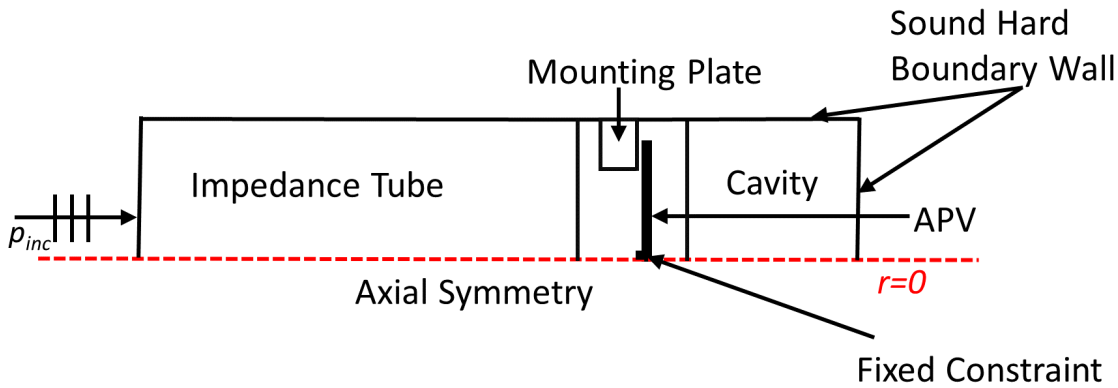


Figure 6.1: Simplified 2D axisymmetric geometric model for numerical simulation.

simulate the change in thermo-viscous conduction, two boundary layers have been added along the wall of the air gap. The complete mesh consists of 3587 domain elements and 608 boundary elements. The number of degrees of freedom solved for is 24830. A parametric frequency sweep was performed from 50 Hz to 1500 Hz with a 1 Hz frequency increment for frequency domain analysis. The average

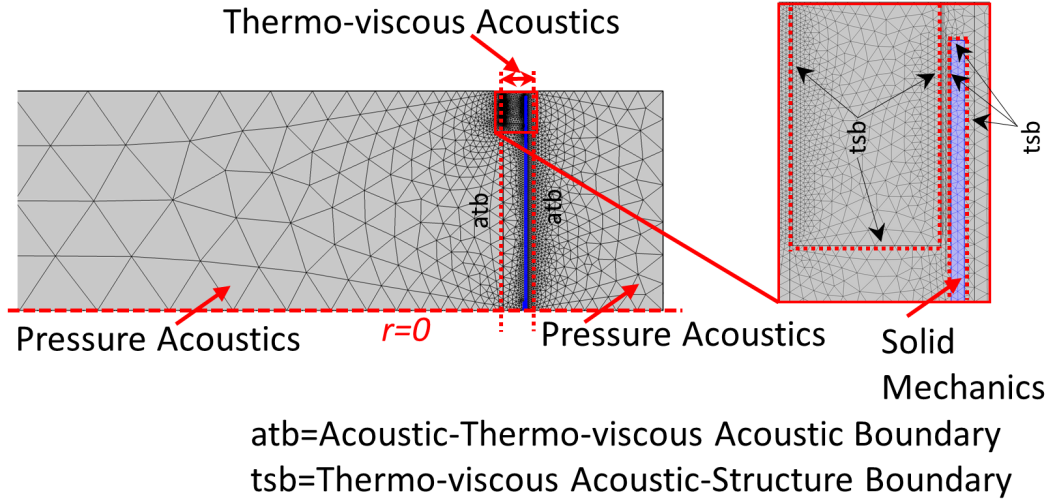


Figure 6.2: Simplified 2D axisymmetric geometric model for numerical simulation (meshed).

simulation time was 13 minutes and 45 seconds on a workstation with the following specifications: an 8-core 2.40 GHz processor and 64 GB RAM.

6.1.3 Calculation of the Absorption Coefficient

The absorption coefficient can be obtained in the form of the total visco-thermal dissipation (P_{diss}) in the small opening area or air gap, the energy lost per cycle (Q_h) in the elastic material and terms of incident power (P_{in}) [13].

$$\alpha = \frac{P_{diss} + Q_h}{P_{in}} = \frac{P_{diss} + Q_h}{\frac{\rho_{inc}^2 A}{2z_0}} \quad (6.12)$$

where, p_{inc} is the incident pressure and A is the area of the tube.

6.2 Mesh Convergence

A mesh convergence study has been performed for the 2D FEM numerical model using the different DOFs. Figure (6.3) shows the absorption coefficients with two different meshes. Mesh-1 consists of 24830 nodes or DOF and in Mesh-2 number of nodes has been increased to 33040 nodes. The relative percentage error of the absorption coefficients can be calculated as:

$$\text{Error}\% = \frac{|\alpha_{A2} - \alpha_{A1}|}{\alpha_{A2}} 100\% \quad (6.13)$$

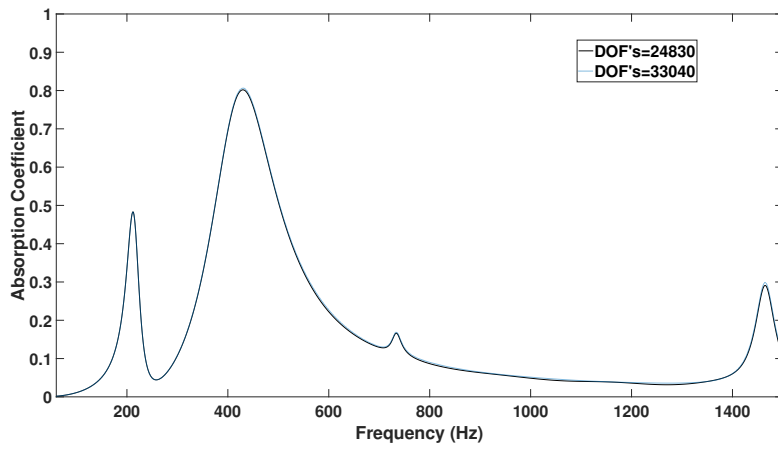


Figure 6.3: Absorption coefficient for different no. of DOFs in the 2D FEM numerical simulation.

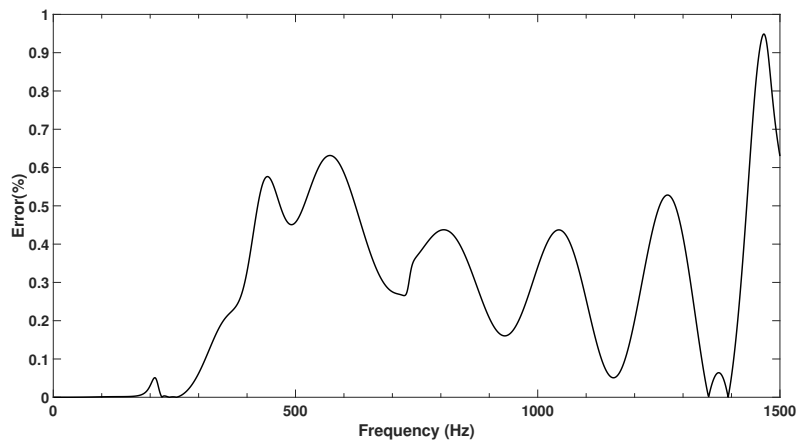
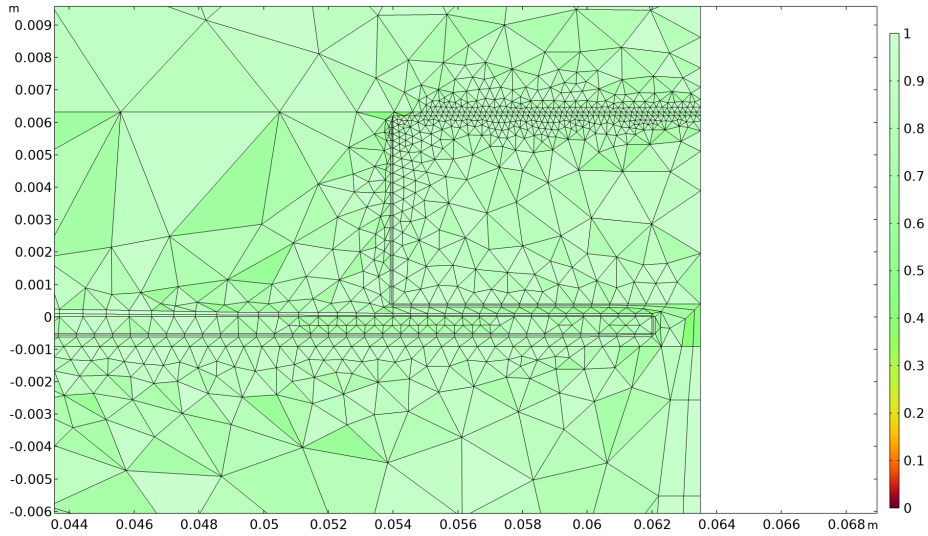
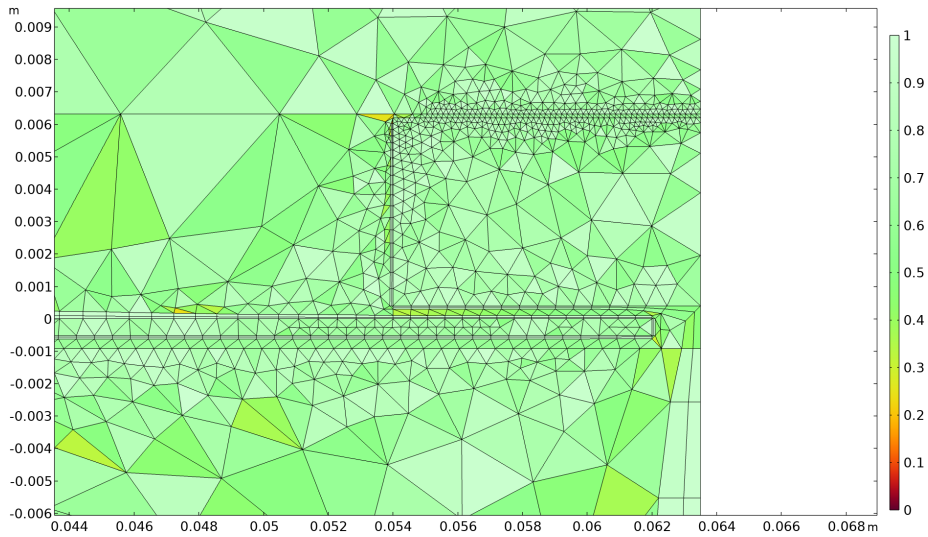


Figure 6.4: Relative percentage of error in the absorption coefficient using different mesh. The maximum relative error is less than 1%.

where, α_{A1} and α_{A2} are the absorption coefficients obtained from the simulations using Mesh-1 and Mesh-2, respectively. The relative percentage of error in the absorption coefficient has been shown in Fig. (6.4) using two meshes. It can be seen that the relative error is less than 1%. So, further mesh refinement is not necessary.



(a) Mesh element quality based on maximum angle



(b) Mesh element quality based on skewness

Figure 6.5: Mesh element quality for different quality measures obtained from mesh statistics of COMSOL.

6.3 Parametric Analysis of Plate-type Acoustic Valve Resonator

A parametric analysis has been performed to understand the effects of different material properties and geometric parameters on the absorption performance.

6.3.1 Influence of the Material Properties

To get the suitable fitted material properties and to show the effect of the material properties in the absorption coefficient, a parametric analysis has been performed using a numerical model varying the

E_m , ρ_m , ν_m and η_m one by one. The mass of the plate-type acoustic valve can be changed by varying either the thickness or the density of the plate-type acoustic valve.

6.3.1.1 Young's Modulus (E_m) and structural loss factor η_m

The acoustic performance of the plate-type acoustic valve resonator has been investigated by varying Young's modulus (E_m) and shown in Fig. (6.6). It can be seen that by increasing the E_m , structural resonance frequency is shifted to a higher value. Since, the relationship between the f_{mn} and E_m is directly proportional ($f_{mn} \propto \sqrt{E_m}$) increasing E_m will help increase the fundamental natural frequency.

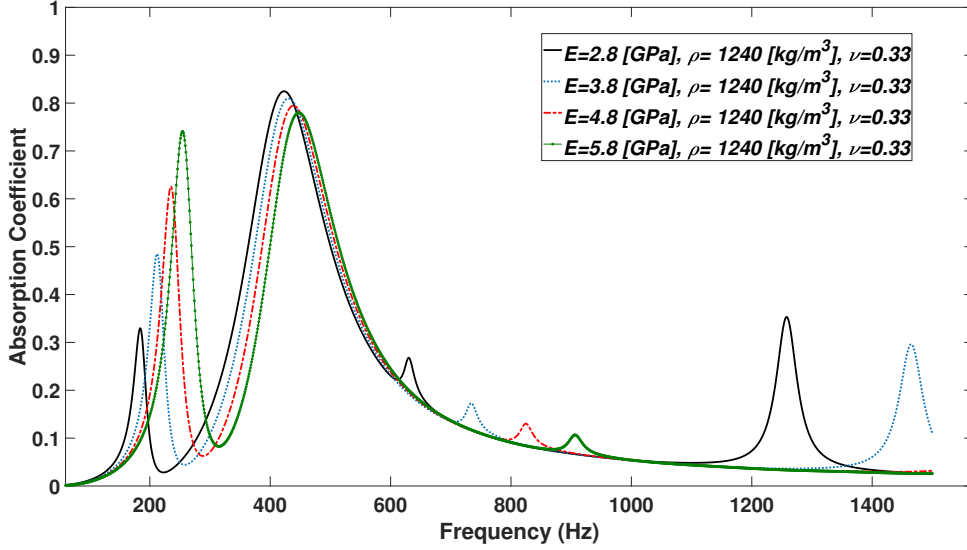


Figure 6.6: Absorption coefficient with different Young's modulus (E_m) of the material in the 2D numerical model.

The loss factor can be defined using the energy terms of a system. Those terms are: the dissipated energy per cycle (\bar{E}_{diss}), the maximum energy stored in the plate (\bar{E}_p), and the potential energy stored in the air-gap boundary layer (\bar{E}_{al}). The loss factor can be expressed as:

$$\eta_m = \frac{\bar{E}_{diss}}{2\pi[\bar{E}_p + \bar{E}_{al}]} \quad (6.14)$$

with

$$\begin{aligned} \bar{E}_{diss} &= -\frac{\pi p_0 c_0}{\omega} \int_{A_p} \text{Re}(p v_p^*) dA_p \\ \bar{E}_p &= -\frac{1}{2} D_p c_0^2 \int_{A_p} \left[\frac{\partial^2 v_p}{\partial \bar{x}^2} \right]^2 dA_p \end{aligned} \quad (6.15)$$

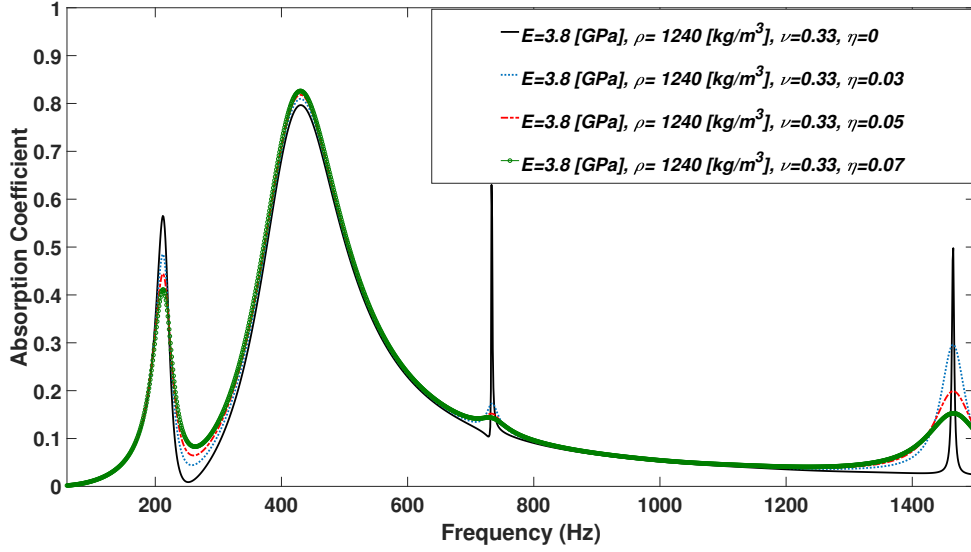


Figure 6.7: Absorption coefficient with different structural damping of the material in the 2D numerical model.

$$\bar{E}_{al} = -\frac{1}{2} \frac{p_0^2}{\rho c_0^2} \int_{A_p} \int_{z=-h_d/2}^{h_d/2} [\text{Re}(p)]^2 d\bar{z} dA_p$$

where, A_p is the surface area of the plate and $(*)$ stands for complex conjugate. Hence, the relationship between the energy stored in the plate and the structural loss factor is inversely proportional. Fig. (6.7) shows the sound absorption coefficients of the plate-type acoustic valve resonator with varying loss factor (η_m) as damping of the plate-type acoustic valve. It can be observed that, as η_m increases, the amplitude of the structural resonance peaks in the sound absorption coefficient declines, widening the bandwidth.

6.3.1.2 Density (ρ_m) and Poisson's ratio ν_m

The relationship between the f_{mn} and ρ_m is inversely proportional ($f_{mn} \propto 1/\sqrt{\rho_m}$) increasing ρ_m will help decrease the fundamental natural frequency and can be seen in Fig. (6.8). Also, the relationship between the f_{mn} and ν_m is proportional ($f_{mn} \propto 1/\sqrt{1-\nu_m^2}$) increasing ν_m will help increase the fundamental natural frequency and can be seen in Fig. (6.9).

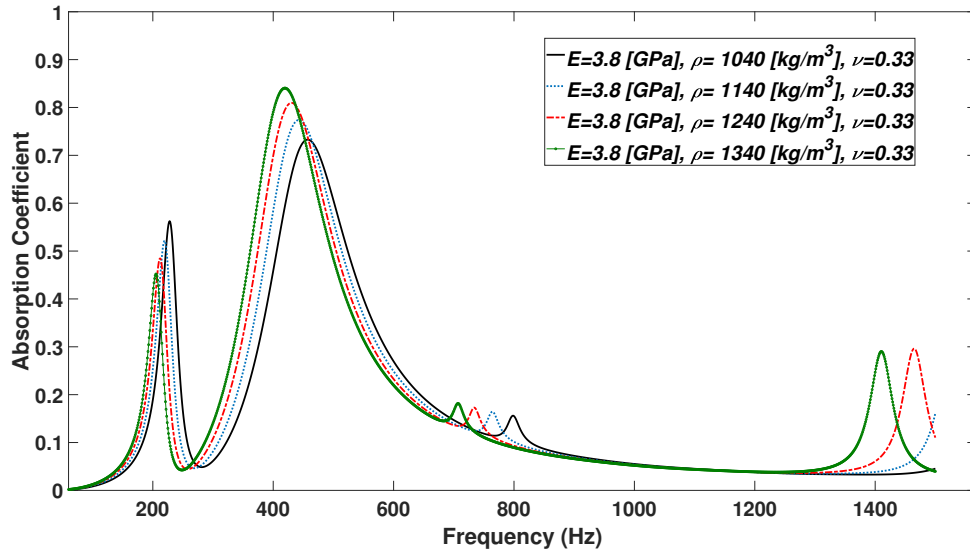


Figure 6.8: Absorption coefficient with different density (ρ_m) of the material in the 2D numerical model.

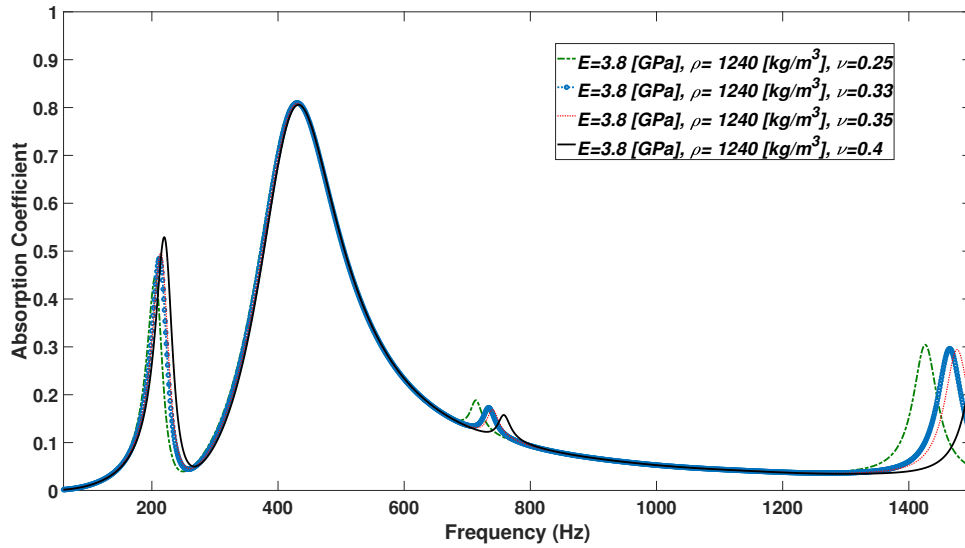


Figure 6.9: Absorption coefficient with different Poisson's ratio (ν_m) of the material in the 2D numerical model.

6.3.1.3 The ratio of Young's modulus and density ($\frac{E_m}{\rho_m}$)

The ratio of Young's modulus and density of the material known as the specific modulus or specific stiffness

$$\frac{E_m}{\rho_m} \quad (6.16)$$

For solid PLA, the specific modulus is $1.20 \times 10^6 \text{ m}^2/\text{s}^2$ [143]. Figure (6.10) shows the sound

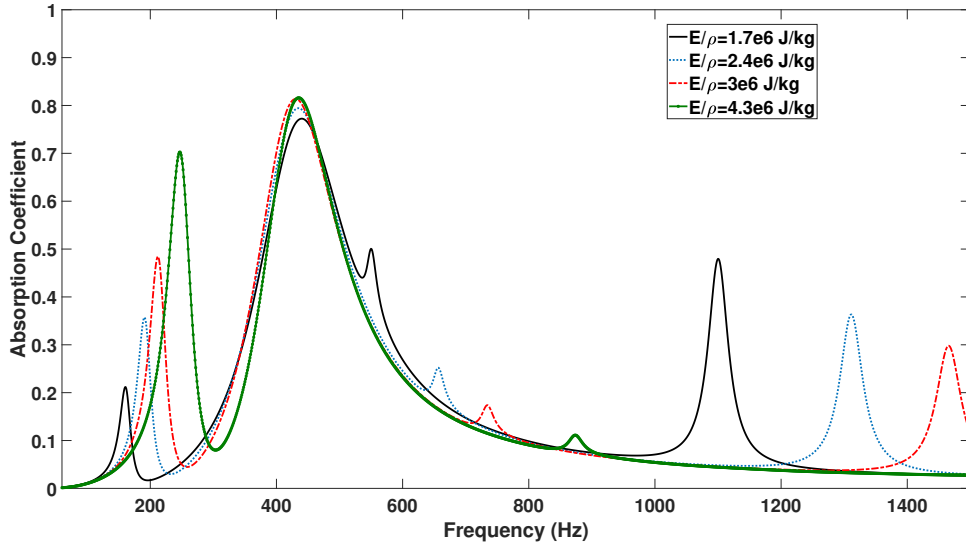


Figure 6.10: Absorption coefficient with different specific modulus ($\frac{E_m}{\rho_m}$) of the material in the 2D numerical model.

absorption coefficients of the plate-type acoustic valve resonator with varying specific modulus ($\frac{E_m}{\rho_m}$) of the plate-type acoustic valve. It can be observed that by increasing the specific modulus of the plate-type acoustic valve, the frequency position shifts to a higher frequency for structural resonance peak of f_{01} . This incorporates the directly proportional relationship between f_{mn} and E_m , expressed as $f_{mn} \propto \sqrt{E_m}$. However, there is a shift to a lower frequency position for the structural resonance peaks of f_{02} and f_{03} . This incorporates the inversely proportional relationship between f_{mn} and ρ_m , expressed as $f_{mn} \propto 1/\sqrt{\rho_m}$. It's intriguing to note that the position of the structural resonance peak before the Helmholtz resonance is affected by Young's modulus, whereas the position of the structural resonance peak after the Helmholtz resonance is influenced by the density of the material.

6.3.2 Thickness of the plate-type acoustic valve (t_{APV})

Figure (6.11) shows the sound absorption coefficients of the plate-type acoustic valve resonator with varying thickness (t_{APV}) of the plate-type acoustic valve. According to Eq. (3.30) substituting the D , the relationship between the f_{mn} and t_{APV} directly proportional ($f_{mn} \propto t_{APV}$) increasing t_{APV} will help increase the fundamental natural frequency. It can be seen that the amplitude of the absorption coefficient increased by increasing the thickness of the plate. The increase in the thickness results in decreasing the air-gap height between the plate-type acoustic valve and mounting plate results in modifying the neck size in Helmholtz resonance. This effect is known as the “pumping effect” and will be explained in detail in the next section.

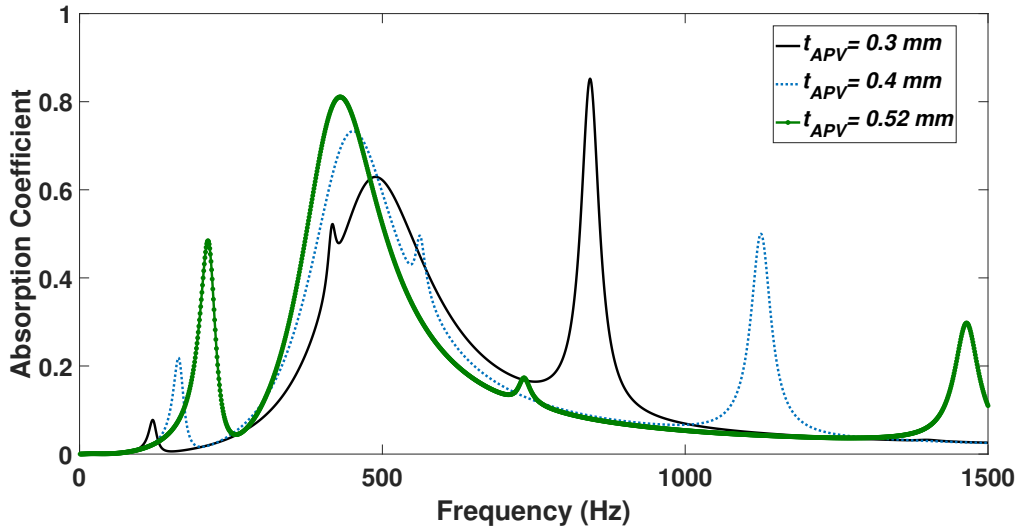


Figure 6.11: Absorption coefficient with different thickness (t_{APV}) of the plate-type acoustic valve in the 2D numerical model.

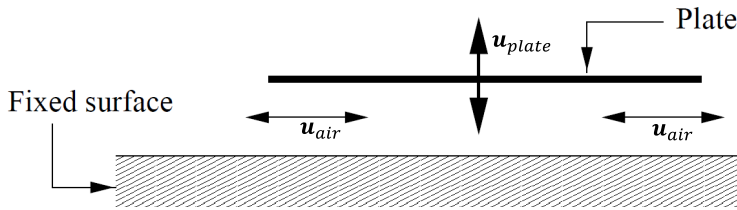


Figure 6.12: Schematic of pumping effect where \mathbf{u}_{air} is the motion of the air and \mathbf{u}_{plate} is the motion of the flexible plate [121].

6.3.3 Air-gap between Mounting plate and plate-type acoustic valve (h_d)

Figure (6.13) shows the effect of changing the air gap between the flexible plate-type acoustic valve and the fixed mounting plate. The motion of the plate-type acoustic valve is principally perpendicular to the motion of the air particles. The amplitude of the absorption coefficient shows a significant increase as a result of decreasing air-gap height. This could be explained by the “pumping effect” or “pumping mechanism”. The pumping of air occurs when a flexible plate of a system vibrates with different amplitude or phase even different amplitude and phase than air, the relative displacement results in periodic movement of the air in and out of the air gap between the two plates (see Fig. (6.12)). The pumping mechanism induces high viscous losses near the boundary walls of the air gap, which results in increasing damping of the plate-type acoustic valve. From Fig. (6.13) it can be seen that, although the Helmholtz resonance is controlled by the air-gap and cavity depth, structural

resonance is also affected by the air-gap due to the pumping mechanism. To create a pumping effect successfully in the system, a small air gap must be chosen with some consideration while allowing the plate-type acoustic valve to vibrate independently. If the air-gap height to be chosen is very large, the incident energy dissipation by the visco-thermal effects is very small. If the air-gap height to be chosen is very small, no pumping effects occur due to the strong coupling between two plates resulting in negligible energy dissipation [121].

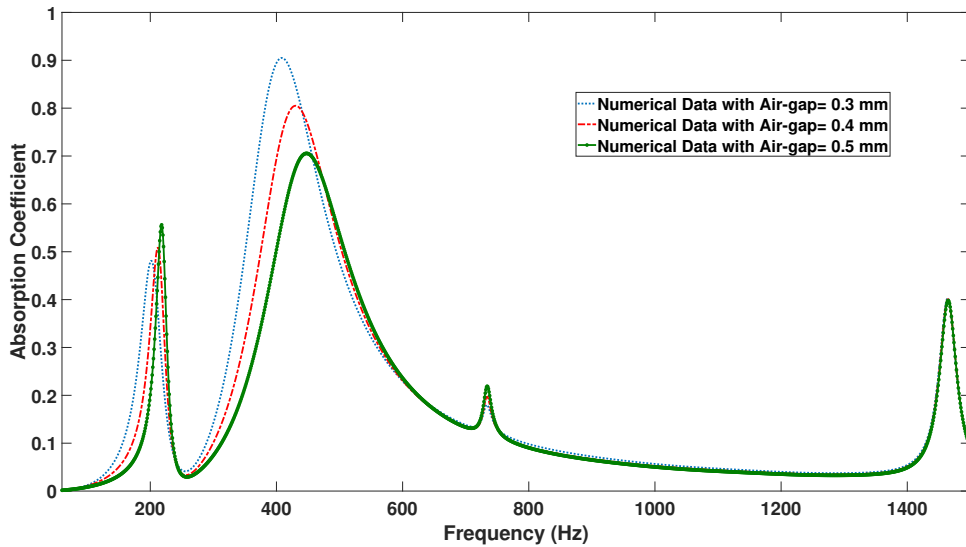


Figure 6.13: Absorption coefficient with different air-gap in the 2D model.

6.3.4 Cavity Depth (l_{cav})

The last design parameter to be investigated is the air-cavity depth (l_{cav}) behind the plate-type acoustic valve. The effect of three cavity depths of 20mm, 30 mm, and 40 mm in the absorption coefficient of the plate-type acoustic valve resonator has been included in Fig. (6.14). The corresponding Helmholtz resonance frequencies are 600 Hz, 492 Hz, and 433 Hz for the cavity depths of 20mm, 30 mm, and 40 mm, respectively. It can be seen that Helmholtz resonance frequency has been shifted to the lower frequency increasing the cavity depth as the relationship between the Helmholtz resonance frequency is inversely proportional to the squared root of the cavity volume according to the Eq. (2.20). Three other distinctive resonance peaks can be seen in the absorption curves. Interestingly, they are not affected significantly by the varying cavity depths. Those three resonance peaks can be identified as the structural resonance peaks i.e. $f_{01} = 212$ Hz, $f_{02} = 735$ Hz, and $f_{03} = 1465$ Hz. Also, a gradual decrease in the amplitude of the absorption coefficient at the Helmholtz resonance frequency can be seen in decreasing the cavity depths. In general, if the Helmholtz resonance frequency and the structural

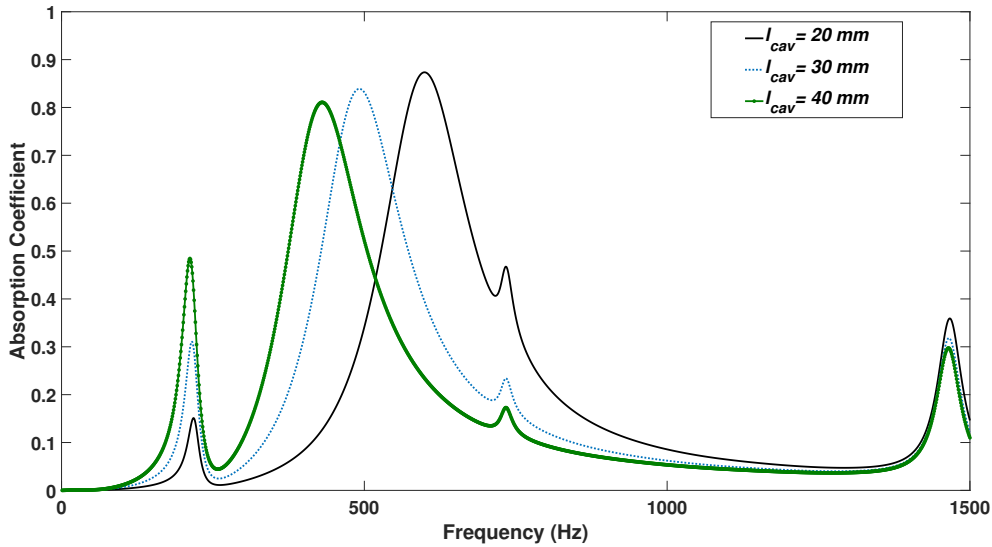


Figure 6.14: Absorption coefficient with different cavity depth in the 2D model.

resonance frequency are reasonably apart from each other, both absorption peaks are distinctively separated. However, if the Helmholtz resonance frequency and the structural resonance frequency are reasonably close to each other two peaks essentially combined widening the effective absorption bandwidth [94]. According to the theoretical and experimental investigation for the flexible MPP by Lee et al. [9], if the resonance frequency due to the perforations is higher than the structural resonance frequency (i.e. $f_{MPP} > f_{mn}$), absorption coefficient degrades due to the structural vibration. In that case, MPP vibrates in the same direction as the air particle movements at the air gap. The velocities of the air particles are lower than the velocity of MPP which results in a lower relative velocity thus lower absorption coefficient. When $f_{mn} > f_{MPP}$, the MPP vibrates in the opposite direction of the motion of the air particle. At the structural resonance, the change of phase happens by 180° . The velocities of the air particles are relatively higher than the MPP vibration which results in the higher relative velocity causing a higher absorption coefficient. From Fig. (6.14), it can be observed that when $f_{h,20mm} < f_{02}$ the two relatively close absorption peaks from the Helmholtz resonance and structural resonance are merged broadening the absorption bandwidth of the plate-type acoustic valve resonator. In contrast, when $f_{h,40mm} > f_{01}$, the two absorption peaks are relatively far apart, resulting in lower absorption at the Helmholtz resonance frequency. However, an improvement in the absorption coefficient at the frequencies between the structural resonant frequency and Helmholtz resonance frequency can be observed.

6.4 Alternative Modelling Techniques in COMSOL

Modelling using the Thermoviscous Acoustics interface can become computationally demanding due to the intricate details required to capture all physical effects. For a simple geometry, it is possible to address thermoviscous losses more efficiently by utilizing the Narrow Region Acoustics and Thermoviscous Boundary Layer Impedance feature within the Pressure Acoustics interface.

6.4.1 Modelling with Narrow-region Acoustics Interface

The fluid models within Narrow Region Acoustics serve to replicate the thermal and viscous losses apparent in slender tubes where the length scale of the tube's cross-section aligns with the thickness of the thermal and viscous boundary layers (referred to as boundary-layer absorption). Including these losses is crucial for obtaining accurate results. This model, as an equivalent-fluid representation, proves effective in lengthy tubes of uniform cross sections (or those with gradual variations), serving as an alternative to a highly detailed thermoviscous acoustics model. This particular model significantly reduces computational requirements compared to a comprehensive thermoviscous acoustic model. For instance, when examining lengthy, narrow ducts or tubes with uniform cross-sections, these models offer the option to integrate or diffuse boundary layer losses into the bulk of the fluid, creating an equivalent fluid model.

In many geometries, there are established analytical expressions specifically detailing the losses linked to the acoustic boundary layers. These models can be applied under various assumptions (i.e. wide ducts approximation, slit, circular duct, rectangular duct, and equilateral triangular duct, very narrow circular ducts (isothermal)) to accommodate different conditions. Among them, the models for the slit, circular duct, rectangular duct, and equilateral triangular duct are built upon the low reduced frequency (LRF) model. This model specifically characterizes how acoustic waves propagate in compact waveguides, encompassing both ducts and slits, while accounting for thermal and viscous losses [21]. Within a narrow waveguide, the values for the complex wave number (k_c) and complex specific acoustic impedance (Z_c) are provided as follows:

$$k_c^2 = k_0^2 \left(\frac{\gamma - (\gamma - 1)\Psi_t}{\Psi_v} \right) \quad k_0 = \frac{\omega}{c}$$

$$Z_c^2 = \frac{Z_0^2}{\Psi_v(\gamma - (\gamma - 1)\Psi_t)} \quad Z_0 = \rho c$$

Here, Ψ_v and Ψ_h denote functions dependent on geometry and materials, which are detailed below, while γ represents the ratio of specific heats. The fluid's density (ρ), speed of sound (c), and angular frequency (ω) establish the free space wave number (k_0) and specific acoustic impedance (Z_0).

The subscripts v and t specifically denote the viscous and thermal fields, respectively. Once these parameters are determined, the complex speed of sound and complex density can be expressed as follows:

$$c_c = \frac{\omega}{k_c}$$

$$\rho_c = \frac{k_c Z_c}{\omega} = \frac{k_0 Z_0}{\omega} \frac{1}{\Psi_v} = \frac{\rho}{\Psi_v}$$

The values of the Ψ_j functions are obtained through the resolution of the complete set of linearized Navier-Stokes equations. This involves breaking down these equations into an isentropic (adiabatic), a viscous, and a thermal component.

$$k_v^2 = -i\omega \frac{\rho}{\mu} \quad k_t^2 = -i\omega \frac{\rho C_p}{k}$$

The equations can be analytically solved based on the following assumptions:

$$\left| \frac{k_j}{k_0} \right| \gg 1 \Rightarrow \lambda_0 \gg \delta_j$$

where, k_j is the viscous and thermal wave numbers and δ_j is the boundary layer thickness. The resulting analytical expressions, for the viscous and thermal Ψ_j functions, are for the slit of height h_s can be represented as:

$$\Psi_j = 1 - \frac{\tan(k_j h_s / 2)}{k_j h_s / 2}$$

Also,

$$h_s \ll \frac{c}{\omega}, 1 \ll \left| \frac{k_j c}{\omega} \right|$$

In COMSOL, the Pressure Acoustic module utilizes the Narrow Region Acoustics (NRA) interface, which accounts for thermal and viscous losses within the system. In the current model, the slit configuration in the NRA interface has been included with a slit height of 0.4 mm.

6.4.2 Modelling with Thermoviscous Boundary Layer Impedance

The Boundary Layer Impedance (BLI) model, proposed by Bossart et al. [144] in 2003, seeks to incorporate the visco-thermal effects arising from acoustic boundary layers. This model employs an impedance-like boundary condition to address these effects. The Thermoviscous Boundary Layer Impedance condition defines the inward normal velocity $-\mathbf{n} \cdot \mathbf{v}$ at the boundary in terms of the pressure and its tangential derivatives. This condition relates the fluid velocity vector \mathbf{v} to the pressure distribution and its gradients in the tangential direction at the boundary.

$$-\mathbf{n} \cdot \mathbf{v} = -i\omega \left(T_{\text{bnd}} - \frac{\beta_p T}{\rho C_p} p \right) \frac{\delta_t \beta_p}{1+i} - v_n + \frac{\delta_v}{1+i} \left(\nabla_{\parallel} \cdot \mathbf{v}_{\parallel}^0 + \frac{1}{i\omega \rho} \Delta_{\parallel} p \right)$$

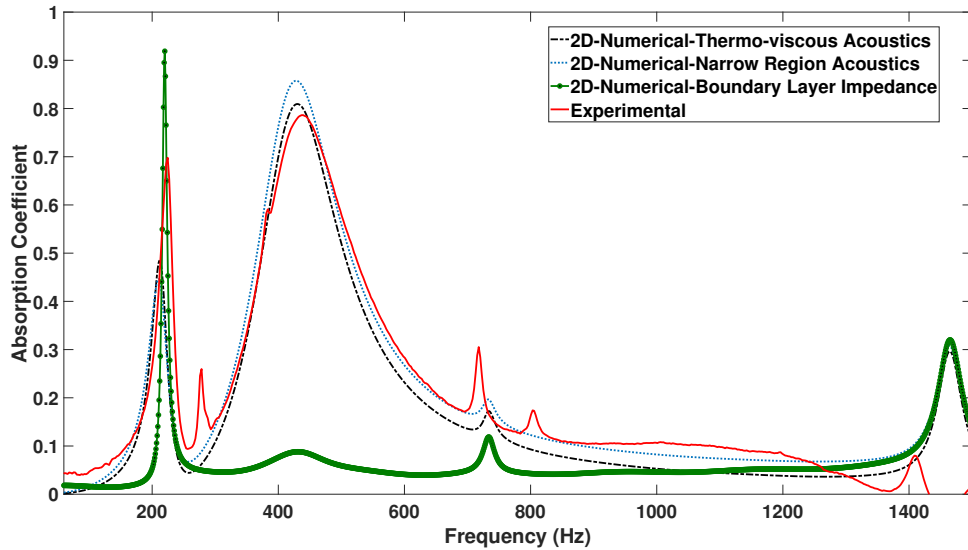


Figure 6.15: Comparison between simulated absorption coefficients using thermo-viscous acoustics, narrow region acoustics, and boundary layer impedance interfaces in 2D numerical modelling.

where the (isobaric) coefficient of thermal expansion is $\beta_p = \frac{1}{c} \sqrt{\frac{C_p(\gamma-1)}{T}}$, T_{bnd} representing a potential boundary temperature variation source, v_n representing a possible normal velocity source, and \mathbf{v}_{\parallel}^0 representing a potential tangential velocity source. These sources contribute to the overall formulation of the impedance-like boundary condition in the model. In the present model, an impedance-like boundary condition using a boundary layer has been incorporated into the wall of the impedance tube.

Figure (6.15) displays the absorption coefficient obtained from both thermo-viscous acoustics and thermo-viscous boundary layer impedance, as well as narrow-region acoustics within 2D numerical models. Narrow region acoustics and thermoviscous acoustics provide a similar absorption profile to the experimental absorption curve. It should be noted that the 2D prediction with thermo-viscous acoustics is closer to the experimental absorption curves, as it was fitted to those curves using different geometric and material properties in the numerical model. Utilizing the fitting parameters in the model with the narrow region acoustics brings it closer to the experimental curve. In this scenario, the narrow region acoustics interface proves to be a reliable alternative to the thermoviscous acoustics interface. The 2D numerical model of thermo-viscous boundary layer impedance predicted losses due to structural resonance. However, it underpredicted losses attributed to Helmholtz resonance since it is not applicable in a very narrow waveguide and only works for higher frequencies[145].

6.5 Summary

This chapter includes extensive studies of the 2D FEM numerical model based on COMSOL's FEM implementation. Modelling techniques in the frequency domain and eigenfrequency analysis have been presented. The acoustic performance and vibrational behaviour have been investigated using the model of frequency domain and eigenfrequency analysis. A parametric analysis has been performed using the geometric and material properties of the plate-type acoustic valve resonators. A detailed investigation of the absorption mechanism will be presented the Chapter 7.

Chapter 7

Characterisation of the Sub-wavelength Plate-type Acoustic Valve Resonator

In this section, analytical, experimental and numerical results are presented as a function of the cavity depth, material properties and plate thickness.

Figure (7.1) provides some initial baseline results. The absorption coefficient was measured experimentally for an empty tube, and then, with the mounting plate installed but without the plate-type acoustic valve, see Fig. (4.8). In both cases, there was a 40 mm cavity depth. The empty tube, as expected, results in effectively near-zero absorption (high reflection), demonstrating the correct functioning of the rig and methods. The frequency domain numerical solution provides an identical result, confirming the proper functioning of the numerical model. When the mounting plate is inserted, it results in non-zero absorption, with the numerical and experimental results in close agreement. Some losses are assumed to occur due to acoustic velocity flow around the edges of the mounting plate, but since the absorption value is less than 0.1 in the frequency range, it is assumed from here on that the mounting plate itself has little effect on the absorption coefficient. Some resonance peaks corresponding to the acoustic resonance modes of the impedance tube can be observed. Additionally, negative absorption is visible at very low frequencies (19 Hz), which is attributed to the lower frequency limit of the experimental setup being 45 Hz.

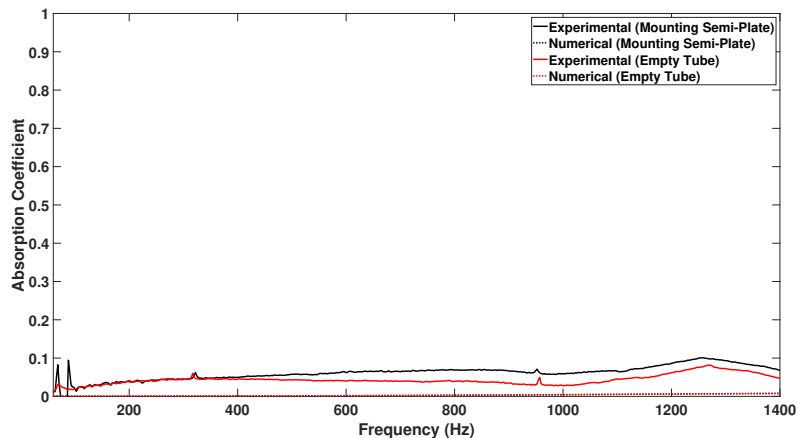


Figure 7.1: Absorption coefficient for mounting plate only with no plate-type acoustic valve. 40 mm cavity depth.

Figure (7.2) shows the absorption coefficient when the plate-type acoustic valve is inserted with a very shallow 5 mm cavity depth. The numerical result shows two relatively broadband peaks with very high absorption coefficients, the first being at 1140 Hz and the second at 1460 Hz. The experimental result is again in very close agreement with a slight frequency shift at the lower frequency but also to be noted are indications of other peaks not found in the numerical result. This will be discussed further in the thesis. A very significant result for this configuration is that the lower frequency peak

has perfect absorption experimentally at a cavity depth of only 5 mm. This means for a frequency of 1184 Hz, which has a wavelength of 0.29 m, the plate-type acoustic valve technology is deeply sub-wavelength with perfect absorption at a wavelength-to-depth ratio of 58.

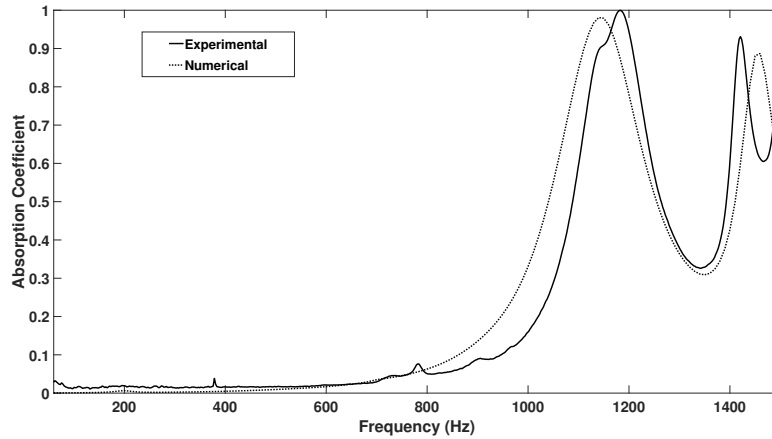


Figure 7.2: Absorption coefficient for 5 mm cavity depth.

Figure (7.3) compares the experimental and numerical absorption coefficients for the plate-type acoustic valve with differing: 10 mm, 20 mm, 30 mm and 40 mm, cavity depths. The absorption coefficient for the numerical main peaks seems to monotonically decrease whereas, for the experimental results, the absorption coefficient is higher for the 40 mm cavity depth than the 30 mm cavity depth. This point will also be further investigated in the thesis. Examining now the general results for the absorption coefficient for the plate-type acoustic valves, we see that the results are extremely good. By increasing the depth of the cavity, lower frequencies can be attenuated, and although the magnitude of absorption decreases with frequency, it remains quite high.

7.1 Helmholtz Resonance of the Plate-type Acoustic Valve Resonator

With regard to the frequency at which the main peak occurs in Fig. (7.3), there seems to be a non-linear relationship between the depth and the frequency. This behaviour allows us to identify the main peak as resulting from a Helmholtz resonance. Through observation of the standard Helmholtz equation in Eq. (7.1),

$$f_{HR} = \frac{c_0}{2\pi} \sqrt{\frac{S_n}{l_n V_c}} \quad (7.1)$$

where, l_n and S_n are the neck's effective length and area respectively, and V_c is the effective cavity volume, we can see that when the depth of the back-cavity is doubled, the frequency of the main peak

7.1 HELMHOLTZ RESONANCE OF THE PLATE-TYPE ACOUSTIC VALVE RESONATOR

decreases by $\frac{1}{\sqrt{2}}$. The frequencies of peak absorption from the numerical analysis in Fig. (7.3) are 860 Hz, 600 Hz, 490 Hz and 430 Hz. As, for example, 600 Hz is very close to $\frac{860}{\sqrt{2}}$ and 430 Hz is very close to $\frac{600}{\sqrt{2}}$ it is reasonable to deduce that these main peaks result from a Helmholtz resonance where the neck is the circumferential gap between the plate-valve and the mounting plate. Unlike typical Helmholtz resonators, the orifice here is not a single hole whose axis is parallel to that of the cavity, but rather it is a circular gap whose axis is perpendicular. Additionally, because the plate valve vibrates, causing the gap to change over time and as a function of radius, determining the geometry of the neck is less straightforward.

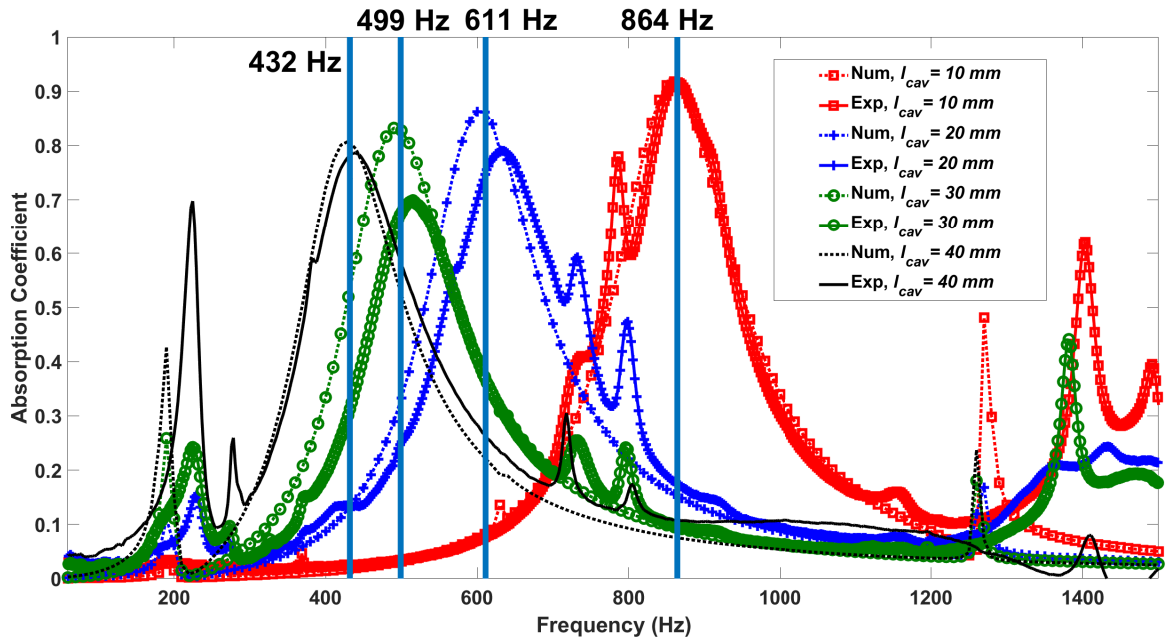


Figure 7.3: Absorption coefficient for 10 mm, 20 mm, 30 mm and 40 mm cavity depths. Solid line: Experimental. Dotted line: Numerical.

To try and understand the underlying mechanism of Helmholtz resonance in the acoustic plate-valve configuration, the geometry is examined as shown in Fig. (7.4), which is considered to be axisymmetric around its axis at $r=0$. This assumption ignores the effect, if any, of the presence of the mounting plate ribs, as seen in Fig. 4.8. The definition and value of the terms are provided in Table 7.1. The nominal neck length is considered to be the overlap of the plate-type acoustic valve over the mounting plate: l_n , and the volume of the cavity, V_c , is straightforward to calculate. However, the area of the neck is complicated by the fact that the radius at the beginning of the neck, r_p , is different to that at its end, r_{APV} . A reasonable approximation is to calculate the area as $2\pi r_{av} h_d$, where $r_{av} = (r_p + r_{APV})/2$. Using these values and the same value for the air gap as used in the numerical

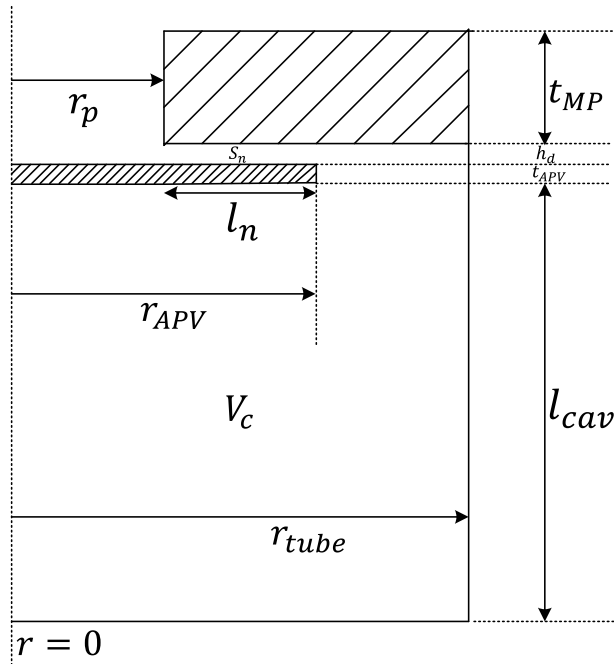


Figure 7.4: Axisymmetric schematic of the plate-type acoustic valve and cavity (restated from Chapter 4, highlighting its importance in comprehending the absorption mechanism of Helmholtz resonance within the acoustic plate-valve configuration).

analysis (see Section 6.1), $h_d = 0.4mm$, the analytical results calculated using Eq. 7.1 are compared to those from the experiments and the numerical analysis and are shown in Table 7.2. However, it can be seen that the analytical results shown in column 4 underestimate both the experimental and numerical values.

To gain further insight, an additional numerical analysis of the system was performed. In this case, the plate valve was held fixed and rigid, not allowed to vibrate. For the initial analysis, where the same value of the air gap is used for the rigid plate ($h_d = 0.4mm$), the Helmholtz frequencies were significantly different. This highlights the fact that the physics of the systems with flexible and rigid plates are different. The analysis was then repeated until a gap was found which gave the same Helmholtz peak frequencies as for the flexible plate case. These values are tabulated in column 5 of Table 7.2 and the absorption curve spectra are provided in Fig. (7.5). The gap value which provided the same Helmholtz peak frequencies was found to be much greater at $h_d = 1.3mm$. The observation here is that a flexible plate valve behaves as a rigid plate resonator with a larger gap, but only from a Helmholtz frequency perspective. It can be observed that the absorption magnitudes of the flexible plate-type acoustic valve resonator are greater at the Helmholtz peak frequencies. In addition, the

7.1 HELMHOLTZ RESONANCE OF THE PLATE-TYPE ACOUSTIC VALVE RESONATOR

Geometric Parameter	Symbol	Value
Mounting Plate Hole Radius	r_p	54 mm
Plate-type acoustic valve Radius	r_{APV}	62 mm
Impedance Tube Inner Radius	r_{tube}	63.5 mm
Neck Nominal Length	l_n	8 mm
Mounting Plate Thickness	t_{MP}	5.8 mm
Nominal Gap	h_d	0.4 mm
Plate Thickness	t_{APV}	0.52 mm
Cavity Depth	l_{cav}	5 mm - 40 mm

Table 7.1: Parameters and values of the terms in Fig. 7.4.

Cavity Depth	Experimental	Numerical <i>Flex.</i>	Analytical <i>Rigid</i>	Numerical <i>Rigid</i>	Analytical <i>Rigid</i>
$l_{cav}(mm)$	$f_{HR}(Hz)$	($h_d = 0.4mm$) $f_{HR}(Hz)$	($h_d = 0.4mm$) $f_{HR}(Hz)$	($h_d = 1.3mm$) $f_{HR}(Hz)$	End Correction ($h_d = 1.3mm$)
40	439	430	328	427	432
30	515	490	379	496	499
20	634	600	465	613	611
10	861	860	657	861	864

Table 7.2: Helmholtz frequencies as a function of backing cavity depths.

additional high absorption peaks seen in Fig. (7.3) are not present when the plate valve is rigid. Both of these facts demonstrate the benefit of making the plate flexible.

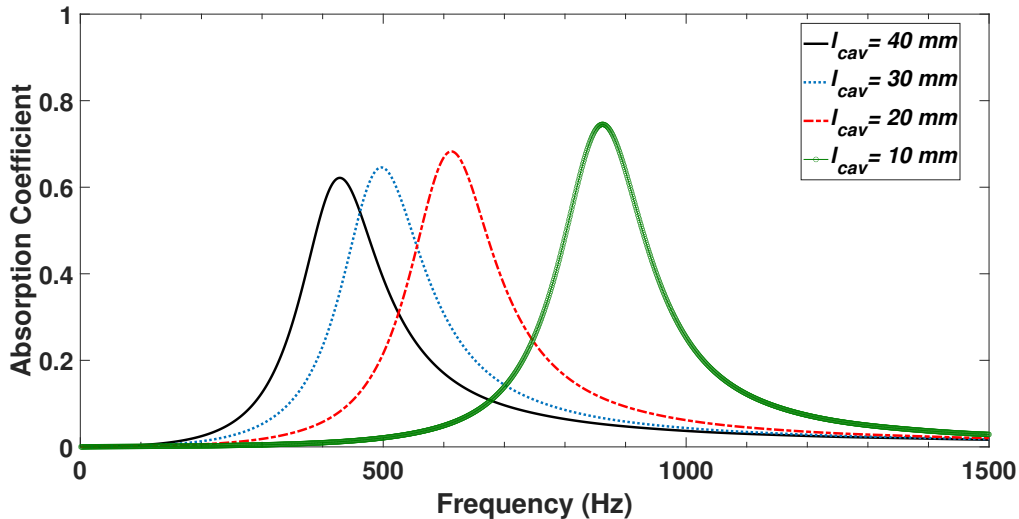


Figure 7.5: Absorption coefficient for 10 mm, 20 mm, 30 mm and 40 mm cavity depths. Numerical solution for a rigid plate which does not vibrate ($h_d = 1.3mm$).

Furthermore, the acoustic particle velocity in the vicinity of the air gap was examined for the rigid plate case. An example of this is provided in Fig. (7.6). It is clear in this figure that the viscous boundary layer is not confined to the air gap alone but, as is commonly observed in ducts, effects

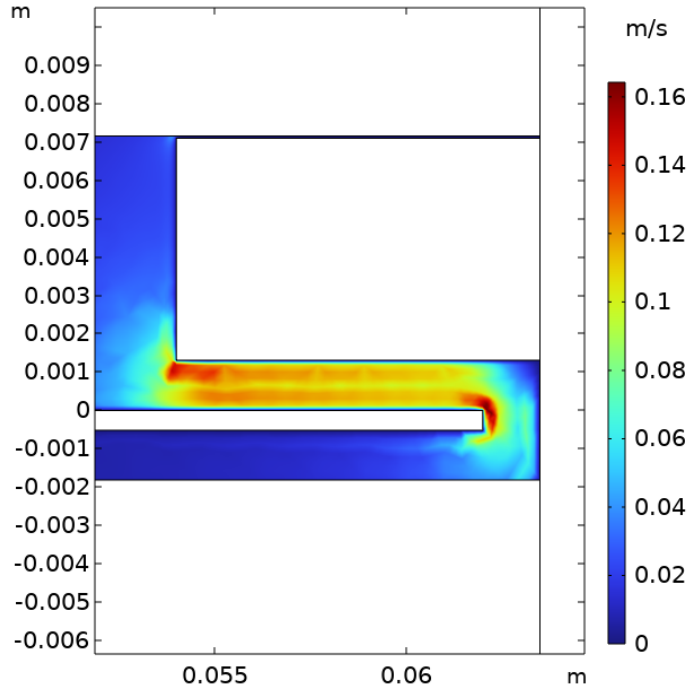


Figure 7.6: Particle velocity in the vicinity of the air gap from a 2D axisymmetric FEM simulation. Numerical solution for rigid plate which does not vibrate ($l_{cav} = 40\text{mm}$, $h_d = 1.3\text{mm}$).

continue into the field at both ends. This implies that end corrections to the term l_n as a function of gap size must be implemented into the analytical analysis. Once the effective length of the neck is increased to accommodate for the end corrections, we see in column 6 of Table 7.2, that the same peak frequencies can be correctly modelled.

Further research must be undertaken to determine a means to estimate the effective average gap, but in this study, it seems clear that the principle absorption peak that varies with cavity depth is due to Helmholtz resonance.

7.2 Vibrational Analysis of the Plate-type Acoustic Valve

In Fig. (7.3), we saw high absorption from the plate-type acoustic valve at the Helmholtz frequency and good agreement between experimental and numerical results in the Helmholtz frequency range for the 10 mm and 40 mm cavity depth. There are small discrepancies in amplitude and frequency for the 20 mm and 30 mm deep cavities.

In addition to the plate-type acoustic valve providing high absorption at the Helmholtz frequencies, we can also see absorption peaks at other frequencies. Figure (7.7) separates out Fig. (7.3) into the numerical and experimental results for clarity. In Fig. (7.7(a)) it is clear that there are three frequency ranges: N1, N2 and N3 where, for each of the cavity depths, there are absorption peaks which

do not vary with depth. These are considered to be associated with structural vibrational modes of the flexible plate-type acoustic valve whose frequencies are more a function of material properties than cavity depth. The peaks in the N2 range tend to be masked by the Helmholtz curves, whereas, for the N1 and N2 frequency ranges, the peaks increase in magnitude as the Helmholtz peaks approach them in frequency.

In Fig. (7.7(b)) we see, that in the experimental results, additional absorption peaks associated with vibrational modes are present. This can be explained by the fact that the frequency domain numerical solution is an axisymmetric analysis and thus only radial nodes for the axisymmetric zeroth azimuthal mode, i.e., $A_{(m,n)} = A_{(0,n)}$ can be resolved. For the inherently 3D experimental results, as can be assumed at this point, all vibrational modes can be excited to different degrees of amplitude response.

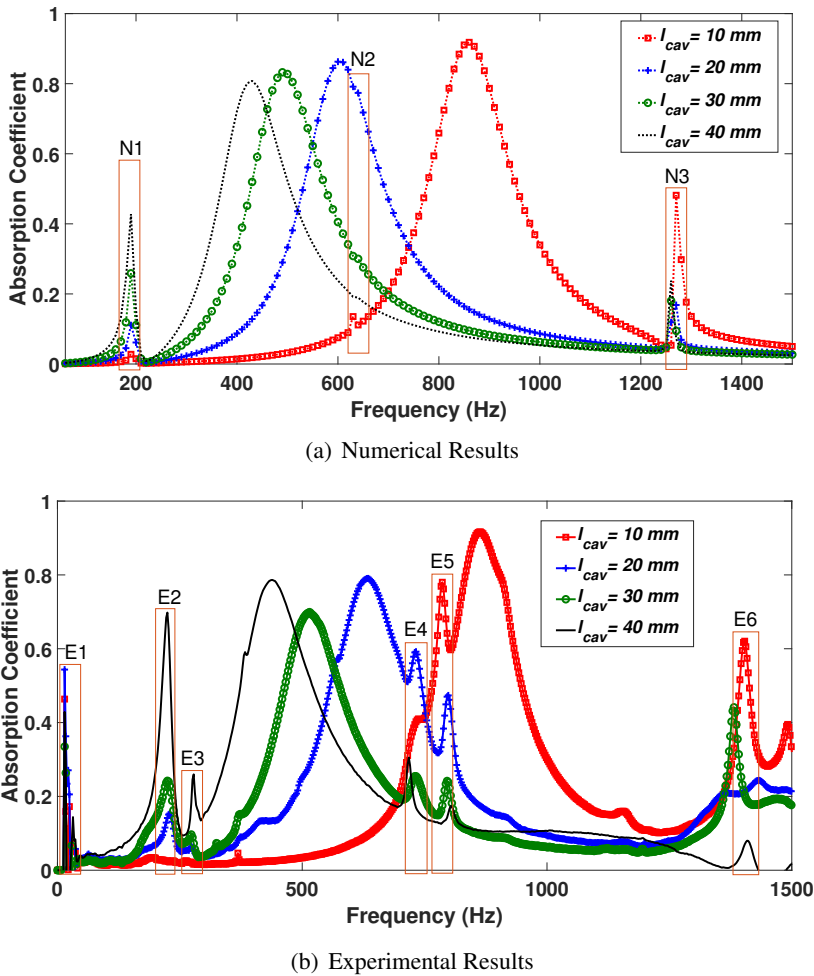


Figure 7.7: Plate-type acoustic valve absorption results as a function of cavity depth.

It is clear that, whilst there is a similarity in frequency between the vibrational peaks in both the experimental and numerical results the exact frequencies and amplitudes are not the same. A short study was conducted, as shown in Fig. (7.8), where the material properties of the PLA were altered from the values used. The values of ρ_m , E_m , ν_m and η_m , were varied for $l_{cav}=40$ mm to $\rho_m = 1240$ kgm^{-3} , $E_m = 3.8 \times 10^9$ Pa, $\nu_m = 0.33$ and $\eta_m = 0.03$ as opposed to the results used in Section 6.1. Through observation of Fig. (7.8), it can be seen that the vibrational peaks are sensitive to these material property parameters whereas the Helmholtz frequency remains unchanged. The frequencies and amplitudes have increased and a peak at approximately 750 Hz has now appeared where before there was none.

Referring back to Fig. (7.7), it is plausible to think that the numerical peaks at N1 correspond to either E2 or E3, N2 correspond to either E4 or E5 and that N3 corresponds to E6.

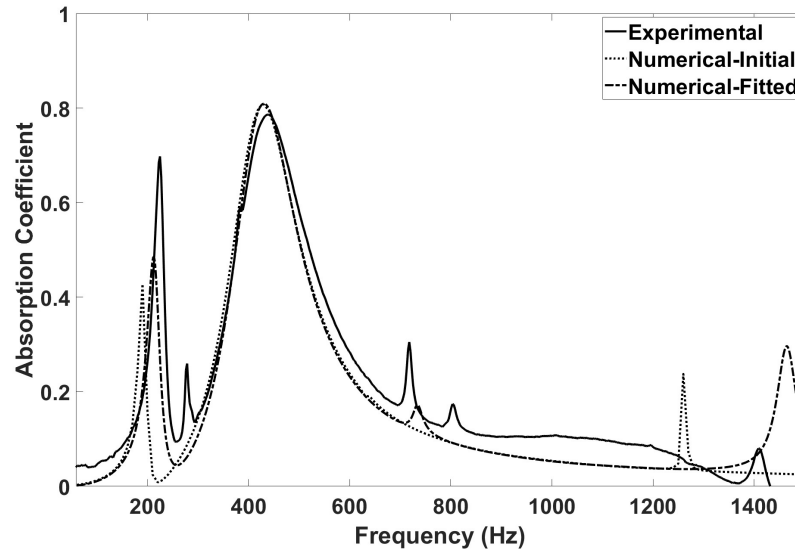


Figure 7.8: Comparison of absorption response when the material properties in the numerical model are altered (40 mm cavity depth).

7.2.1 Analytical and Numerical Eigenfrequency Analysis

To gain further insight into the nature of the vibrational modes responsible for the absorption peaks, analytical models from the literature have been examined. For analytical modelling, the plate-type acoustic valve can be considered as a thin circular plate. The eigenfrequencies of a thin circular plate ($t_{APV} \ll r_{APV}$) are given by Chiang and Huang [111] in the following equation:

$$f_{mn} = \frac{\lambda_{mn}^2}{2\pi r_{APV}^2} \sqrt{\frac{D}{\rho_m t_{APV}}} \quad (7.2)$$

with

$$D_p = \frac{E_m t_{APV}^3}{12(1 - \nu_m^2)} \tag{7.3}$$

where, D_p is the flexural rigidity. The parameter λ_{mn} can vary to represent the eigenvalues corresponding to specific boundary conditions (e.g., free, clamped all around, simply supported, centrally clamped free edge, etc.). The calculated eigenvalues for different boundary conditions for a thin plate are provided by Timoshenko et al. [108], Southwell [109] Colwell and Hardy [110] and are well documented by Leissa [93]. For example, if we consider the symmetric mode $A_{(m,n)}$ where $m=0, n=1,2,3...$ and $\nu=0.33$ for a completely free plate, the analytical eigenvalues are calculated to be: $\lambda_{0n} = 3.014, 6.209, 9.370, 12.53...$ [93]. Table 7.3 shows the first four analytical eigenfrequencies of a completely free thin circular plate.

In addition, a vibrational (eigenfrequency) analysis was conducted in COMSOL of the same free thin circular plate. The medium is that of a vacuum to match that in the analytical model. The numerical and analytical eigenfrequencies are well matched and validate each other as models.

Analytical $f_{0n}(Hz)$	Numerical $f_{0n}(Hz)$
94.4	94.2
400.5	399.9
912	912
1631	1628

Table 7.3: Eigenfrequencies of a completely free thin circular plate in a vacuum.

For the plate-type acoustic valve attached to the experimental rig, it can be considered as a thin circular plate free at the edge but fixed at the center. Southwell [109] solved a similar problem with a free circular disk clamped at the centre, considering it as an annulus plate free on the outside and clamped on the inner edge, which is well-suited for the current configuration of the plate-type acoustic valve. The first column of Table 7.4 shows the eigenfrequencies (in a vacuum) from the analytical model of the plate-type acoustic valve modelled as a centrally fixed free edge thin plate[93].

The simulated eigenfrequencies and mode shapes of the plate-type acoustic valve from the COMSOL eigenfrequency analysis are shown in Table 7.5 and the eigenfrequencies are also tabulated in the second column of Table 7.4. Although the FEM simulation is based on a 2D axisymmetric model, the 3D mode shapes of the plate-type acoustic valve were generated using post-processing of the 2D results for better visualization. A comprehensive three-dimensional model will be presented in Chapter 8. The eigenfrequency analysis in a vacuum for this simplified boundary condition allows for this 3D visualization, whereas the full frequency domain COMSOL numerical analysis in Section 6.1 as

7.2 VIBRATIONAL ANALYSIS OF THE PLATE-TYPE ACOUSTIC VALVE

Fundamental natural frequency f_{mn} (Hz)				
Mode (m, n)	Analytical	Numerical (Eigenfrequency)	Experimental	Numerical (Frequency Domain)
(0,0)	43	43	E1 (31)	
(0,1)	240	242	E2 (224)	N1 (190)
(0,2)	703	698	E4 (717)	N2 (630)
(0,3)	1384	1378	E6 (1411)	N3 (1270)
(1,0)	–	14	E1 (31)	
(1,1)	236	245	E3 (278)	
(1,2)	687	705	E5 (805)	
(1,3)	1366	1392	E6 (1411)	
(2,0)	60	61	•	
(2,1)	405	406	•	
(2,2)	963	972	–	
(3,0)	140	141	–	
(3,1)	607	609	–	
(3,2)	1278	1288	•	

Table 7.4: Modal frequency comparison.

shown in Fig. (7.7(a)), for example, does not. First of all, reviewing the first two columns of Table 7.4 we see that the analytical results compare extremely well with the eigenfrequency numerical analysis. Looking at the mode shapes in Table 7.5 we see the azimuthal and radial mode shapes and their combinations providing us with a valuable understanding of the vibration of the plate-type acoustic valve. By comparing these frequencies with those of the non-Helmholtz frequency peaks to be found in the experimental and frequency domain numerical results in Fig. (7.7), we can verify that these are indeed due to excited natural vibrations in the plate-type acoustic valve as postulated.

Referring to Fig. (7.7(a)) initially, it seems clear that the peaks to be found in frequency ranges N1, N2 and N3 correspond to $A_{(m,n)} = A_{(0,1)}, A_{(0,2)}, A_{(0,3)}$, being radial modes with no azimuthal modes present. When these frequencies are entered into column four in Table 7.4, we see that, although the frequencies themselves aren't exactly precise, the difference can be explained by the fact that the analysis was performed in air and not a vacuum, that the full impedance tube assembly including mounting plate, tube and back cavity were included in the model and also by the issues related to uncertain material properties.

Referring now to Fig. (7.7(b)), we conclude that the many additional non-Helmholtz frequency peaks can be attributed to plate-type acoustic valve natural frequencies being excited by the white noise in the impedance tube. Not all theoretical modes are easily identifiable in the experimental data and their amplitude response varies both as a function of frequency and cavity depth, but it is possible to make reasonable assumptions concerning many of the modes. Frequency ranges E1-E6

contain cavity depth independent absorption peaks which do correspond reasonably with theoretically predicted vibrational modes. This can be seen in Table 7.4 in column four where E1-E6 have been entered. Experimental peaks with low amplitude have also been represented but with a bullet point in the table, indicating that these modes seem to have been experimentally excited but with a low amplitude response. Once again, where frequencies are lower than those derived in a vacuum, the added mass effect of the air can be used as an explanation [117, 146–154].

The analysis in Tables 7.4 and 7.5 allows us to explain the presence of the additional peaks in Fig. (7.7) and to visualise them.

7.3 PARTICLE VELOCITY IN PLATE-TYPE ACOUSTIC VALVE NECK/GAP

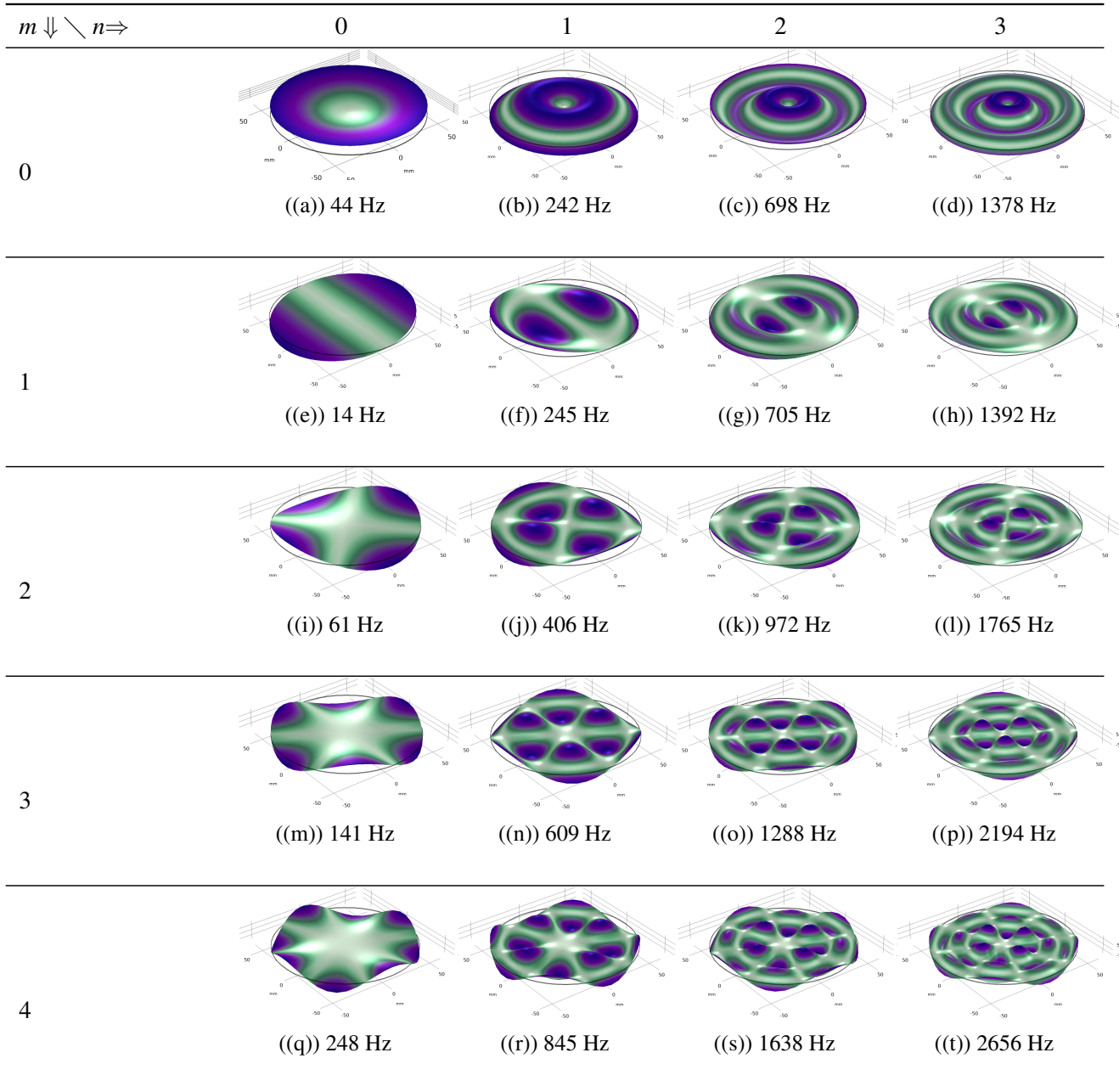


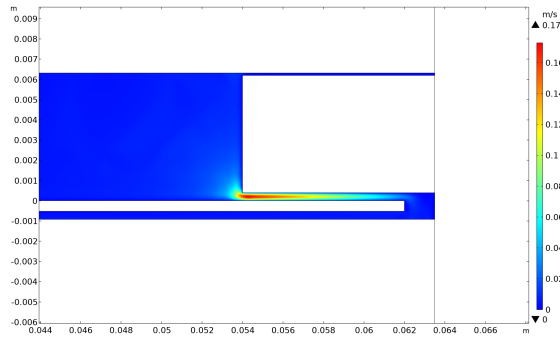
Table 7.5: Eigenfrequencies and corresponding mode shape from 2D axis-symmetric numerical model for the centrally fixed free edge circular plate: Eigenfrequency Analysis.

7.3 Particle Velocity in Plate-type Acoustic Valve Neck/Gap

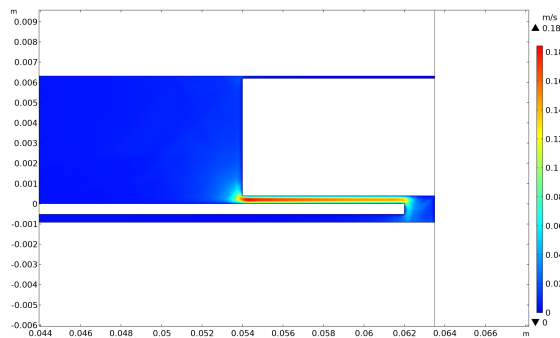
The particle velocity profile in the air gap between the mounting plate and plate-type acoustic valve (neck of the Helmholtz resonator) was calculated using the frequency domain numerical model for the 40 mm depth cavity and the results are shown in Fig. (7.9). The three radial mode peaks $A_{(m,n)} = A_{(0,1)}, A_{(0,2)}, A_{(0,3)}$ and the Helmholtz resonance peak were examined for the fitted numerical case in

Fig. (7.8). A viscous boundary layer formation can be observed in each of the plots. Figure (7.9(b)) shows the velocity profile for the Helmholtz resonance and not only does it have the highest particle velocity but it is also the only frequency for which uniform velocity along the full length of the neck is found. This can be expected as a Helmholtz resonance is the result of a compressibility effect with the entire slug of air in the neck oscillating harmonically. The maximum point velocity in Fig. (7.9(a)) is also high but as it is not as distributed as that for the Helmholtz resonance case, it makes sense that its peak in Fig. (7.8) is not as high. The velocity distribution for the three radial modes, unlike that for the Helmholtz resonance frequency, Fig. (7.9(b)), is not uniform, presumably being influenced by the fluctuation of the flexible plate-type acoustic valve. The displacement and velocity amplitudes from the 2D numerical model at an arbitrary edge point of the plate-type acoustic valve can be seen in Fig. (7.10) and Fig. (7.11), respectively. The clear resonances at 212 Hz, 735 Hz, and 1465 Hz denote the structural resonance peaks of the plate-type acoustic valve. It is also worth noting that at the Helmholtz resonance position of 430 Hz, the displacement and velocity amplitudes remain low, providing validation for these resonance peaks associated with the structural resonance.

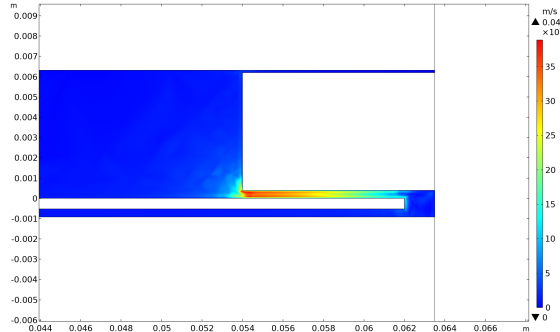
7.3 PARTICLE VELOCITY IN PLATE-TYPE ACOUSTIC VALVE NECK/GAP



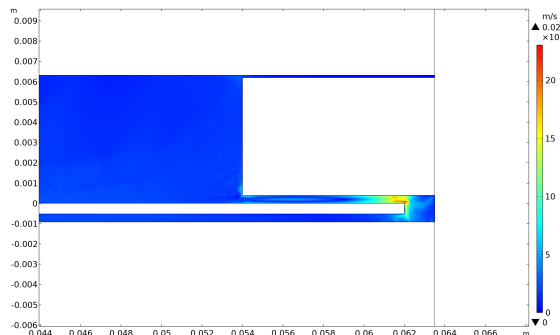
(a) Total acoustic velocity at 212 Hz



(b) Total acoustic velocity at 430 Hz



(c) Total acoustic velocity at 735 Hz



(d) Total acoustic velocity at 1465 Hz

Figure 7.9: The distribution of the particle velocity from the 2D axisymmetric FEM simulation. Viscous boundary layer formation can be seen inside the airgap between the mounting plate and plate-type acoustic valve (Excitation level = 94 dB).

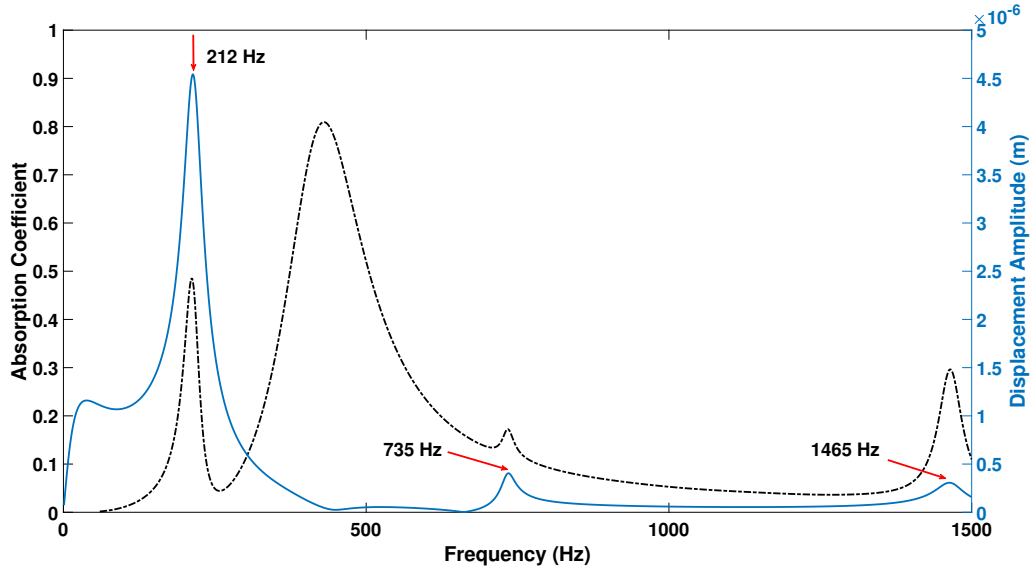


Figure 7.10: Displacement amplitude at the edge point of plate-type acoustic valve concerning the Absorption coefficient in the 2D numerical model.

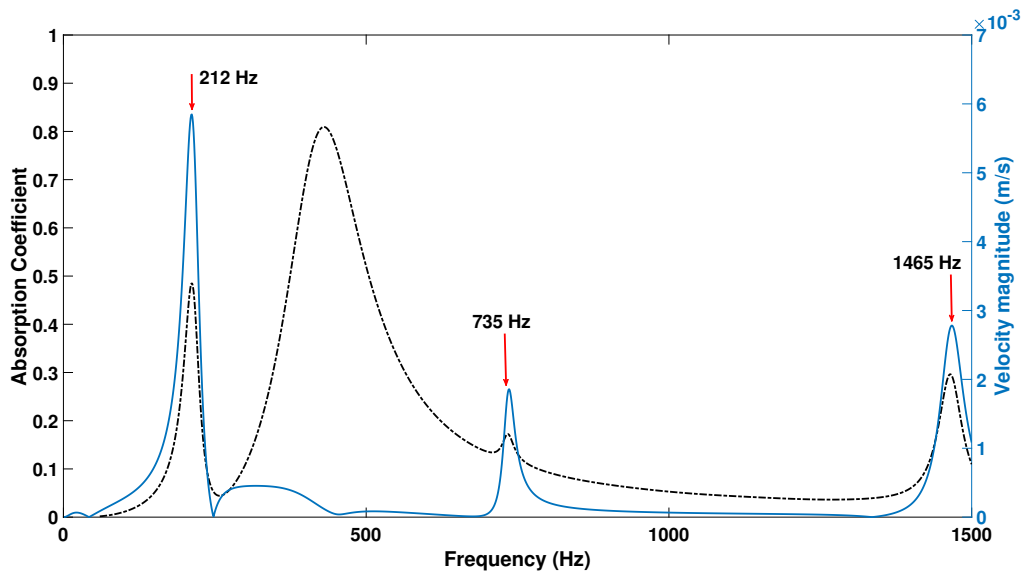


Figure 7.11: Velocity Magnitude at the edge point of plate-type acoustic valve concerning the Absorption coefficient in the 2D numerical model.

7.4 Structural-Helmholtz Resonance Coincidence.

In Fig. (7.7) we observed that, as with micro-perforated panel absorbers, there is not only a decrease in the frequency of the Helmholtz resonance with increasing cavity depth but also a decrease in the magnitude of absorption. As has been noted, for the experimental results, the decrease in amplitude does not monotonically decrease with frequency. Given that there are additional vibrational modes with significantly high absorption peaks in that frequency range, an investigation was conducted to determine whether a frequency coincidence between the structural and Helmholtz resonance frequencies could influence the amplitude response.

From observation of Fig. (7.7(b)), there are two dominant structural resonances in the frequency range between the Helmholtz resonance peaks when the cavity depths are 10 mm and 20 mm, i.e. E4 and E5, which possibly correspond to the $A_{(0,2)}$ and $A_{(1,2)}$ modes. By varying the cavity depth more precisely, it is possible to adjust the frequency of the Helmholtz resonance peak so that it coincides with one of these structural resonance frequencies.

In Fig. (7.12) we see the result of the investigation. By using Eq. (7.1), it is possible to predict the Helmholtz resonance frequency as a function of cavity depth. Fig. (7.12) shows the result for three cavity depths between 10 mm and 20 mm i.e. at 12 mm, 13 mm and 14 mm. The 14 mm cavity depth aligns the Helmholtz frequency well with the $A_{(0,2)}$ mode and results in near-perfect absorption ($\alpha = 0.995$) at the coincident frequency. Similarly, the 12 mm cavity aligns, perhaps not quite as well, the Helmholtz resonance with the $A_{(1,2)}$ mode resulting in a very high absorption coefficient ($\alpha = 0.97$) and certainly higher than that of the original 10 mm cavity depth. The 13 mm cavity depth locates the Helmholtz resonance in between the two structural resonances and it can be seen that it and the structural resonance magnitudes are all higher than when the cavity depth is 20 mm, for example. It should be noted that under normal incidence, the plate experiences no flexural deformation [155]. Since the $A_{(1,2)}$ mode is a higher-order mode, it typically remains dormant under normal incidence but could be stimulated under oblique incidence or through an oblique mounting of the acoustic plate-valve. Initially, it can be speculated that E5 does not align with the $A_{(1,2)}$ mode, or there may be an angled mounting of the acoustic plate-valve. However, a more thorough investigation will be carried out in Chapter 8 using experimental vibration analysis with laser Doppler vibrometry to validate this assumption.

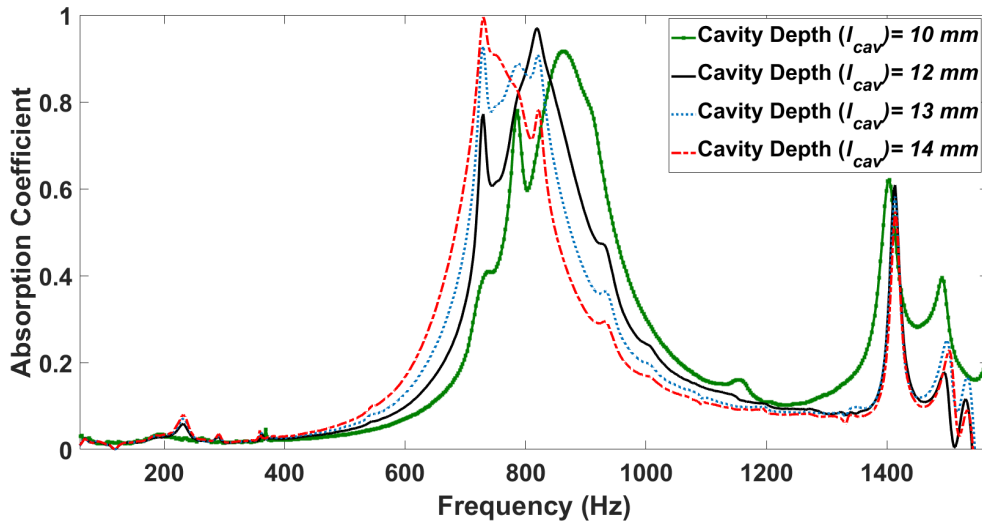


Figure 7.12: Structural-Helmholtz resonance coincidence through varying the cavity depth.

7.5 Effect of Thickness

In the previous section, it was seen that it is possible to attain coincidence by adjusting the cavity depth so that its Helmholtz frequency changes to that of the structural resonance frequency. Similarly, it should be possible to adjust the properties of the plate-type acoustic valve itself so that a structural eigenfrequency can be changed to match the Helmholtz frequency. We saw in Fig. 7.8 that changing material properties such as the values of ρ , E , ν and η results in structural resonant mode alteration without affecting the Helmholtz frequency. A change in the 3D printing filament from PLA to say ABS would achieve this but in order to minimize the number of parameters changed at any one time, PLA was maintained and instead, the thickness of the plate-type acoustic valve was increased. Through observation, it can be seen that by substituting D in Eq. (7.3) into Eq. (7.2), the relationship between the thickness of the thin circular plate and resonant frequency becomes directly proportional. It can be seen in Fig. 7.7(b), that the E2 structural resonance frequency for the 40 mm cavity depth is approximately half that of the 40 mm Helmholtz frequency. Figure 7.13 shows the experimental impedance tube result for the same design 3D printed plate-type acoustic valve but whose thickness is now 1 mm. Its absorption coefficient is superimposed on the original 0.52 mm thickness curve. The result is very satisfactory with the new coincident absorption response at 440 Hz increasing from ($\alpha = 0.79$) to ($\alpha = 0.97$) when the structural resonance is designed to align with the Helmholtz resonance. The cavity depth to wavelength ratio for 440 Hz is 20 demonstrating that deep subwavelength absorption can be achieved with almost perfect absorption at low frequencies such as this.

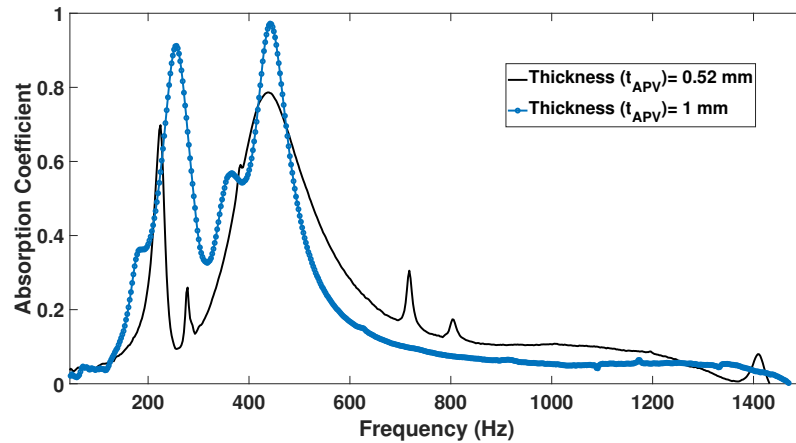


Figure 7.13: Structural-Helmholtz resonance coincidence through varying the plate thickness.

7.6 Summary

This chapter demonstrates the impact of Helmholtz resonance and structural resonance on the absorption mechanism. The influence of geometric parameters associated with Helmholtz resonance on absorption performance has been investigated, considering air-gap height (neck size) and cavity lengths. Additionally, structural resonance has been identified from the absorption curves using thin plate theory. The presentation includes instances of deep sub-wavelength high absorption achieved by aligning the Helmholtz resonance and structural resonance at the same or close frequency position, known as the coincidence effect.

Chapter 8

Vibration Analysis of Plate-type Acoustic Valve Resonator

In this section, the accuracy of the analytical and numerical models was assessed through experimental acoustic and laser Doppler vibrometer measurements. Acoustic measurements were obtained using the impedance tube, as presented in Chapter 7, and the experimental vibration analysis was performed using the single-point laser vibrometer (PDV-100). Additionally, a three-dimensional FEM model of a plate-type acoustic valve resonator for frequency domain analysis and a three-dimensional FEM model of a plate-type acoustic valve for eigenfrequency analysis have been developed.

8.1 Three-dimensional FEM Model

A three-dimensional FEM numerical model was developed to validate the analytical model of the plate-type acoustic valve resonator using the commercial software COMSOL Multiphysics version 6.0. Figure (8.1) illustrates the conversion procedure from the 2D model to the 3D model. The complete 3D model comprises two cylindrical volumes representing the impedance tube and backing cavity, separated by the plate-type acoustic valve sample. The vibroacoustic behaviour of the plate-type acoustic valve resonator under normal incidence is examined using both the acoustics module and structural mechanics module in the frequency domain, following a similar approach as outlined in Section 6.1.

User-defined meshing was applied to the geometry by setting the maximum element size as $c_0/(12 * f_{max})$, where f_{max} represents the maximum frequency of interest. To account for changes in thermo-viscous conduction, four boundary layers were added along the air gap's wall between the plate-type acoustic valve and the mounting plate. The complete mesh comprises 105,464 domain elements, 14,406 boundary elements, and 736 edge elements.

The average simulation time for frequency domain analysis on a workstation, equipped with 8-core 2.40 GHz processors and 64 GB RAM, was 41 hours, 43 minutes, and 6 seconds.

To numerically determine the natural frequencies of the plate-type acoustic valve, a 3D FEM model was developed using the COMSOL Structural Mechanics module. The model employed a physics-controlled mesh with a normal element size. Achieving the desired 12 eigenfrequencies around 50Hz required a simulation run time of 24s on the same workstation used for frequency domain analysis.

Eigenfrequencies and their corresponding mode shapes were obtained through eigenfrequency analysis. Figure (3.1) illustrates the developed FEM model of the plate-type acoustic valve, while Figure (8.2) provides a view of the model during eigenfrequency analysis. The modelling parameters and material properties for the plate-type acoustic valve are detailed in Table 3.1.

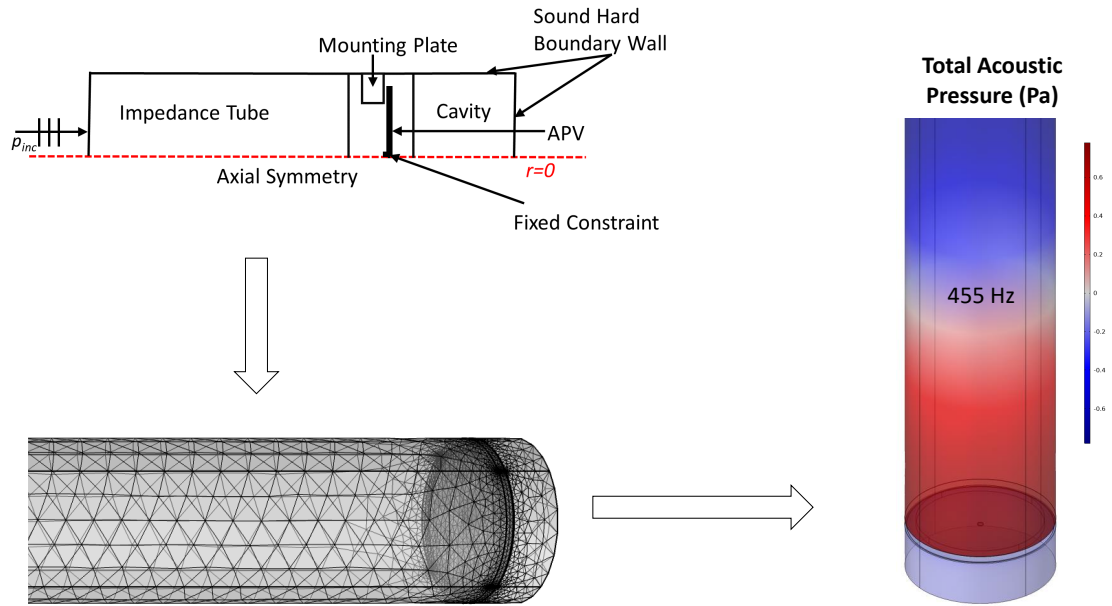


Figure 8.1: Conversion steps from 2D to 3D numerical model (vibroacoustic simulation) for plate-type acoustic valve resonator using frequency domain analysis.

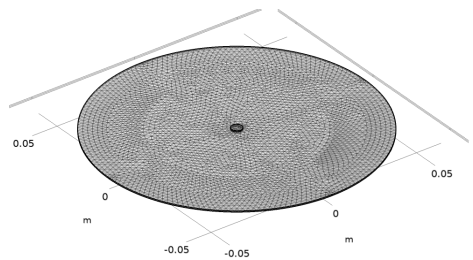


Figure 8.2: 3D FEM model of plate-type acoustic valve for eigenfrequency analysis. The small central circular portion is clamped with fixed constraints.

8.2 Results & Discussions

Figure (8.3) displays the absorption coefficient of the plate-type acoustic valve resonator with $l_{cav}=40$ mm from both 2D and 3D numerical simulations, without incorporating any damping in the numerical models. Notably, the 3D result exhibits more absorption peaks compared to the 2D result, confirming predictions made in Section 7. The inclusion of both radial and azimuthal modes in the 3D model results in more visible structural resonance peaks, as opposed to the 2D axis-symmetric modes, which only provide radial modes ($m=0$).

Figure (8.4) presents a comparison between the experimental absorption coefficient and the velocity profile (for the edge point 24 on the plate-type acoustic valve) obtained from acoustic and vibration measurements, respectively. From the measured velocity profile, one can observe two dis-

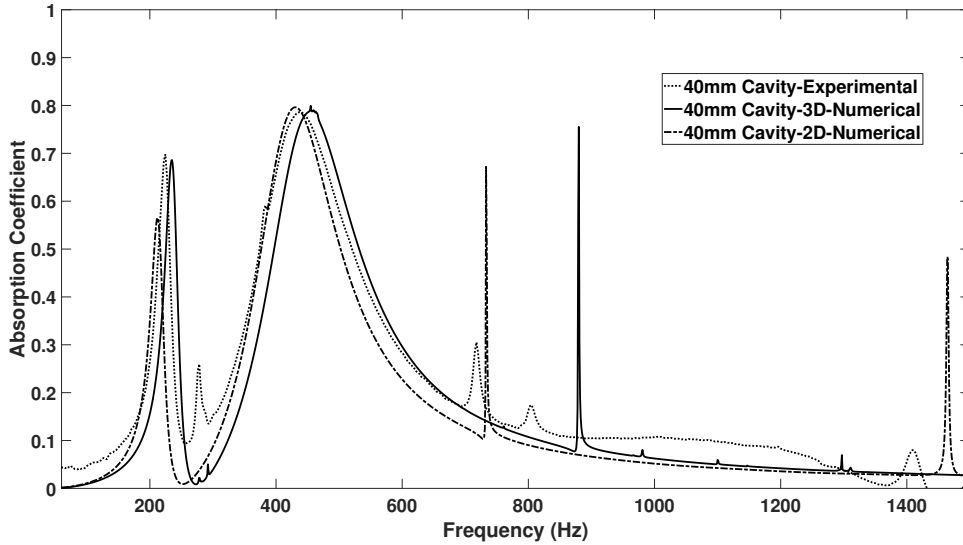


Figure 8.3: Absorption coefficient for $l_{cav}=40$ mm cavity depth from experiment, 2D and 3D numerical simulation (without damping).

tinct resonance peaks at 227 Hz and 385 Hz, denoted by the clear resonance peaks in the spectrum. Additionally, potential resonance peaks are observable at 278 Hz and 722 Hz. In Fig. (8.5), the absorption coefficient of the plate-type acoustic valve resonator with $l_{cav}=40$ mm is shown for both 2D and 3D numerical simulations, with the addition of damping in the form of a structural loss factor $\eta_m=0.03$ in the numerical models. Most of the azimuthal modes vanish in the 3D results, while the majority of radial modes are evident in both the 2D and 3D outcomes. Figure (8.6) illustrates the comparison of the experimental velocity profile at the edge point of the plate-type acoustic valve with respect to the velocity magnitude in both the 2D and 3D numerical models. Both the 2D and 3D numerical models have successfully predicted resonance peaks corresponding to the experimental resonance peak (f_{01}) at 227 Hz. Another resonance peak at 735 Hz from the 2D model and 902 Hz from the 3D model corresponds to the experimental resonance peak (f_{02}) at 722 Hz. Evidently, the 3D outcome seems to be missing a particular radial mode, namely (0,3). This absence is attributed to the use of fitted material properties from the 2D model for the 3D-printed plate-type acoustic valve. It is anticipated that employing different fitted material properties may reveal the missing radial mode (0,3) within the desired frequency range.

A parametric analysis was conducted, focusing on material properties to align the experimental resonance peak f_{01} in the absorption curve with a 3D numerical resonance peak.

Firstly, Young's modulus (E_m) of the plate-type acoustic valve material was considered, and the corresponding absorption coefficient is depicted in Fig. (8.7). Subsequently, using $E_m=3.5$ GPa, a

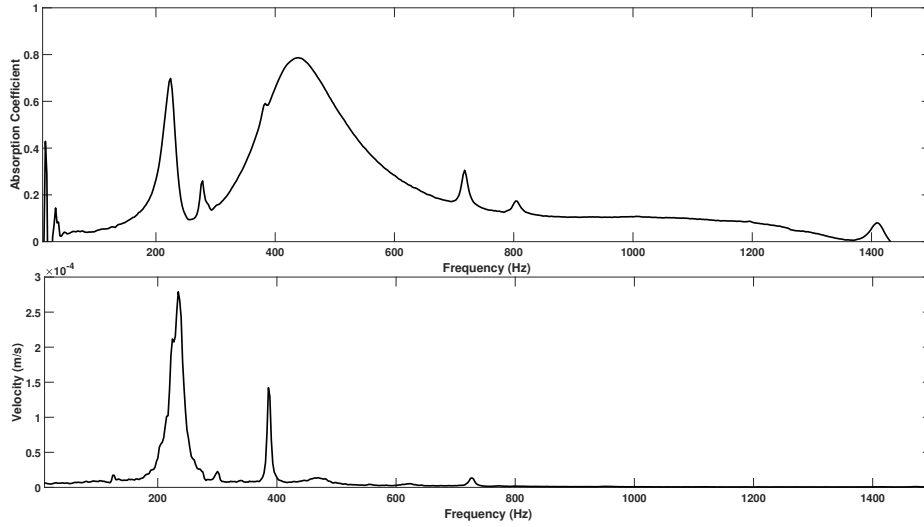


Figure 8.4: Experimental absorption coefficient and velocity profile from acoustic measurements and laser Doppler vibrometer measurements, respectively.

structural loss factor (η_m) was introduced for parametric analysis. Figure (8.8) illustrates the absorption coefficient with different structural loss factors. Notably, the frequency position of the numerical resonance peak at $f_{01} = 227$ Hz perfectly aligns with the experimental resonance peak. While resonance peaks for f_{02} and f_{03} can be identified in Fig. (8.9), they do not match perfectly, with a relative difference less than 10%. These discrepancies are attributed to variations in printed material properties.

It's worth noting that structural loss factors exhibit frequency dependency, as confirmed by experimental results (see Section 8.4). The parametric analysis using Young's modulus and structural loss factor revealed that Young's modulus influences the frequency position of the structural resonance peak, while the structural loss factor affects the amplitude. In a recent study conducted by Neubauer et al. [96], it is demonstrated that Young's modulus and the structural loss factor of a material are interconnected.

The linear regression technique with a polynomial basis function has been employed to approximate the numerical correlation between Young's modulus and the structural loss factor as [95] [96]:

$$\eta_m = 0.0335 \cdot E_m^{-0.633} \quad \text{where } E_m \text{ in GPa} \quad (8.1)$$

Hence, any change in E_m and η_m will result in a change in frequency position and amplitude of the resonance peak.

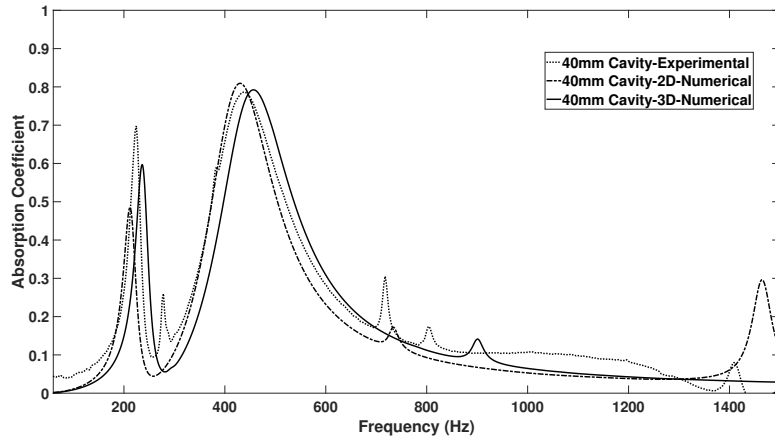


Figure 8.5: Absorption coefficient for $l_{cav} = 40$ mm cavity depth from experiment, 2D and 3D numerical simulation (with damping factor $\eta = 0.03$).

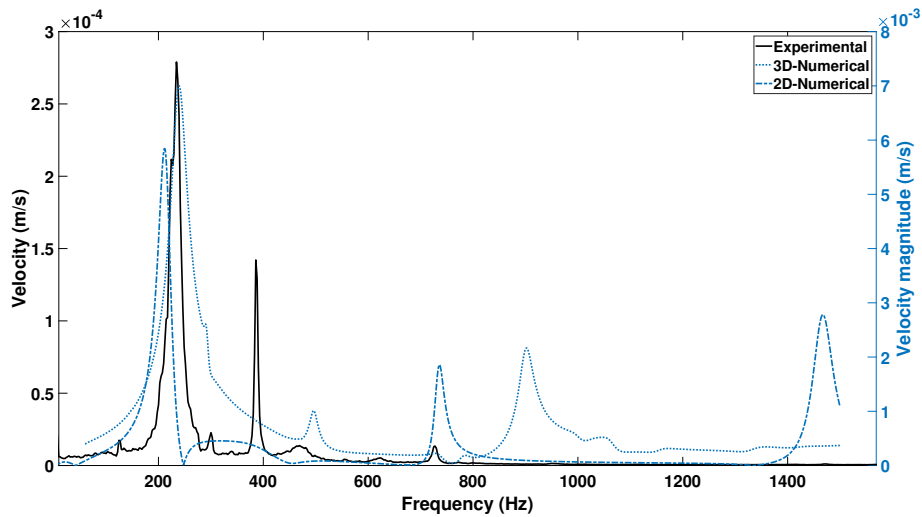


Figure 8.6: Comparison between experimental and 2d-3D numerical velocity profile.

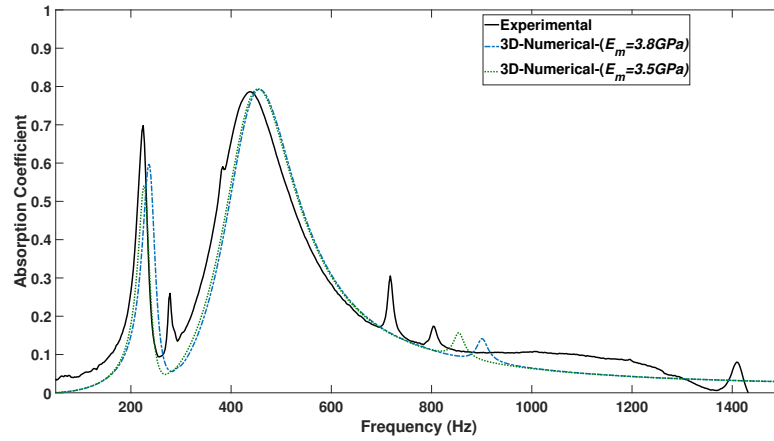


Figure 8.7: 3D Numerical simulation using parametric analysis varying Young's modulus (E_m) of the material.

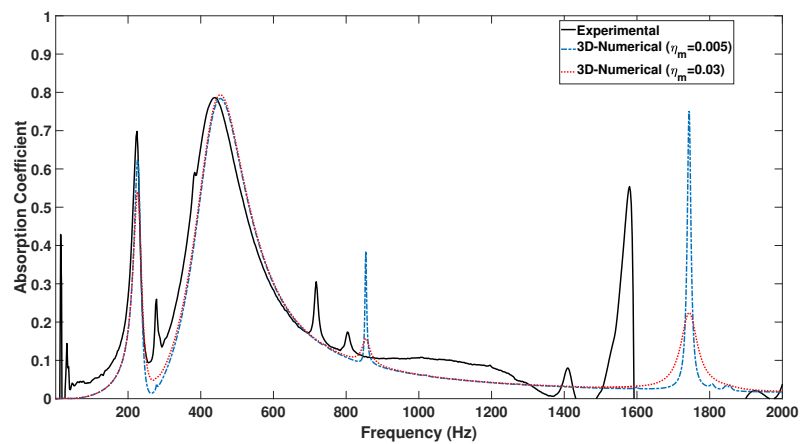


Figure 8.8: 3D Numerical simulation using parametric analysis varying structural loss factor (η_m) of the material.

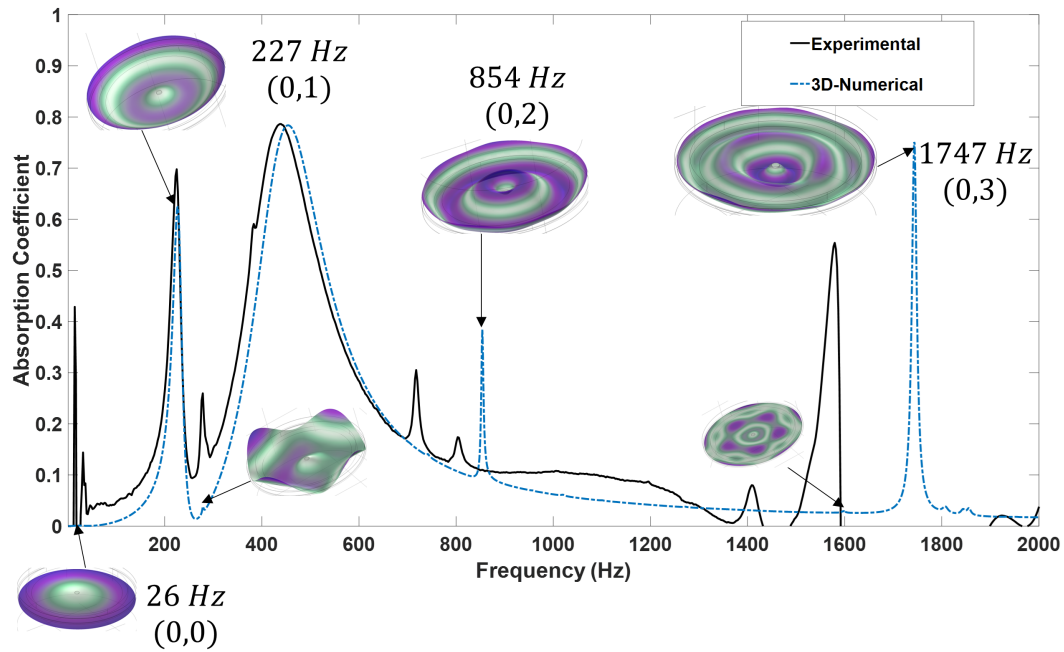


Figure 8.9: 3D Numerical vibrational modes for plate-type acoustic valve in presence of acoustic cavity with structural damping (loss factor $\eta_m=0.005$). Also, coupled mode can be seen at 280 Hz and 1598 Hz.

8.3 Experimental Structural Resonance Modes

In this section, numerical structural resonance modes are investigated in comparison to both experimental acoustic measurements and LDV measurements. The eigenfrequencies of the plate-type acoustic valve, along with their corresponding mode shapes from the 3D FEM model, are tabulated in Table 8.1. A comparison with the eigenfrequencies from the 2D model is presented in Table 8.4. Figure (8.3) illustrates the absorption peaks and corresponding structural mode shapes of the plate-type acoustic valve without structural damping in the presence of the cavity behind it. It is evident that both radial and azimuthal modes are present, contributing to higher or lower absorption peaks. The assumption was made that while radial modes ($m = 0$) result in higher absorption peaks, azimuthal modes ($m \geq 1$) mainly contribute to very small absorption peaks. This validates the assumption made by Hossain and Bennett [156], as the 2D fully coupled vibroacoustic FEM model in the frequency domain only includes radial modes of vibration. Figure (8.9) presents the absorption peaks and corresponding structural mode shapes of the plate-type acoustic valve with structural damping in the form of a loss factor $\eta_m=0.005$ in the presence of the acoustic cavity. Notably, all azimuthal modes have disappeared from the absorption curve. The observation from these two plots leads to the conclusion that the absorption performance of the plate-type acoustic valve is primarily dominated by the radial modes of vibration.

From the experimental absorption coefficient curve, structural resonance peaks are identified at $f_{mn} = 14$ Hz, 31 Hz, 224 Hz, 278 Hz, 383 Hz, 717 Hz, 805 Hz, 1411 Hz, and 1579 Hz. To validate and explore the mode shapes corresponding to these resonance frequencies, experimental modal analysis was conducted using a single-point laser vibrometer.

For resonance mode identification, 12 points were selected along the diameter of the plate-type acoustic valve, with 6 points along each radius, separated by the fixed centre. These points were chosen for their ability to capture multiple peaks and troughs, providing insight into all resonance modes within the frequency of interest. Figures (8.10) and (8.11) display the real and imaginary parts of the Frequency Response Functions (FRFs) corresponding to 6 scanning points from 19 to 24 along the radius of the plate-type acoustic valve, respectively. Figure (8.12) illustrates the corresponding coherence functions for each FRF. Similarly, Figures (8.13) and (8.14) exhibit the real and imaginary parts of the FRFs, respectively for another set of 6 scanning points from 43 to 48 along the radius of the plate-type acoustic valve. Figure (8.15) illustrates the corresponding coherence functions for each FRF. Additionally, Figures (8.16) and (8.17) display the magnitude and phase plots of the FRFs corresponding to 6 scanning points from 19 to 24 along the radius of the plate-type acoustic valve,

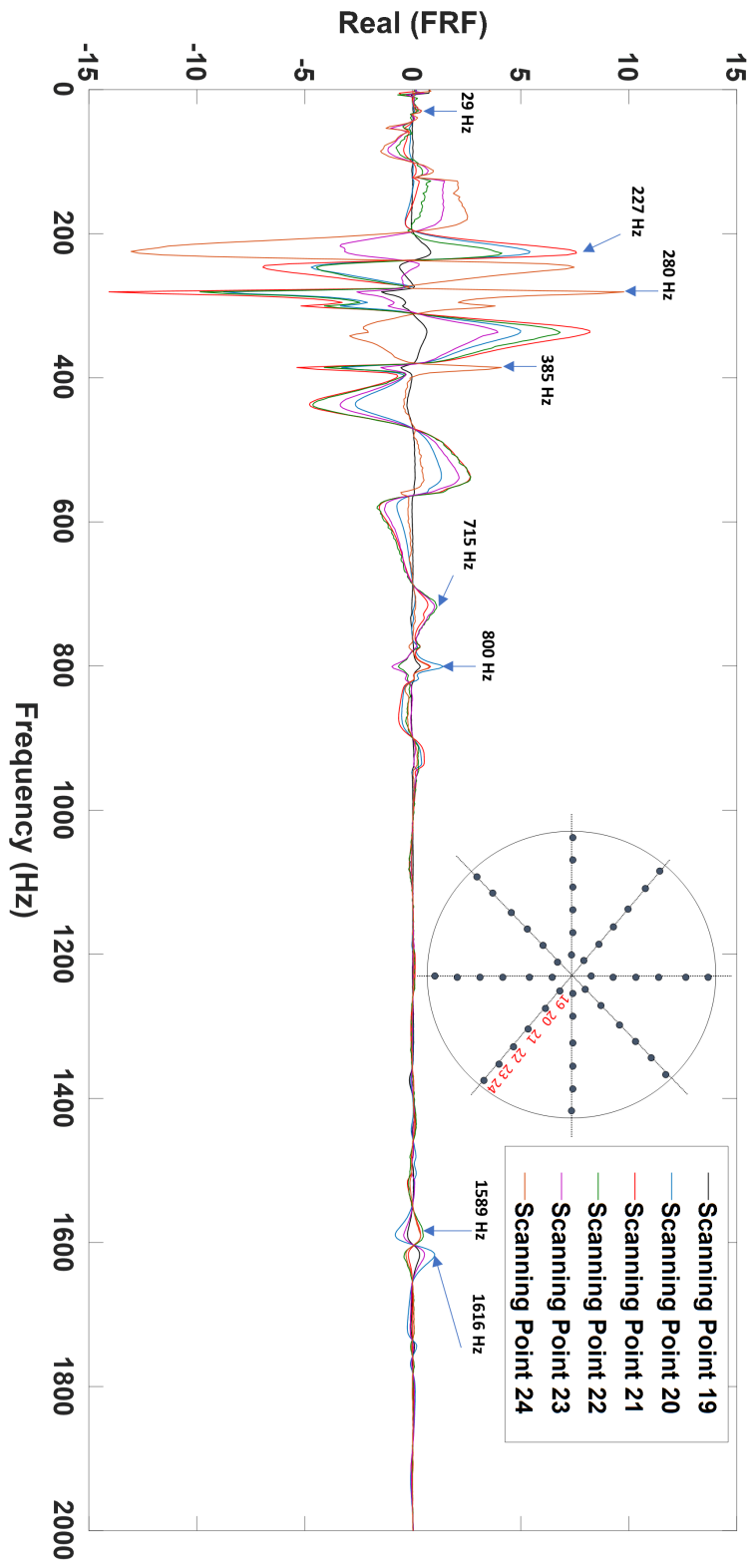


Figure 8.10: The experimental frequency response function (FRF) in different points (19–24) along the nodal diameter of the thin circular plate.

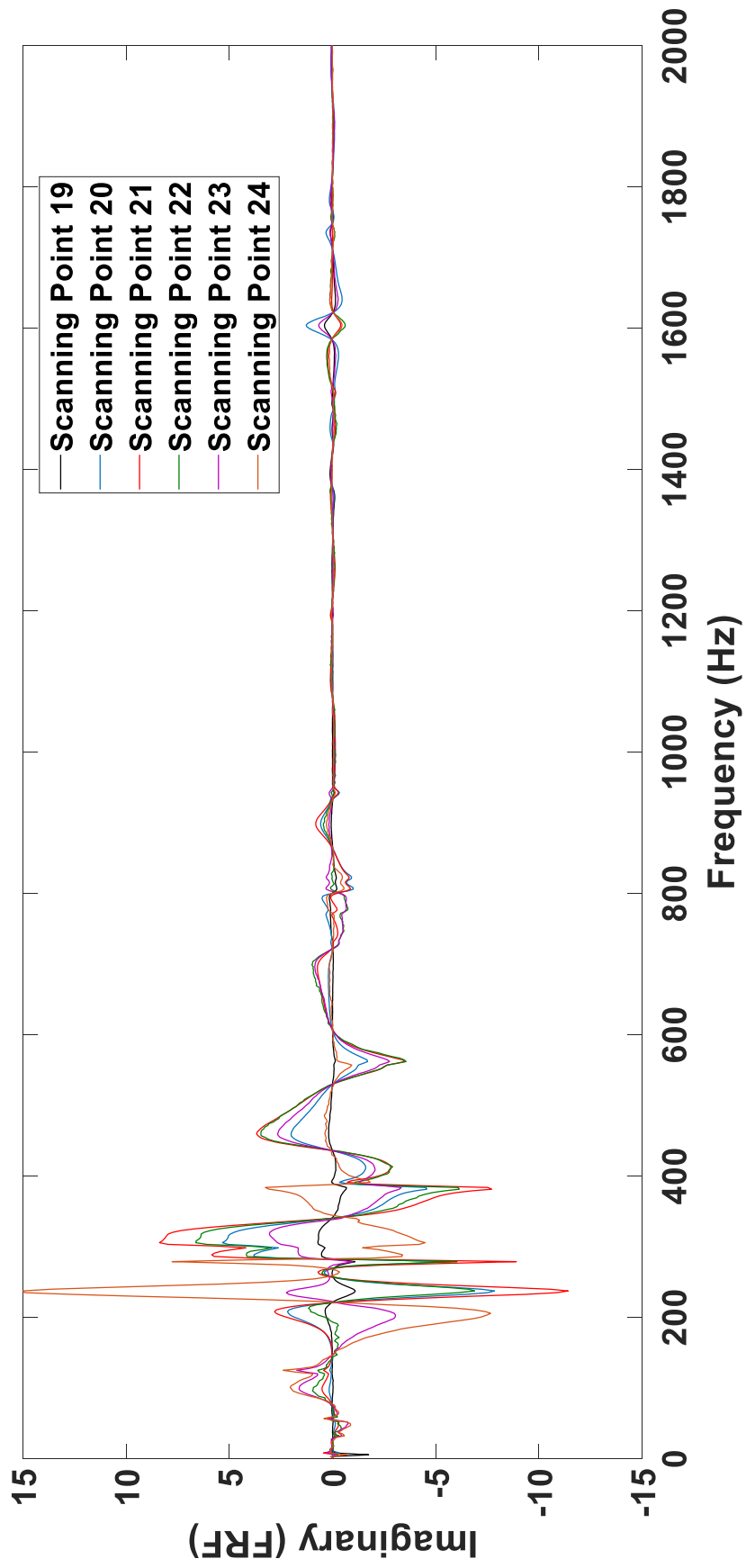


Figure 8.11: The imaginary part of the experimental frequency response function (FRF) in different points (19–24) along the nodal diameter of the thin circular plate.

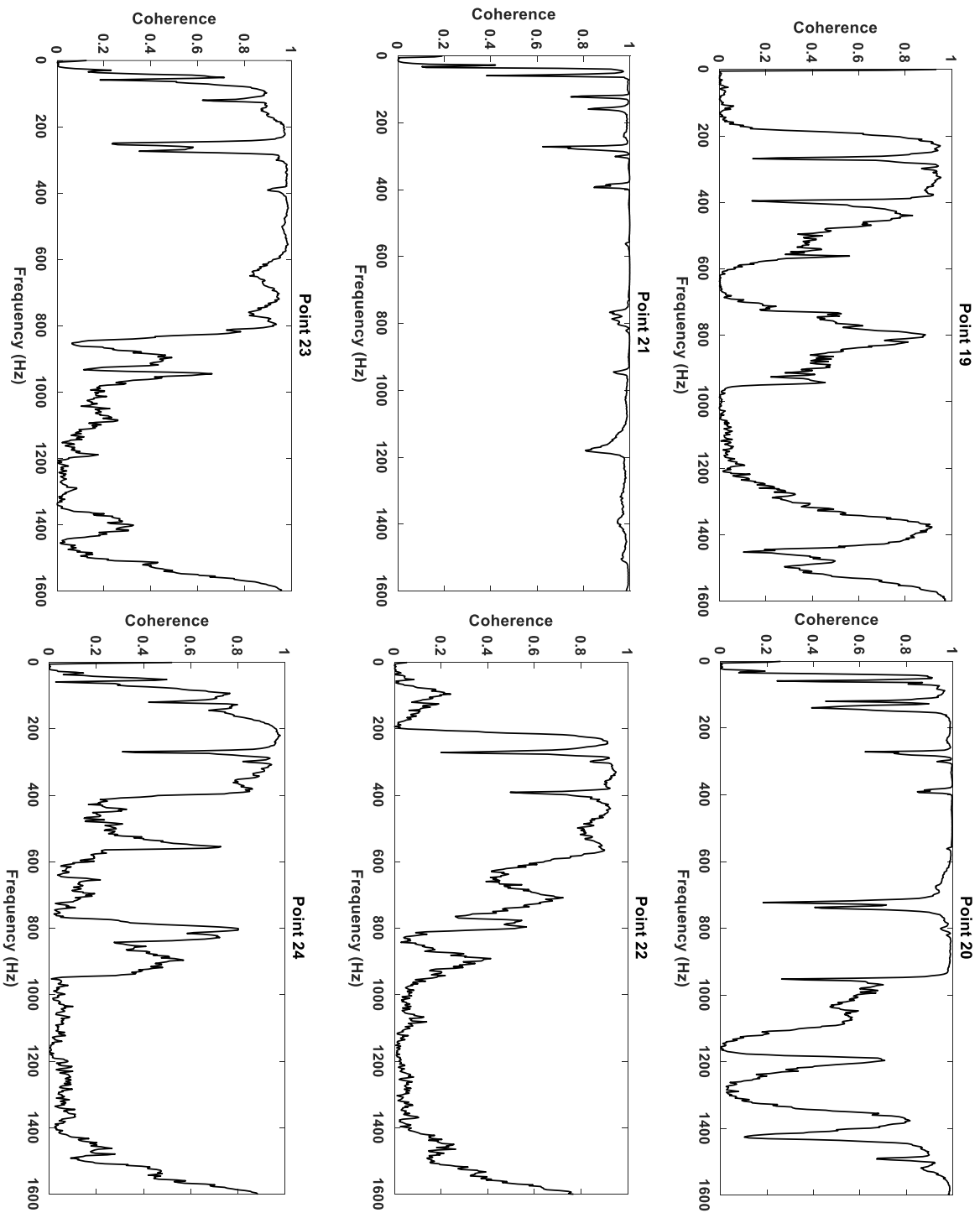


Figure 8.12: The experimental coherence function in different points (19–24) along the nodal diameter of the thin circular plate.

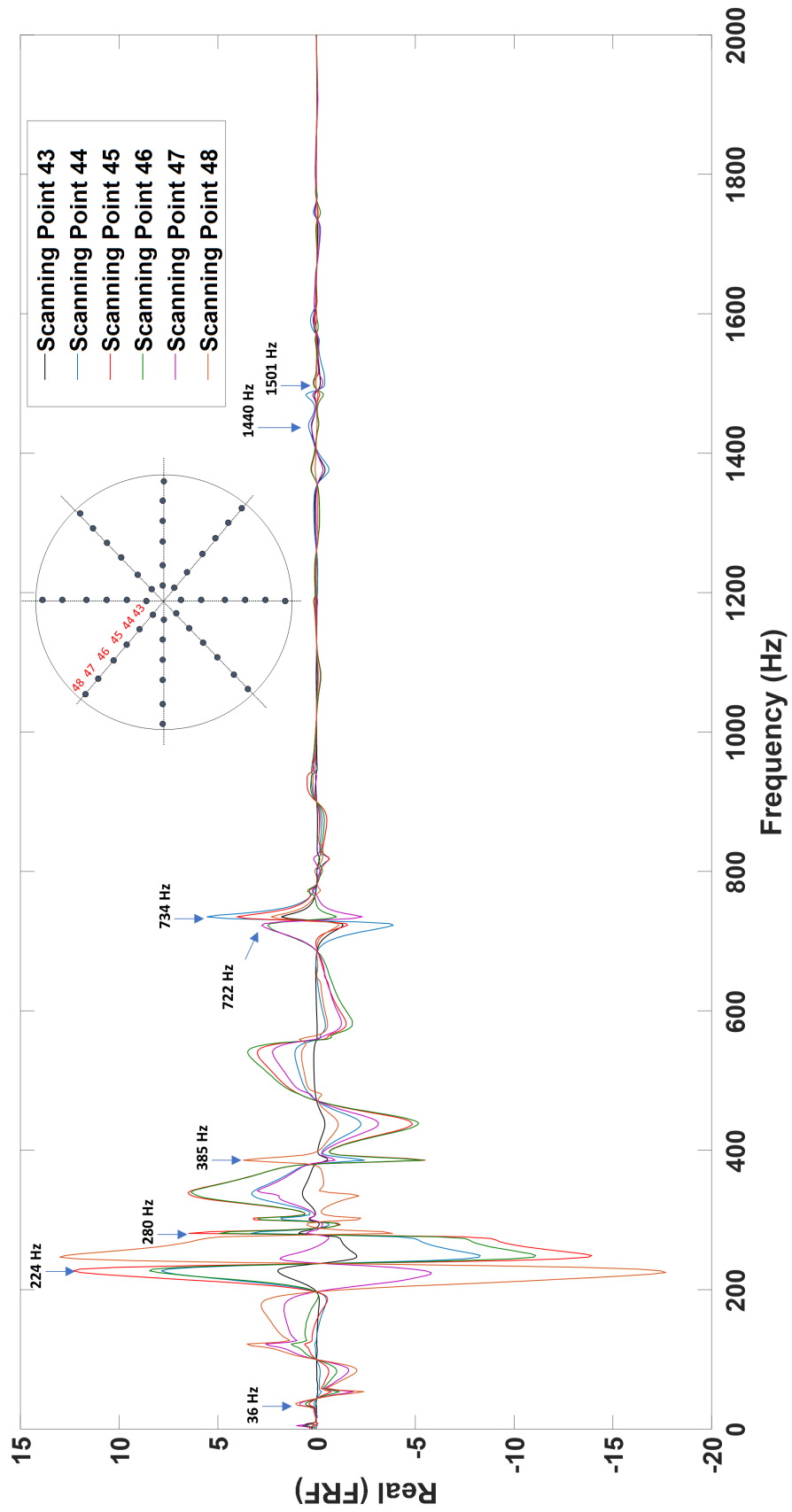


Figure 8.13: The experimental frequency response function (FRF) in different points (43–48) along the nodal diameter of the thin circular plate.

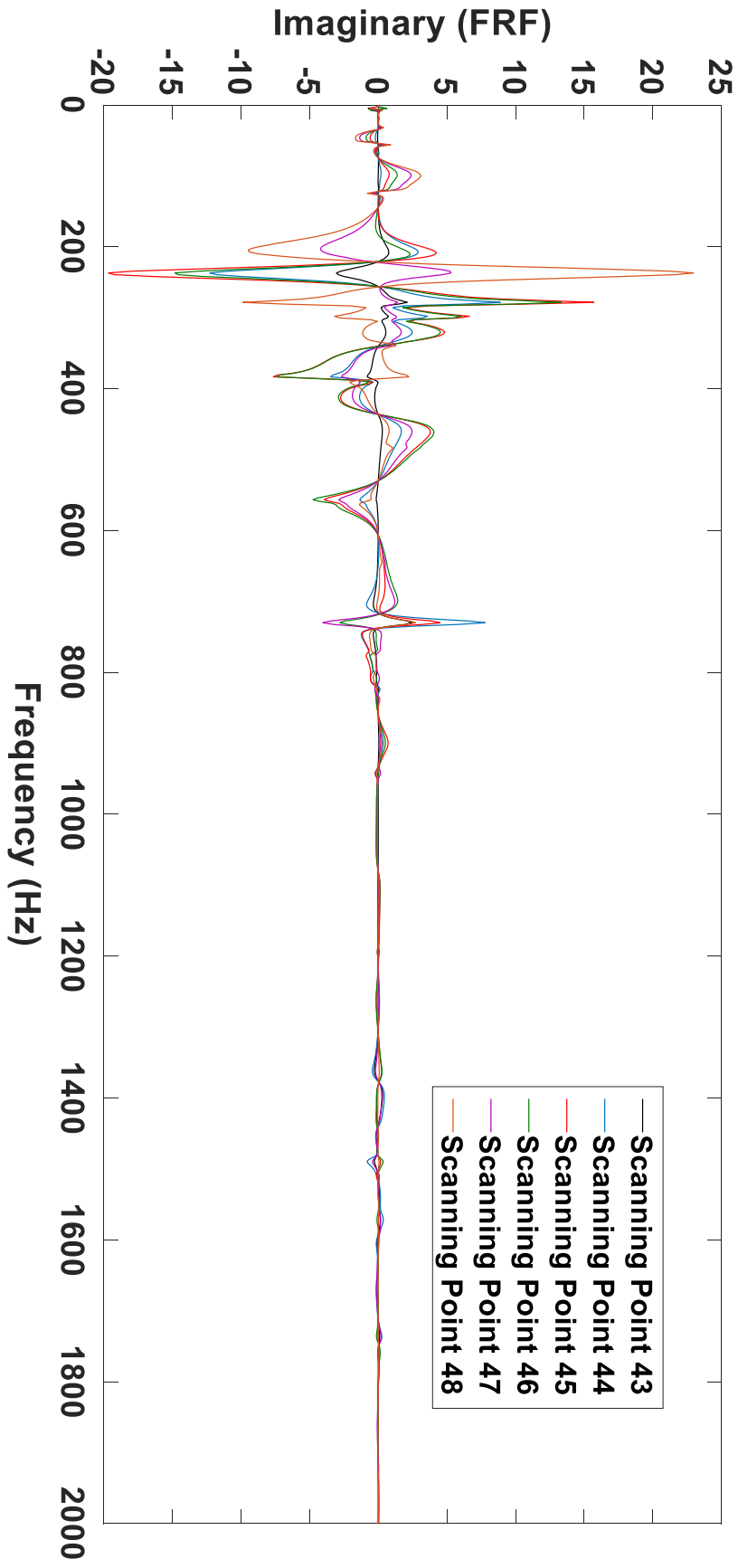


Figure 8.14: The imaginary part of the experimental frequency response function (FRF) in different points (43–48) along the nodal diameter of the thin circular plate.

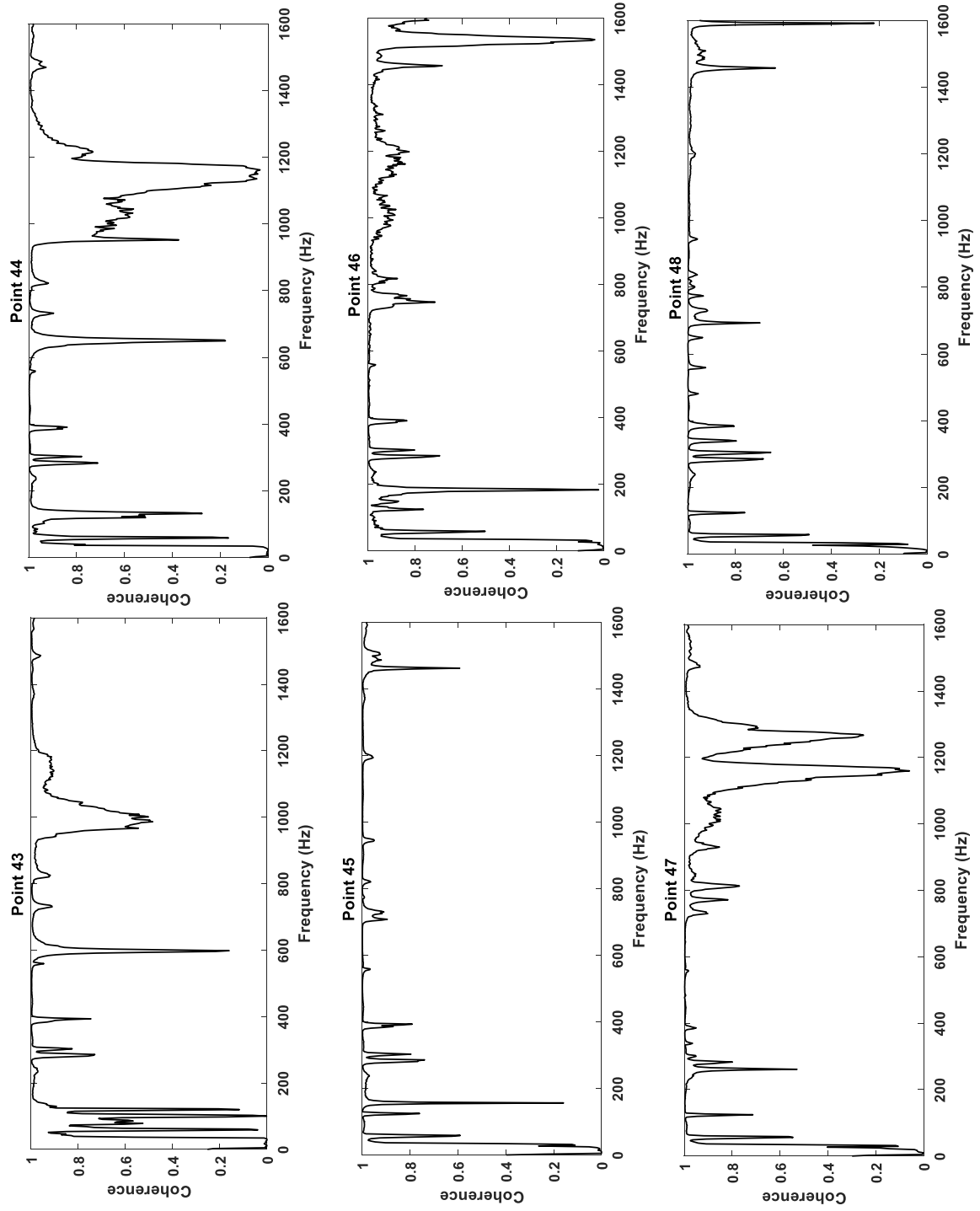


Figure 8.15: The experimental coherence function in different points (43–48) along the nodal diameter of the thin circular plate.

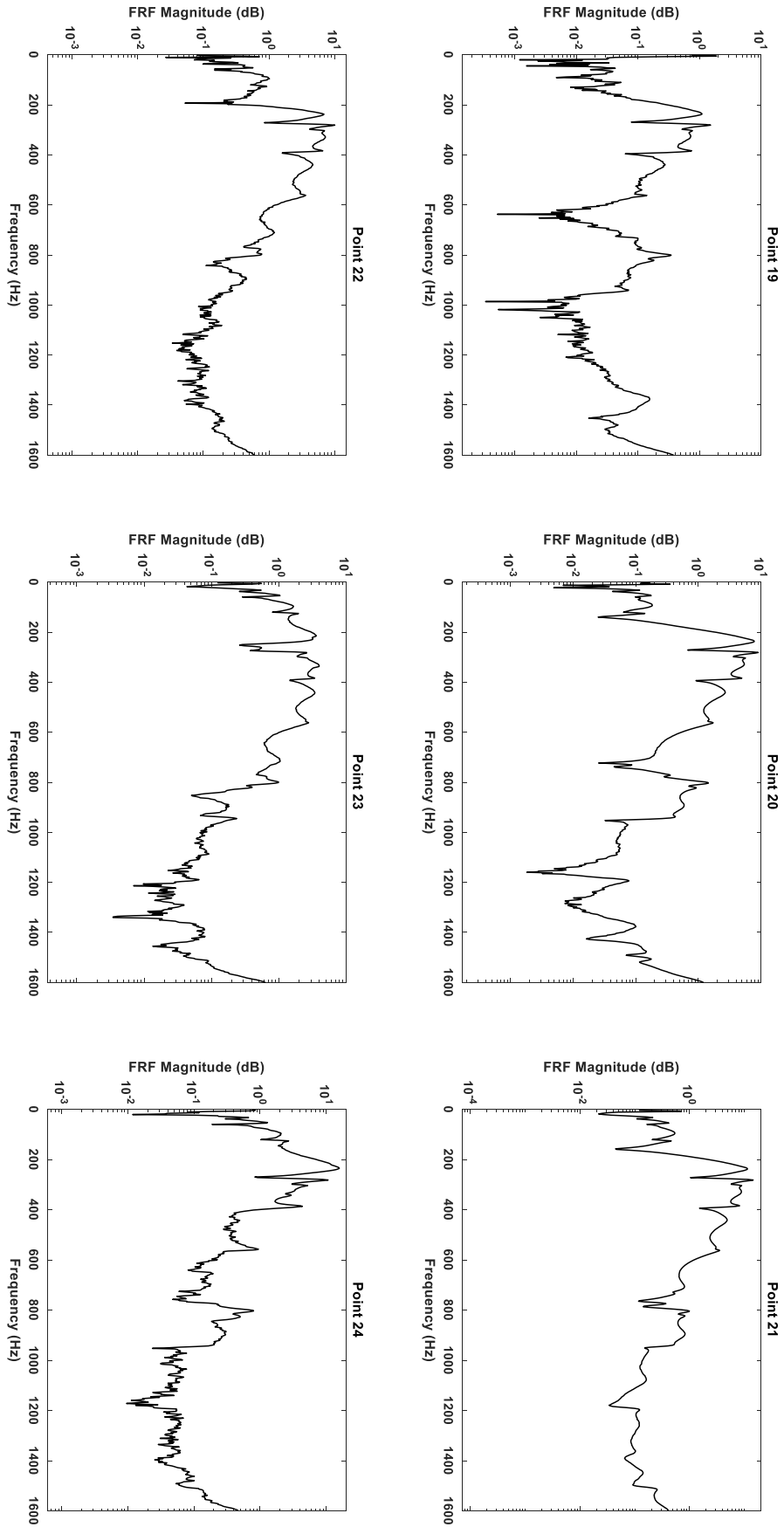


Figure 8.16: The experimental FRF magnitude diagram in different points (19–24) along the nodal diameter of the thin circular plate.

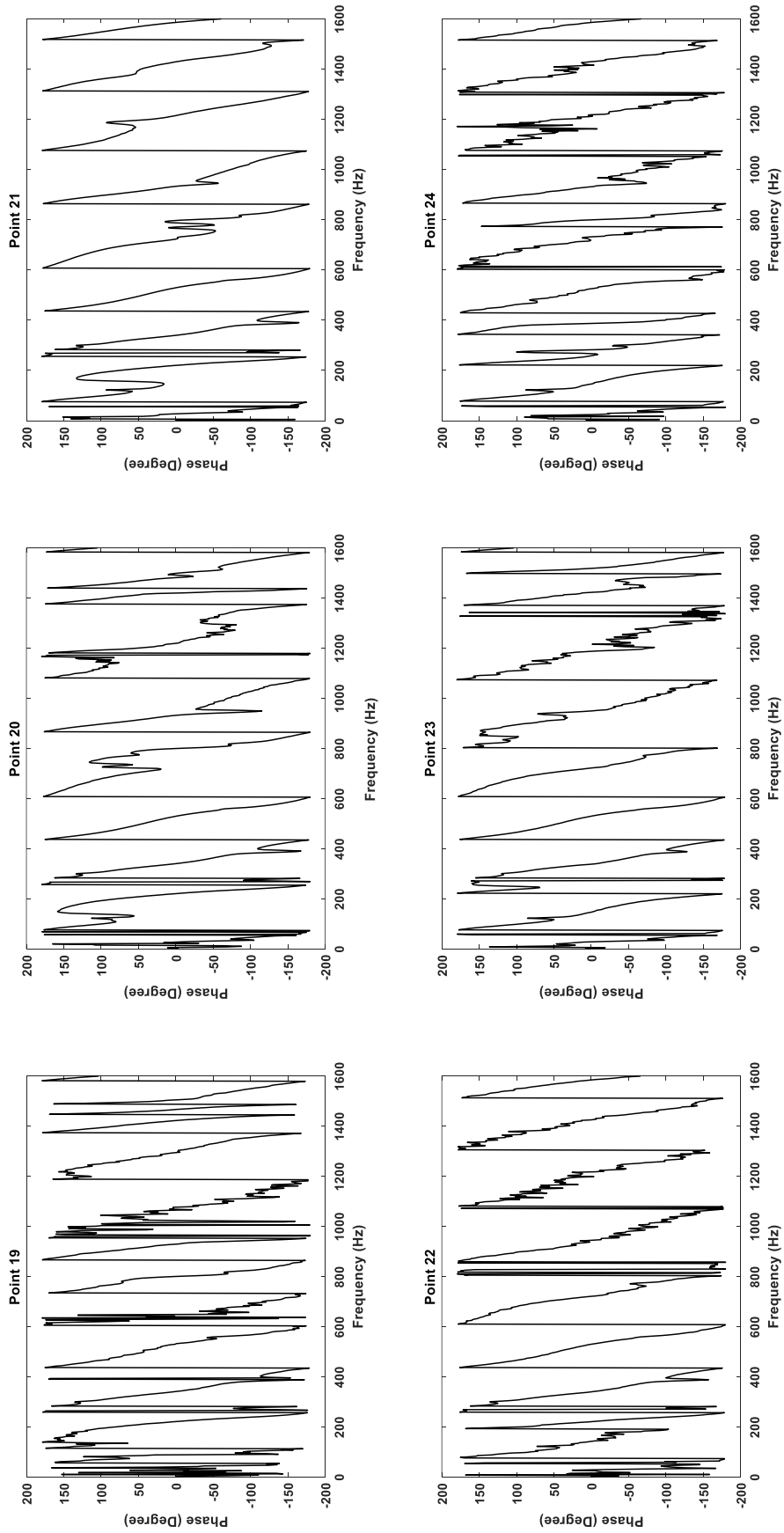


Figure 8.17: The experimental FRF phase diagram in different points (19–24) along the nodal diameter of the thin circular plate.

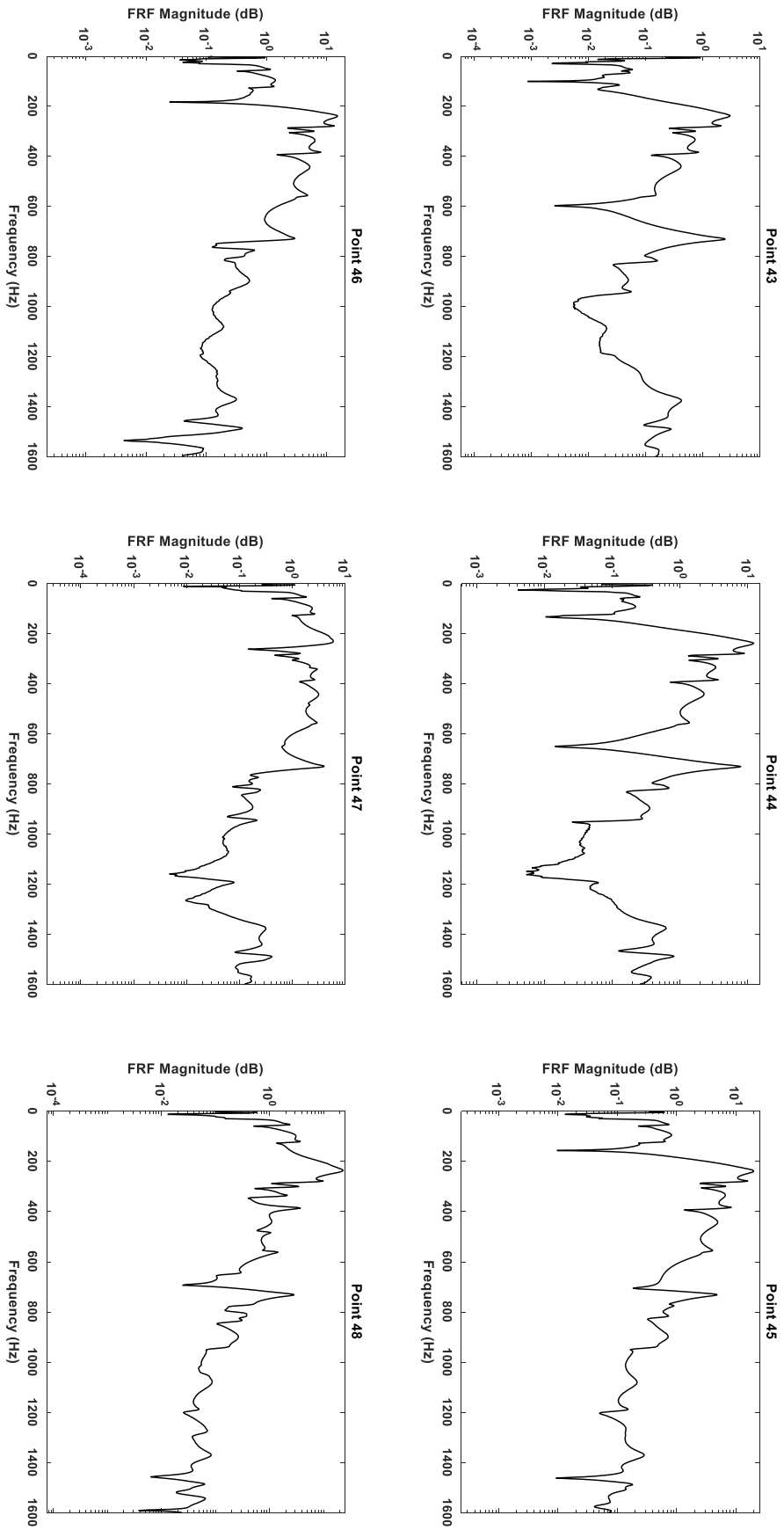


Figure 8.18: The experimental FRF magnitude diagram in different points (43–48) along the nodal diameter of the thin circular plate.

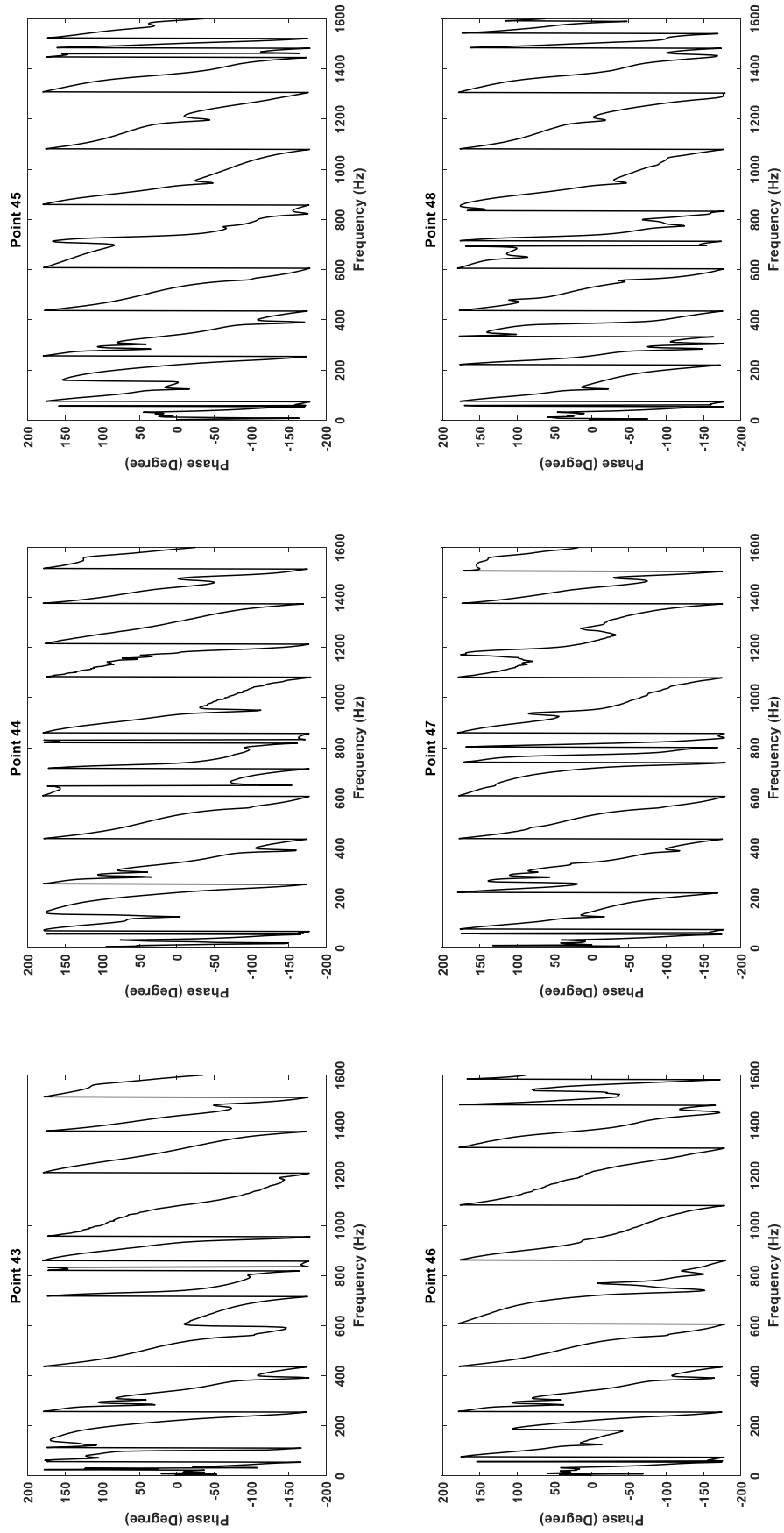


Figure 8.19: The experimental FRF phase diagram in different points (43–48) along the nodal diameter of the thin circular plate.

8.3 EXPERIMENTAL STRUCTURAL RESONANCE MODES

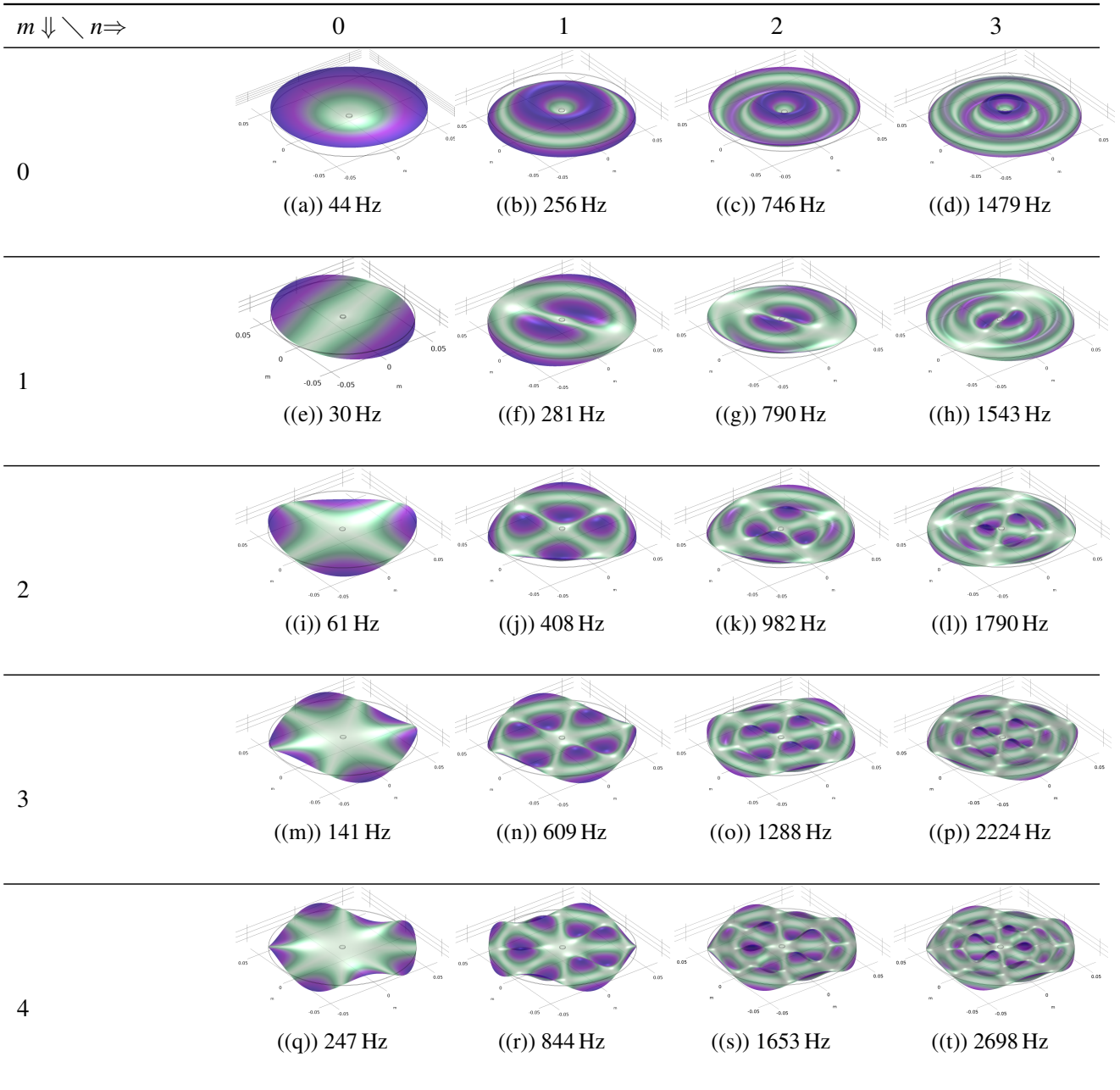


Table 8.1: Eigenfrequencies and corresponding mode shape from 3D numerical model: Eigenfrequency Analysis.

respectively. Similarly, Figures (8.18) and (8.19) display the magnitude and phase plots of the FRFs corresponding to another set of 6 scanning points from 43 to 48 along the radius of the plate-type acoustic valve, respectively.

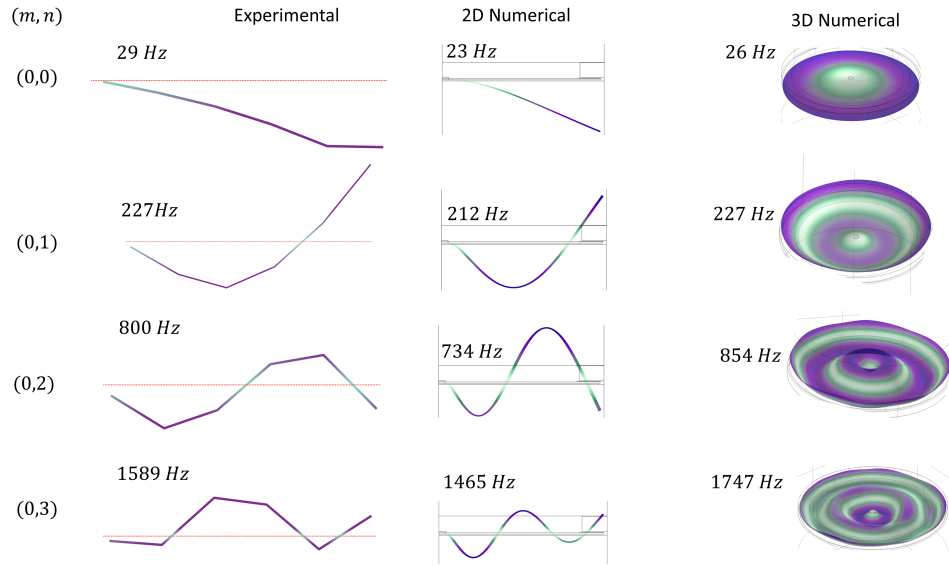


Figure 8.20: Section view of experimental measurements with LDV(Considering the scanning points 19–24) (left) and numerical (right) mode shapes for the plate-type acoustic valve in the presence of an acoustic cavity.

8.3.1 Identifying the radial modes (0, n)

Initially, the radial modes (0, n) were examined using laser vibrometer measurements within the frequency range of interest. Fig. (8.20) presents the experimental and 2D numerical mode shapes and resonant frequencies of the plate-type acoustic valve interacting with the air cavity, considering 6 scanning points from 19 to 24 along the radius.

From these scanning points, the experimental resonance frequencies are identified as $f_{0n} = 29$ Hz, 227 Hz, 800 Hz, and 1589 Hz. Similarly, for the 6 scanning points from 43 to 48, the experimental resonance frequencies are identified as $f_{0n} = 36$ Hz, 224 Hz, 722 Hz, and 1501 Hz. A comparison of the obtained experimental results from different scanning lines is tabulated in Table 8.2. Significant differences are observed for the resonance frequencies f_{00} and f_{02} , while the differences for f_{01} and f_{03} are less than 6%. The variations in resonance frequencies between the two scanning lines can be attributed to geometric variations, considering the non-uniform thickness of the 3D printed plate-type acoustic valve.

From the 3D FEM model, the corresponding natural frequencies under vacuum are $f_{00} = 44$ Hz, $f_{01} = 256$ Hz, $f_{02} = 746$ Hz, and $f_{03} = 1479$ Hz. It's worth noting that the shift in resonance frequency position can be explained as a result of fluid-structure interaction, as mentioned in Section 3.3.3.

Mode (m, n)	f_{mn} [Hz] (Point 19–24)	f_{mn} [Hz] (Point 43–48)	% Difference (Δf_{mn})
(0, 0)	29	36	21.5385
(0, 1)	227	224	1.33038
(0, 2)	800	722	10.2497
(0, 3)	1589	1501	5.69579

Table 8.2: Experimental radial modes and corresponding resonance frequencies using different scanning points.

8.3.2 Identifying the azimuthal modes (m, n) and $m \neq 0$

Since all the radial modes are identified from the acoustic absorption curve with laser measurements, the rest of them can be assumed as azimuthal modes. From the experimental absorption coefficient curve, the structural resonance peaks with azimuthal modes can be identified as $f_{mn} = 14, 278 \text{ Hz}, 383 \text{ Hz}$. The resonance frequency of 14 Hz could not be identified as FRFs in selected scanning points do not show any recognizable vibrational mode below 29 Hz. Azimuthal modes are not symmetric modes. To identify them correctly we need to consider another line with scanning points along the diameter of the plate-type acoustic valve. Two lines along the radius with scanning points 7 to 12 and 31 to 36 have been selected. Figure (8.21) shows the azimuthal mode shapes in the presence of the acoustic cavity and identified as (1, 1) and (2, 1) vibrational modes for the resonance frequencies of $f_{11} = 280 \text{ Hz}$ and $f_{21} = 385 \text{ Hz}$. From the 3D FEM model, the corresponding natural frequencies under vacuum are $f_{11} = 281 \text{ Hz}$, $f_{21} = 408 \text{ Hz}$ respectively. Comparison between the experimentally obtained azimuthal modes and 3D numerical azimuthal modes has been tabulated in Table 8.3. The relative difference in resonance frequencies using different experimental methods and 3D numerical simulation are very small. Again, the shift in resonance frequency position can be explained as a result of fluid-structure interaction as mentioned in Section 3.3.3.

The fairly good agreement between experimental modal analysis and the 3D numerical model has been demonstrated, successfully identifying the vibrational modes experimentally. Structural resonance frequencies at 717 Hz and 805 Hz were identified as the same in the experimental measurements, referred to as 'twin modes or frequencies' [157]. The occurrence of these twin modes in experiments is attributed to the anisotropy [158] of the 3D printed samples, which may result from non-uniform geometric parameters or variations in material properties. Similarly, twin frequencies are observed at 1411 Hz and 1579 Hz.

Although fitting properties for the absorption performance of the plate-type acoustic valve resonator were obtained using the 'trial and error' method, better fitting properties can be achieved using

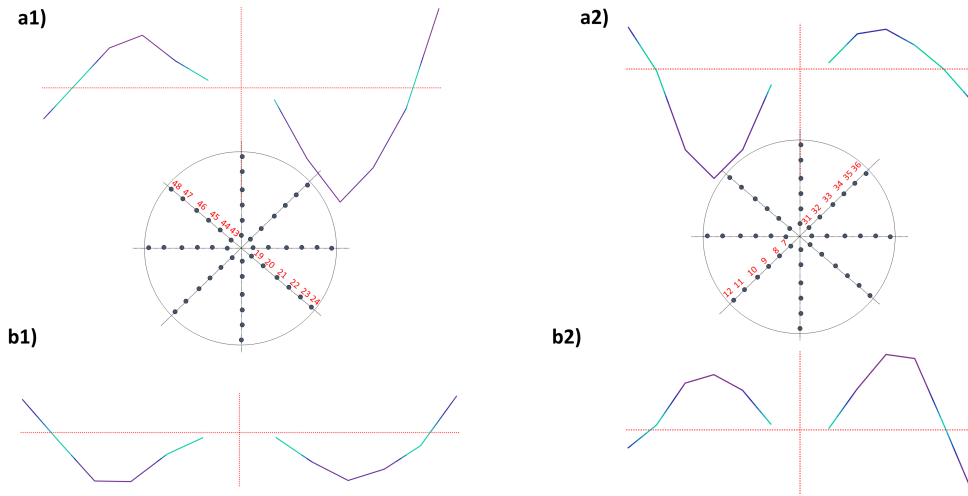


Figure 8.21: Experimental azimuthal mode shapes for (1, 1) and (2, 1) vibrational modes. Corresponding resonance frequencies are $f_{11}= 280$ Hz and $f_{21}= 385$ Hz. a) Vibrational mode shape for resonance frequency $f_{11}= 280$ Hz a1) Mode shape along the points 43-48 and 19-24 a2) Mode shape along the points 7-12 and 31-36. b) Vibrational mode shape for resonance frequency $f_{21}= 385$ Hz b1) Mode shape along the points 43-48 and 19-24 b2) Mode shape along the points 7-12 and 31-36.

Mode (m, n)	f_{mn} [Hz] (Acoustic)	f_{mn} [Hz] (Laser)	f_{mn} [Hz] (3D FEM)
(1, 1)	278 Hz	280	281
(2, 1)	383	385	408

Table 8.3: Comparison between experimental and numerical azimuthal modes.

the optimization module in COMSOL. By manipulating the structural resonance and Helmholtz resonance, it is possible to achieve maximum absorption in broadband low-frequency applications by optimizing the design parameters and material properties.

Mode (m, n)	Structural resonance frequency, f_{mi} (Hz)							
	Analytical (<i>in vacuo</i>)	Numerical (2D) (<i>in vacuo</i>)	Numerical (3D) (<i>in vacuo</i>)	Numerical (2D) (<i>in air</i>)	Numerical (3D) (<i>in air</i>)	Experimental (Acoustic)	Experimental (Laser)	
(0,0)	43.071	43	44	23	26	31	29	
(0,1)	240.0364	241	256	212	227	224	227	
(0,2)	702.5455	698	746	734	854	717 (805)	800	
(0,3)	1384.4	1377	1479	1465	1747	1411 (1579)	1589	
(1,0)	12.25	14	30					
(1,1)	235.5594	244	281			278	280	
(1,2)	687.1630	704	790					
(1,3)	1366.1	1392	1543					
(2,0)	60.3018	60	61					
(2,1)	404.6524	405	408			383	385	
(2,2)	963.1302	971	982					
(3,0)	140.3943	141	141					
(3,1)	607.3804	609	609					
(3,2)	1277.7	1288	1288					

Table 8.4: Comparison of experimental modal frequencies to those obtained using an analytical model and numerical model.

8.4 Measured Structural Loss Factor

The experimental structural loss factor has been obtained using the half-power bandwidth method based on the magnitude curve of the frequency-response functions. For each resonance mode and the damping ratio $\xi \ll 1$, the material damping can be written as in the form of loss factor (η_m):

$$\eta_m = \frac{1}{Q} = 2\xi = \frac{\Delta f}{f_r}$$

where, $\Delta f = f_U - f_L$, f_r is the resonance frequency of the mode and Δf is the half-power bandwidth of the mode (the -3 dB points) which is defined as the width of the FRF amplitude curve when the amplitude is $0.707 (\frac{1}{\sqrt{2}})$ times of the peak amplitude (A_{max}), f_U and f_L are the upper and lower frequencies at the corresponding value of the $A_{max}/\sqrt{2}$ respectively, Q is the quality factor.

Considering the FRF from the scanning point 47, for $f_{r,01} = 224$ Hz, the loss factor evaluated from the laser vibrometer measurements: $\eta_{m,01} = 0.0366$ which is very close to the value $\eta_m = 0.03$ used for initial numerical simulation. For $f_{r,02} = 800$ Hz, the loss factor evaluated from the laser vibrometer measurements: $\eta_{m,02} = 0.004027$ and for $f_{r,03} = 1589$ Hz, the loss factor evaluated from the laser vibrometer measurements: $\eta_{m,03} = 0.00495$ which are relatively closer to the numerical loss factor $\eta_m = 0.005$.

Considering the FRF from the scanning point 21, for $f_{r,02} = 227$ Hz, the loss factor deduced from the laser vibrometer measurements: $\eta_{m,02} = 0.033$ which is also very close to the value $\eta_m = 0.03$ used for initial numerical simulation.

8.5 Summary

A detailed theoretical and experimental analysis of the structural resonance of plate-type acoustic valve resonators is presented in this chapter. The theoretical analysis encompasses analytical modelling using thin plate theory with relevant boundary conditions and numerical simulations with a 3D FEM model. The experimental analysis incorporates both acoustic and laser vibrometer measurements. Comparative studies involving analytical, numerical (2D and 3D), and experimental results showcase strong agreement. Vibrational modes and modal shapes are obtained and compared in the presence and absence of fluid-structure interaction. Furthermore, the absorption performance, concerning material properties such as Young's modulus and loss factor of the plate-type acoustic valve resonator, has been thoroughly investigated.

Chapter 9

Conclusions and Future Recommendations

The current research presents work to date on a novel acoustic resonator that minimizes reflections from the walls of an enclosed space and thus absorbs sound. The technology employs the original idea of a flexible plate valve applied to acoustics. Inspired by off-the-shelf elastomeric fluidic one-way valves, plate-type acoustic valves were 3D printed in PLA to have a large diameter. The research demonstrates that the technology combines a Helmholtz resonator with structural vibrations in the plate which themselves result in sound absorption for this small gap/air cavity configuration. It was shown that parameters such as the air cavity depth or the material properties of the plate-valve plate can be tailored at any required frequency so that resonant coincidence can be attained which can result in near-perfect absorption (e.g. $\alpha = 0.995$) which is greater than could be achieved by the Helmholtz resonator itself. Given that the thickness of the plate-type acoustic valve plus the depth of the cavity can be a very small percentage of the acoustic wavelength that it is absorbing, deep subwavelength ratio absorbers can be designed, e.g. a ratio of up to 58 was achieved in this study. The technology presents the possibility for innovative acoustic absorbers for low-frequency noise attenuation in a thin profile. A FEM-based frequency domain modelling approach for the plate-type acoustic valve has been validated to predict acoustic performance. A simple 2D axisymmetric model has been implemented to reduce computational complexity and costs. The frequency domain model was compared with experimental results and demonstrated strong agreement. An analytical model of the plate dynamics and a numerical eigenfrequency analysis allowed the natural frequencies to be calculated and the latter allowed for a visualization of the mode shapes.

The effect of structural resonance in acoustic absorption has been investigated experimentally for the plate-type acoustic valve resonator using the single-point laser vibrometer. Most of the vibrational mode shapes (radial modes and azimuthal modes) and corresponding resonance peaks (resonance frequency positions) in the absorption curves have been identified successfully. The identified radial modes are (0,0)-(0,3) and azimuthal modes are (1, 1) and (1, 2). Investigating the absorption curves and vibrational mode shapes, it can be stated that the absorption performance is dominated by the radial modes. 3D scanning laser vibrometer would be a good choice for better visualization of the modal shapes.

The 3D FEM numerical model has been provided with the validation that only the 3D model includes both radial and azimuthal modes of the vibration which was assumed in the previous studies. Both radial and azimuthal modes have been identified from the 3D numerical model without including the damping. 3D numerical model including the damping, mostly includes the radial modes. The proper choice of a structural loss factor ($\eta_m=0.005$ has been used) should contain both radial and

azimuthal modes in the absorption curves. The optimization module from COMSOL contains the optimization of the parameters and parameter estimation according to the experimental results. Although, they are computationally demanding and require a significant amount of computational time and cost (e.g. for a single frequency simulation with optimizing 4 parameters it requires a simulation time of 35 hrs 33 mins 48s). In that case, better numerical data can be obtained for optimizing the design and material properties of plate-type acoustic valve resonators using High-Performance Computing (HPC) facilities.

For further investigation, a narrow region acoustics interface can be utilized in both the 2D and 3D models instead of the computationally intensive thermoviscous acoustics interface. Although the thermoviscous boundary layer impedance doesn't provide a reliable prediction alone, it would be interesting to investigate combining it with the narrow region acoustics to include losses in the boundary wall of the impedance tube.

In numerous practical applications, absorbing materials face incoming waves arriving from angles that aren't perpendicular to the surface, including various room acoustic scenarios. Despite demonstrations in published works showcasing the potential of periodically arranged resonators as acoustic absorbing materials, their characterization typically relies on assessing the normal incidence absorption coefficient. However, as highlighted in the research conducted by Gao et al. [159], alterations in the angle of incidence can bring about changes not only in the absorption coefficient concerning different frequencies but also impact the frequency range where these materials exhibit superior absorption characteristics. Hence, there's a crucial necessity to delve into the behaviour of these periodic surfaces when subjected to oblique incidence angles. Understanding the absorption properties under oblique incidence becomes pivotal in leveraging these materials more effectively in real-world scenarios, enabling a deeper comprehension of their performance when encountering waves at non-normal angles. Further research involving varying angles of incidence, both in experimental and theoretical investigations, will notably bolster the practical application of plate-type acoustic valve resonators across diverse scenarios. This emphasis on exploring different angles becomes especially crucial in contexts where waves approach surfaces at different angles, such as in room acoustics. The findings will significantly enhance the understanding and utilization of these resonators in various applications.

Bibliography

- [1] Sanjay Kumar and Heow Pueh Lee. The present and future role of acoustic metamaterials for architectural and urban noise mitigations. In *Acoustics*, volume 1, pages 590–607. Multidisciplinary Digital Publishing Institute, 2019.
- [2] Yong Wang, Kun Zhao, Xiang-Yu Lu, Yu-Bao Song, and Gareth J. Bennett. Bio-Inspired Aerodynamic Noise Control: A Bibliographic Review. *Applied Sciences*, 9(11):2224, May 2019. ISSN 2076-3417. doi: 10.3390/app9112224. URL <https://www.mdpi.com/2076-3417/9/11/2224>.
- [3] Kun Zhao, Patrick Okolo, Eleonora Neri, Peng Chen, John Kennedy, and Gareth J. Bennett. Noise reduction technologies for aircraft landing gear-A bibliographic review. *Progress in Aerospace Sciences*, 112:100589, November 2019. ISSN 03760421. doi: 10.1016/j.paerosci.2019.100589. URL <https://linkinghub.elsevier.com/retrieve/pii/S0376042119300338>.
- [4] Daniel Torrent and José Sánchez-Dehesa. Acoustic cloaking in two dimensions: a feasible approach. *New Journal of Physics*, 10(6):063015, 2008.
- [5] Jun Mei, Guancong Ma, Min Yang, Zhiyu Yang, Weijia Wen, and Ping Sheng. Dark acoustic metamaterials as super absorbers for low-frequency sound. *Nature communications*, 3(1):1–7, 2012.
- [6] Yong Li and Badreddine M Assouar. Acoustic metasurface-based perfect absorber with deep subwavelength thickness. *Applied Physics Letters*, 108(6), 2016.
- [7] Krupali Donda, Yifan Zhu, Shi-Wang Fan, Liyun Cao, Yong Li, and Badreddine Assouar. Extreme low-frequency ultrathin acoustic absorbing metasurface. *Applied Physics Letters*, 115(17):173506, 2019.

-
- [8] Yifan Zhu, Krupali Donda, Shiwang Fan, Liyun Cao, and Badreddine Assouar. Broadband ultra-thin acoustic metasurface absorber with coiled structure. *Applied Physics Express*, 12(11):114002, 2019.
- [9] YY Lee, EWM Lee, and CF Ng. Sound absorption of a finite flexible micro-perforated panel backed by an air cavity. *Journal of Sound and Vibration*, 287(1-2):227–243, 2005.
- [10] Chunqi Wang, Li Cheng, Jie Pan, and Ganghua Yu. Sound absorption of a micro-perforated panel backed by an irregular-shaped cavity. *The Journal of the Acoustical Society of America*, 127(1):238–246, 2010.
- [11] Muttalip Aşkın Temiz, Jonathan Tournadre, Ines Lopez Arteaga, and Avraham Hirschberg. Modelling vibro-acoustic coupling in flexible micro-perforated plates by a patch-impedance approach. *Applied Acoustics*, 125:80–90, 2017.
- [12] Emile Martincic, Alexandre Houdouin, Stéphane Durand, Nourdin Yaakoubi, Elie Lefeuvre, and Yves Auregan. Acoustic absorber, acoustic wall and method for design and production, November 12 2019. US Patent 10,477,302.
- [13] Andrew McKay, Ian Davis, Jack Killeen, and Gareth J. Bennett. Semsas: a compact super absorber optimised for broadband, low-frequency noise attenuation. *Scientific Reports*, 10(1):17967, 2020. ISSN 2045-2322. URL <https://doi.org/10.1038/s41598-020-73933-0>.
- [14] Ian Davis, Andrew McKay, and Gareth J. Bennett. A graph-theory approach to optimisation of an acoustic absorber targeting a specific noise spectrum that approaches the causal optimum minimum depth. *Journal of Sound and Vibration*, 505:116135, 2021. ISSN 0022-460X. URL <https://doi.org/10.1016/j.jsv.2021.116135>.
- [15] Killeen, Jack, Davis, Ian, Wang, Jiayu, and Bennett, Gareth J. Fan-noise reduction of data-center telecommunications server racks, with an acoustic metamaterial broadband, low frequency sound absorbing liner (To appear). *Applied Acoustics*, 2022.
- [16] Jiayu Wang and Gareth J. Bennett. Multi-chamber micro-perforated panel absorbers optimised for high amplitude broadband absorption using a two-point impedance method. *Journal of Sound and Vibration*, 547:117527, March 2023. ISSN 0022460X. doi: 10.1016/j.jsv.2022.117527. URL <https://linkinghub.elsevier.com/retrieve/pii/S0022460X22007106>.

-
- [17] Maaz Farooqui and Yves Aurégan. Compact beam liners for low frequency noise. In *2018 AIAA/CEAS Aeroacoustics Conference*, page 4101, 2018.
- [18] Massimo Emiliano Delia, Thomas Humbert, and Yves Aurégan. On articulated plates with micro-slits to tackle low-frequency noise. *Acta Acustica*, 5:31, 2021.
- [19] Yves Aurégan and Maaz Farooqui. In-parallel resonators to increase the absorption of sub-wavelength acoustic absorbers in the mid-frequency range. *Scientific reports*, 9(1):1–6, 2019.
- [20] Gareth J Bennett, Robiul Hossain, Andrew McKay, and Eoghan P Ross. Acoustic diode meta-material for sound absorption. In *25th AIAA/CEAS Aeroacoustics Conference*, page 2422, 2019.
- [21] AB COMSOL. Comsol multiphysics reference manual, version 5.5, 2019.
- [22] Viktor G Veselago. The electrodynamics of substances with simultaneously negative values of ϵ and μ . *Soviet Physics Uspekhi*, 10(4):509, 1968. URL <http://stacks.iop.org/0038-5670/10/i=4/a=R04>.
- [23] J. B. Pendry, A. J. Holden, W. J. Stewart, and I. Youngs. Extremely Low Frequency Plasmons in Metallic Mesostructures. *Physical Review Letters*, 76(25):4773–4776, June 1996. ISSN 0031-9007, 1079-7114. doi: 10.1103/PhysRevLett.76.4773. URL <https://link.aps.org/doi/10.1103/PhysRevLett.76.4773>.
- [24] J.B. Pendry, A.J. Holden, D.J. Robbins, and W.J. Stewart. Magnetism from conductors and enhanced nonlinear phenomena. *IEEE Transactions on Microwave Theory and Techniques*, 47(11):2075–2084, November 1999. ISSN 00189480. doi: 10.1109/22.798002. URL <http://ieeexplore.ieee.org/document/798002/>.
- [25] D. Schurig, J. J. Mock, B. J. Justice, S. A. Cummer, J. B. Pendry, A. F. Starr, and D. R. Smith. Metamaterial Electromagnetic Cloak at Microwave Frequencies. *Science*, 314(5801): 977–980, November 2006. ISSN 0036-8075, 1095-9203. doi: 10.1126/science.1133628. URL <http://www.sciencemag.org/cgi/doi/10.1126/science.1133628>.
- [26] Yanxia Cui, Kin Hung Fung, Jun Xu, Hyungjin Ma, Yi Jin, Sailing He, and Nicholas X. Fang. Ultrabroadband Light Absorption by a Sawtooth Anisotropic Metamaterial Slab. *Nano Letters*, 12(3):1443–1447, March 2012. ISSN 1530-6984, 1530-6992. doi: 10.1021/nl204118h. URL <http://pubs.acs.org/doi/10.1021/nl204118h>.

-
- [27] Manvir S Kushwaha, Peter Halevi, Leonard Dobrzynski, and Bahram Djafari-Rouhani. Acoustic band structure of periodic elastic composites. *Physical review letters*, 71(13):2022, 1993.
- [28] Rosa Martínez-Sala, J Sancho, Juan V Sánchez, Vicente Gómez, Jaime Llinares, and Francisco Meseguer. Sound attenuation by sculpture. *nature*, 378(6554):241–241, 1995.
- [29] Guancong Ma and Ping Sheng. Acoustic metamaterials: From local resonances to broad horizons. *Science advances*, 2(2):e1501595, 2016.
- [30] Zhengyou Liu, Xixiang Zhang, Yiwei Mao, YY Zhu, Zhiyu Yang, Che Ting Chan, and Ping Sheng. Locally resonant sonic materials. *science*, 289(5485):1734–1736, 2000.
- [31] Nicholas Fang, Dongjuan Xi, Jianyi Xu, Muralidhar Ambati, Werayut Srituravanich, Cheng Sun, and Xiang Zhang. Ultrasonic metamaterials with negative modulus. *Nature materials*, 5(6):452–456, 2006.
- [32] Sam Hyeon Lee, Choon Mahn Park, Yong Mun Seo, Zhi Guo Wang, and Chul Koo Kim. Composite acoustic medium with simultaneously negative density and modulus. *Physical review letters*, 104(5):054301, 2010.
- [33] Zhiyu Yang, Jun Mei, Min Yang, NH Chan, and Ping Sheng. Membrane-type acoustic metamaterial with negative dynamic mass. *Physical review letters*, 101(20):204301, 2008.
- [34] Romain Fleury and Andrea Alù. Extraordinary sound transmission through density-near-zero ultranarrow channels. *Physical review letters*, 111(5):055501, 2013.
- [35] Norbert Cselyuska, Milan Sečujski, and Vesna Crnojević Bengin. Compressibility-near-zero acoustic metamaterial. *Physics Letters A*, 378(16-17):1153–1156, 2014.
- [36] Marc Dubois, Chengzhi Shi, Xuefeng Zhu, Yuan Wang, and Xiang Zhang. Observation of acoustic dirac-like cone and double zero refractive index. *Nature communications*, 8(1):1–6, 2017.
- [37] Farzad Zangeneh-Nejad and Romain Fleury. Active times for acoustic metamaterials. *Reviews in Physics*, page 100031, 2019.
- [38] Dah-You Maa. Theory and design of microperforated panel sound-absorbing constructions. *Scientia Sinica*, 18(1):55–71, 1975.

- [39] Dah-You Maa. Potential of microperforated panel absorber. *the Journal of the Acoustical Society of America*, 104(5):2861–2866, 1998.
- [40] Chenxi Li, Ben Cazzolato, and Anthony Zander. Acoustic impedance of micro perforated membranes: Velocity continuity condition at the perforation boundary. *The Journal of the Acoustical Society of America*, 139(1):93–103, 2016.
- [41] Xiao-Ling Gai, Tuo Xing, Xian-Hui Li, Bin Zhang, and Wen-Jiang Wang. Sound absorption of microperforated panel mounted with helmholtz resonators. *Applied Acoustics*, 114:260–265, 2016.
- [42] RD Ford and MA McCormick. Panel sound absorbers. *Journal of Sound and Vibration*, 10(3): 411–423, 1969.
- [43] Jinkyoo Lee and George Warner Swenson. Compact sound absorbers for low frequencies. *Noise Control Engineering Journal*, 38(3):109–117, 1992.
- [44] W Frommhold, HV Fuchs, and S Sheng. Acoustic performance of membrane absorbers. *Journal of Sound and Vibration*, 170(5):621–636, 1994.
- [45] Jesús Carbajo, Jaime Ramis, Luís Godinho, Paulo Amado-Mendes, and Jesús Alba. A finite element model of perforated panel absorbers including viscothermal effects. *Applied Acoustics*, 90:1–8, 2015.
- [46] Cong-shuang Jiang, Xian-hui Li, Wu-yi Cheng, Yun Luo, and Tuo Xing. Acoustic impedance of microperforated plates with stepwise apertures. *Applied Acoustics*, 157:106998, 2020.
- [47] Irving Bardshar Crandall. *Theory of vibrating systems and sound*. D. Van Nostrand Company, 1926.
- [48] Trevor J Cox and Peter D’antonio. *Acoustic absorbers and diffusers: theory, design and application*. Crc Press, 2009.
- [49] Kimihiro Sakagami, Masakazu Kiyama, Masayuki Morimoto, and Daiji Takahashi. Sound absorption of a cavity-backed membrane: a step towards design method for membrane-type absorbers. *Applied Acoustics*, 49(3):237–247, 1996.
- [50] J Kang and HV Fuchs. Predicting the absorption of open weave textiles and micro-perforated membranes backed by an air space. *Journal of sound and vibration*, 220(5):905–920, 1999.

- [51] Kimihiro Sakagami, Masayuki Morimoto, and Motoki Yairi. A note on the effect of vibration of a microperforated panel on its sound absorption characteristics. *Acoustical science and technology*, 26(2):204–207, 2005.
- [52] Taewook Yoo. *The modeling of sound absorption by flexible micro-perforated panels*. PhD thesis, Purdue University, 2008.
- [53] Honggang Zhao, Qiquan Zheng, Yang Wang, Junhui Cao, Chao Wang, and Jihong Wen. Acoustic absorption of a metamaterial panel: Mechanism, boundary effect and experimental demonstration. *Applied Acoustics*, 184:108369, 2021.
- [54] Yang Liu, Kean Chen, Yanni Zhang, Xiyue Ma, and Lei Wang. Low-frequency and large-scale hybrid sound absorption using active force control. *Acoustics Australia*, 49(1):93–103, 2021.
- [55] Amr Baz. The structure of an active acoustic metamaterial with tunable effective density. *New Journal of Physics*, 11(12):123010, 2009.
- [56] Frédéric Bongard, Hervé Lissek, and Juan R Mosig. Acoustic transmission line metamaterial with negative/zero/positive refractive index. *physical Review B*, 82(9):094306, 2010.
- [57] Christina J Naify, Chia-Ming Chang, Geoffrey McKnight, Florian Scheulen, and Steven Nutt. Membrane-type metamaterials: Transmission loss of multi-celled arrays. *Journal of applied physics*, 109(10):104902, 2011.
- [58] Fuyin Ma, Jiu Hui Wu, Meng Huang, Weiquan Zhang, and Siwen Zhang. A purely flexible lightweight membrane-type acoustic metamaterial. *Journal of Physics D: Applied Physics*, 48(17):175105, 2015.
- [59] Li Fan, Zhe Chen, Shu-yi Zhang, Jin Ding, Xiao-juan Li, and Hui Zhang. An acoustic metamaterial composed of multi-layer membrane-coated perforated plates for low-frequency sound insulation. *Applied Physics Letters*, 106(15):151908, 2015.
- [60] Xiaole Wang, Hui Zhao, Xudong Luo, and Zhenyu Huang. Membrane-constrained acoustic metamaterials for low frequency sound insulation. *Applied Physics Letters*, 108(4):041905, 2016.
- [61] Linus Yinn Leng Ang, Yong Khiang Koh, and Heow Pueh Lee. Broadband sound transmission loss of a large-scale membrane-type acoustic metamaterial for low-frequency noise control. *Applied Physics Letters*, 111(4):041903, 2017.

- [62] Yves Aurégan. Ultra-thin low frequency perfect sound absorber with high ratio of active area. *Applied Physics Letters*, 113(20):201904, 2018.
- [63] Xiaodong Zhang, Fei Chen, Zhongsheng Chen, and Gang Wang. Membrane-type smart metamaterials for multi-modal sound insulation. *The Journal of the Acoustical Society of America*, 144(6):3514–3524, 2018.
- [64] Chong Rui Liu, Jiu Hui Wu, Kuan Lu, Zi Ting Zhao, and Zhen Huang. Acoustical siphon effect for reducing the thickness in membrane-type metamaterials with low-frequency broadband absorption. *Applied Acoustics*, 148:1–8, 2019.
- [65] Lucas YM Sampaio, Gabriel K Rodrigues, Jaime A Mosquera-Sánchez, Carlos De Marqui Jr, and Leopoldo PR de Oliveira. Membrane smart metamaterials for unidirectional wave propagation problems. *Journal of Sound and Vibration*, 512:116374, 2021.
- [66] Junyu Li, Yuanyuan Shi, Renjie Jiang, Zhifu Zhang, and Qibai Huang. Acoustic insulation mechanism of membrane-type acoustic metamaterials loaded with arbitrarily shaped mass blocks of variable surface density. *Materials*, 15(4):1556, 2022.
- [67] Dianlong Yu, Yaozong Liu, Gang Wang, Honggang Zhao, and Jing Qiu. Flexural vibration band gaps in timoshenko beams with locally resonant structures. *Journal of applied physics*, 100(12):124901, 2006.
- [68] Carl Q Howard. Transmission loss of a panel with an array of tuned vibration absorbers. *Acoustics Australia*, 36(3):98–103, 2008.
- [69] Yong Xiao, Jihong Wen, and Xisen Wen. Broadband locally resonant beams containing multiple periodic arrays of attached resonators. *Physics Letters A*, 376(16):1384–1390, 2012.
- [70] P Frank Pai, Hao Peng, and Shuyi Jiang. Acoustic metamaterial beams based on multi-frequency vibration absorbers. *International Journal of Mechanical Sciences*, 79:195–205, 2014.
- [71] Yongzhen Mi and Xiang Yu. Sound transmission of acoustic metamaterial beams with periodic inertial amplification mechanisms. *Journal of Sound and Vibration*, 499:116009, 2021.
- [72] Hui Chen, XP Li, YY Chen, and GL Huang. Wave propagation and absorption of sandwich beams containing interior dissipative multi-resonators. *Ultrasonics*, 76:99–108, 2017.

- [73] Yong Xiao, Jihong Wen, and Xisen Wen. Sound transmission loss of metamaterial-based thin plates with multiple subwavelength arrays of attached resonators. *Journal of Sound and Vibration*, 331(25):5408–5423, 2012.
- [74] M Badreddine Assouar, Matteo Senesi, Mourad Oudich, Massimo Ruzzene, and Zhilin Hou. Broadband plate-type acoustic metamaterial for low-frequency sound attenuation. *Applied Physics Letters*, 101(17):173505, 2012.
- [75] Pei Li, Shanshan Yao, Xiaoming Zhou, Guoliang Huang, and Gengkai Hu. Effective medium theory of thin-plate acoustic metamaterials. *The Journal of the Acoustical Society of America*, 135(4):1844–1852, 2014.
- [76] Ting Wang, Mei-Ping Sheng, Zhi-Wei Guo, and Qing-Hua Qin. Flexural wave suppression by an acoustic metamaterial plate. *Applied acoustics*, 114:118–124, 2016.
- [77] Linus Yinn Leng Ang, Yong Khiang Koh, and Heow Pueh Lee. Plate-type acoustic metamaterial with cavities coupled via an orifice for enhanced sound transmission loss. *Applied Physics Letters*, 112(5):051903, 2018.
- [78] Linus Yinn Leng Ang, Yong Khiang Koh, and Heow Pueh Lee. Plate-type acoustic metamaterials: Evaluation of a large-scale design adopting modularity for customizable acoustical performance. *Applied Acoustics*, 149:156–170, 2019.
- [79] Noe Jiménez, Weichun Huang, Vicent Romero-García, Vincent Pagneux, and J-P Groby. Ultra-thin metamaterial for perfect and quasi-omnidirectional sound absorption. *Applied Physics Letters*, 109(12):121902, 2016.
- [80] Chang-Lin Ding and Xiao-Peng Zhao. Multi-band and broadband acoustic metamaterial with resonant structures. *Journal of Physics D: Applied Physics*, 44(21):215402, 2011.
- [81] AI Komkin, MA Mironov, and AI Bykov. Sound absorption by a helmholtz resonator. *Acoustical Physics*, 63(4):385–392, 2017.
- [82] Sedigheh Basirjafari. Innovative solution to enhance the helmholtz resonator sound absorber in low-frequency noise by nature inspiration. *Journal of Environmental Health Science and Engineering*, 18(2):873–882, 2020.
- [83] CAI Chenzhi and Cheuk Ming Mak. Noise attenuation capacity of a helmholtz resonator. *Advances in Engineering Software*, 116:60–66, 2018.

- [84] U Ingård and RH Bolt. Absorption characteristics of acoustic material with perforated facings. *The Journal of the Acoustical Society of America*, 23(5):533–540, 1951.
- [85] LW Dean. Coupling of helmholtz resonators to improve acoustic liners for turbofan engines at low frequency. Technical report, 1975.
- [86] Keiji Oguchi and Kyoji Fujiwara. Perforated plateporous material broadband absorption system with screen strips. *J. Acoust. Soc. Jp*, 59:396–398, 2003.
- [87] Sang-Ryul Kim and Yang-Hann Kim. Absorptive characteristics of a helmholtz resonator damped by a flexible porous screen. In *Proceedings of the Korean Society for Noise and Vibration Engineering Conference*, pages 865–868. The Korean Society for Noise and Vibration Engineering, 2005.
- [88] Akira Sanada and Nobuo Tanaka. Extension of the frequency range of resonant sound absorbers using two-degree-of-freedom helmholtz-based resonators with a flexible panel. *Applied Acoustics*, 74(4):509–516, 2013.
- [89] Shahin S Nudehi, G Scott Duncan, and Umar Farooq. Modeling and experimental investigation of a helmholtz resonator with a flexible plate. *Journal of vibration and acoustics*, 135(4), 2013.
- [90] Mohammad H Kurdi, G Scott Duncan, and Shahin S Nudehi. Optimal design of a helmholtz resonator with a flexible end plate. *Journal of vibration and acoustics*, 136(3), 2014.
- [91] Karsten Knobloch, Lars Enghardt, and Friedrich Bake. Helmholtz resonator liner with flexible walls. In *2018 AIAA/CEAS Aeroacoustics Conference*, page 4102, 2018.
- [92] Fleming Kohlenberg, Anita Schulz, Lars Enghardt, and Karsten Knobloch. Modelling of acoustic liners consisting of helmholtz resonators coupled with a second cavity by flexible walls. In *28th AIAA/CEAS Aeroacoustics 2022 Conference*, page 2824, 2022.
- [93] Arthur W Leissa. *Vibration of plates*, volume 160. Scientific and Technical Information Division, National Aeronautics and Space Administration, 1969.
- [94] Felix Langfeldt, AJ Khatokar, and Wolfgang Gleine. Plate-type acoustic metamaterials with integrated helmholtz resonators. *Applied Acoustics*, 199:109019, 2022.
- [95] Moritz Neubauer, Julia Genßler, Vincent Radmann, Fleming Kohlenberg, Michael Pohl, Kurt Böhme, Karsten Knobloch, Ennes Sarradj, Klaus Höschler, Niels Modler, et al. Experimental

- and numerical investigation of novel acoustic liners and their design for aero-engine applications. *Aerospace*, 10(1):5, 2022.
- [96] Moritz Neubauer, Felix Schwaericke, Vincent Radmann, Ennes Sarradj, Niels Modler, and Martin Dannemann. Material selection process for acoustic and vibration applications using the example of a plate resonator. *Materials*, 15(8):2935, 2022.
- [97] Quin RS Miller, Satish K Nune, H Todd Schaef, Ki Won Jung, Kayte M Denslow, Matthew S Prowant, Paul F Martin, and B Peter McGrail. Microporous and flexible framework acoustic metamaterials for sound attenuation and contrast agent applications. *ACS applied materials & interfaces*, 10(51):44226–44230, 2018.
- [98] Yanni Zhang and Li Cheng. Ultra-thin and broadband low-frequency underwater acoustic meta-absorber. *International Journal of Mechanical Sciences*, 210:106732, 2021.
- [99] Xiaobin Cui, Chenkai Liu, Jinjie Shi, Changhui Shen, Xiaozhou Liu, and Yun Lai. A flexible meta-curtain for simultaneous soundproofing and ventilation. *Symmetry*, 14(11):2348, 2022.
- [100] Ryohei Tsuruta, Xiaopeng Li, Ziqi Yu, Hideo Iizuka, and Taehwa Lee. Reconfigurable acoustic absorber comprising flexible tubular resonators for broadband sound absorption. *Physical Review Applied*, 18(1):014055, 2022.
- [101] WR Kampinga, Ysbrand H Wijnant, and Andries de Boer. A finite element for viscothermal wave propagation. In *Proceedings of ISMA*, volume 2008, pages 4271–4278. Citeseer, 2008.
- [102] Lawrence E Kinsler, Austin R Frey, Alan B Coppens, and James V Sanders. *Fundamentals of acoustics*. John wiley & sons, 2000.
- [103] Abdelkrim Khelif and Ali Adibi. *Phononic Crystals*. Springer, 2016.
- [104] Peter Risby Andersen. Modelling of acoustic viscothermal losses using the boundary element method: From method to optimization. 2018.
- [105] Axel van de Walle. The power of model order reduction in vibroacoustics and its applications in model-based sensing. 2018.
- [106] John William Strutt Baron Rayleigh. *The theory of sound*, volume 1. Macmillan, 1894.
- [107] Thomas D Rossing. Chladni law for vibrating plates. *American Journal of Physics*, 50(3): 271–274, 1982.

- [108] S Timoshenko, W Weaver, and D Young. Vibration problems in engineering. c 1928, 1937, by d, 1928.
- [109] Richard Vynne Southwell. On the free transverse vibrations of a uniform circular disc clamped at its centre; and on the effects of rotation. *Proceedings of the Royal Society of London. Series A, Containing Papers of a Mathematical and Physical Character*, 101(709):133–153, 1922.
- [110] RC Colwell and HC Hardy. Lxxxix. the frequencies and nodal systems of circular plates. *The London, Edinburgh, and Dublin Philosophical Magazine and Journal of Science*, 24(165): 1041–1055, 1937.
- [111] Hsin-Yuan Chiang and Yu-Hsi Huang. Resonance mode and sound pressure produced by circular diaphragms of electrostatic and piezoelectric speakers. *Applied Acoustics*, 129:365–378, 2018.
- [112] M Amabili, A Pasqualini, and G Dalpiaz. Natural frequencies and modes of free-edge circular plates vibrating in vacuum or in contact with liquid. *Journal of sound and vibration*, 188(5): 685–699, 1995.
- [113] S Timoshenko. Vibration problems in engineering, second edition. *Professor of the Stanford University, USA, D. van Nostrand Company Inc., New York, USA*, 1937.
- [114] SM Vogel and DW Skinner. Natural frequencies of transversely vibrating uniform annular plates. 1965.
- [115] K Itao and SH Crandall. Natural modes and natural frequencies of uniform, circular, free-edge plates. 1979.
- [116] John R Airey. The vibrations of circular plates and their relation to bessel functions. *Proceedings of the Physical Society of London (1874-1925)*, 23(1):225, 1910.
- [117] NW McLachlan. The accession to inertia of flexible discs vibrating in a fluid. *Proceedings of the Physical Society (1926-1948)*, 44(5):546, 1932.
- [118] MK Kwak and KC Kim. Axisymmetric vibration of circular plates in contact with fluid. *Journal of Sound and Vibration*, 146(3):381–389, 1991.
- [119] M Amabili, G Frosali, and MK Kwak. Free vibrations of annular plates coupled with fluids. *Journal of sound and vibration*, 191(5):825–846, 1996.

- [120] Thomas Geertruida Henricus Basten. *Noise reduction by viscothermal acousto-elastic interaction in double wall panels*. Universiteit Twente, Enschede, The Netherlands, 2001.
- [121] Willem Marinus Beltman. Viscothermal wave propagation including acousto-elastic interaction. *PhD The*, 1998.
- [122] MJH Fox and PN Whitton. The damping of structural vibration by thin gas films. *Journal of Sound and Vibration*, 73(2):279–295, 1980.
- [123] M Bruneau, Ph Herzog, J Kergomard, and JD Polack. General formulation of the dispersion equation in bounded visco-thermal fluid, and application to some simple geometries. *Wave motion*, 11(5):441–451, 1989.
- [124] Minivalve international, 2018. URL <http://www.minivalve.com/newsite/index.php/en/home>. Accessed = 2017-11-30.
- [125] Matteo Da Ponte. *A Novel Acoustic Liner Design*. Master’s thesis, Trinity College Dublin, Dept. of Mechanical and Manufacturing Engineering, 2018.
- [126] Luis Suárez and María del Mar Espinosa. Assessment on the use of additive manufacturing technologies for acoustic applications. *The International Journal of Advanced Manufacturing Technology*, 109(9):2691–2705, 2020.
- [127] A Fl Seybert and D Fl Ross. Experimental determination of acoustic properties using a two-microphone random-excitation technique. *the Journal of the Acoustical Society of America*, 61(5):1362–1370, 1977.
- [128] JY Chung and DA Blaser. Transfer function method of measuring in-duct acoustic properties. ii. experiment. *The Journal of the Acoustical Society of America*, 68(3):914–921, 1980.
- [129] Kang Hou and J Stuart Bolton. Calibration methods for four-microphone standing wave tubes. In *INTER-NOISE and NOISE-CON Congress and Conference Proceedings*, volume 2008, pages 1012–1020. Institute of Noise Control Engineering, 2008.
- [130] Bryan H Song and J Stuart Bolton. A transfer-matrix approach for estimating the characteristic impedance and wave numbers of limp and rigid porous materials. *The Journal of the Acoustical Society of America*, 107(3):1131–1152, 2000.

- [131] T Iwase, Y Izumi, and R Kawabata. A new measuring method for sound propagation constant by using sound tube without any air spaces back of a test material. In *INTER-NOISE and NOISE-CON Congress and Conference Proceedings*, volume 1998, pages 1265–1268. Institute of Noise Control Engineering, 1998.
- [132] Seung-Ho Jang and Jeong-Guon Ih. On the multiple microphone method for measuring in-duct acoustic properties in the presence of mean flow. *The journal of the acoustical society of America*, 103(3):1520–1526, 1998.
- [133] Y Aurégan and M Leroux. Failures in the discrete models for flow duct with perforations: an experimental investigation. *Journal of Sound and Vibration*, 265(1):109–121, 2003.
- [134] Mathew G Pelletier, Greg A Holt, and John D Wanjura. Simplified three-microphone acoustic test method. *Instruments*, 1(1):4, 2017.
- [135] BS EN ISO 15034-2:2001. Acoustics - Determination of sound absorption coefficient and impedance in impedance tubes - Part 2: Transfer-function method. Technical Standard BS EN ISO 15034-2:2001, British Standard, April 2002.
- [136] ASTM E2611-09. Standard Test Method for Measurement of Normal Incidence Sound Transmission of Acoustical Materials Based on the Transfer Matrix Method. Technical Report ASTM E2611-09, ASTM International, 2009.
- [137] Andrew McKay. Sound Transmission Loss Measurements of Thixotropic Materials. Technical report, October 2017.
- [138] Anthony B Stanbridge, David J Ewins, and AZ Khan. Modal testing using impact excitation and a scanning ldv. *Shock and Vibration*, 7(2):91–100, 2000.
- [139] Júlio M Montalvão e Silva and Nuno MM Maia. *Modal analysis and testing*, volume 363. Springer Science & Business Media, 2012.
- [140] Jenna Gietl, Joseph Vignola, John Sterling, and Teresa Ryan. Characterization of damping properties in 3d printed structures. In *Journal of Physics: Conference Series*, volume 1149, page 012002. IOP Publishing, 2018.
- [141] SM Mirkhalaf and M Fagerström. The mechanical behavior of polylactic acid (pla) films: fabrication, experiments and modelling. *Mechanics of Time-Dependent Materials*, 25(2):119–131, 2021.

- [142] K Arunprasath, M Vijayakumar, M Ramarao, TG Arul, S Peniel Pauldoss, M Selwin, B Radhakrishnan, and V Manikandan. Dynamic mechanical analysis performance of pure 3d printed polylactic acid (pla) and acrylonitrile butadiene styrene (abs). *Materials Today: Proceedings*, 50:1559–1562, 2022.
- [143] Zhengning Li, Ge Chen, Haichen Lyu, and Frank Ko. Experimental investigation of compression properties of composites with printed braiding structure. *Materials*, 11(9):1767, 2018.
- [144] R Bossart, N Joly, and M Bruneau. Hybrid numerical and analytical solutions for acoustic boundary problems in thermo-viscous fluids. *Journal of Sound and Vibration*, 263(1):69–84, 2003.
- [145] COMSOL Multiphysics Inc. Acoustics module user’s guide, 2022. URL <https://www.comsol.com/>. Accessed = 2023-03-30.
- [146] RW Guy and MC Bhattacharya. The transmission of sound through a cavity-backed finite plate. *Journal of Sound and Vibration*, 27(2):207–223, 1973.
- [147] Jie Pan and David Alan Bies. The effect of fluid–structural coupling on sound waves in an enclosure theoretical part. *The Journal of the Acoustical Society of America*, 87(2):691–707, 1990.
- [148] Jie Pan and David Alan Bies. The effect of fluid–structural coupling on sound waves in an enclosure experimental part. *The Journal of the Acoustical Society of America*, 87(2):708–717, 1990.
- [149] Daniel G Gorman, JM Reese, J Horacek, and K Dedouch. Vibration analysis of a circular disc backed by a cylindrical cavity. *Proceedings of the Institution of Mechanical Engineers, Part C: Journal of Mechanical Engineering Science*, 215(11):1303–1311, 2001.
- [150] DG Gorman, CK Lee, JM Reese, and J Horáček. Vibration analysis of a thin circular plate influenced by liquid/gas interaction in a cylindrical cavity. *Journal of sound and vibration*, 279(3-5):601–618, 2005.
- [151] C Rajalingham, RB Bhat, and GD Xistris. Vibration of circular membrane backed by cylindrical cavity. *International journal of mechanical sciences*, 40(8):723–734, 1998.

- [152] Li Yuanqi, Lei Wang, Zuyan Shen, and Yukio Tamura. Added-mass estimation of flat membranes vibrating in still air. *Journal of Wind Engineering and Industrial Aerodynamics*, 99(8): 815–824, 2011.
- [153] Haijun Liu, Douglas A Olson, and Miao Yu. Modeling of an air-backed diaphragm in dynamic pressure sensors: Effects of the air cavity. *Journal of Sound and Vibration*, 333(25):7051–7075, 2014.
- [154] Alexandre Presas, David Valentin, Eduard Egusquiza, Carme Valero, Mònica Egusquiza, and Matias Bossio. Accurate determination of the frequency response function of submerged and confined structures by using pzt-patches. *Sensors*, 17(3):660, 2017.
- [155] Jean Allard and Noureddine Atalla. *Propagation of sound in porous media: modelling sound absorbing materials*. John Wiley & Sons, 2009.
- [156] Md. Robiul Hossain and Gareth J. Bennett. Acoustic plate-valve resonator for low-frequency sound absorption. *AIP Advances*, 2023.
- [157] A Kaczmarek, L Javorek, and K Orłowski. Mode vibrations of plates-experimental analysis. *Annals of Warsaw University of Life Sciences-SGGW. Forestry and Wood Technology*, 88, 2014.
- [158] Kerem Ege, Xavier Boutillon, and Bertrand David. High-resolution modal analysis. *Journal of sound and vibration*, 325(4-5):852–869, 2009.
- [159] Yong-xin Gao, Yuan-peng Lin, Yi-fan Zhu, Bin Liang, Jing Yang, Jun Yang, and Jian-chun Cheng. Broadband thin sound absorber based on hybrid labyrinthine metastructures with optimally designed parameters. *Scientific Reports*, 10(1):10705, 2020.
- [160] Alexa M Melvin and Thomas J Roussel. Modeling 3d printed check valves for microfluidic systems. In *2018 IEEE International Symposium on Signal Processing and Information Technology (ISSPIT)*, pages 179–184. IEEE, 2018.
- [161] [] COMSOL AB. Structural mechanics module users guide, 2022. URL <https://www.comsol.com/>. Accessed = 2022-06-30.
- [162] Yusuf Özyörük, Lyle N Long, and Michael G Jones. Time-domain numerical simulation of a flow-impedance tube. *Journal of Computational Physics*, 146(1):29–57, 1998.

- [163] Christopher KW Tam, Hongbin Ju, Michael G Jones, Willie R Watson, and Tony L Parrott. A computational and experimental study of slit resonators. *Journal of Sound and Vibration*, 284(3-5):947–984, 2005.
- [164] C Cai, KC Hung, and MS Khan. Simulation-based analysis of acoustic absorbent lining subject to normal plane wave incidence. *Journal of Sound and Vibration*, 291(3-5):656–680, 2006.
- [165] Pierre A Deymier. *Acoustic metamaterials and phononic crystals*, volume 173. Springer Science & Business Media, 2013.
- [166] Wenjiong Chen, Shutian Liu, Liyong Tong, and Sheng Li. Design of multi-layered porous fibrous metals for optimal sound absorption in the low frequency range. *Theoretical and Applied Mechanics Letters*, 6(1):42–48, 2016.

Appendix A

A.1 Paper

Acoustic plate-valve resonator for low-frequency sound absorption

Cite as: AIP Advances 13, 065210 (2023); doi: 10.1063/5.0142908

Submitted: 15 March 2023 • Accepted: 19 May 2023 •

Published Online: 6 June 2023



Md Robiul Hossain, , Eoghan P. Ross, , and Gareth J. Bennett^{a)} 

AFFILIATIONS

Trinity College Dublin, The University of Dublin, Dublin D02 PN40, Ireland

^{a)} Author to whom correspondence should be addressed: gareth.bennett@tcd.ie

ABSTRACT

An acoustic plate-valve resonator is developed and optimized to maximize absorption by enhancing the Helmholtz resonance with coincident structural vibrations of the plate-valve. The current research initially examines the concept experimentally with a 3D printed valve. Then with the use of analytical and numerical modeling, a structural analysis is performed, which allows the eigenmodes and eigenfrequencies of the plate-valve to be determined. When the resonator properties are modified by changing either the depth of the backing cavity or the thickness of the plate-valve, the system can be designed in such a way that the Helmholtz resonance can be coincident with a particular eigenfrequency, leading to absorption higher than that achieved in the absence of such a flexible plate-valve. In addition, absorption also occurs at frequencies other than the Helmholtz frequency due to the vibration of the plate at additional eigenfrequencies. Both of these aspects of the technology advance the state-of-the-art in Helmholtz resonator design. Good agreement has been found between the modeling and experimental results. Near-perfect absorption was achieved experimentally, e.g., up to $\alpha = 0.995$ below 1 kHz; in addition, given that the thickness of the technology can be a very small percentage of the acoustic wavelength that it is absorbing, deep sub-wavelength ratio absorbers can be designed, e.g., a ratio of up to 58 was achieved in this study with a 5 mm deep technology at 1.18 kHz.

© 2023 Author(s). All article content, except where otherwise noted, is licensed under a Creative Commons Attribution (CC BY) license (<http://creativecommons.org/licenses/by/4.0/>). <https://doi.org/10.1063/5.0142908>

I. INTRODUCTION

Noise is an alarming concern due to its harmful effects on the environment, health, and the quality of human life. Growing urban population leads to growth in the construction of buildings and private or public transportation systems. The aviation industry has also seen dramatic growth over the last 20 years, with passenger numbers increasing from 1.5×10^9 in 1998 to 4×10^9 in 2017. People who live in the vicinity of major airports experience considerable amounts of sound pollution. Exposure to loud noise increases the risk of developing several adverse health conditions such as high blood pressure, hypertension, fatigue, stress, coronary heart diseases, etc.¹ Sleep disturbance due to noise pollution also leads to reduced work and school performance, hence making it vital to eliminate this undesired noise.

Traditional natural porous materials such as wool and cotton as well as synthetic glass fiber and melamine foams have been used for noise reduction for many years. However, these materials are effective only at reducing high-frequency noise at reasonable

thicknesses. According to the mass density law, a thicker porous material is required to attenuate low-frequency noise. Adding mass and increasing thicknesses (which can equate to reducing useful space) are to be avoided in the construction of buildings and factories where people can be exposed to noise. With regard to transportation noise, both weight and space are critical parameters, which need to be minimized in order to reduce fuel consumption and the associated environmental cost.^{2,3} Although composite structures such as perforated absorbers, acoustic mufflers, double walls with cladding, etc., have been used in rooms, auditoriums, offices, aircraft fuselages, cars, trains, etc., to attenuate low-frequency noise, the attenuation of low-frequency noise in a thin form factor still remains an intractable challenge.

Since the early 2000s, research in the field of acoustic metamaterials (AMMs) has expanded considerably with respect to the application of low-frequency noise reduction. Originating in the fields of electromagnetics and optics, the extension of research to acoustic metamaterials has led to this nascent research activity in acoustics, which has tremendous potential for the development

of fundamental science and for revolutionary technological breakthroughs. Acoustic metamaterials are artificial structures that are periodic in nature and that often involve local resonators designed to resonate at specific frequencies, rendering them, therefore, often tonal or highly narrow band in nature.

Traditionally, micro-perforated panel absorbers (MPPA) have been used for broadband sound absorption, but these typically only work in mid- to high-frequency ranges. Some AMM research has been reported for low-frequency sound absorption. Mei *et al.*⁴ demonstrated a membrane plate system for low-frequency absorption as low as 164 Hz. Subsequently, Li *et al.*⁵ proposed a metasurface-based structure that can absorb the incident acoustic energy at a low-frequency of around 125 Hz. Their structures are composed of a perforated plate and a labyrinthine structure. They also presented extremely low-frequency absorption (around 50 Hz) with a multi-coiled metasurface⁶ and broadband sound absorption in the frequency ranges of 460–972 Hz and 232–494 Hz with supercell-based acoustic metasurface coiled absorbers.⁷ Lee *et al.*,⁸ Wang *et al.*,⁹ Temiz *et al.*,¹⁰ and Martincic *et al.*¹¹ studied the MPP-based low-frequency absorber including the vibro-acoustic and panel vibration effect of the structure. McKay *et al.*¹² very successfully developed a novel low-frequency broadband sound absorber, called a SeMSA, by combining decorated membranes and micro-perforated plates, and Davis *et al.*¹³ used graph theory based on a two point impedance method to optimize a multi-chamber SeMSA, which resulted in a very broadband low-frequency absorption response or even an absorption response tailored for fan noise. Killeen *et al.*¹⁴ applied the SeMSA to reduce the fan-noise of data-center telecommunications' server racks, which is particularly challenging as it is a grazing acoustic and grazing flow boundary condition. Wang and Bennett¹⁵ applied the two point impedance method to optimize a multi-chamber MPPA, which has resulted in a very broadband low frequency absorber.

In the literature, AMMs typically comprised an inhomogeneous technology where components are directly connected to one another. Some exceptions to this are cited here where the motion of a cantilever beam absorbs sound through the resultant micro-slits. Farooqui and Aurégan¹⁶ and D'elia *et al.*¹⁷ proposed a numerical and analytical model for a structure composed of a flexible cantilever beam producing acoustic micro-slits with a compact cavity and demonstrating attenuation around 500 Hz with a 3 cm cavity depth. Aurégan and Farooqui¹⁸ developed a sub-wavelength acoustic absorber using an MPP-based thin flexible beam with micro-slits for perfect sound absorption in the mid-frequency range.

In the current work, the concept of an acoustic plate-valve design has been developed based on the promising preliminary investigations of off-the-shelf elastomeric valves,¹⁹ which are used as one-way valves in fluidic-control. As is well understood, the standard Helmholtz resonator consists of a rigid volume with an orifice, which is stationary. In this work, a Helmholtz resonator has been developed, which has an unusual plate-valve located at the opening. The plate-valve is flexible with the capacity to vibrate at its natural frequencies. When the resonator properties are modified by either changing the depth of the backing cavity or the thickness of the plate-valve, the system can be designed in such a way that the Helmholtz resonance can be coincident with a particular eigenfrequency, leading to absorption higher than that achieved in the absence of such a flexible plate-valve.

II. ACOUSTIC PLATE-VALVE METAMATERIAL DESIGN AND FABRICATION

Further to the work of Bennett *et al.*¹⁹ discussed in the introduction, testing has been performed using 3D printed valves similar to one of the original elastomeric umbrella valves¹⁹ but of a much larger diameter, $\phi_{APV} = 124$ mm, with a thickness of $t_{APV} = 0.5$ mm, as shown in Fig. 1. The diameter of 124 mm was chosen to maximize the size of the plate-valve when measured in a cylindrical impedance tube of 127 mm diameter, but by allowing for a gap of 1.5 mm between the outer diameter of the plate-valve and the inner diameter of the tube, local edge viscous losses are minimized, focusing the attention of the study on the interaction between the plate-valve and the mounting plate.

This one-way valve was manufactured with an Ultimaker-3 FDM 3D printer using a print layer resolution of 0.15 mm. The Ultimaker-3 was chosen as it has two printer heads, which enable printing with two different materials at the same time. In this case, a polylactic acid (PLA) was chosen as the main material of the plate-valve while water-soluble polyvinyl alcohol (PVA) was used as the support scaffolding. By using a water-soluble PVA, the scaffolding is more easily and completely removed, resulting in a more accurate shape and a better surface finish.

Figure 2 shows the one-way valve examined in this current research along with its mounting plate. The mounting plate was manufactured using aluminum and is 5.8 mm thick. Similar to the spacer plates used in the impedance tube, see Fig. 14, it is square, 200×200 mm², and designed to have a sliding fit inside the square test section. Its hole is designed to provide maximum open area while allowing an overlap of 8 mm with the plate-valve, see Fig. 1(c). Due to the need to mount the plate-valve on the plate, two narrow ribs are required, so the opening is not complete, see Fig. 2(d). The plate-valve was designed with a central strut, which allows for a simple push-and-twist installation process into the mounting plate. The length of the strut was designed in such a way that the plate-valve is in contact with the mounting plate around its perimeter once installed.

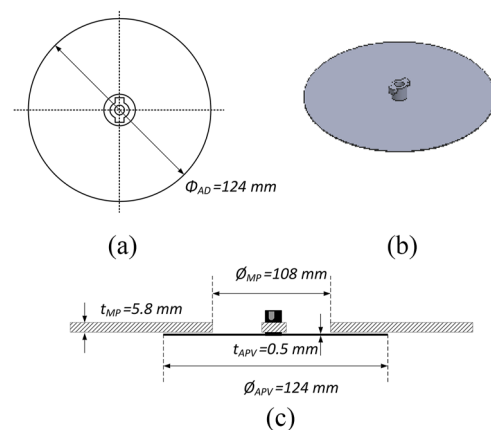


FIG. 1. Nominal geometric parameters of the acoustic plate-valve. (a) Plan view. (b) CAD design. (c) Elevation view.

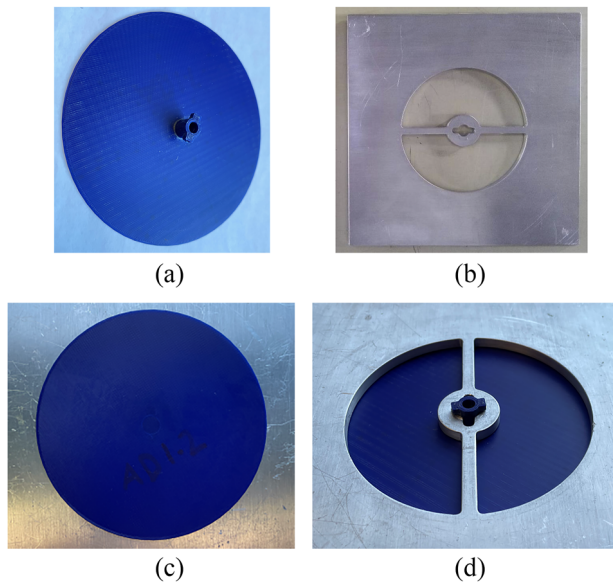


FIG. 2. 3D printed acoustic plate-valve sample and the mounting plate. (a) 3D printed acoustic plate-valve sample. (b) Mounting plate for acoustic plate-valve. (c) Mounted 3D printed acoustic plate-valve sample (Top view). (d) Mounted 3D printed acoustic plate-valve sample (Bottom view)

Although the designed thickness of the valve was 0.5 mm, the printed sample had a slightly non-uniform thickness over the surface area. The average thickness was measured to be 0.52 mm using a micrometer calipers. The value of 0.52 mm was subsequently used for the numerical and analytical analysis.

III. RESULTS AND DISCUSSION

In this section, analytical, experimental, and numerical results are presented as a function of the cavity depth, material properties, and plate thickness.

Figure 3 provides some initial baseline results. The absorption coefficient was measured experimentally for an empty tube, and then with the mounting plate installed but without the acoustic plate-valve, see Fig. 2(b). In both cases, there was a 40 mm cavity depth. The empty tube, as expected, results in effectively zero absorption (full reflection), demonstrating the correct functioning of the rig and methods. The frequency domain numerical solution provides an identical result, demonstrating the correct functioning of the numerical model. When the mounting plate is inserted, it results in non-zero absorption, with the numerical and experimental results in close agreement. Some losses are assumed to occur due to acoustic velocity flow around the edges of the mounting plate, but as the value of absorption is less than 0.1 in the frequency range, it is assumed from here on that the mounting plate itself has little effect on the absorption coefficient.

Figure 4 shows the absorption coefficient when the acoustic plate-valve is inserted with a very shallow 5 mm cavity depth. The numerical result shows two relatively wideband peaks with very high absorption coefficients, the first being at 1140 Hz and the second at 1460 Hz. The experimental result is again in very close agreement with a slight frequency shift at the lower frequency, but also to be noted are indications of other peaks not found in the numerical result. This will be discussed further in the paper. A very significant result for this configuration is that the lower frequency peak has perfect absorption experimentally at a cavity depth of only 5 mm. This means for a frequency of 1184 Hz, which has a wavelength of 0.29 m, the acoustic plate-valve technology is deeply sub-wavelength with perfect absorption at a depth-to-wavelength ratio of 58.

Figure 5 shows the comparison of the experimental and numerical absorption coefficients for the acoustic plate-valve with differing cavity depths: 10, 20, 30, and 40 mm. The absorption coefficient for the numerical main peaks seems to monotonically decrease whereas for the experimental results, the absorption coefficient is higher for the 40 mm cavity depth than for the 30 mm cavity depth. This point will also be further investigated in the paper. Examining the general results for the absorption coefficient for the acoustic plate-valves now, we see that the results are extremely good, with the numerical

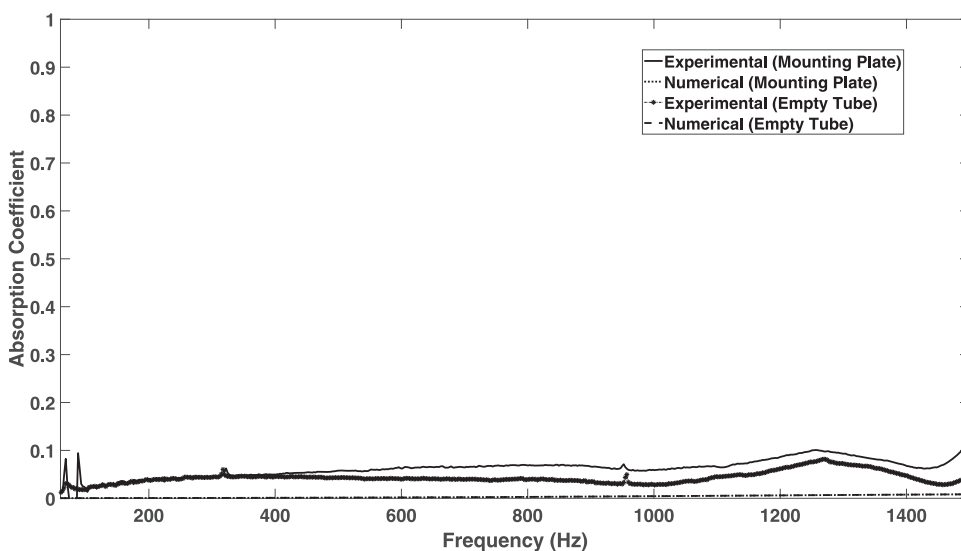


FIG. 3. Absorption coefficient for the mounting plate only with no acoustic plate-valve. 40 mm cavity depth.

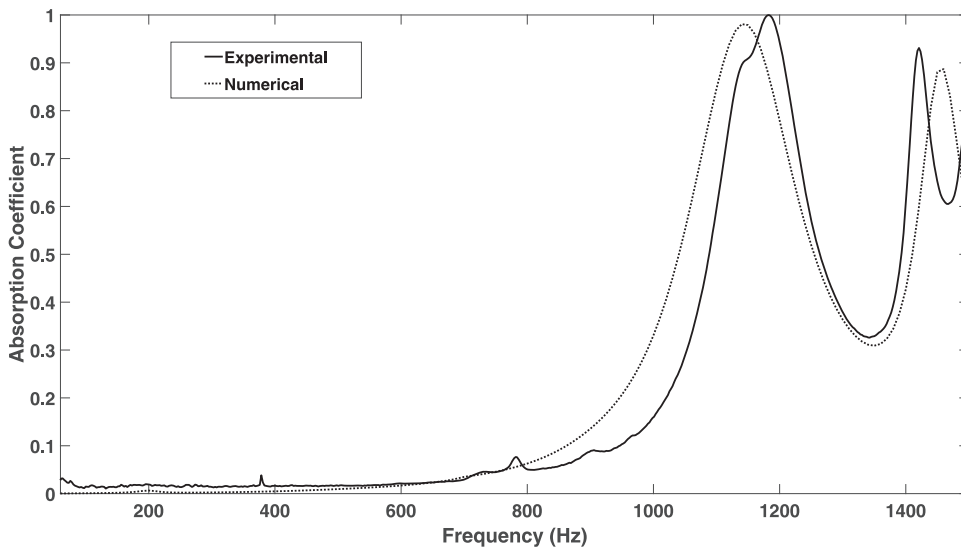


FIG. 4. Absorption coefficient for 5 mm cavity depth.

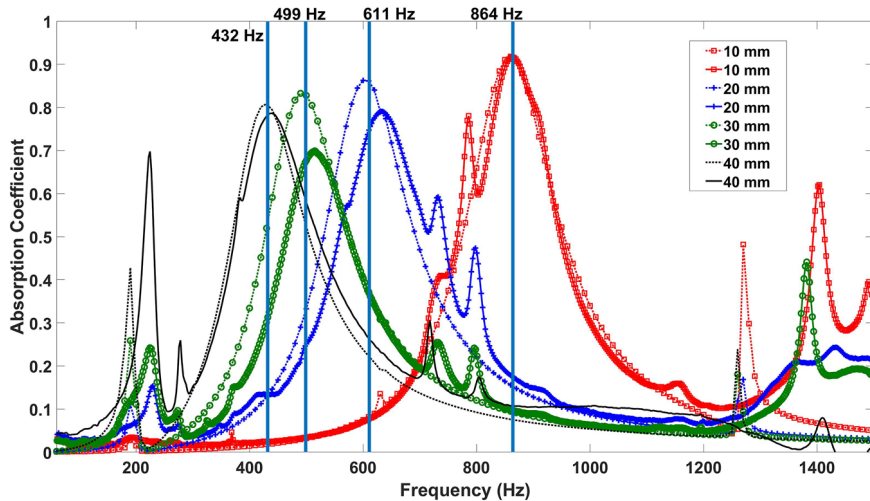


FIG. 5. Absorption coefficient for 10, 20, 30, and 40 mm cavity depths. Solid line: experimental. Dotted line: numerical.

and experimental results agreeing well with each other. By increasing the depth of the cavity, lower frequencies can be attenuated, and although the magnitude of absorption decreases with frequency, it remains quite high.

A. Helmholtz resonance of the acoustic plate-valve metasurface

With regard to the frequency at which the main peak occurs in Fig. 5, there seems to be a non-linear relationship between the depth and the frequency. This behavior allows us to identify the main peak as resulting from a Helmholtz resonance. Through observation of the standard Helmholtz equation,

$$f_{HR} = \frac{c_0}{2\pi} \sqrt{\frac{S_n}{L_n V_c}}, \quad (1)$$

where L_n and S_n are the neck's effective length and area, respectively, and V_c is the effective cavity volume, we can see that when the depth of the back-cavity is doubled, the frequency of the main peak decreases by $\frac{1}{\sqrt{2}}$. The frequencies of peak absorption from the numerical analysis shown in Fig. 5 are 860, 600, 490, and 430 Hz. As an example, 600 Hz is very close to $\frac{860}{\sqrt{2}}$, and 430 Hz is very close to $\frac{600}{\sqrt{2}}$; it is reasonable to deduce that these main peaks result from a Helmholtz resonance where the neck is the circumferential gap between the plate-valve and the mounting plate. Unlike typical Helmholtz resonators, the orifice here is not a single hole whose axis is parallel to that of the cavity, but rather it is a circular gap whose axis is perpendicular. In addition, due to the fact that the plate-valve vibrates, which causes the gap to change over time and is a function of radius, the geometry of the neck is less straightforward to determine.

To try and understand the underlying mechanism of Helmholtz resonance in the acoustic plate-valve configuration, the geometry is

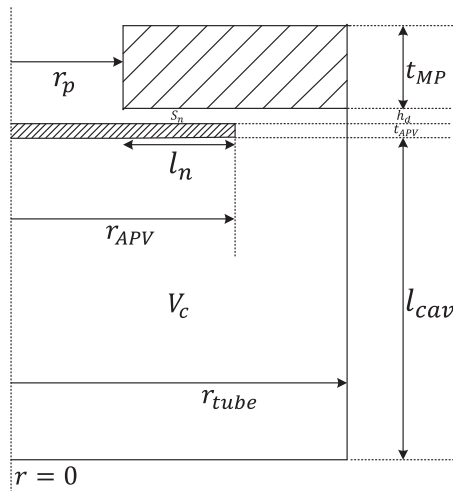


FIG. 6. Axisymmetric schematic of the acoustic plate-valve and cavity.

TABLE I. Parameters and values of the terms shown in Fig. 6.

Geometric parameter	Symbol	Value (mm)
Mounting plate hole radius	r_p	54
Acoustic plate-valve radius	r_{APV}	62
Impedance tube inner radius	r_{tube}	63.5
Neck nominal length	l_n	8
Mounting plate thickness	t_{MP}	5.8
Nominal gap	h_d	0.4
Plate thickness	t_{APV}	0.52
Cavity depth	l_{cav}	5–40

examined as shown in Fig. 6, which is considered to be axisymmetric around its axis at $r = 0$. This assumption ignores the effect, if any, of the presence of the mounting plate ribs, as seen in Fig. 2(b). The definition and value of the terms are provided in Table I.

The nominal neck length is considered to be the overlap of the plate-valve over the mounting plate, l_n , and the volume of the cavity,

V_c , is straightforward to calculate. However, the area of the neck is complicated by the fact that the radius at the beginning of the neck, r_p , is different from that at its end, r_{APV} . A reasonable approximation is to calculate the area as $2\pi r_{av} h_d$, where $r_{av} = (r_p + r_{APV})/2$. Using these values and the same value for the air gap as used in the numerical analysis (see Appendix A 2), $h_d = 0.4$ mm, the analytical results calculated using Eq. (1) are compared to those calculated by the experiments and the numerical analysis and are shown in Table II. However, it can be seen that the analytical results shown in column 4 underestimate both the experimental and numerical values.

To gain further insight, an additional numerical analysis of the system was performed, but in this case, the plate valve was held fixed and rigid and was not allowed to vibrate. For the initial analysis, where the same value of the air gap is used for the rigid plate, $h_d = 0.4$ mm, the Helmholtz frequencies were significantly different. This highlights the fact that the physics of the systems with flexible and rigid plates are different. The analysis was then repeated until a gap was found, which gave the same Helmholtz peak frequencies as for the flexible plate case. These values are tabulated in column 5 of Table II, and the absorption curve spectra are provided in Fig. 7. The gap value, which provided the same Helmholtz peak frequencies, was found to be much greater at $h_d = 1.3$ mm. The observation here is that a flexible plate valve behaves as a rigid plate resonator with a larger gap but only from a Helmholtz frequency perspective. It can be observed that the absorption magnitudes of the flexible acoustic plate-valve resonator are greater at the Helmholtz peak frequencies. In addition, the additional high absorption peaks seen in Fig. 5 are not present when the plate valve is rigid. Both of these facts demonstrate the benefit of making the plate flexible.

Furthermore, the acoustic particle velocity in the vicinity of the air gap was examined for the rigid plate case. An example of this is provided in Fig. 8. It is clear in this figure that the viscous boundary layer is not confined to the air gap alone, but, as is commonly observed in ducts, effects continue into the field at both ends. This implies that end corrections to the term l_n as a function of gap size must be implemented into the analytical analysis. Once the effective length of the neck is increased to accommodate for the end corrections, we see in column 6 of Table II that the same peak frequencies can be correctly modeled.

Further research must be undertaken to determine a means to estimate the effective average gap, but in this study, it seems clear that the principal absorption peak that varies with the cavity depth is due to Helmholtz resonance.

TABLE II. Helmholtz frequencies as a function of backing cavity depths.

Cavity depth l_{cav} (mm)	Experimental <i>flex.</i> f_{HR} (Hz)	Numerical <i>flex.</i> ($h_d = 0.4$ mm) f_{HR} (Hz)	Analytical <i>flex.</i> ($h_d = 0.4$ mm) f_{HR} (Hz)	Numerical <i>rigid</i> ($h_d = 1.3$ mm) f_{HR} (Hz)	Analytical <i>rigid end correction</i> ($h_d = 1.3$ mm)
40	439	430	328	427	432
30	515	490	379	496	499
20	634	600	465	613	611
10	861	860	657	861	864

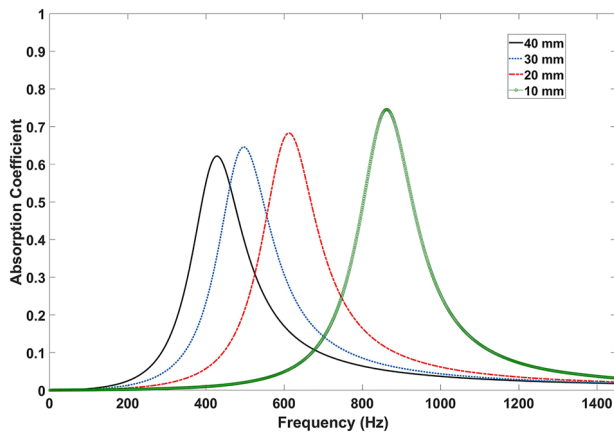


FIG. 7. Absorption coefficient for 10, 20, 30, and 40 mm cavity depths. Numerical solution for a rigid plate that does not vibrate. $h_d = 1.3$ mm.

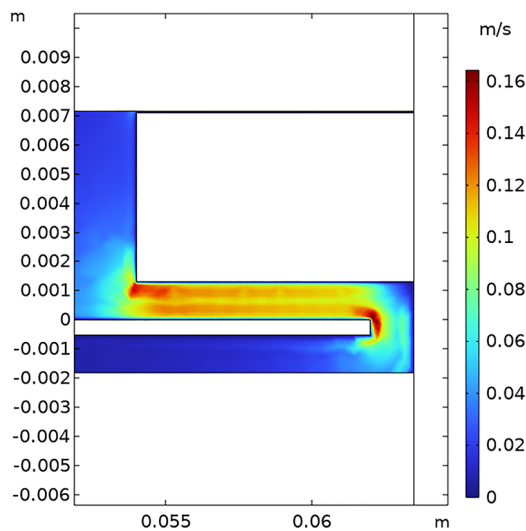
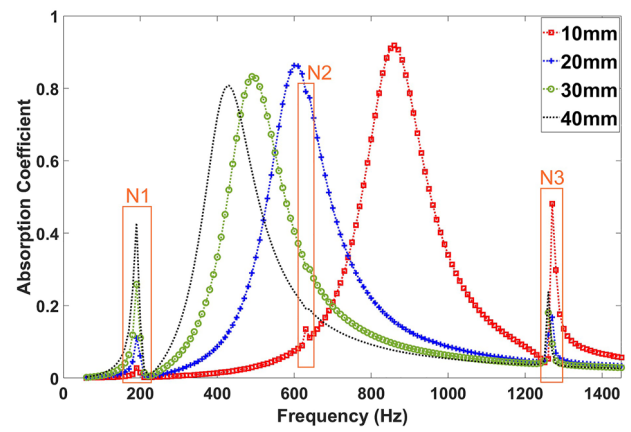


FIG. 8. Particle velocity in the vicinity of the air gap from a 2D axisymmetric FEM simulation. Numerical solution for a rigid plate that does not vibrate. $l_{cav} = 40$ mm; $h_d = 1.3$ mm.

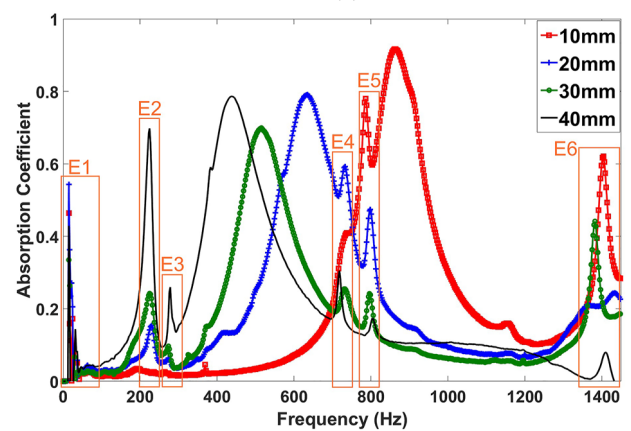
B. Vibrational analysis of the acoustic plate-valve

In Fig. 5, we saw high absorption from the acoustic plate-valve at the Helmholtz frequency and good agreement between experimental and numerical results in the Helmholtz frequency range for the 10 and 40 mm cavity depths. There are small discrepancies in amplitude and frequency for the 20 and 30 mm deep cavities.

In addition to the acoustic plate-valve providing high absorption at the Helmholtz frequencies, we can also see absorption peaks at other frequencies. Figure 9 separates out Fig. 5 into the numerical and experimental results for clarity. In Fig. 9(a), it is clear that there are three frequency ranges—N1, N2, and N3—where for each of the cavity depths, there are absorption peaks that do not vary with depth. These are considered to be associated with structural



(a)



(b)

FIG. 9. Acoustic plate-valve absorption results as a function of cavity depth. (a) Numerical results. (b) Experimental results.

vibrational modes of the flexible acoustic plate-valve whose frequencies are more a function of material properties than of cavity depth. The peaks in the N2 range tend to be masked by the Helmholtz curves, whereas for the N1 and N3 frequency ranges, the peaks increase in magnitude as the Helmholtz peaks approach them in frequency.

In Fig. 9(b), we see that in the experimental results, additional absorption peaks associated with vibrational modes are present. This can be explained by the fact that the frequency domain numerical solution is an axisymmetric analysis, and thus, only radial nodes for the axisymmetric zeroth azimuthal mode, i.e., $A_{(m,n)} = A_{(0,n)}$, can be resolved. For the inherently 3D experimental results, as can be assumed at this point, all vibrational modes can be excited to different degrees of amplitude response.

It is clear that, while there is a similarity in frequency between the vibrational peaks in both the experimental and numerical results, the exact frequencies and amplitudes are not the same. A short study was conducted, as shown in Fig. 10, where the material properties of the PLA were altered from the values used. The values of ρ , E , ν , and η were varied for $l_{cav} = 40$ mm to $\rho = 1240$ kg m⁻³, $E = 3.8 \times 10^9$ Pa,

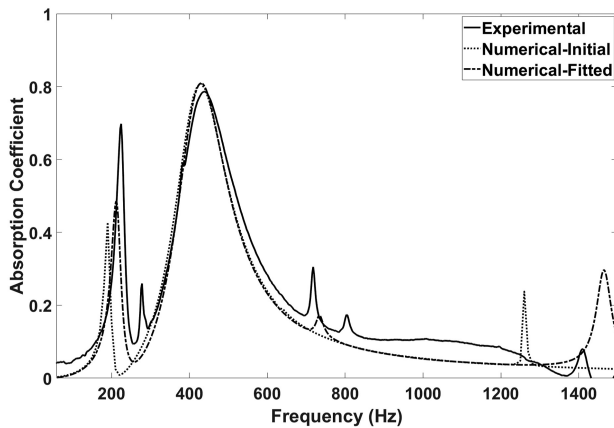


FIG. 10. Comparison of the absorption response when the material properties in the numerical model are altered. 40 mm cavity depth.

$\nu = 0.33$, and $\eta = 0.03$ as opposed to the results shown in Appendix A 2. Through observation of Fig. 10, it can be seen that the vibrational peaks are sensitive to these material property parameters whereas the Helmholtz frequency remains unchanged. The frequencies and amplitudes have increased, and a peak at ~ 750 Hz has now appeared where there was none before.

Referring back to Fig. 9, it is plausible to think that the numerical peaks at N1 correspond to either E2 or E3, those at N2 correspond to either E4 or E5, and those at N3 correspond to E6.

1. Analytical and numerical eigenfrequency analysis

To gain further insight into the nature of the vibrational modes responsible for these absorption peaks, analytical models from the literature have been examined. For analytical modeling, the acoustic plate-valve can be considered as a thin circular plate. The eigenfrequencies of a thin circular plate ($t_{APV} \ll r_{APV}$) are given by Chiang and Huang²⁰ in the following equation:

$$f_{mn} = \frac{\lambda_{mn}^2}{2\pi r_{APV}^2} \sqrt{\frac{D}{\rho t_{APV}}}, \quad (2)$$

with

$$D = \frac{Et_{APV}^3}{12(1-\nu^2)}, \quad (3)$$

where D is the flexural rigidity. The parameter λ_{mn} can vary to represent the eigenvalues of specific particular boundary conditions (e.g., free, clamped all around, simply supported, centrally clamped free edge, etc.). The calculated eigenvalues for different boundary conditions for a thin plate are provided by Timoshenko *et al.*,²¹ Southwell,²² and Colwell and Hardy²³ and are well documented by Leissa.²⁴ For example, if we consider the symmetric mode $A_{(m,n)}$ where $m = 0$, $n = 1, 2, 3, \dots$, and $\nu = 0.33$ for a completely free plate, the analytical eigenvalues are calculated to be $\lambda_{0n} = 3.014, 6.209, 9.370, 12.53, \dots$ ²⁴ Table III shows the first four analytical eigenfrequencies of a completely free thin circular plate.

In addition, a vibrational (eigenfrequency) analysis of the same free thin circular plate was conducted in COMSOL. The medium is

TABLE III. Eigenfrequencies of a completely free thin circular plate in vacuum.

Analytical f_{0n} (Hz)	Numerical eigenfrequency analysis f_{0n} (Hz)
94.4	94.2
400.5	399.9
912	912
1631	1628

vacuum to match that in the analytical model. The numerical and analytical eigenfrequencies are well matched and validate each other as models.

For the acoustic plate-valve attached to the experimental rig, it can be considered as a thin circular plate free at the edge but fixed at the center. Southwell²² solved the problem with a free circular disk clamped at the center as an annulus plate free on the outside and clamped on the inner edge, which is well suited for the current configuration of the acoustic plate-valve. The first column of Table IV shows the eigenfrequencies (in a vacuum) from the analytical model of the acoustic plate-valve modeled as a centrally fixed free edge thin plate.²⁴

The simulated eigenfrequencies and mode shapes of the acoustic plate-valve from the COMSOL eigenfrequency analysis are shown in Table V, and the numerically determined eigenfrequencies are also tabulated in the second column of Table IV. Although the FEM simulation is based on a 2D axisymmetric model, the 3D mode shapes of the acoustic plate-valve were generated using post-processing of the 2D results for better visualization. The eigenfrequency analysis in vacuum for this simplified boundary condition allows for this 3D prediction, whereas the full frequency domain COMSOL numerical analysis in Appendix A 2, as shown in Fig. 9(a), for example, does not. First of all, by reviewing the first two columns of Table IV, we see that the analytical results compare extremely well with the eigenfrequency numerical analysis. Looking at the mode shapes in Table V, we see the azimuthal and radial mode shapes and their combinations, providing us with a valuable understanding of the vibration of the acoustic plate-valve. By comparing these frequencies with those of the non-Helmholtz frequency peaks to be found in the experimental and frequency domain numerical results in Fig. 9, we can verify that these are indeed due to excited natural vibrations in the acoustic plate-valve, as postulated.

Referring to Fig. 9(a) initially, it seems clear that the peaks to be found in frequency ranges N1, N2, and N3 correspond to $A_{(m,n)} = A_{(0,1)}, A_{(0,2)}, A_{(0,3)}$, which are radial modes with no azimuthal modes present. When these frequencies are entered into column four in Table IV, we see that, although the frequencies themselves are not exactly precise, the difference can be explained by the fact that the analysis was performed in air and not vacuum and that the full impedance tube assembly including the mounting plate, tube, and back cavity was included in the model and also by the issues related to uncertain material properties.

Referring now to Fig. 9(b), we conclude that the many additional non-Helmholtz frequency peaks can be attributed to acoustic

TABLE IV. Modal frequency comparison.

Mode (m, n)	Fundamental natural frequency f_{mn} (Hz)			
	Analytical	Numerical (eigenfrequency)	Experimental	Numerical (frequency domain)
(0,0)	43	43	E1	
(0,1)	240	242	E2	N1
(0,2)	703	698	E4	N2
(0,3)	1384	1378	E6	N3
(1,0)	...	14	E1	
(1,1)	236	245	E3	
(1,2)	687	705	E5	
(1,3)	1366	1392	E6	
(2,0)	60	61	•	
(2,1)	405	406	•	
(2,2)	963	972	...	
(3,0)	140	141	...	
(3,1)	607	609	...	
(3,2)	1278	1288	•	

plate-valve natural frequencies being excited by the white noise in the impedance tube. Not all theoretical modes are easily identifiable in the experimental data, and their amplitude response varies both as a function of frequency and cavity depth, but it is possible to make reasonable assumptions with regard to many of the modes. Frequency ranges E1-E6 contain cavity depth independent absorption peaks, which do correspond reasonably with the theoretically predicted vibrational modes. This can be seen in Table IV in column four where E1-E6 have been entered. Experimental peaks with low amplitude have also been represented but with a bullet point in the table, indicating that these modes seem to have been experimentally excited but with a low amplitude response. Once again, where frequencies are lower than those derived in vacuum, the added mass effect of the air can be used as an explanation.²⁵⁻³⁴

The analysis in Tables IV and V allows us to explain the presence of the additional peaks in Fig. 9 and to visualize them.

C. Particle velocity in the acoustic plate-valve neck/gap

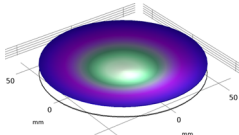
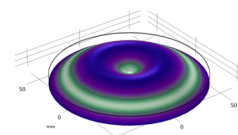
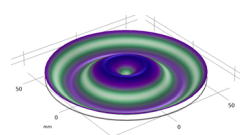
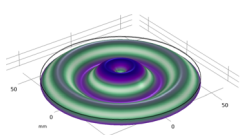
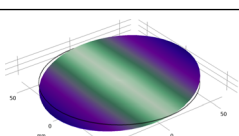
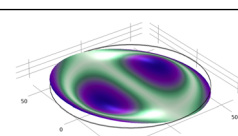
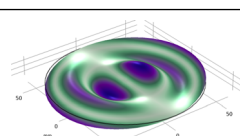
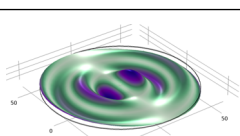
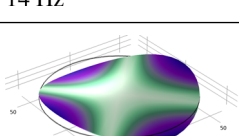
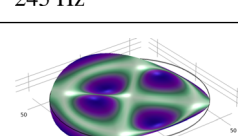
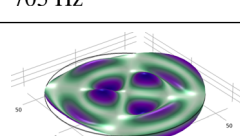
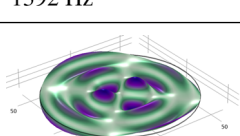
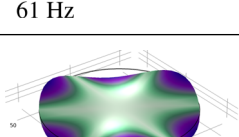
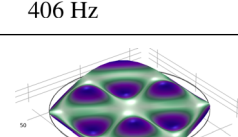
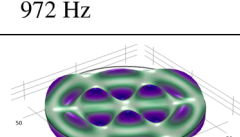
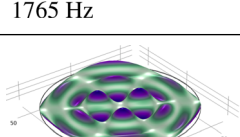
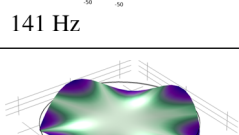
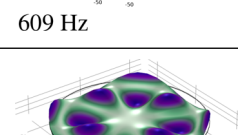
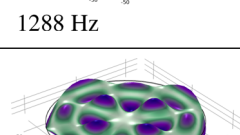
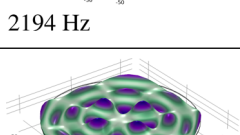
The particle velocity profile in the air gap, $h_d = 0.4$ mm, between the mounting plate and acoustic plate-valve (neck of the Helmholtz resonator) was calculated using the frequency domain numerical model for the 40 mm depth cavity, and the results are shown in Fig. 11. The three radial mode peaks $A_{(m,n)} = A_{(0,1)}$, $A_{(0,2)}$, $A_{(0,3)}$ and the Helmholtz resonance peak were examined for the fitted numerical case in Fig. 10. A viscous boundary layer formation can be observed in each of the plots. Figure 11(b) shows the velocity profile for the Helmholtz resonance, and not only does it have the highest particle velocity but it is also the only frequency for which uniform velocity along the full length of the neck is found. This proves that Helmholtz resonance is the result of the compressibility effect with the entire slug of air in the neck oscillating

harmonically. The maximum point velocity in Fig. 11(a) is also high, but as it is not as distributed as that for the Helmholtz resonance case, it makes sense that its peak in Fig. 10 is not that high. The velocity distribution for the three radial modes, unlike that for the Helmholtz resonance frequency, shown in Fig. 11(b), is not uniform, presumably being influenced by the fluctuation of the flexible plate-valve.

D. Structural-Helmholtz resonance coincidence

In Fig. 9 we observed that, as with micro-perforated panel absorbers, there is not only a decrease in the frequency of the Helmholtz resonance with increasing cavity depth but also a decrease in the magnitude of absorption. As has been noted, in the experimental results, the decrease in amplitude does not monotonically decrease with frequency. Given that there are additional vibrational modes with significantly high absorption peaks in that frequency range, an investigation was conducted to determine whether a frequency coincidence between the structural and Helmholtz resonance frequencies could influence the amplitude response. From observation of Fig. 9(b), it can be seen that there are two dominant structural resonances in the frequency range between the Helmholtz resonance peaks when the cavity depths are 10 and 20 mm, i.e., E4 and E5, which possibly correspond to the $A_{(0,2)}$ and $A_{(1,2)}$ modes. By varying the cavity depth more precisely, it is possible to adjust the frequency of the Helmholtz resonance peak so that it coincides with one of these structural resonance frequencies. In Fig. 12, we see the result of the investigation. By using Eq. (1), it is possible to predict the Helmholtz resonance frequency as a function of cavity depth. Figure 12 shows the result for three cavity depths between 10 and 20 mm, i.e., at 12, 13, and 14 mm. The 14 mm cavity depth aligns the Helmholtz frequency well with the $A_{(0,2)}$ mode and results in near-perfect absorption ($\alpha = 0.995$) at the coincident

TABLE V. Eigenfrequencies and the corresponding mode shape from the 2D axis-symmetric numerical model for the centrally fixed free edge circular plate: eigenfrequency analysis.

$m \downarrow \setminus n \Rightarrow$	0	1	2	3
0	 44 Hz	 242 Hz	 698 Hz	 1378 Hz
1	 14 Hz	 245 Hz	 705 Hz	 1392 Hz
2	 61 Hz	 406 Hz	 972 Hz	 1765 Hz
3	 141 Hz	 609 Hz	 1288 Hz	 2194 Hz
4	 248 Hz	 845 Hz	 1638 Hz	 2656 Hz

frequency. Similarly, the 12 mm cavity aligns the Helmholtz resonance, perhaps, not quite as well with the $A_{(1,2)}$ mode, resulting in a very high absorption coefficient ($\alpha = 0.97$), which is certainly higher than that of the original 10 mm cavity depth. The 13 mm cavity depth has the Helmholtz resonance in between the two structural resonances, and it can be seen that it and the structural resonance magnitudes are all higher than that when the cavity depth is 20 mm, for example.

E. Effect of thickness

In Sec. III D, it was seen that it is possible to attain coincidence by adjusting the cavity depth so that its Helmholtz frequency changes to that of the structural resonance frequency. Similarly, it should be possible to adjust the properties of the acoustic plate-valve itself so that a structural eigenfrequency can be changed to match the Helmholtz frequency. We saw in Fig. 10 that changing the material properties such as the values of ρ , E , v , and η results in structural resonant mode alteration without affecting the Helmholtz frequency. A

change in the 3D printing filament from the PLA to say ABS would achieve this, but in order to minimize the number of parameters changed at any one time, the PLA was maintained, and instead the thickness of the plate-valve was increased. Through observation, it can be seen that by substituting D in Eq. (3) into Eq. (2), the relationship between the thickness of the thin circular plate and resonant frequency becomes directly proportional. It can be seen in Fig. 9(b), that the E2 structural resonance frequency for the 40 mm cavity depth is approximately half that of the 40 mm Helmholtz frequency. Figure 13 shows the experimental impedance tube result for the same design 3D printed acoustic plate-valve but whose thickness is now 1 mm. Its absorption coefficient is superimposed on the original 0.52 mm thickness curve. The result is very satisfactory with the new coincident absorption response at 440 Hz increasing from ($\alpha = 0.79$) to ($\alpha = 0.97$) when the structural resonance is designed to align with the Helmholtz resonance. The cavity depth to wavelength ratio for 440 Hz is 20, demonstrating that deep subwavelength absorption can be achieved with almost perfect absorption at low frequencies such as this.

IV. CONCLUSIONS AND FUTURE RECOMMENDATIONS

The current research presents work to date on a novel acoustic resonator, which minimizes reflections from the walls of an enclosed space and thus absorbs sound. The technology employs the original idea of a flexible plate-valve applied to acoustics. Inspired by

off-the-shelf elastomeric fluidic one-way valves, acoustic plate-valves were 3D printed in a PLA to have a large diameter. The research demonstrates that the technology combines a Helmholtz resonator with structural vibrations in the plate, which themselves result in sound absorption for this small gap/air cavity configuration. It was shown that parameters such as the air

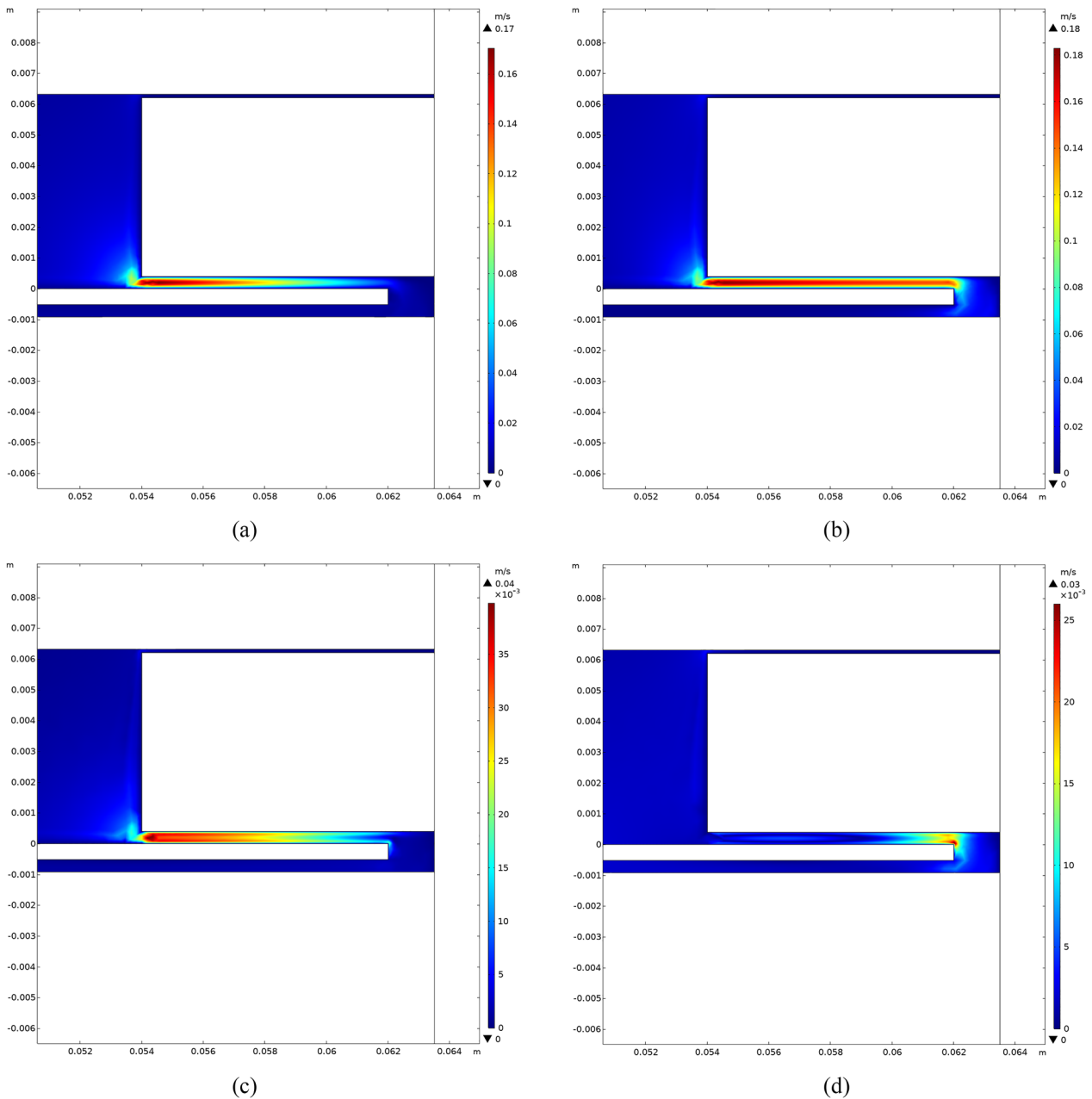


FIG. 11. Distribution of the particle velocity from the 2D axisymmetric FEM simulation. Viscous boundary layer formation can be seen inside the air gap between the mounting plate and acoustic plate-valve. $l_{cav} = 40$ mm; $h_d = 0.4$ mm. (a) Total acoustic velocity at 212 Hz. (b) Total acoustic velocity at 430 Hz. (c) Total acoustic velocity at 735 Hz. (d) Total acoustic velocity at 1465 Hz.

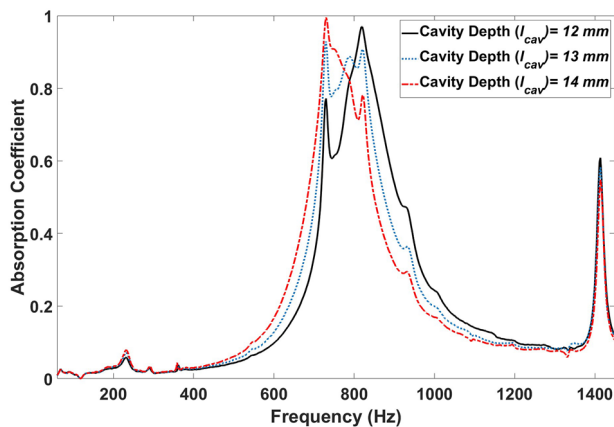


FIG. 12. Structural-Helmholtz resonance coincidence through varying the cavity depth.

cavity depth or the material properties of the plate-valve plate can be tailored at any required frequency so that resonant coincidence can be attained, which can result in near-perfect absorption (e.g., $\alpha = 0.995$), which is thus greater than what could be achieved by the Helmholtz resonator itself. Given that the thickness of the acoustic plate-valve plus the depth of the cavity can be a very small percentage of the acoustic wavelength that it is absorbing, deep subwavelength ratio absorbers can be designed, e.g., a ratio of up to 58 was achieved in this study. The technology presents the possibility for innovative acoustic absorbers for low-frequency noise attenuation in a thin profile. An FEM-based frequency domain modeling approach for the acoustic plate-valve has been validated to predict the acoustic performance. A simple 2D axisymmetric model has been implemented to reduce computational complexity and costs. The frequency domain model was compared with experimental results, which demonstrated strong agreement. An analytical model of the plate dynamics and a numerical eigenfrequency analysis allowed the natural frequencies to be calculated, and the latter allowed for visualization of the mode shapes. Future work will examine a fully 3D numerical model of the acoustic plate-valve, and a laser vibrometer-based measurement

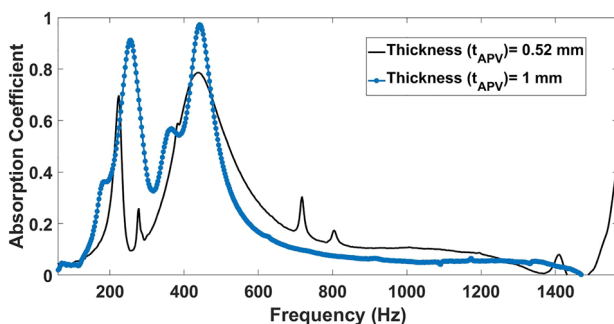


FIG. 13. Structural-Helmholtz resonance coincidence through varying the plate thickness.

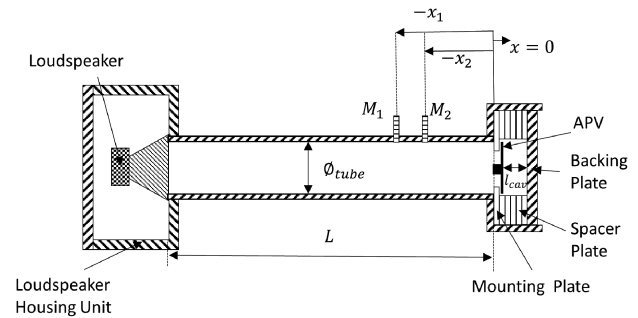


FIG. 14. Impedance tube schematic.

system will attempt to directly measure the mode shapes experimentally. A closer examination of the gap itself including viscous loss mechanisms and the case when the valve is fully closed due to negative pressure should also be investigated.

ACKNOWLEDGMENTS

This work was supported by Provost's Ph.D. Project Award from Trinity College Dublin. The financial support is gratefully acknowledged by the authors.

AUTHOR DECLARATIONS

Conflict of Interest

The authors have no conflicts to disclose.

Author Contributions

M.R.H., E.P.R., and G.J.B. contributed equally to this work.

Md. Robiul Hossain: Conceptualization (equal); Data curation (equal); Formal analysis (equal); Investigation (equal); Methodology (equal); Software (equal); Validation (equal); Writing – original draft (equal). **Eoghan P. Ross:** Conceptualization (equal); Formal analysis (equal); Investigation (equal); Methodology (equal); Software (equal). **Gareth J. Bennett:** Conceptualization (lead); Data curation (lead); Formal analysis (equal); Funding acquisition (lead); Investigation (equal); Methodology (equal); Project administration (lead); Resources (lead); Software (equal); Supervision (lead); Validation (equal); Visualization (equal); Writing – original draft (lead); Writing – review & editing (lead).

DATA AVAILABILITY

The data that support the findings of this study are available from the corresponding author upon reasonable request.

APPENDIX A: METHODS

1. Experimental rig

Experimental measurement of the absorption coefficient was performed using the two-microphone impedance tube method. The

tube was designed in accordance with the ISO standard 10534-2:2001³⁵ for impedance, reflection, and absorption measurements. A schematic of the experimental setup is shown in Fig. 14. The impedance tube, which was designed for high amplitude testing, is made of aluminum of 12.7 mm wall thickness, minimizing leakage and external noise ingress interfering with the data acquisition process. The tube has a circular cross section with an internal diameter of $\phi_{tube} = 0.127$ m and therefore has a plane wave cut-off frequency of ~ 1.5 kHz. The tube has a length $L = 0.78$ m with the capacity to attach a second length of tube for sound transmission loss measurements in accordance with the ASTM standard E2611³⁶ although this is not investigated in this work. A high-amplitude loudspeaker is attached to the tube at one end. The loudspeaker used in this rig is a JBL 2206H/J 12 in. subwoofer. The frequency response of the subwoofer ranges from 45 Hz to 3.5 kHz, allowing for testing at low frequencies often not reproducible by smaller speakers and impedance tube rigs. The speaker is contained in a custom-built 18 mm thick plywood unit with a flange opening, allowing it to be mounted to the tube. A termination/test section to the tube was designed to allow for adjustable back-cavity depths. The termination is an aluminum, square section housing with a 24.75 mm wall thickness, which allows square spacer plates with circular holes of the same diameter as the internal diameter as the tube to be inserted behind the mounting plate, creating a back cavity. Spacer plates of different thicknesses can be combined to create a variety of back-cavity depths. A thick, 20 mm, solid aluminum backing plate with no holes was inserted downstream of the spacer plates to form the hard wall termination. Figure 15 shows a photo of the test setup with an additional solid hard wall backing bolted to the rear of the square test-section. Two G.R.A.S. 40 PH microphones (M_1 and M_2), with a frequency range of 20 Hz–20 kHz, were used in the rig and calibrated in accordance with the ISO 10534-2:2001³⁵ standard. The microphones were recessed into the wall of the impedance tube and were separated from the internal pressure field of the tube by a 2 mm diameter hole 1 mm in length. The microphones were located $x_1 = 0.212$ m and $x_2 = 0.127$ m from the face of the acoustic plate-valve mounting plate. The sample was tested using white noise with a sound pressure level (SPL) of 94 dB for 120 s. Other SPLs ranging from 100 to 120 dB were tested, but no significant non-linear effects were observed. The transfer function method was used in the analysis where the complex pressure reflection coefficient, r , is obtained from Cox and d’Antonio³⁷ as

$$r = \frac{H_{12}e^{jkx_1} - e^{jkx_2}}{e^{-jkx_2} - H_{12}e^{-jkx_1}}, \tag{A1}$$

where $H_{12} = \frac{p(x_2)}{p(x_1)}$ is the transfer function between microphone positions and $k = \omega/c$ is the acoustic wave number. The absorption coefficient, α , is calculated from the reflection coefficient,

$$\alpha = 1 - |r|^2. \tag{A2}$$

2. Numerical analysis

FEM simulations were performed using the commercial software COMSOL Multiphysics[®] version 5.6 with preset pressure acoustics, thermoviscous acoustics, and solid mechanics interfaces.

The acoustics module is well suited for all frequency-domain simulations with harmonic variations in the pressure field. A frequency domain analysis of the plane wave propagation has been performed where the acoustic plate-valve was modeled as a linear elastic material using the solid mechanics interface and the interior of the impedance tube was modeled as air with the pressure and thermoviscous acoustics interfaces. Coupling between thermoviscous acoustic and pressure acoustics is achieved with an acoustic-thermoviscous acoustic boundary while coupling between solid mechanics and thermoviscous acoustics is performed with a thermoviscous acoustic-structure boundary. The geometric parameters used in the simulation are chosen from the experimental setup described in Appendix A 1 with a variable cavity length (l_{cav}).

The geometric model for the FEM simulation, as shown in Fig. 16, is a simplified 2D axisymmetric model to reduce computational costs and time with little compromise of the fundamental characteristics. Sound-hard boundary walls and symmetry conditions are shown. The model represents the cylindrical impedance tube setup with the acoustic plate-valve, mounting plate, and back-cavity. The geometric coordinates for the plane in the 2D axisymmetric implementation are (r, z) and the angle ϕ is not defined since it is not a part of the computational domain implemented in the simplified model.

The material properties of PLA were taken from the literature:³⁸ mass density $\rho = 1270$ kg m⁻³, Young’s modulus $E = 3.5 \times 10^9$ Pa, Poisson’s ratio $\nu = 0.3$,³⁹ and damping factor $\eta = 0.025$,⁴⁰ with typical values taken for air—mass density $\rho_0 = 1.23$ kg m⁻³—and the speed of sound in air being $c_0 = 343$ m s⁻¹. To avoid domain overlapping in the FEM modeling, a very small gap was introduced between the mounting plate and the plate-valve. Due to the meshing requirements, it is not possible to model the setup without the gap. The value for the air gap ($h_d = 0.4$ mm) was chosen iteratively to match the experimental results.

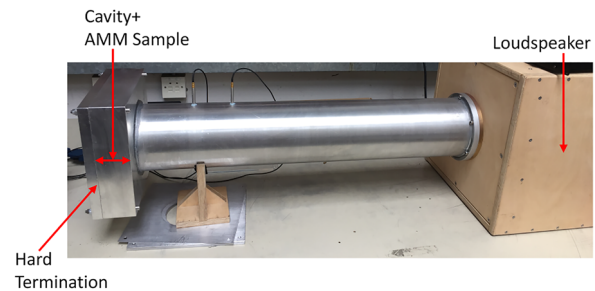


FIG. 15. Photograph of the experimental test section with an impedance tube.

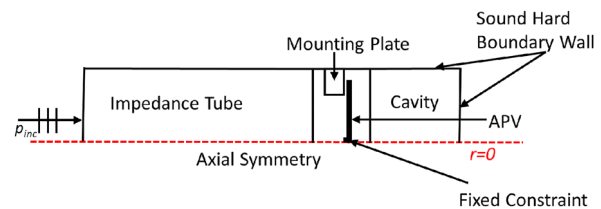


FIG. 16. Simplified 2D axisymmetric geometric model for numerical simulation.

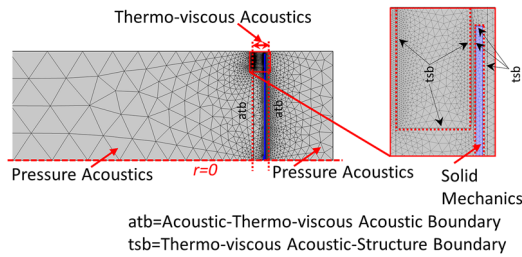


FIG. 17. Mesh plot of the simplified 2D axisymmetric geometric model for numerical simulation.

The complete mesh consists of 9688 domain elements and 880 boundary elements. The number of degrees of freedom solved for is 33 040. A parametric frequency sweep was performed from 50 to 1500 Hz with a 1 Hz frequency increment for frequency domain analysis. The average simulation time was 18 min 45 s on a workstation with the following specifications: an 8-core 2.40 GHz processor and 64 GB RAM.

In addition, an eigenfrequency analysis was also performed using only the solid mechanics part of the model for the acoustic plate-valve in order to obtain its structural resonance modes. The free vibration of the acoustic plate-valve (considered as a centrally fixed thin circular plate) *in vacuo* was investigated using this eigenfrequency analysis (for further details, see Appendix B). The meshing and the calculations of the reflection and absorption coefficient are demonstrated in the following sections.

a. Meshing

A user-controlled mesh with free triangular elements was used to create the mesh. The acoustic mesh element size criterion depends on the smallest acoustic wavelength (λ_0) of interest. Considering that the largest acoustic mesh element should never be larger than $\frac{1}{6}$ of the wavelength λ_0 , the maximum and minimum element size are defined as $\frac{c_0}{6f_0}$ and $d_{visc}/3 = \frac{1}{3}\sqrt{\left(\frac{2\mu}{\omega\rho_0}\right)} = 220 \mu\text{m} \cdot \frac{1}{3} \cdot \sqrt{\left(\frac{100 \text{ Hz}}{f_0}\right)}$ respectively. Figure 17 shows a portion of the mesh plot and highlights some of the mesh features in the vicinity of the acoustic plate-valve.

b. Estimation of the reflection and absorption coefficient

The absorption coefficient can be obtained using the incident acoustic impedance, which can be written as

$$Z_{in} = \frac{\langle p_t \rangle}{\langle -v_z \rangle}, \tag{A3}$$

where p_t is the total acoustic pressure, v_z is the acoustic velocity in the vertical direction, and $\langle \cdot \rangle$ is an operator referring to the average on the top surface of the system. The total impedance of the whole system can be obtained using the impedance translation theorem⁴¹ in the form of transfer impedance as

$$Z_T = Z_0 \frac{Z_{in} + iZ_0 \tan(kL)}{Z_0 + iZ_{in} \tan(kL)}. \tag{A4}$$

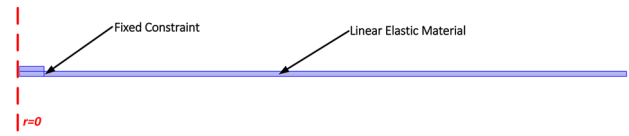


FIG. 18. Linear elastic material model for eigenfrequency analysis.

Using the transfer impedance (Z_T), the reflection coefficient r has been obtained as

$$r = \frac{Z_T - Z_0}{Z_T + Z_0}, \tag{A5}$$

where $Z_0 = \rho_0 c_0$ is the specific acoustic impedance of the medium (i.e., air). Finally, the normal-incidence sound-absorption coefficient (α) is given by Eq. (A2).

APPENDIX B: EIGENFREQUENCY ANALYSIS

An eigenfrequency analysis provides the eigenfrequencies (natural frequencies) and mode shape (eigenmode) of a linear or linearized model. An eigenfrequency analysis has been performed using only the solid mechanics part of the model for the acoustic plate-valve to obtain the structural resonance modes according to the model shown in the schematic in Fig. 18. The eigenfrequency analysis was set to find the first 10 eigenfrequencies for symmetric modes. The physics-controlled mesh has been adapted for the model using a normal element size. To get the 10 desired number of eigenfrequencies around 50 Hz, the simulation run time was 2 s using the same workstation for frequency domain analysis.

The governing equation for the eigenfrequency analysis is

$$-\lambda_{mn} = i2\pi f_{mn} = i\omega_{mn}, \tag{B1}$$

where the fundamental eigenvalue is λ_{mn} and the eigenfrequency is f_{mn} . The eigenvalue problem without damping can be expressed as

$$[\mathbf{K} - \omega_{mn}^2 \mathbf{M}] \mathbf{u} = 0, \tag{B2}$$

where \mathbf{K} is the stiffness matrix, \mathbf{M} is the mass matrix, and \mathbf{u} is the eigenmode displacement vector. The eigenvalue problem with damping can be represented as

$$[\mathbf{K} + i\omega_{mn} \mathbf{C} - \omega_{mn}^2 \mathbf{M}] \mathbf{u} = 0, \tag{B3}$$

where \mathbf{C} is the viscous damping matrix and \mathbf{K} can be complex valued.

REFERENCES

- ¹S. Kumar and H. Lee, *Acoustics* (Multidisciplinary Digital Publishing Institute, 2019), Vol. 1, pp. 590–607.
- ²Y. Wang, K. Zhao, X.-Y. Lu, Y.-B. Song, and G. J. Bennett, *Appl. Sci.* **9**, 2224 (2019).
- ³K. Zhao, P. Okolo, E. Neri, P. Chen, J. Kennedy, and G. J. Bennett, *Prog. Aerosp. Sci.* **112**, 100589 (2019).
- ⁴J. Mei, G. Ma, M. Yang, Z. Yang, W. Wen, and P. Sheng, *Nat. Commun.* **3**, 756 (2012).
- ⁵C. Li, B. Cazzolato, and A. Zander, *J. Acoust. Soc. Am.* **139**, 93 (2016).

- ⁶K. Donda, Y. Zhu, S.-W. Fan, L. Cao, Y. Li, and B. Assouar, *Appl. Phys. Lett.* **115**, 173506 (2019).
- ⁷Y. Zhu, K. Donda, S. Fan, L. Cao, and B. Assouar, *Appl. Phys. Express* **12**, 114002 (2019).
- ⁸Y. Y. Lee, E. W. M. Lee, and C. F. Ng, *J. Sound Vib.* **287**, 227 (2005).
- ⁹C. Wang, L. Cheng, J. Pan, and G. Yu, *J. Acoust. Soc. Am.* **127**, 238 (2010).
- ¹⁰M. A. Temiz, J. Tournadre, I. Lopez Arteaga, and A. Hirschberg, *Appl. Acoust.* **125**, 80 (2017).
- ¹¹E. Martincic, A. Houdouin, S. Durand, N. Yaakoubi, E. Lefeuvre, and Y. Auregan, “Acoustic absorber, acoustic wall and method for design and production,” US Patent 10,477,302 (2019).
- ¹²A. McKay, I. Davis, J. Killeen, and G. J. Bennett, *Sci. Rep.* **10**, 17967 (2020).
- ¹³I. Davis, A. McKay, and G. J. Bennett, *J. Sound Vib.* **505**, 116135 (2021).
- ¹⁴J. Killeen, I. Davis, J. Wang, and G. J. Bennett, *Appl. Acoust.* **203**, 109229 (2022).
- ¹⁵J. Wang and G. J. Bennett, *J. Sound Vib.* **547**, 117527 (2023).
- ¹⁶M. Farooqui and Y. Aurégan, in *2018 AIAA/CEAS Aeroacoustics Conference* (AIAA, 2018), p. 4101.
- ¹⁷M. E. D’elia, T. Humbert, and Y. Aurégan, *Acta Acust.* **5**, 31 (2021).
- ¹⁸Y. Aurégan and M. Farooqui, *Sci. Rep.* **9**, 11140 (2019).
- ¹⁹G. J. Bennett, R. Hossain, A. McKay, and E. P. Ross, in *25th AIAA/CEAS Aeroacoustics Conference* (AIAA, 2019), p. 2422.
- ²⁰H.-Y. Chiang and Y.-H. Huang, *Appl. Acoust.* **129**, 365 (2018).
- ²¹S. Timoshenko, W. Weaver, and D. Young, *Vibration Problems in Engineering* (John Wiley & Sons, 1928), c 1928, 1937, by d.
- ²²R. V. Southwell, *Proc. R. Soc. London, Ser. A* **101**, 133 (1922).
- ²³R. C. Colwell and H. C. Hardy, *London, Edinburgh Dublin Philos. Mag. J. Sci.* **24**, 1041 (1937).
- ²⁴A. W. Leissa, *Vibration of Plates* (Scientific and Technical Information Division, National Aeronautics and Space Administration, 1969), Vol. 160.
- ²⁵N. McLachlan, *Proc. Phys. Soc.* **44**, 546 (1932).
- ²⁶R. W. Guy and M. C. Bhattacharya, *J. Sound Vib.* **27**, 207 (1973).
- ²⁷J. Pan and D. A. Bies, *J. Acoust. Soc. Am.* **87**, 691 (1990).
- ²⁸J. Pan and D. A. Bies, *J. Acoust. Soc. Am.* **87**, 708 (1990).
- ²⁹D. G. Gorman, J. M. Reese, J. Horáček, and K. Dedouch, *Proc. Inst. Mech. Eng., Part C* **215**, 1303 (2001).
- ³⁰D. G. Gorman, C. K. Lee, J. M. Reese, and J. Horáček, *J. Sound Vib.* **279**, 601 (2005).
- ³¹C. Rajalingham, R. B. Bhat, and G. D. Xistris, *Int. J. Mech. Sci.* **40**, 723 (1998).
- ³²L. Yuanqi, L. Wang, Z. Shen, and Y. Tamura, *J. Wind Eng. Ind. Aerodyn.* **99**, 815 (2011).
- ³³H. Liu, D. A. Olson, and M. Yu, *J. Sound Vib.* **333**, 7051 (2014).
- ³⁴A. Presas, D. Valentin, E. Egusquiza, C. Valero, M. Egusquiza, and M. Bossio, *Sensors* **17**, 660 (2017).
- ³⁵BS EN ISO 15034-2:2001, “Acoustics—Determination of sound absorption coefficient and impedance in impedance tubes—Part 2: Transfer-function method,” Technical Standard BS EN ISO 15034-2:2001, British Standard, 2002.
- ³⁶ASTM E2611-09, “Standard test method for measurement of normal incidence sound transmission of acoustical materials based on the transfer matrix method,” Tech. Rep. ASTM E2611-09, ASTM International, 2009.
- ³⁷T. Cox and P. d’Antonio, *Acoustic Absorbers and Diffusers: Theory, Design and Application* (CRC Press, 2016).
- ³⁸J. Gietl, J. Vignola, J. Sterling, and T. Ryan, *J. Phys.: Conf. Ser.* **1149**(1), 012002 (2018).
- ³⁹S. Mirkhalaf and M. Fagerström, *Mech. Time-Depend. Mater.* **25**, 119 (2021).
- ⁴⁰K. Arunprasath, M. Vijayakumar, M. Ramarao, T. G. Arul, S. Peniel Pauldoss, M. Selwin, B. Radhakrishnan, and V. Manikandan, *Mater. Today: Proc.* **50**, 1559 (2022).
- ⁴¹B. E. Anderson and S. D. Sommerfeldt, *J. Acoust. Soc. Am.* **150**, 4155 (2021).

A.2 Numerical Prediction of Plate-type Acoustic Valve Resonator using Time Domain Analysis

In this section, numerical techniques of the FEM model have been provided for the complete plate-type acoustic valve resonator system using time domain analysis. To build the complete numerical model of the plate-type acoustic valve with relevant interfaces, the following assumptions were made:

- The premise of the current technology is that high acoustic pressure at the metasurface from incident acoustic waves will cause the one-way valve to open allowing some flow to pass through the small gap which opens. When the pressure drops the valve closes once more causing a reduction in the amplitude of the reflected wave. Energy can also be lost through absorption in the flexible valve itself, through viscous losses in the small gap which opens up between the valve and the solid surface, as well as losses related to the cavity behind the valve once the valves has opened.
- The technology possess non-linear acoustic behavior. The viscous forces both linear and non-linear in the gap/film layer need to be modelled ideally as well as the effect of the squeeze film in the airgap.
- High magnitude of the displacement of the plate-type acoustic valve is expected interacting with deforming domain. The movement of the valve includes squeeze film losses, kinetic losses, and acoustic trapping additional to thermal and viscous losses. This plate-type acoustic valve or one way valve can also be considered as squeeze film resonator.

A.2.1 Initial Strategies for Numerical Modeling

- All the interfaces for a Frequency Domain study in the Acoustics Module of COMSOL Multiphysics are linearised equations, therefore they are not suitable for very large amplitude acoustic modelling. However, an acoustics interface can be used either adding the Nonlinear node or couple to a CFD interface. The Nonlinear Acoustics node does not include losses but the Single Phase Flow (e.g. Laminar Flow) interface is rather computationally heavy but includes losses. These must be implemented in the time domain. A test time domain model of MPP's has been developed (see Appendix A.3) to understand initial strategies for numerical modeling in time domain.

- Within COMSOL Multiphysics it is nontrivial to model fluid flow forcing the domains to open and close - this is because the number of domains changes.
- General mesh is not enough to replicate the opening and closing effect of the valve. Moving mesh needs to be included in the model.
- This is a nonlinear analysis that is not suitable for frequency domain simulation.
- To avoid domain overlapping in the model, a very small gap needs to be placed between the mounting plate and the plate-type acoustic valve. Due to the numerical limitations, it is not possible to model the set-up without the gap.

A.2.2 2D FEM Model: Time Domain

A FEM numerical analysis based on experimental setup with plate-type acoustic valve in the time domain is implemented including nonlinear effects. Simulations are performed using commercial software COMSOL Multiphysics[®] version 5.4 with preset pressure acoustics, thermoviscous acoustic and solid mechanics. At first, laminar flow interface has been used instead of thermo-viscous acoustics interface. It has been found that, including the laminar flow interface generates significant complexity in the model. There are no automatic coupling for laminar flow interface with pressure acoustics interface so coupling needs to be done manually. Laminar flow interface is computationally heavy and require significant amount of time just for computing short time range. To avoid all these disadvantages, thermo-viscous acoustics interface has been adopted which can be coupled with pressure acoustics automatically and computationally less time consuming. The plate-type acoustic valve was modelled as a linear elastic material using the solid mechanics interface and the interior of the impedance tube and cavity was modelled as air with the pressure acoustics and thermoviscous acoustics interface. Coupling between solid mechanics and thermoviscous acoustics are done with thermoviscous acoustic-structure boundary while coupling between pressure acoustics and thermoviscous acoustics are done with acoustic-thermoviscous acoustic boundary.

A.2.2.1 FEM Geometric Model

The geometric model for FEM simulation is a simplified 2D axis-symmetric model to reduce computational costs and time without sacrificing the fundamental characteristics as shown in Fig. (A.1). The model represents a cylindrical impedance tube set-up with the plate-type acoustic valve with maximum porosity mounting plate) sample to estimate the absorption coefficient. The geometric coordinates for the plane in the 2D axisymmetric implementation are (r, z) and the angle φ is not defined

A.2 NUMERICAL PREDICTION OF PLATE-TYPE ACOUSTIC VALVE RESONATOR USING TIME DOMAIN ANALYSIS

since it is not part of the computational domain implemented in the simplified model. We assume the mass density $\rho_m = 1240 \text{ kgm}^{-3}$, Youngs modulus $E_m = 3.8 \times 10^9 \text{ Pa}$ and Poissons ratio $\nu_m = 0.33$ for the PLA valve, as well as the mass density $\rho_0 = 1.23 \text{ kgm}^{-3}$, and the wave velocity $c_0 = 343 \text{ ms}^{-1}$ for the fluid material (air). The geometric parameters used in the simulation are chosen from experimental setup described in Section (5.1) with cavity length, $l_{cav} = 40 \text{ mm}$. The system of equations is solved by using a direct time dependent solver. Generalized alpha with manual time stepping has been used as the time stepping methods for the time dependent solver. Complete mesh consists of 8630 domain elements and 759 boundary elements and 58953 degrees of freedom. Parametric frequency sweep performed from 60 Hz to 500 Hz with 1 Hz frequency increment. The average simulation time is 177 hrs on a workstation with the following specifications: 8-core 2.40 GHz processor and 64 GB RAM.

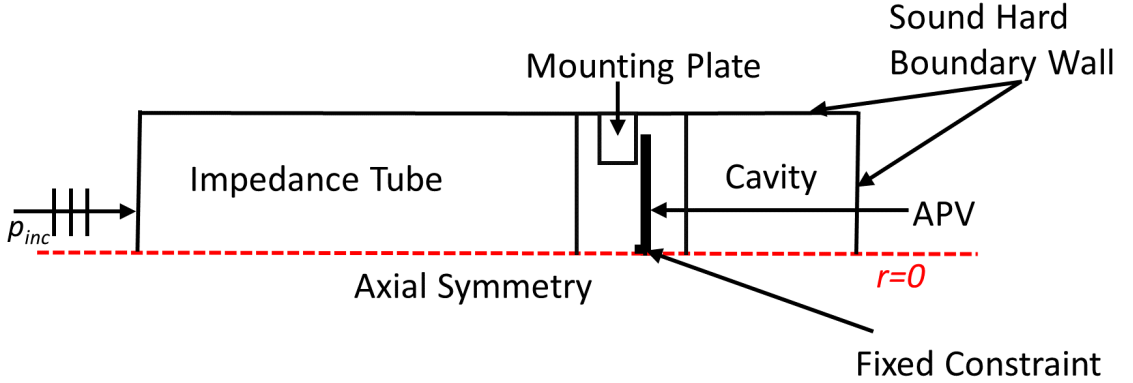


Figure A.1: Simplified 2D axisymmetric geometric model for numerical simulation.

A.2.2.2 Boundary Conditions

Acoustic and thermoviscous acoustic boundary conditions are important to accurately solve the governing equations. For fluid domain, the time-dependent (transient) pressure acoustics modeling defined by the scalar wave equation,

$$\frac{1}{\rho_0 c_0^2} \frac{\partial^2 p_t}{\partial t^2} + \nabla \cdot \left(-\frac{1}{\rho_0} \nabla p_t \right) = 0 \quad (\text{A.1})$$

A.2 NUMERICAL PREDICTION OF PLATE-TYPE ACOUSTIC VALVE RESONATOR USING TIME DOMAIN ANALYSIS

where, $p_t = p + p_b$, p_t is the the total acoustic pressure, p_b is the the background pressure, ρ_0 is the density of fluid and c_0 is the speed of sound in the air. A plane incident wave p_0 is applied from the left-hand side of the impedance tube with unit amplitude, part of the acoustic energy is reflected and the rest is absorbed by the plate-type acoustic valve and the cavity. But, very small movement of the valve has been observed. So, instead of using unit amplitude of incident pressure, $p_0 = 20$ Pa has been used for further modeling. With incident pressure field, $p_{inc} = p_i = p_0 \sin(2\pi f_0 t)$, the plane wave radiation BC can be defined as [145],

$$\frac{1}{\rho_0} \left(\frac{1}{c_0} \frac{\partial p}{\partial t} \right) - \mathbf{n} \cdot \left(-\frac{1}{\rho_0} \nabla p_t \right) = Q_i \quad (\text{A.2})$$

where, $Q_i = \frac{1}{\rho_0} \left(\frac{1}{c_0} \frac{\partial p_i}{\partial t} \right) + \mathbf{n} \cdot \frac{1}{\rho_0} \nabla p_i$.

The current model has small geometric dimension such as small opening area in between mounting plate and one way valve. It is very important to include the thermal and viscous losses to accurately capture the effects of this narrow regions. Thermoviscous acoustics domain represents the small regions where thermal and viscous loss accounts for energy losses of the acoustic wave of the system. Time domain representation of the governing equation for thermoviscous acoustics are as follows:

$$\begin{aligned} \frac{\partial p_t}{\partial t} + \nabla \cdot (\rho_0 \mathbf{v}_t) &= 0 \\ \rho_0 \frac{\partial \mathbf{v}_t}{\partial t} &= \nabla \cdot \left\{ -p_t \mathbf{I} + \mu (\nabla \mathbf{v}_t + (\nabla \mathbf{v}_t)^T) + \left(\mu_B - \frac{2}{3} \mu \right) (\nabla \cdot \mathbf{v}_t) \mathbf{I} \right\} \\ \rho_0 C_p \left(\frac{\partial T_t}{\partial t} + \mathbf{v}_t \cdot \nabla T_0 \right) - \alpha_p T_0 \left(\frac{\partial p_t}{\partial t} + \mathbf{v}_t \cdot \nabla p_0 \right) &= \nabla \cdot (k \nabla T_t) \\ \rho_t &= \rho_0 (\beta_T p_t - \alpha_p T_t) \end{aligned} \quad (\text{A.3})$$

where, $p_t = p + p_b$, p_t is the the total acoustic pressure for thermoviscous region, $\mathbf{v}_t = \mathbf{v} + \mathbf{v}_b$ and $T_t = T + T_b$.

The solid mechanics solver uses solid domain as linear elastic material model. The deformation can be defined as [160]:

$$\nabla \cdot \boldsymbol{\sigma} + \mathbf{f}_v = \rho \frac{\partial^2 \mathbf{u}}{\partial t^2} \quad (\text{A.4})$$

where, $\boldsymbol{\sigma}$, is described by,

$$\boldsymbol{\sigma} = \mathbf{J}^{-1} \mathbf{F} \mathbf{S} \mathbf{F}^T \quad (\text{A.5})$$

Symbol	Term
$\boldsymbol{\sigma}$	Cauchy stress
\mathbf{f}_v	Volume force vector
S	Second Piola-Kirchhoff stress
F	Displacement gradient
C	Cauchy-Green deformation tensor
$\boldsymbol{\sigma}_{ex}$	An extra stress contribution
$\boldsymbol{\sigma}_0$	Initial stress

Table A.1: Parameters for linear elastic material model

and F is defined by,

$$F = (I + \nabla \mathbf{u}) \quad (\text{A.6})$$

The Green-Lagrange strain tensor is evaluated with respect to the displacement gradient as:

$$\boldsymbol{\varepsilon} = \frac{1}{2} [(\nabla \mathbf{u})^T + \nabla \mathbf{u} + (\nabla \mathbf{u})^T \nabla \mathbf{u}] \quad (\text{A.7})$$

where, $\boldsymbol{\varepsilon}$, is the total strain tensor under axial symmetry assumptions [160]. For a linear elastic material, the stress tensor can be represented by an elastic strain tensor using Hooke's law:

$$\boldsymbol{\sigma} = \boldsymbol{\sigma}_{ex} + C : \boldsymbol{\varepsilon}_{el} = \boldsymbol{\sigma}_{ex} + C : (\boldsymbol{\varepsilon} - \boldsymbol{\varepsilon}_{inel}) \quad (\text{A.8})$$

The elastic strain energy density can be defined as [161]:

$$W_s = \frac{1}{2} \boldsymbol{\varepsilon}_{el} : (C : \boldsymbol{\varepsilon}_{el} + 2\boldsymbol{\sigma}_0) = \frac{1}{2} \boldsymbol{\varepsilon}_{el} : (\boldsymbol{\sigma} + \boldsymbol{\sigma}_0) \quad (\text{A.9})$$

The coupling between pressure acoustics and thermoviscous acoustics are defined by the following equations:

$$\begin{aligned}
 & -\mathbf{n} \cdot \left(-\frac{1}{\rho} \nabla p_t \right) = -\mathbf{n} \cdot \frac{\partial \mathbf{v}_t}{\partial t} \\
 -p_t \mathbf{n} = & \left[-p_t \mathbf{I} + \mu (\nabla \mathbf{v}_t + (\nabla \mathbf{v}_t)^T) + \left(\mu_B - \frac{2}{3} \mu \right) (\nabla \cdot \mathbf{v}_t) \mathbf{I} \right] \mathbf{n} \\
 & -\mathbf{n} \cdot (-k \nabla T_t) = 0
 \end{aligned} \quad (\text{A.10})$$

For thermoviscous acoustic and solid mechanics interaction:

$$\mathbf{v}_{t,fluid} = \frac{\partial \mathbf{u}_{struct}}{\partial t} \quad \text{and} \quad T_t = 0 \quad (\text{A.11})$$

Figure (A.2) shows the movement of mesh which represents the displacement of the plate-type acoustic valve and squeezing the air between mounting plate and the valve. Valve opening and closing can be seen by the mesh displacement of the valve.

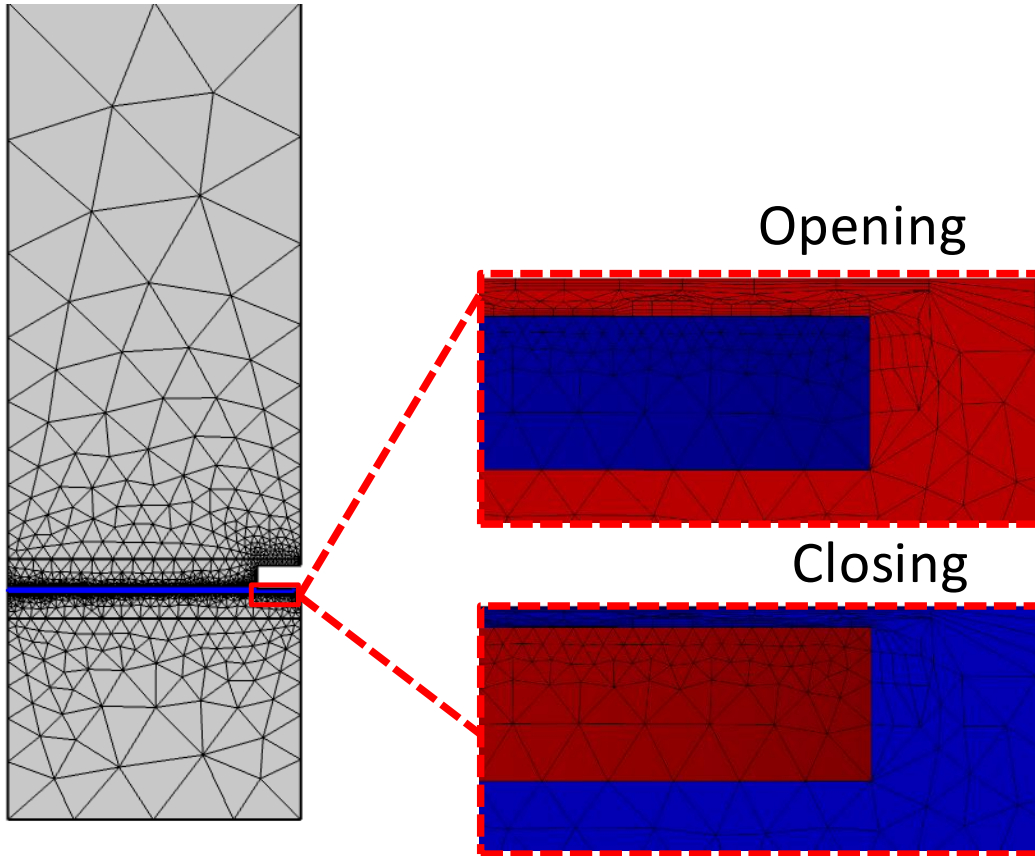


Figure A.2: Close up of the deforming domain in the open area between plate-type acoustic valve and mounting plate. In the inset we can see the deformation from the equilibrium position with movement of the mesh.

A.2.2.3 Meshing

- General mesh:** The general meshing is performed using user controlled mesh with free triangular elements. The acoustic mesh element size criterion depends on the smallest acoustic wavelength (λ_0) of the interest. Considering that largest acoustic element is never larger than the $\frac{1}{6}$ of the λ_0 , maximum and minimum element size are defined as: $\frac{c_0}{6f_0}$ and $d_v/3 = \frac{1}{3}\sqrt{\left(\frac{2\mu}{\omega\rho_0}\right)} = 220\mu\text{m} \cdot \frac{1}{3} \cdot \sqrt{\left(\frac{100\text{Hz}}{f_0}\right)}$ respectively. The mesh in the vicinity of plate-type acoustic valve is shown in Fig. (A.2).

- Moving mesh (ALE):** Within COMSOL Multiphysics it is nontrivial to model fluid flow forcing the domains to open and close, this is because the number of domains changes. To capture the effects of valve opening and closing, the model in this study utilizes an Arbitrary Lagrangian-Eulerian (ALE) formulation termed as moving mesh in COMSOL. By using the ALE formulation, the fluid moving mesh is used to track the deformation of the solid mesh. Moving mesh defines a displacement of the spatial frame relative to the material frame and directly tracks the free surfaces and allows for a sharp interface to apply boundary conditions. The deformation of this mesh relative to the initial shape of the domain is computed using Yeoh smoothing. Distortion type automatic re-meshing also added in the time dependent solver to ensure creation of new meshes according to time steps with remeshed solution. Inset of the Fig. (A.2) shows the movement of the mesh.

A.2.2.4 Estimation of the Reflection and Absorption Coefficient

To calculate reflection coefficient, a time dependent study with parametric frequency sweep is applied to numerical model. The total sound pressure field (p) can be simulated by COMSOL and the reflected sound pressure field is expressed as:

$$p_r = p - p_{inc} \quad (\text{A.12})$$

In above equation, r is the pressure reflection coefficient that gives the ratio of the scattered pressure to the incident pressure

$$r = \frac{p_r}{p_{inc}} \quad (\text{A.13})$$

The calculation for reflection coefficient performed as a integration of a time-dependent expression over a time interval. A trapezoidal integration rule is used to calculate the root-mean-square (rms) pressure [162] and calculated as:

$$p_{rms}^2 = \frac{1}{t_{end} - t_{start}} \int_{t_{start}}^{t_{end}} p^2(t) dt \quad (\text{A.14})$$

Finally, the absorption coefficient, which represents the ratio of the absorbed and incident pressure can be calculated by Eq. (5.7) under the approximation of zero transmission. The numerical model presented in this section is largely based on a direct numerical simulation (DNS) model of a “nonlinear slit resonators” by Tam et al. [163] and FEM model of a “acoustic absorbent lining structure” by Cai et al. [164]. Although this is not an application that has a clearly defined simulation strategy, similar implementation procedure and calculations are used to ensure validity of the current model.

A.2.2.5 Model including Structural Damping

Damping is related to the kinetic and elastic energy dissipation in the wave propagation or amplitude decay during free vibrations as the intrinsic property of the materials. Usually two types of damping are considered because of diverse and complex dissipative techniques: Viscous damping and Viscoelastic damping or nonviscous damping [165]. Rayleigh type viscous damping is a simple model is considered here mainly in case of energy dissipation associated with the presence of a standard viscous medium (e.g., a Newtonian fluid). But more realistic model is the viscoelastic model which depends on the wider assortment of state variables. In matrix form, equation of motion can be represented as:

$$[\mathbf{M}]\left(\frac{d^2u}{dt^2}\right) + [\mathbf{C}]\left(\frac{du}{dt}\right) + [\mathbf{K}](u(t)) = f(t) \quad (\text{A.15})$$

Where,

$u(t)$ = displacement as a function of time

$[\mathbf{M}]$ = the mass matrix

$[\mathbf{C}]$ = the viscous damping matrix

$[\mathbf{K}]$ = the stiffness matrix

The mass and stiffness matrices can be calculated with the geometry and material properties such as mass density and Young's modulus. The damping matrix can be modelled with different damping types.

In the frequency domain, the excitation and response are assumed to be harmonic. This equation can be written as

$$(-\omega^2\mathbf{M} + i\omega\mathbf{C} + \mathbf{K})\tilde{\mathbf{u}} = \tilde{\mathbf{f}} \quad (\text{A.16})$$

In COMSOL Multiphysics, there is an option to put damping in the model in **Linear Elastic Material** of **Solid Mechanics** as **Attributes**. Four types of damping are defined there namely Rayleigh damping, Isotropic loss factor, An-isotropic loss factor and Viscous damping. According to COMSOL modeling algorithm, isotropic and anisotropic loss factor does not have contribution to the time domain analysis due to frequency dependency. So, viscous damping has been used for the time domain analysis including the structural loss factor $\eta=0.1$.

- **Viscous Damping:** For a viscous damping model, stresses of solid material are proportional to the strain rate. In the most common case, the constitutive tensor that relates to the stress to strain rate can have 21 independent constants. However it's very difficult to measure damping and these values are often known. In COMSOL, viscous damping defined with two constants:

Bulk viscosity (η_b) which represents volume change and shear viscosity (η_v) which represents shape change. The viscous stress can be represented as:

$$\boldsymbol{\sigma}_v = \eta_b \dot{\boldsymbol{\epsilon}}_v \mathbf{I} + \eta_v \dot{\boldsymbol{\epsilon}}_d \quad (\text{A.17})$$

where $\boldsymbol{\epsilon}_v$ and $\boldsymbol{\epsilon}_d$ is the volumetric strain and deviatoric part of the strain tensor respectively and

$$\eta_b = K\eta / \omega_0 \quad (\text{A.18})$$

$$\eta_v = G\eta / \omega_0 \quad (\text{A.19})$$

where, η is the structural loss factor, K is the equivalent bulk modulus, and G is the equivalent shear modulus. For the time domain simulation, viscous damping has been used.

- **Structural Loss Factor:** Considering material properties as complex valued we can write complex valued stress strain rate as:

$$\tilde{\boldsymbol{\sigma}} = \tilde{E} \tilde{\boldsymbol{\epsilon}} = (E' + iE'') \tilde{\boldsymbol{\epsilon}} \quad (\text{A.20})$$

Real part of the Young's modulus known as storage modulus and imaginary part is known loss modulus. In general loss modulus defined by a loss factor η .

$$\tilde{E} = E(1 + j\eta) \quad (\text{A.21})$$

Loss factor damping is equivalent to loss tangent defined as:

$$\tan \delta = \frac{E''}{E'} = \eta \quad (\text{A.22})$$

where δ is the loss angle which represents phase shift between stress and strain. Now, we can write the damping matrix as:

$$\mathbf{C} = \frac{\eta \mathbf{K}}{\omega} \quad (\text{A.23})$$

and the equation of motion can be written as:

$$(-\omega^2 \mathbf{M} + (1 + i\eta) \mathbf{K}) \tilde{\mathbf{u}} = \tilde{\mathbf{f}} \quad (\text{A.24})$$

Relationship between several measures of damping are shown below for Single-Degree-of-Freedom Damping (SDOF) Models:

$$\eta = \frac{1}{Q} = 2\xi = \frac{\%C_r}{50} = \frac{\delta}{\pi} = \frac{D}{2\pi U} = \frac{\Delta\omega_{3dB}}{\omega_0}$$

Where: η is loss factor, Q is amplification factor, ξ is damping ratio, $\%C_r$ is percent of critical damping ($\%C_r = 100\% \times \xi$), δ is the log decrement of a transient response, D is the energy dissipation per cycle and U is the stored energy during loading.

- **Rayleigh Damping:** For the Rayleigh damping model, the damping matrix $[\mathbf{C}]$ is defined by the linear combination of mass and stiffness matrix:

$$[\mathbf{C}] = \alpha_M[\mathbf{M}] + \beta_K[\mathbf{K}] \quad (\text{A.25})$$

where α_M and β_K represents the mass and stiffness damping coefficients with units of s^{-1} and s respectively. Traditionally to obtain α_M and β_K , two reference vibration modes (i - and j -order) have been selected and their damping ratios ξ_i and ξ_j obtained through experiments or test data prediction with respective natural frequencies ω_i and ω_j :

$$\begin{bmatrix} \alpha_M \\ \beta_K \end{bmatrix} = \frac{2\omega_i\omega_j}{\omega_j^2 - \omega_i^2} \begin{pmatrix} \omega_j & -\omega_i \\ -\frac{1}{\omega_j} & \frac{1}{\omega_i} \end{pmatrix} \begin{bmatrix} \xi_i \\ \xi_j \end{bmatrix} \quad (\text{A.26})$$

When $\xi_i = \xi_j = \xi$ this equation can be simplified as:

$$\begin{bmatrix} \alpha_M \\ \beta_K \end{bmatrix} = \frac{2\xi}{\omega_i + \omega_j} \begin{bmatrix} \omega_i\omega_j \\ 1 \end{bmatrix} \quad (\text{A.27})$$

This damping model does not represent physical damping processes of a material. However the stiffness matrix directly proportional to the strain rate. A pure beta damping can be represented as viscous damping with

$$\begin{aligned} \eta_b &= \beta_K K \\ \eta_v &= \beta_K G \end{aligned} \quad (\text{A.28})$$

In COMSOL, we can add Rayleigh damping either as a direct input of α_M and β_K or as two damping ratios in two different frequencies.

A.2.3 Results

FEM numerical simulation provided validation and insights into the absorption coefficient behavior of the plate-type acoustic valve resonator. The comparison between the absorption coefficient predicted by the FEM numerical model and obtained by experiments are given in Fig. (A.3). The figure shows two significant peaks for the numerical and experimental results. For the experimental results, the first peak at 224 Hz with an absorption coefficient of $\alpha=0.69789$, the second peak with absorp-

A.2 NUMERICAL PREDICTION OF PLATE-TYPE ACOUSTIC VALVE RESONATOR USING TIME DOMAIN ANALYSIS

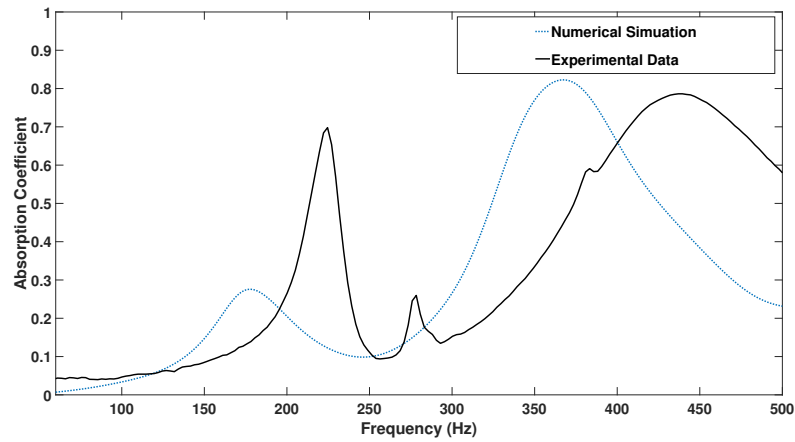


Figure A.3: Comparison between absorption coefficients as a function of frequency from numerical results with moving mesh and experimental results.

tion $\alpha=0.78625$ at 439 Hz. For the numerical results, the first peak at 178 Hz with an absorption coefficient of $\alpha=0.27572$, the second peak with absorption $\alpha=0.82262$ at 368 Hz. Although similar shape of the absorption curve is obtained, the significant difference can be seen in numerical result compared to experimental result. In general, the main reasons behind the discrepancies between the FEM simulation and experimental results are thought to lie in the material properties and geometric tolerances in the fabrication. The accurate material properties of the fabricated PLA is unknown and PLA material properties from literature was used as a close replacement of the printed material in the FEM simulation. The exact geometric dimensions of the fabricated sample also possess minor variations and unknowns. Using parametric studies of the material properties (e.g. density, Young's modulus, damping loss factor) closer match with experimental result can be obtained.

To avoid domain overlapping in the FEM model, a very small gap has been included in between mounting plate and plate-type acoustic valve. Due to the computational limitations it is not possible to model without the gap. The value for the gap is a arbitrary chosen value and kept as small as possible. Figure (A.4) shows the absorption coefficient with two different air-gap. With the smallest possible gap height $h_d=0.1$ mm, first peak at 178 Hz with an absorption coefficient of $\alpha=0.27572$ and second peak appeared at 368 Hz with an absorption coefficient of $\alpha=0.82262$. So, $h_d=0.4$ mm provided with better match with the experimental results and this value has been used for further studies. Figure (A.5) shows the absorption coefficient for two different sound pressure levels (SPL's) 94 dB and 120 dB. It can be seen from the inset that, the only first absorption peak is affected by the high sound pressure level.

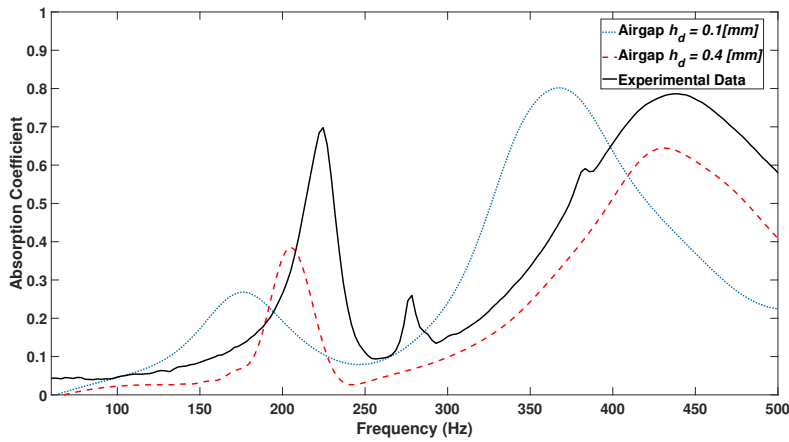


Figure A.4: Comparison of absorption coefficients as a function of frequency from numerical results with two different airgap $h_d = 0.1$ mm and 0.4 mm.

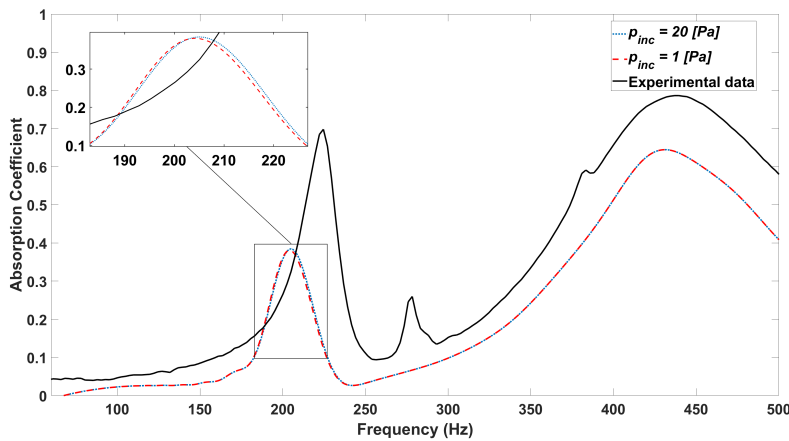


Figure A.5: Comparison of absorption coefficients as a function of frequency from numerical results with two different incident pressure $p_{inc} = 20$ Pa and 1 Pa.

A.2.4 Conclusions

Several conclusions can be made for the numerical time domain analysis of the plate-type acoustic valve resonator. For example, to simulate for the frequency ranges 50-500 Hz, the average simulation time is approximately 177 hrs. Time domain analysis requires significant computational time. Although, time domain analysis provided with reliable simulation, the frequency domain analysis proved to be the more efficient for the simulation purposes. No significant non-linear effects has been reported from the experimental results. Since the solid displacements due to the acoustic excitation relatively very small, linear estimation for the acoustic dissipation remains valid for the complete plate-type acoustic valve resonator system. Hence, the frequency domain analysis has been exten-

A.2 NUMERICAL PREDICTION OF PLATE-TYPE ACOUSTIC VALVE RESONATOR USING TIME DOMAIN ANALYSIS

sively performed for further numerical modeling of the complete plate-type acoustic valve resonator system.

A.3 FEM Modeling of Microperforated plate

Two numerical model of micro perforated plate based on finite element method (FEM) are implemented to estimate absorption coefficient. The geometric model for FEM simulation is a simplified 2D axisymmetric model to reduce computational costs and time without sacrificing the fundamental characteristics as shown in Fig. (A.6). The model represents a cylindrical impedance tube set-up with the microperforated plate to estimate the absorption coefficient. The geometric parameters used in the simulation are chosen from experimental setup described in Chapter 5. The geometric coordinates for the plane in the 2D axisymmetric implementation are (r, z) and the angle ϕ is not defined since it is not part of the computational domain implemented in the simplified model. The microperforated plate was made of rigid PCB, with a 0.2 x 0.2 m square cross-section. The physical characteristics of the micro perforation are found in the Table A.2. The microperforated plate was inserted into the square test section flush against the end of the tube. A 0.5 m cavity was created behind the microperforated plate using a series of inserts and a 2 mm extension plate at the end, followed by the hard wall backing plate. The plate was tested using a 93 dB white noise source for 120 seconds. The meshing performed using user-controlled mesh with free triangular elements. The acoustic mesh element size criterion depends on the smallest acoustic wavelength (λ_0) of the interest. Considering that largest acoustic element is never larger than the $\frac{1}{6}$ of the (λ_0), maximum and minimum element size are defined as: $\frac{c_0}{6 * f_0}$ and $d_{visc} = 220 \mu\text{m} \cdot \frac{1}{3} \cdot \sqrt{\frac{100\text{Hz}}{f_0}}$ respectively. Some boundary layer also added in the mesh to capture the viscous and thermal losses in the boundary accurately. The mesh in the vicinity of perforation hole is shown in Fig. (A.6)

A.3.1 Frequency Domain Analysis

A frequency domain analysis of the plane wave propagation is performed using the Acoustics module coupling preset Pressure Acoustics and Thermoviscous Acoustics Model. The geometric parameters used in the simulation are chosen from experimental setup described in Chapter 5. Coupling between thermoviscous acoustic and pressure acoustics is achieved with an acoustic-thermoviscous acoustic

Model	Hole diameter d [mm]	Overall porosity σ	Plate Thickness t [mm]	Cavity Depth l [mm]
A. Conceptual perforated plate	5	0.01	0.5	50
B. Micro-perforated plate	0.4	0.005	1.18	50

Table A.2: Geometrical parameters of the microperforated plates

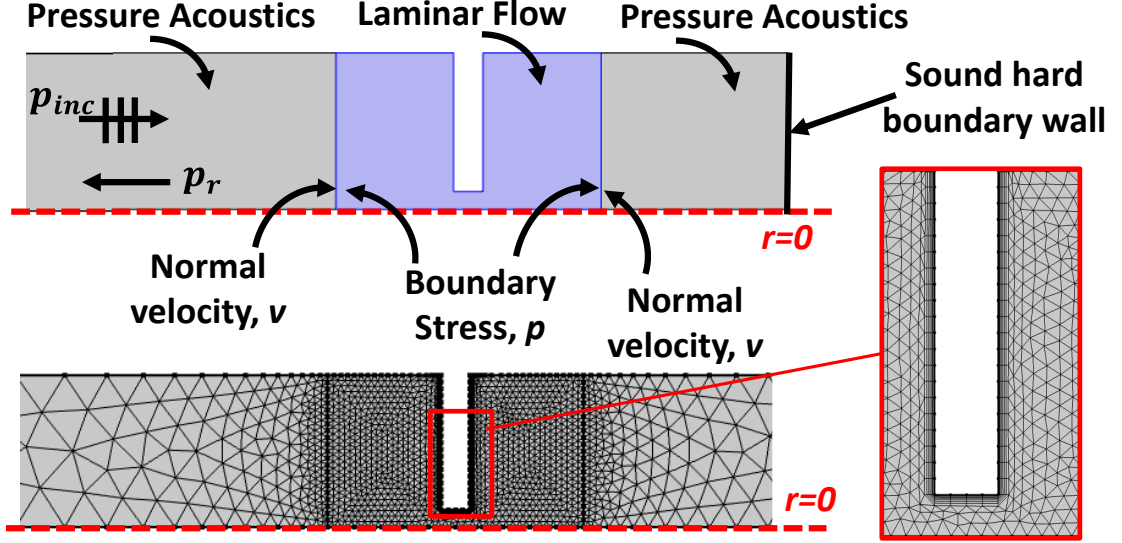


Figure A.6: Simplified 2D axisymmetric geometric model of the numerical simulation for time domain analysis (top), overview of the mesh for the setup (bottom) and the mesh shown in the vicinity of the hole with boundary layer (inset).

boundary. The Pressure Acoustics module is well suited for all frequency-domain simulations with harmonic variations of the pressure field. Governing equation for the sound pressure is defined by the Helmholtz equation in this module:

$$\nabla^2 p = \frac{1}{c_0^2} \frac{\partial^2 p}{\partial t^2} \quad (\text{A.29})$$

where, p is the sound pressure of the pressure acoustic field, t is the time and c_0 is the speed of sound. Thermal and viscous losses became significant in the region of the small perforations when sound propagates and attenuates through micro perforated plate. Therefore, the ‘‘Thermoviscous-Acoustics’’ interface is applied. Governing equations are defined by the linear Navier-Stokes equation:

$$\begin{aligned} i\omega\rho &= -\rho_0(\nabla \cdot \mathbf{v}) \\ i\omega\rho\mathbf{v} &= \nabla \cdot \left\{ -p\mathbf{I} + \mu(\nabla\mathbf{v} + (\nabla\mathbf{v})^T) + \left(\mu_B - \frac{2}{3}\mu\right)(\nabla \cdot \mathbf{v})\mathbf{I} \right\} \\ i\omega(\rho_0 C_p T - T_0 \alpha_0 p) &= -\nabla \cdot (-k\nabla T) \\ \rho &= \rho_0(\beta_T p - \alpha_0 T) \end{aligned} \quad (\text{A.30})$$

The following boundary conditions are used in numerical simulations. Incident pressure field as plane wave radiation applied as source and sound hard boundary wall and symmetry conditions also applied as shown in Fig. (A.6). In the vicinity of the walls of circular holes, rigid wall isothermal and no-slip boundary conditions are applied.

The surface impedance Z_s of the perforated plate is calculated according to average velocity reported at the surface.

$$Z_s = \frac{P}{v \cdot \mathbf{n}} \quad (\text{A.31})$$

where, v is the mean velocity in the perforation hole, \mathbf{n} is the surface normal of the perforate. The total impedance of the system can be obtained with impedance translation theorem [166].

$$Z_T = Z_0 \frac{-iZ_s \cot(kL) + Z_0}{Z_s - iZ_0 \cot(kL)} \quad (\text{A.32})$$

The reflection coefficient r is obtained as

$$r = \frac{Z_T - Z_0}{Z_T + Z_0} \quad (\text{A.33})$$

where, $Z_0 = \rho_0 c_0$ is the specific acoustic impedance of the medium (i.e., air in this case) and the absorption coefficient (α) is given as in Eq. (5.7).

A.3.2 Time Domain Analysis

The presented numerical simulation was generated using the Acoustics and Fluid Flow module (Pressure Acoustics, Transient manually coupled with Laminar Flow). A time-dependent study with a parametric frequency sweep is applied to the numerical model and the calculation for the absorption coefficient is performed as an integration of a time-dependent expression over a time interval. The fluid flow is described by laminar flow, incompressible Navier-Stokes equations:

$$\begin{aligned} \rho \frac{\partial \mathbf{u}}{\partial t} + \rho(\mathbf{v} \cdot \nabla) \mathbf{v} &= \nabla \cdot \left[-p \mathbf{I} + \mu \left(\nabla \mathbf{v} + (\nabla \mathbf{v})^T \right) \right] + F \\ \rho \nabla \cdot \mathbf{v} &= 0 \end{aligned} \quad (\text{A.34})$$

where, \mathbf{v} represents the velocity (m/s), μ is the viscosity (Pa · s), ρ is the density (kg/m^3), T is the absolute temperature (K). A no-slip ($\mathbf{v} = 0$) boundary condition is applied to all boundary walls.

A plane incident wave p_0 is applied from the left-hand side of the impedance tube with unit amplitude as incident pressure field, $p_{inc} = p_0 * \sin(2\pi f_0 t)$.

Part of the acoustic energy is reflected, and the rest is absorbed by the microperforated plate and the cavity. Pressure acoustics and laminar flow coupling done with normal velocity (v, w) and boundary stress, p . To calculate reflection coefficient, a time dependent study with parametric frequency sweep is applied to numerical model. The total sound pressure field (p) can be simulated by COMSOL and

the reflected sound pressure field is expressed as:

$$p_r = p - p_{inc} \quad (A.35)$$

In the above equation, r is the pressure reflection coefficient that gives the ratio of the scattered pressure to the incident pressure

$$\frac{p_r}{p_{inc}} \quad (A.36)$$

The calculation for reflection coefficient is performed as a integration of a time-dependent expression over a time interval. A trapezoidal integration rule is used to calculate the root-mean-square (rms) pressure [162] and calculated as:

$$p_{rms}^2 = \frac{1}{t_{end} - t_{start}} \int_{t_{start}}^{t_{end}} p^2(t) dt \quad (A.37)$$

Finally, the absorption coefficient, which represents the ratio of the absorbed and incident pressure can be calculated by Eq. (5.7). The numerical model presented in this section is largely based on a direct numerical simulation (DNS) model of a “nonlinear slit resonators” by Tam et al. [163] and FEM model of a “acoustic absorbent lining structure” by Cai et al. [164]. Similar implementation procedure and calculations are used to ensure validity of the current model. Initially, the absorption performance of the conceptual perforated plate has been presented. Both frequency domain and time domain numerical results of absorption coefficients of the absorber are compared and shown in Fig. (A.7).

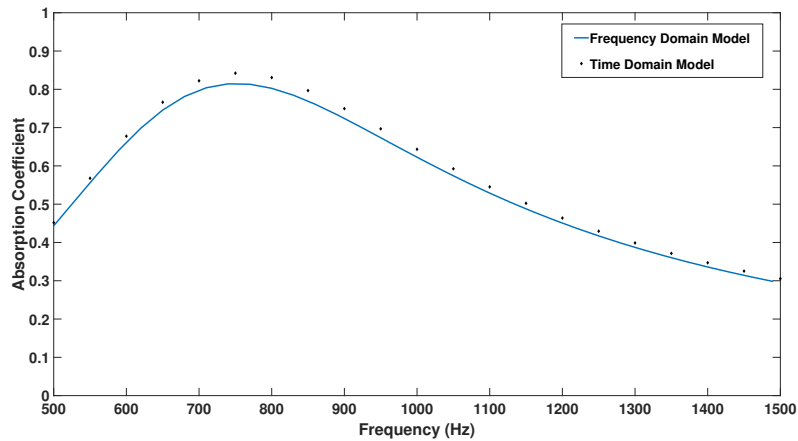
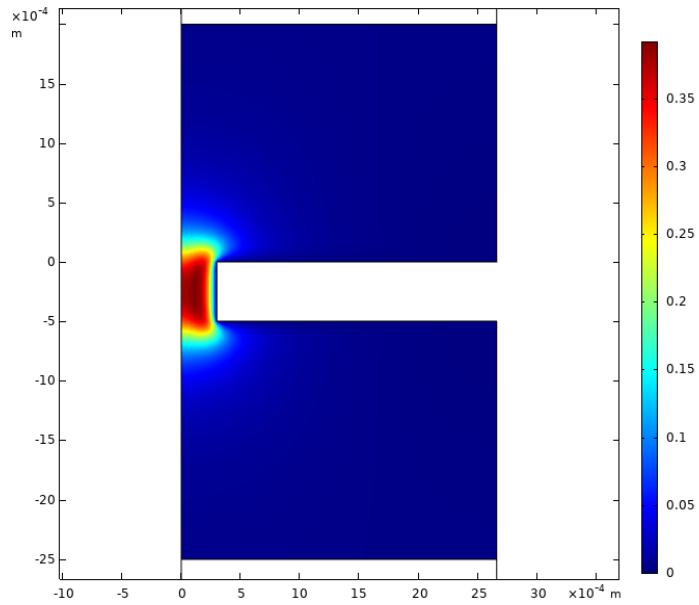
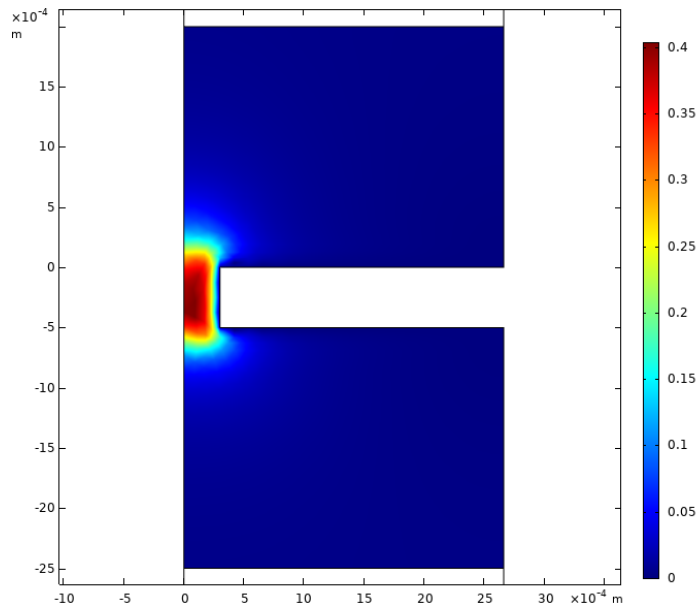


Figure A.7: Comparison of absorption coefficients in frequency domain and time domain model as a function of frequency.

Figure (A.7) shows that numerical results from the time domain analysis agree excellently with the frequency domain analysis and provide validation of modeling approach and calculation. Slight differences between the curves thought to be due to meshing effects. Using more refined mesh would be helpful to resolve this difference. Maximum absorption ($\alpha \approx 0.825$) has been observed at frequency around 750 Hz. Figure (A.8) shows the comparison of the velocity field vicinity to the perforations around 750 Hz with user defined mesh in between frequency domain and time domain model. We can observe the similar velocity profile for both numerical modeling approach.



(a)



(b)

Figure A.8: Comparison of the velocity field vicinity to the perforations with user defined mesh in (a) time domain and (b) frequency model.

A comparison of the absorption coefficients as a function of frequency from analytical, numerical (time domain) and experimental results are shown in Fig. (A.9).

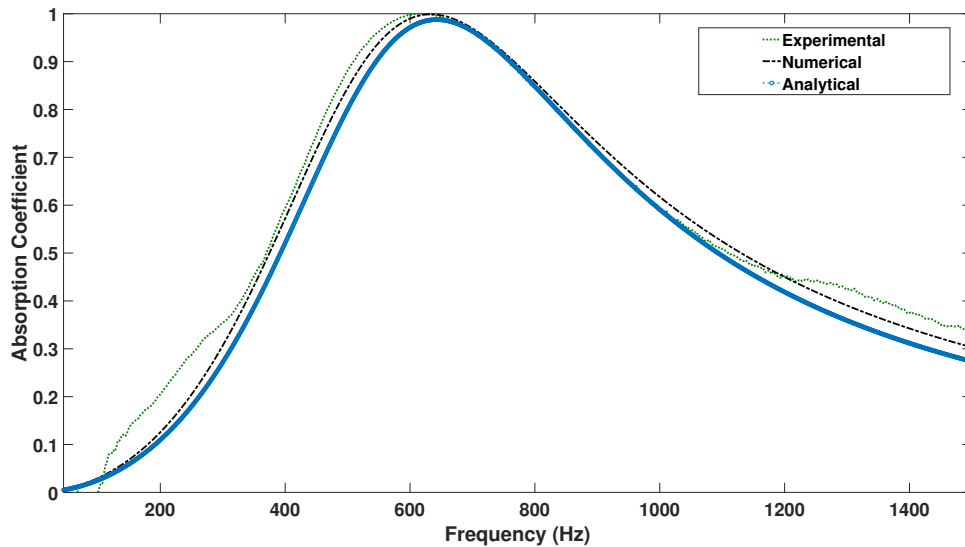


Figure A.9: Comparison of absorption coefficients as a function of frequency from analytical, numerical (time domain) and experimental results.

According to Fig. (A.9), analytical, numerical (time domain) and experimental results also shows good agreement. Numerical and experimental results show a good match for the absorption coefficients with small variations. The main reasons behind the discrepancies between the FEM simulation and experimental results are thought to lie in the small manufacturing imperfections and mechanical resonances of the plate. According to the measured and simulated results presented in this research, high absorption coefficient (almost 100%) can be obtained over a relatively big bandwidth for micro perforated absorbers.

Presented time domain MPP modeling approach is very efficient for the large amplitude acoustic modeling. In case of frequency domain analysis, it's failed to provide reliable results due to linearity involves in the modeling equations and vortex shedding effects is completely ignored. But for the large amplitude acoustic modeling time domain modeling approach provides reliable results including non-linearity in the modeling techniques. Therefore, this time domain modelling approach can be efficiently used with confidence to simulate nonlinear problems where frequency domain analysis is not suitable.

Appendix B

B.1 Eigenfrequency Analysis

An eigenfrequency analysis provides the eigenfrequencies (natural frequencies) and mode shape (eigenmode) of a linear or linearized model. An eigenfrequency analysis has been performed using only the solid mechanics part of the model for the plate-type acoustic valve to obtain structural resonance modes. The eigenfrequency analysis was set to find the first 10 eigenfrequencies for symmetric modes. The physics controlled mesh has been adapted for the model using normal element size. To get the 10 desired number of eigenfrequencies around 50 Hz, simulation run time was 2 s using the same workstation for frequency domain analysis. The governing equation for the eigenfre-

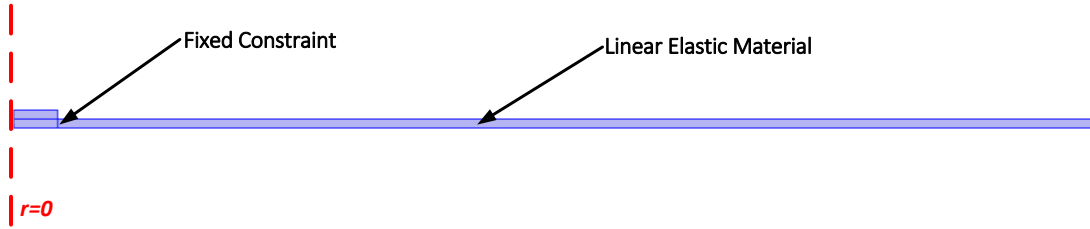


Figure B.1: Linear elastic material model for eigenfrequency analysis.

quency formulation can be written as (source terms are not included):

$$\nabla \cdot \left(-\frac{1}{\rho_0} \nabla p \right) + \frac{\lambda_{mn}^2 p}{\rho_0 c_0^2} = 0 \quad (\text{B.1})$$

and

$$\lambda_{mn} = i2\pi f_{mn} = i\omega_{mn} \quad (\text{B.2})$$

where the fundamental eigenvalue is λ_{mn} which is independent of the pressure (p) and the eigenfrequency is f_{mn} . The eigenvalue problem without damping can be expressed as

$$\left[\mathbf{K} - \omega_{mn}^2 \mathbf{M} \right] \mathbf{u} = 0 \quad (\text{B.3})$$

where \mathbf{K} is the stiffness matrix, \mathbf{M} is the mass matrix and \mathbf{u} is the eigenmode displacement vector.

The eigenvalue problem with damping can be represented as

$$\left[\mathbf{K} + i\omega_{mn} \mathbf{C} - \omega_{mn}^2 \mathbf{M} \right] \mathbf{u} = 0 \quad (\text{B.4})$$

where \mathbf{C} is the viscous damping matrix and \mathbf{K} can be complex valued.

B.2 Experimental Modal Analysis

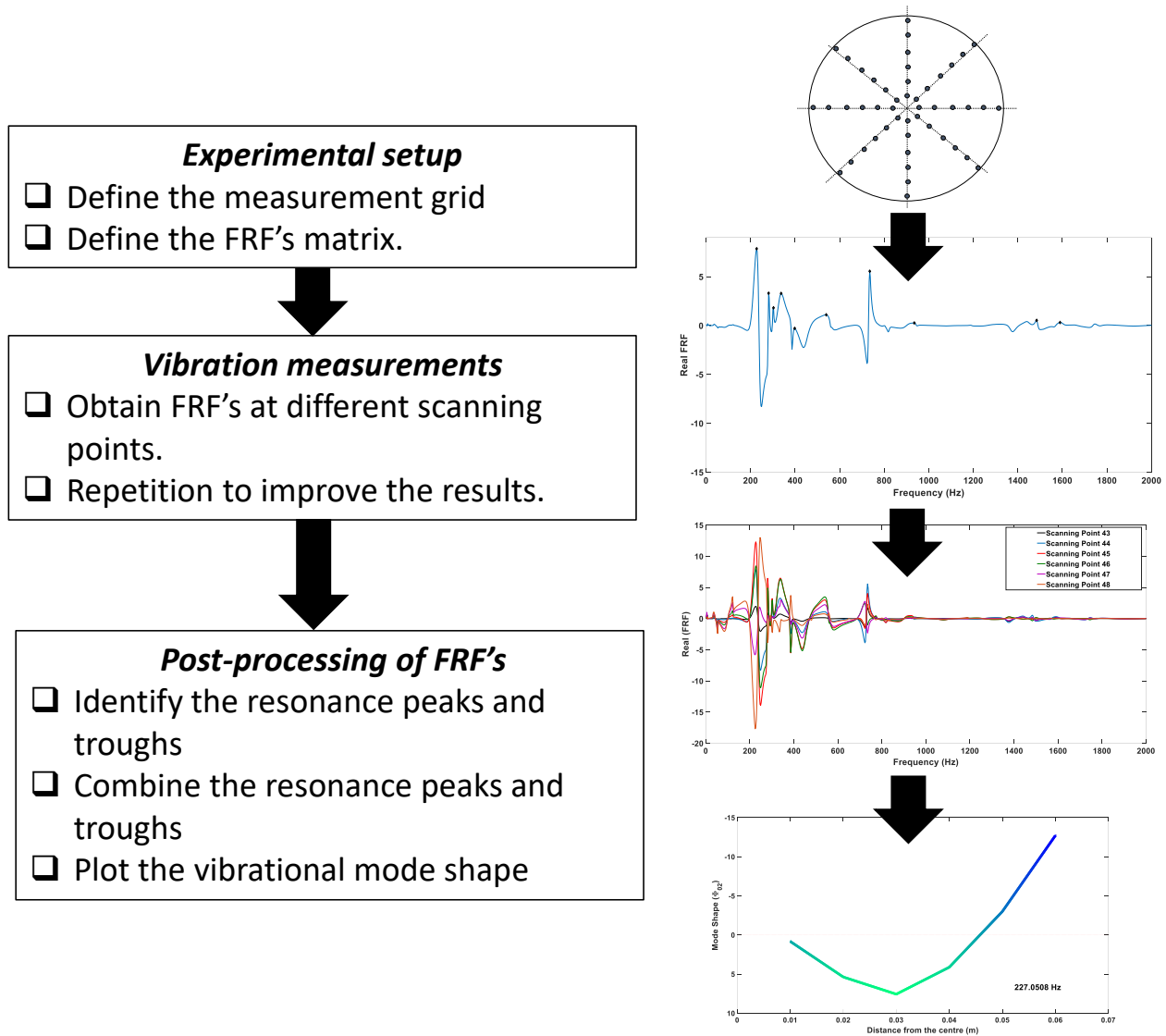


Figure B.2: Flow chart for the experimental modal analysis.

Appendix C

C.1 Cambered Design of Plate-type acoustic valve resonator

In this section, a 3D printed valves with camber similar to an umbrella valve (UM 145) of much larger diameter and thickness of $t_{AD} = 0.54$ mm has been presented. The sole purpose of this work was to investigate the effect of using different design of plate-type acoustic valve in the acoustic absorption performance. Using the cambered design leads to plate-type acoustic valve having no air-gap between the plate-type acoustic valve and mounting plate. Hence, Helmholtz resonance effect of the plate-type acoustic valve resonator should add very little acoustic absorption and only if the valves pops open. Figure. (C.1)-(C.4) shows the 3D printed sample and the it's assembly with the mounting plate.



Figure C.1: 3D printed cambered plate-type acoustic valve sample.

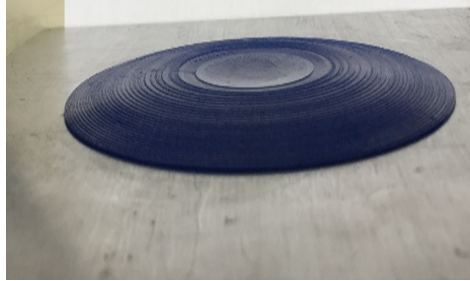


Figure C.2: Mounted 3D printed cambered plate-type acoustic valve sample.

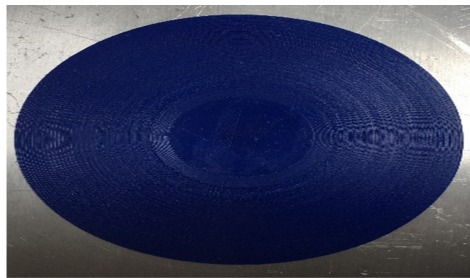


Figure C.3: Mounted 3D printed cambered plate-type acoustic valve sample(Top View).

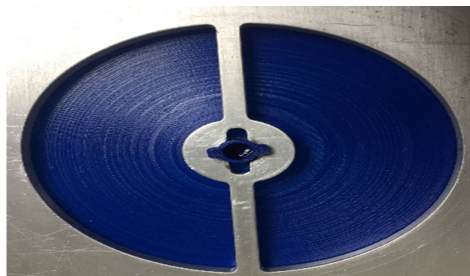


Figure C.4: Mounted 3D printed cambered plate-type acoustic valve sample (Bottom View).

To obtain absorption performance of the cambered plate-type acoustic valve, the sample has been tested in the normal incidence impedance tube similar to the procedure described in Chapter 5.1. Figure (C.5) shows the experimental absorption coefficients for different cavity depths with *SPL* of 94 dB. It can be observe that by varying cavity depths there are no significant shift to the absorption peaks. Since, there are no air-gap between mounting plate and cambered plate-type acoustic valve, Helmholtz resonance effect is not present. It can be approximated that, the acoustic absorption peaks are associated with the structural resonance frequencies of cambered plate-type acoustic valve.

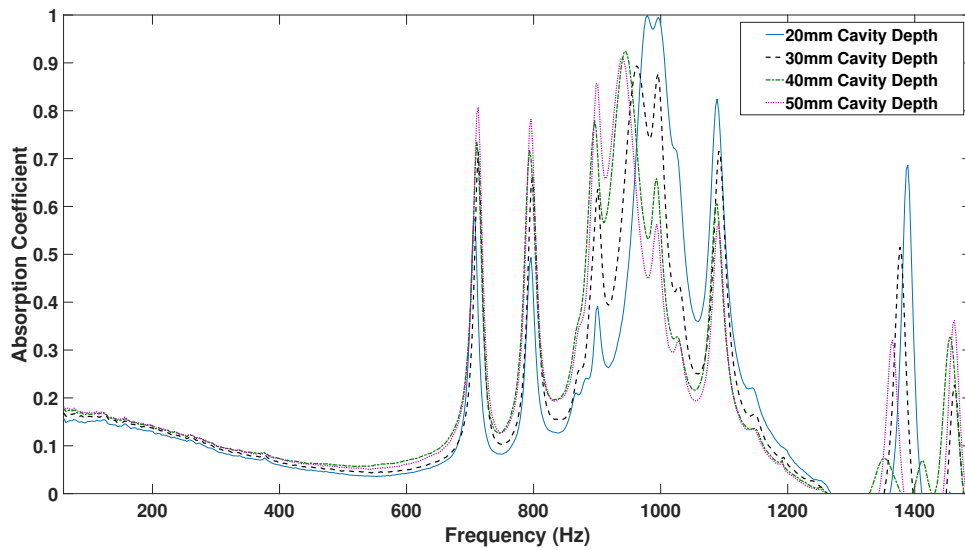


Figure C.5: Experimental absorption coefficients as a function of frequency for different cavity depths with *SPL*= 94 dB.

To predict the natural frequencies of the cambered plate-type acoustic valve, eigenfrequency analysis has been performed using a 2D axisymmetric numerical model. Solid mechanics interface of the COMSOL Multiphysics (commercial FEM software) has been applied to replicate the cambered plate-type acoustic valve. The material properties of the cambered plate-type acoustic valve has been set as: Young's modulus $E_m = 3.5 \times 10^9$ Pa, density $\rho_m = 1240$ kg/m³, and $\nu_m = 0.33$. Table C.1 has tabulated the eigenfrequencies of the cambered plate-type acoustic valve. Figure (C.7) shows the structural eigenfrequencies in the absorption curves for *SPL* of 94 dB. Some of the structural eigenfrequencies can be identified as $f_{70}=710$ Hz, f_{02} or $f_{11}=795$ Hz, $f_{80}=898$ Hz, f_{31} or $f_{03}=996$ Hz, $f_{12}=1088$ Hz, $f_{51}=1389$ Hz. To get the validation of the correct identification of the structural resonance frequencies, a modal analysis with laser Doppler vibrometry can be performed similar to the procedure mentioned in Section 5.2.2. A comparison between experimental and numerical structural resonance frequencies has been tabulated in Table C.2 which shows good agreement.

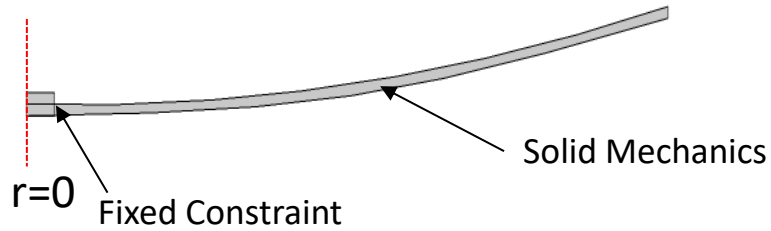


Figure C.6: 2D axisymmetric numerical model of the cambered plate-type acoustic valve for eigenfrequency analysis.

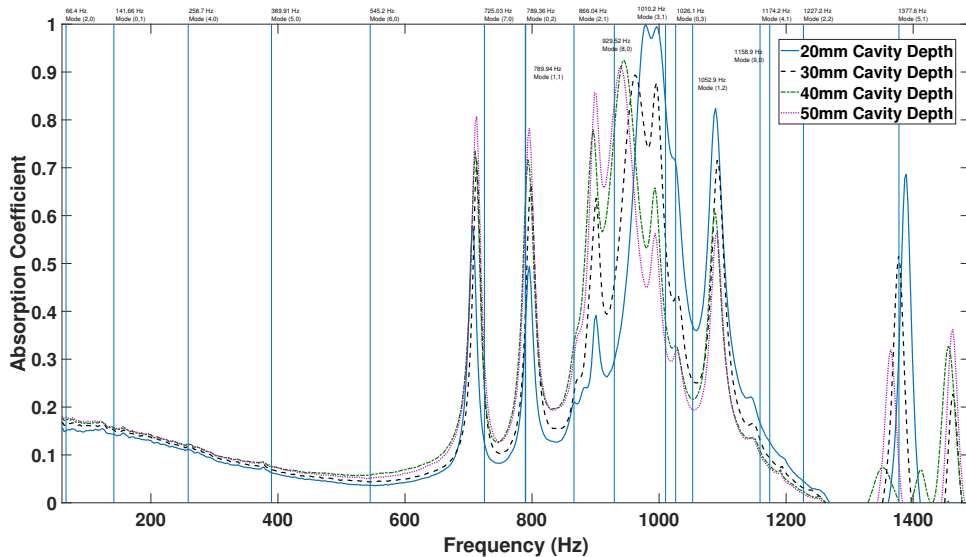


Figure C.7: Structural eigenfrequencies in the experimental absorption coefficients as a function of frequency for different cavity depths with $SPL=94$ dB.

C.1 CAMBERED DESIGN OF PLATE-TYPE ACOUSTIC VALVE RESONATOR

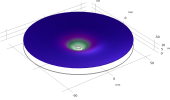
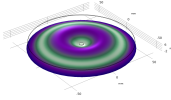
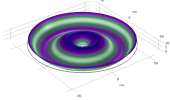
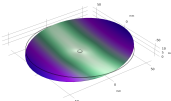
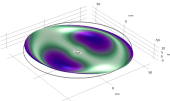
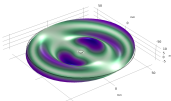
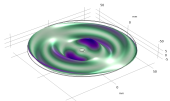
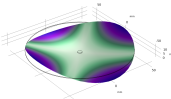
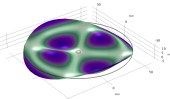
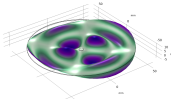
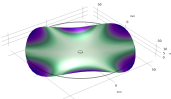
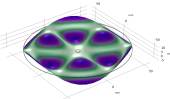
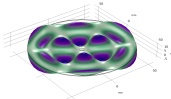
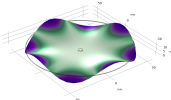
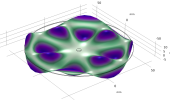
$m \downarrow \setminus n \Rightarrow$	0	1	2	3
0		 ((a)) 141.66 Hz	 ((b)) 789.36 Hz	 ((c)) 1026.1 Hz
1	 ((d)) 37.537 Hz	 ((e)) 789.94 Hz	 ((f)) 1052.9 Hz	 ((g)) 1680.8 Hz
2	 ((h)) 66.4 Hz	 ((i)) 866.04 Hz	 ((j)) 1227.2 Hz	
3	 ((k)) 151.06 Hz	 ((l)) 1010.2 Hz	 ((m)) 1502.3 Hz	
4	 ((n)) 258.7 Hz	 ((o)) 1174.2 Hz		

Table C.1: Some of the eigenfrequencies and corresponding mode shape from 2D numerical model: Eigenfrequency Analysis.

Mode (m, n)	f_{mn} [Hz] (2D Numerical)	f_{mn} [Hz] (Experimental)
(0, 3)	1026.1	996
(0, 2)	789.36	795
(1, 1)	789.94	795
(1, 2)	1052.9	1088
(3, 1)	1010.2	996
(7, 0)	725.03	710
(8, 0)	929.52	898

Table C.2: Comparison between experimental and numerical structural resonance frequencies.